EI Eridani and the Art of Doppler Imaging – A long-term Study

Dissertation
zur Erlangung des akademischen Grades
„Doctor rerum naturalium“
eingereicht von

Mag. Albert Washüttl
an der Mathematisch-Naturwissenschaftlichen Fakultät
der Universität Potsdam

Astrophysikalisches Institut Potsdam
An der Sternwarte 16
D-14482 Potsdam

Potsdam, November 2004

What is love?
What is creation?
What is longing?
What is a star?

Zarathustra

If you love a flower that lives on a star,
it is sweet to look at the sky at night.
All the stars are a-bloom with flowers...

The Little Prince

Abstract

Understanding stars, their magnetic activity phenomena and the underlying dynamo action is the foundation for understanding "life, the universe and everything" – as stellar magnetic fields play a fundamental role for star and planet formation and for the terrestrial atmosphere and climate. Nonetheless, the dynamo process that generates magnetic fields in stars is little understood, and there is still no comprehensive model of magnetic activity on the Sun and other stars. Stellar activity – a term referring to all phenomena inside and outside of a star that are related to its magnetic field – can be spotted by activity tracers such as spots, plages, flares and winds. Those features are the fingerprints of magnetic field lines, and their detailed examination provides constraints for theoretical models and allows to falsify their predictions. Our knowledge can only advance if we include stars other than the Sun in our endeavour, and therefore, it is essential to accomplish comprehensive studies of active stars with a wide range of stellar parameters and a variety of activity phenomena.

In this thesis, I concentrate on spots which are the most important sign of activity in a star's photosphere. Sunspots appear as dark areas on the surface of the Sun, and they mark places where intense magnetic flux tubes break through the Sun's surface. Starspots, however, cannot be observed directly, as it is not (yet) possible to spacially resolve the surfaces of even the nearest neighbouring stars. Therefore, an indirect approach called "Doppler imaging" is applied. This technique uses the relation between wavelength position across a spectral absorption line and spatial position across the stellar disk in order to reconstruct the surface spot distribution on rapidly rotating, active stars.

Data from 11 years of continuous spectroscopic observations of the active RS CVn-type binary star EI Eridani – gained at NSO/McMath-Pierce, KPNO/Coudé Feed and during the MUSICOS 98 campaign – are reduced and analysed. Thereby, up to 34 Doppler maps in three spectroscopic lines for 32 epochs are obtained, 27 of which are independent of each other. I find that the general morphology of the spot pattern remains persistent for the whole period of 11 years; particularly, no decrease of the polar cap was recognised. However, a high level of activity is noticed in the latitude band of 60 – 70° where appendages of the polar spot dissolve and emerge prevalently and where active longitudes are identified that migrate with respect to the orbital reference frame. Short-lived low-latitude spots do exist but are much less pronounced.

Finally, the problem of how to parameterise the information content of Doppler maps is discussed. Three approaches for parameter extraction are introduced and applied to the accumulated heap of Doppler maps: (1) average temperature, separated for several latitude bands; (2) fractional spottedness; and last, for the analysis of structural temperature distribution, (3) longitudinal and latitudinal spot-occurrence functions. The resulting values do not show a distinct correlation with the proposed activity cycle as seen from photometric long-term observations, thereby suggesting that the photometric activity cycle is not accompanied by a spot cycle as seen on the Sun.

In addition, a detailed parameter study is performed. Improved orbital parameters suggest that EI Eri might be complemented by a third component in a wide orbit of about 19 years. Using the Hipparcos parallax, absolute dimensions are derived for the bolometric magnitude, luminosity, radius and inclination of the system. Using evolutionary tracks, EI Eri's position in the HRD is located. It reveals the precise mass and age of the binary components and allows to estimate mass and additional orbital parameters of the proposed tertiary star. Eventually, preliminary differential rotation measurements are carried out, indicating an anti-solar orientation.

Wissenschaftliche Zusammenfassung

Das Verständnis magnetisch verursachter Aktivität auf Sternen sowie der zugrundeliegenden Dynamoprozesse ist von fundamentaler Bedeutung für das Verständnis von Entstehung und Entwicklung von Sternen sowie des Lebens im Universum. Aber trotz des starken Einflusses von stellaren Magnetfeldern auf Stern- und Planetenentstehung sowie auf die Atmosphäre und das Klima der Erde sind unsere Einsichten in die zugrundeliegenden physikalischen Vorgänge noch immer stark begrenzt. Es gibt nach wie vor kein theoretisches Model der magnetischen Tätigkeit auf der Sonne und auf anderen Sternen. Die Bezeichnung ,,stellare Aktivität" bezieht sich dabei auf alle Phänomene inner- und außerhalb eines Sterns, die im Zusammenhang stehen mit seinem Magnetfeld. Sichtbare Erscheinungen dieser stellaren Aktivität sind u.a. Flecken, Fackeln, Flares, Protuberanzen und Winde. Diese Phänomene dienen dabei als Indikatoren der diese verursachenden magnetischen Irregularitäten. Ihre Untersuchung gibt Aufschluß über die damit einhergehenden, jedoch durch direkte Methoden viel schwerer zu entdeckenden Magnetfelder und dient dabei als unumgängliche Überprüfung zum Zwecke der Falsifikation theoretischer Dynamomodelle. Was wir auf der Sonne beobachten, bildet unser Vorurteil über Sternaktivität, und eine Ausdehnung der untersuchten Objekte auf andere Sterne bei einer möglichst breiten Abdeckung stellarer Parameter (wie Rotationsgeschwindigkeit und -periode, Masse, Alter etc.) ist unumgänglich, auch für ein umfassendes Verständnis der magnetischen Vorgänge auf der Sonne.

In dieser Doktorarbeit konzentriere ich mich ausschließlich auf das Phänomen der Sternflecken. Sonnenflecken, die deren Paradigma bilden, erscheinen als dunkle Flächen in der Photosphäre der Sonne, und sie kennzeichnen dabei Orte, an denen starke magnetische Flußröhren durch die Sonnenoberfläche brechen. Flecken auf anderen Sternen können jedoch nicht direkt beobachtet werden, zumal mit den heutigen technischen Mitteln eine Auflösung der Oberfläche selbst der benachbarten Sterne unmöglich ist. Auf Grund dessen wird eine indirekte Rekonstruktionsmethode angewendet (,,Doppler Imaging"), die die Relation zwischen Geschwindigkeitsinformation und zweidimensionaler Intensitätsinformation verbindet, um mittels einer Zeitserie spektroskopischer Aufnahmen auf die Temperaturverteilung auf der Sternoberfläche zu schließen.

Elf Jahre kontinuierlicher spektroskopischer Beobachtungen des aktiven Doppelsterns EI Eridani (vom Typ RS CVn) – aufgenommen am McMath-Pierce-Teleskop (NSO), am Coudé Feed-Teleskop (KPNO) und während der weltumfassenden MUSICOS 98-Beobachtungskampagne – sowie 20 Jahre durchgehender photometrischer Beobachtungen wurden herangezogen, um insgesamt 34 Dopplerkarten, davon 27 voneinander unabhängige, zu erstellen. Dabei zeigt sich, daß die Morphologie der Fleckenverteilung während des kompletten Beobachtungszeitraums von elf Jahren im wesentlichen konstant bleibt; insbesondere kam es zu keiner Abnahme des dominierenden polaren Flecks. Auf hohen Breitengraden von 60 – 70° wird jedoch ein hoher Grad von Aktivität festgestellt; dabei treten bevorzugte, ,,aktive" stellare Längen auf, die innerhalb des orbitalen Bezugsrahmen wandern und nach etlichen Zyklen die (um 180° gegeneinander verschobene) primäre und sekundäre aktive Länge wechseln (Flipflop-Phänomen). Auf niederen Breiten werden kurzlebige Flecken geringer Intensität beobachtet.

Nach Auswertung aller Daten wird versucht, eine Grundlage zu schaffen für die Analyse des zweidimensionalen Informationsgehalts der angesammelten Sternoberflächenkarten. Drei Oberflächenkartenparameter werden vorgeschlagen: (1) gemittelte Temperatur, getrennt für verschiedenen stellare Breitenbänder; (2) relative Fleckenhäufigkeit; und, zum Zwecke der Auswertung der strukturellen Temperaturverteilung, (3) Längen-

und Breiten-Ortsfunktion der Sternfleckenhäufung. Die resultierenden Werte zeigen deutlich, daß kein zeitlicher Zusammenhang mit dem photometrischen Aktivitätszyklus besteht. Im Gegensatz zur Sonne gibt es also, zumindest im beobachteten Zeitraum und innerhalb der bestehenden Genauigkeit, keinen Fleckenzyklus auf dem aktiven Stern EI Eri.

Darüberhinaus wurde eine ausführliche Studie der stellaren Parameter von EI Eri durchgeführt, zumal die genaue Kenntnis etlicher Parametern eine Grundvoraussetzung darstellt für die erfolgreiche Erstellung qualitativ hochwertiger Dopplerkarten. Verbesserte orbitale Bahnparameter geben Hinweis auf einen dritten Begleiter, der den Doppelstern EI Eri möglicherweise in einem weiten Orbit mit einer Periode von ca. 19 Jahren umkreist. Anhand der Hipparcos-Parallaxe konnten außerdem absolute Größen für die bolometrische Helligkeit, Leuchtkraft, Radius sowie des Bahn- bzw. Rotationsneigungswinkels berechnet werden. Die Verwendung von Sternentwicklungsrechnungen erlaubt sodann die Lokalisierung von EI Eridanis Position im Hertzsprung-Russel-Diagramm und folglich die Bestimmung von Masse und Alter. Schlußendlich wurde noch eine vorläufige Abschätzung der differentielen Rotation auf EI Eri durchgeführt, die eine anti-solare Ausrichtung aufweist, d.h. der Pol rotiert schneller als der Äquator.

Allgemeinverständliche Zusammenfassung

Unsere Sonne weist, wie seit längerem bekannt, einen 11-jährigen Zyklus auf, innerhalb dessen die Anzahl der Sonnenflecken sowie die Gesamteinstrahlung auf die Erde zu- und wieder abnimmt. Dieser Sonnenzyklus dürfte von Zeit zu Zeit von Perioden unterbrochen werden, in denen kaum oder gar keine Sonnenflecken auftreten und die Strahlungsintensität geringer ausfällt, was eine Abkühlung des Erdklimas zur Folge hat. Nicht nur die großen Eiszeiten dürften dadurch verursacht worden sein, auch sogenannte ,,kleine Eiszeiten“ werden mit diesen kurzfristigen Zyklusunterbrechungen in Zusammenhang gebracht. Zuletzt kam es von 1645 bis 1715 zu einem solchen Einbruch, währenddessen kaum Sonnenflecken beobachtet wurden. Zu dieser Zeit war die Durchschnittstemperatur auf der Erde deutlich reduziert. In Nordeuropa kam es zu einem massiven Ernteausfall, und historische Aufzeichnungen erzählen davon, daß in einem Jahr die Einwohner Londons im Juni auf der Themse Schlittschuh liefen.

Der physikalische Mechanismus, der den Sonnenfleckenzyklus sowie das zeitweilige Ausbleiben des Zykluses verursacht, ist der sogenannte Dynamoprozeß, der das Magnetfeld der Sonne und dessen Variationen verursacht, welches wiederum für die Sonnenflecken sowie die Gesamtabstrahlung der Sonne verantwortlich ist. Könnte man diesen magnetischen Dynamo berechnen, wäre es auch möglich, die Änderungen zwischen Kalt- und Warmzeiten auf der Erde zu verstehen und dadurch vorauszusagen, wann es wieder zu einer solchen kleinen oder großen Eiszeit kommen wird. Bedauerlicherweise, v.a. wenn man dessen Bedeutung für das Erdklima betrachtet, ist dieser Dynamoprozeß bis heute größenteils unverstanden. Leider können wir in der Astronomie, wie in anderen Zweigen der Physik üblich, keine ,,Experimente“ mit der Sonne durchführen, und so ist die einzige Lösung die, eine große Anzahl von sonnenähnlichen Sternen zu beobachten und darzulegen, wie sich solche Zyklen auf anderen Sternen verhalten. Eine statistische Abschätzung solcher Sternzyklen auf einer möglichst großen Anzahl von Sternen kann somit beitragen, den Sonnenfleckenzyklus und dadurch dessen Einwirkungen auf das zukünftige Erdklima besser zu verstehen.

Einen solchen ,,Sonnenfleckenzyklus“ auf einem anderen Stern zu beobachten, war das Ziel dieser Doktorarbeit. Dazu wurde der sonnenähnliche, aktive Doppelstern EI Eridani über mehr als 10 Jahre hinweg beobachtet. Helligkeitsmessungen dieses Sternes hatten bereits Hinweise auf einen Zyklus gegeben, der eine ähnliche Länge wie der Sonnenzyklus aufweist: 12 Jahre. Flecken auf anderen Sternen als der Sonne zu beobachten, ist allerdings ein schwieriges Unterfangen, zumal auch die nächstgelegenen Nachbarsterne sogar in den größten Teleskopen immer nur als punktförmige Objekte zu sehen sind. Ein indirektes Rekonstruktionsverfahren wird deshalb angewandt (genannt ,,Doppler Imaging“), welches es ermöglicht, aus einer Zeitserie von in seine Spektralfarben zerlegten Lichts eines Sterns eine Oberflächenkarte seiner Temperaturverteilung zu erstellen. Dabei werden dessen Sternflecken sichtbar, welche nichts anderes sind als Regionen geringerer Temperatur, verursacht durch magnetische Irregularitäten.

Auf diese Weise wurde für EI Eridani über beinahe den gesamten 12-jährigen Zyklus des Sterns hinweg Oberflächenkarten erstellt, die dessen Fleckenverteilung aufzeigen. Um diese graphischen Karten quantitativ, also mathematisch auszuwerten, wurden Parametrisierungsverfahren erstellt, die die Fleckenverteilung über den gesamten Zeitraum hinweg anschaulich darstellen. Dabei zeigte sich überraschenderweise, daß – im Gegensatz zur Sonne – der 12-jährige Aktivitätszyklus nicht mit einem Fleckenzyklus einhergeht. Die

Anzahl der Flecken bleibt bei EI Eridani über den gesamten Zyklus hinweg gleich. Es zeigen sich allerdings aktive Längengrade, an denen Flecken gehäuft auftreten. Außerdem weist EI Eridani Flecken auf seinen Polkappen auf – wiederum im Gegensatz zur Sonne, auf der Flecken nur in Äquatornähe vorkommen.

Darüber hinaus wurde der Stern EI Eridani einer genauen allgemeinen Untersuchung unterzogen. Dabei zeigte sich, daß dieses Sternsystem 4.8 Milliarden Jahre alt ist, eineinviertel mal so schwer ist wie die Sonne sowie fast zweieinhalb mal größer. EI Eridani ist gerade dabei, in die Endphase seines Sternenlebens einzutreten und zu einem sogenannten Roten Riesen zu werden – eine Entwicklung, die mit der Explosion des Sterns endet und zu seinem Tod führt.

Offensichtlich ist unser Wissen über Sternzyklen und deren Einfluß auf Planeten, die um einen Stern kreisen, nach wie vor stark begrenzt. Diese Arbeit zeigt nicht zuletzt auf, daß eine größere Anzahl ähnlicher Beobachtungen notwendig ist, um unser Verständnis von Sternflecken und somit deren Einfluß auf Planeten wie die Erde zu erweitern. Insbesondere hat die Frage, in wie weit das Erdklima und die derzeitige Erderwärmung durch langfristige Änderungen der Sonneneinstrahlung bzw. durch menschliche Einflüsse wie den Ausstoß von Treibhausgasen bedingt ist, eine grundlegende Bedeutung für das Fortbestehen des Lebens und der Menschheit auf der Erde.

Contents

List of Figures

List of Tables

Chapter 1

Introduction

"Do not the heavens over-arch us yonder?
Does not the earth lie firm beneath?
Do not eternal stars rise friendly
Looking down upon us?"

Goethe, Faust, Marthens Garden

"Back off man! I'm a scientist!"

Dr. Peter Venkman, Ghostbusters

1.1 Solar and stellar activity

Most of what we know today about dynamo action in stellar atmospheres comes from observations of the Sun, whose proximity allows a very detailed analysis of the associated activity phenomena. The study of *solar activity* forms the basis for understanding *stellar activity* and, conversely, studies of activity in solar-type stars aid in understanding solar phenomena. Stellar activity, and therefore the stellar dynamo, is a fundamental key to understanding life in the Universe and Earth's habitability. Nevertheless, there is still no comprehensive model of solar and stellar magnetic activity, and our knowledge can only advance if we include stars other than the Sun in our dynamo studies.

1.1.1 Sunspots and the solar dynamo

Due to its proximity, activity phenomena are best observed on the Sun, making it our role model for stellar activity. Therefore, I start this introduction from the activity phenomena seen on the Sun, proceeding thereafter to activity on other stars.

One of the most direct (and longest observed) tracers of activity are sunspots. Sunspots are relatively cooler (by about 2000 K) and therefore darker areas in the solar photosphere, denoting places of breakthrough of magnetic lines of force through the Sun's surface. The number of sunspots visible on the solar disk varies continuously, as sunspots are carried on and off the visible disk by solar rotation. True variations occur following the appearance of new sunspots and sunspot groups via magnetic flux emergence as well as fragmentation and disappearance of existing spots and groups. At first glance, observations carried out over time periods of months suggest that these phenomena are stochastic in nature, but observations over time periods of decades reveal an intriguing cyclic pattern of gradual increase and decrease in the average number of sunspots visible on the solar disk. Sunspot records going back several centuries show two distinct classes of activity behaviour: cyclic and virtually steady. Variations of cosmogenic isotopes from geological records indicate that alternating intervals of cyclic activity and much lower activity levels have occurred for the past several millennia. The length of successive sunspot cycles varies from ~ 9 to 11.5 years, with an average cycle period of about 10.8 years. Over this cycle, the "brightness" or total irradiance of the

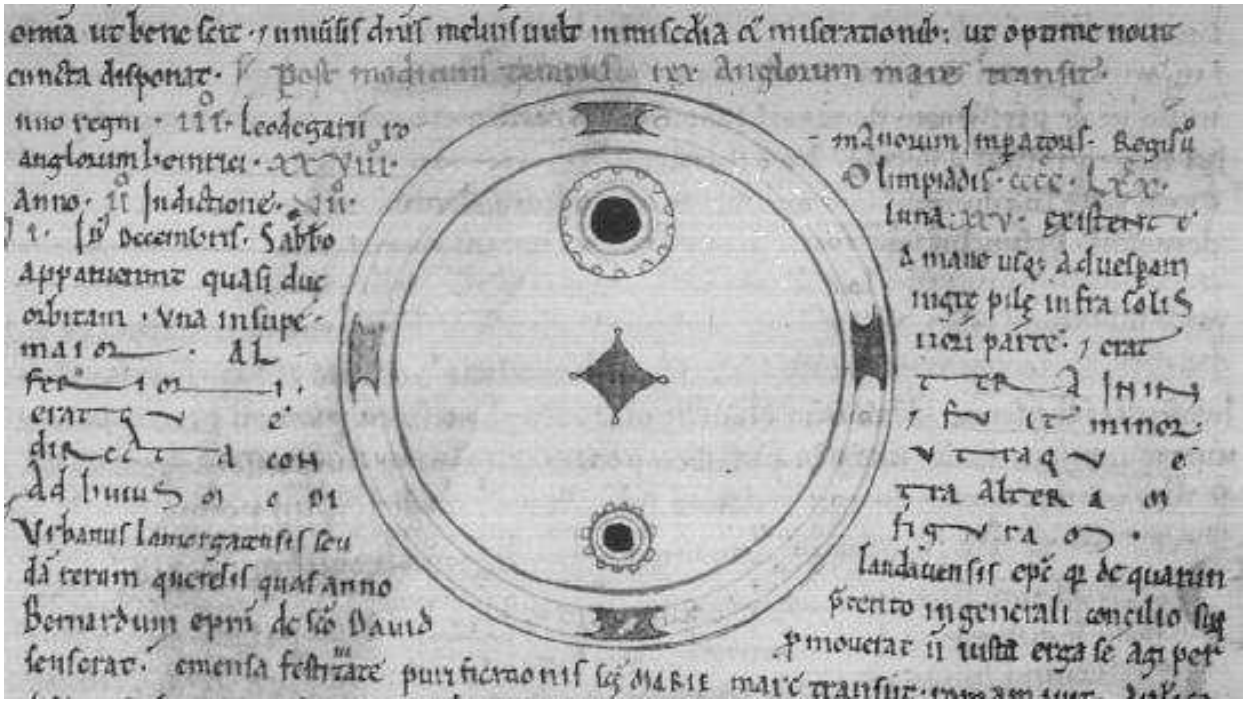

Figure 1.1: Oldest known sunspot drawing in the Chronicles of John of Worcester, twelfth century. Notice the depiction of the penumbra around each spot. Reproduced from R.W. Southern, Medieval Humanism, Harper & Row 1970, [Plate VII].

Sun fluctuates by a few tenths of a percent, with the Sun being brighter at sunspot maximum. The last extended inactive period occurred from 1645 till 1715, known as the so-called Maunder-minimum, when crops failed in Northern Europe and people were skating on London's Thames in June. The number of sunspots observed was dramatically reduced during that period. However, the nature and causes of the sunspot cycle constitute one of the great mysteries of solar astronomy. While we now know many details about the sunspot cycle (and also about some of the dynamo processes that must play key roles in producing it), we are still unable to produce a model that will allow us to reliably predict future sunspot numbers using basic physical principles.

Considering that sunspots are associated with magnetic fields, it is tempting to assume that the sunspot cycle is primarily magnetic in origin. Due to their strong impact on star formation, on the pre-planetary disk, the terrestrial atmosphere, the Sun's radiation and therefore the Earth's climate (Fröhlich & Lean 2002), stellar magnetic fields have played an important role in the entire history of the formation of the solar system and the evolution of life on Earth, and it is therefore of no surprise that we thurst for a better understanding of the solar dynamo process.

The magnetic fields in the Sun and in cool dwarfs are believed to be generated by dynamo action in the rotating star. The fact that the Sun's magnetic field changes over the course of just a few years, and the fact that it changes in a cyclical manner, indicates that the magnetic field continues to be generated within the Sun. Early models of the Sun's magnetic dynamo worked on the idea that the dynamo activity occurs throughout the entire convection zone. It was soon realised, however, that magnetic fields within the convection zone would rapidly rise to the surface and would not have enough time to experience either the α- or the Ω-effect (see Fig. 1.3, right panels). Since a magnetic field exerts a pressure on its surroundings, regions with a magnetic field push aside the surrounding gas and cause a bubble that would continue to rise all the way to the surface. This buoyancy is, however, not produced in the overshoot region which is the boundary layer between a star's radiative core and its convective envelope. Within the radiative zone, the magnetic bubble would rise only a short distance before it would find itself just as dense as its surroundings. This led to the idea that the Sun's magnetic field is produced in the interface layer between the radiative

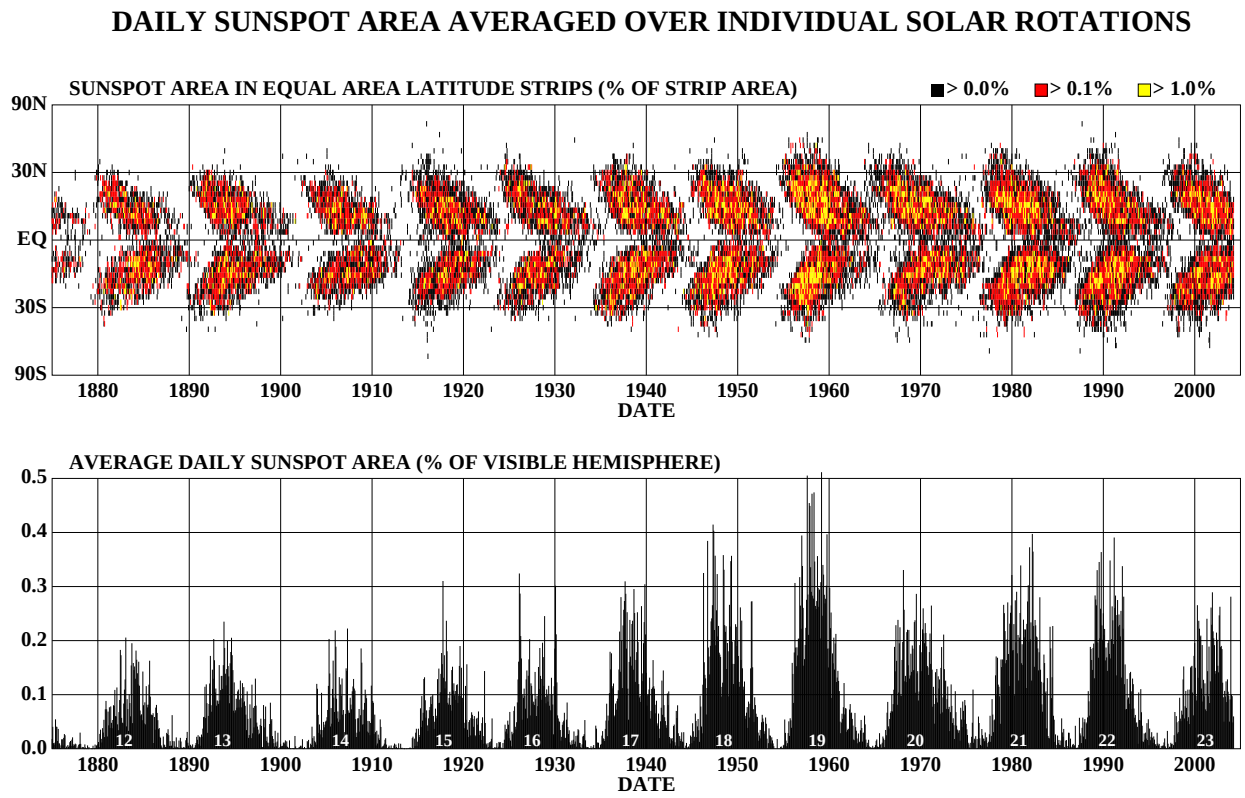

Figure 1.2: Solar butterfly diagram, showing the positions of the spots for each rotation of the Sun since May 1874 (taken from http://science.nasa.gov/ssl/pad/solar/sunspots.htm).

and the convection zone.

Theoretical dynamo models have to comply with a number of observationally established constraints. A successful model for the solar dynamo must explain several observations: 1) the 11-year period of the sunspot cycle, 2) the equator-ward drift of the active latitude as seen in the butterfly diagram, 3) Hale's polarity law and the 22-year magnetic cycle, 4) Joy's law for the observed tilt of sunspot groups and, 5) the reversal of the polar magnetic fields near the time of cycle maximum as seen in the magnetic butterfly diagram. Stellar observations will further narrow these constraints, as outlined below.

1.1.2 A minimalistic introduction to dynamo theory

There are two widely known and accepted, common types of dynamo models which are referred to as the α-Ω-dynamo and the α^2-dynamo. Empirical support for the operation of either of them is provided by the existence of pronounced positive correlations between magnetic properties and rotation: we expect to find such a correlation, if an α-Ω-dynamo is at work, and none for an α^2-dynamo.

The α effect is strongly linked to the helicity of the velocity field $\overrightarrow{v} \cdot \nabla \times \overrightarrow{v}$, where $\overrightarrow{v}$ is plasma velocity. Only non-source-free velocity fields, like turbulent velocity fields in a stellar convection zone, can provide a non-vanishing helicity. Thus, dynamo action is always bound to turbulence. Nevertheless, as outlined above, magnetic flux cannot be stored in the convection zone for long due to magnetic buoyancy (for an overview see e.g. Guinan & Giménez 1992). The overshoot region, being sufficiently stable for storage and amplification, is an ideal place for a dynamo: penetrating convective elements from the convective zone provides helicity, while the sub-adiabatic stratification blocks loss of magnetic field due to buoyancy. This is where an α-Ω-dynamo can work: The combination of the turbulent and the rotational velocity fields enhance the initial magnetic seed field by converting it from a poloidal magnetic field into a toroidal field and vice-versa. The poloidal field is generated by the deformation of the toroidal field due to shearing

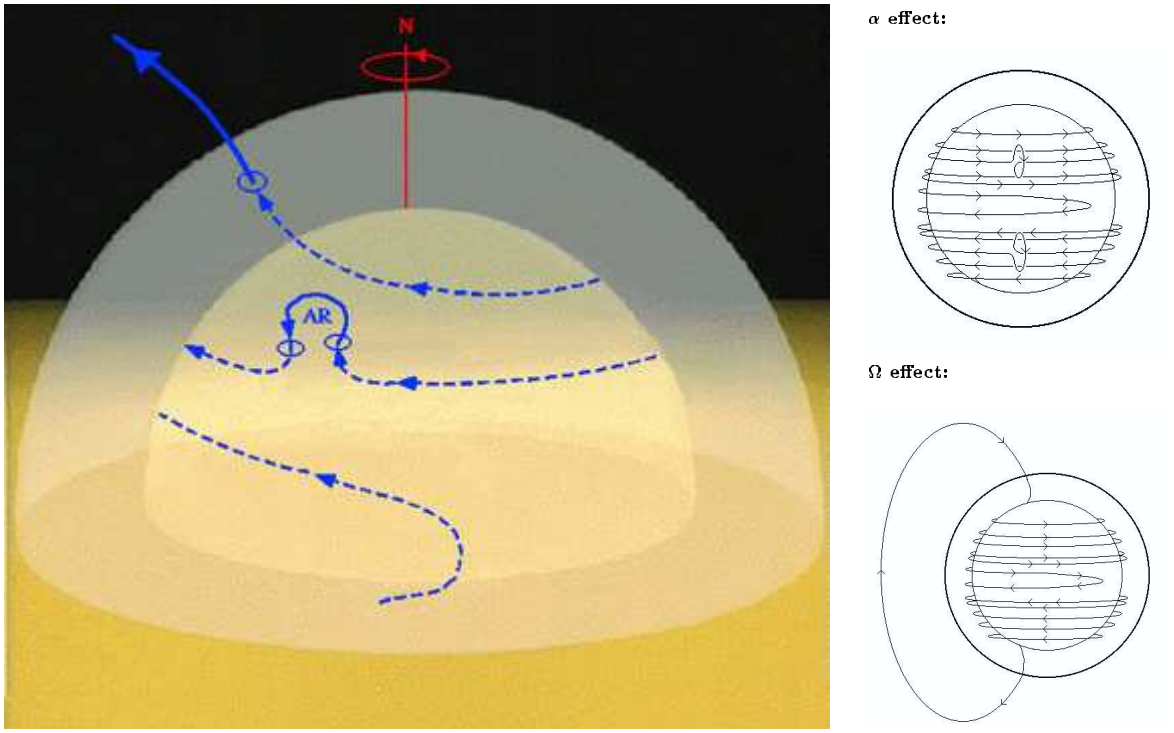

Figure 1.3: Schematic plots of the α effect (upper right) and the Ω effect (lower right). The left graph shows a pseudo three-dimensional look inside the Sun and highlights a single magnetic field line. The two shaded spheres indicate the surface and the bottom of the convection zone, respectively (so do the thick circle and the thin circle in the small panels). "AR" indicates a bipolar active region. The axis of rotation is also indicated. (After David H. Hathaway, Solar Physics Branch, Marshall Space Flight Center, NASA).

plasma motions that arise in the convective layer (α effect), while the toroidal component is generated from the shear of the poloidal field due to differential rotation (Ω effect; Parker 1955, see Fig. 1.3). The magnetic field of such a "shell dynamo" is expected to manifest itself at the stellar surface only on large scales. This means that large active regions are probably a manifestation of the toroidal magnetic field generated in the overshoot layer (Durney et al. 1993).

Other dynamo processes have been suggested, like the distributive dynamo, driven only by the non-vanishing helicity throughout the convection zone and thereby not relying on an overshoot layer (Durney et al. 1993). It is likely to operate in any star where convective turbulence is available, i.e. in stars that have a convection zone. To an observer, the important question is how to distinguish observationally between the effects of fields generated by a shell dynamo or by a distributive dynamo. As Mullan & MacDonald (2001) point out, a shell dynamo is characterised by dependence on rotation, cyclic behaviour and X-ray emissions while a distributive dynamo does not depend on rotation. See Brandenburg & Dobler (2002) for a review on recent dynamo-theory developments.

Conclusio: It is important for the observational astronomer to look out for rotation-activity connections, magnetic cycles and differential rotation on active stars. This will allow to favour or falsify certain dynamo models (see Granzer 2002).

1.1.3 Activity cycles

It's a matter of common knowledge that our Sun exhibits an spot and activity cycle of 11/22 years. In fact, several time scales of cyclic behaviour of its overall activity can be found on the Sun. The most pronounced are:

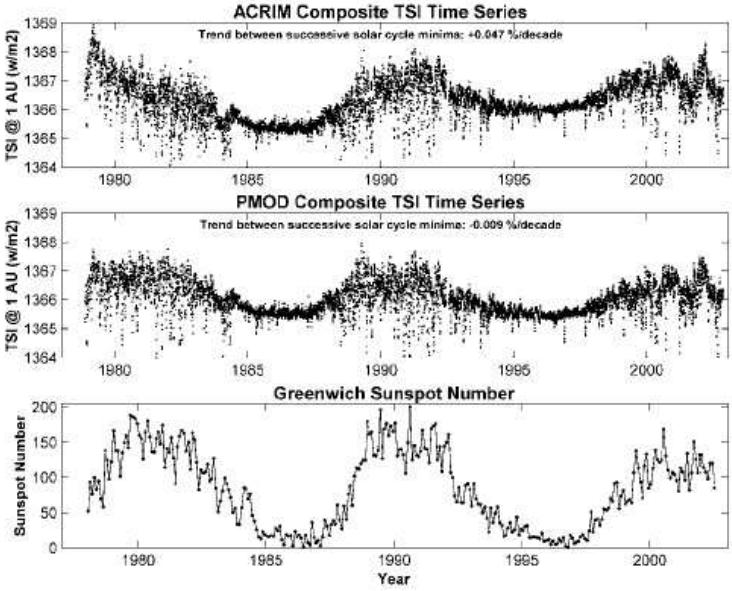

Figure 1.4: Two different measures of the solar irradiance (ACRIM and PMOD) compared to the Greenwich sunspot number. The Sun is brighter when it is most spotted. From Willson & Mordvinov (2003).

- the commonly known 11 years sunspot cycle
- the 80 years long so-called Gleissberg cycle
- an 200–300 years long pseudo-cycle (Wolf, Spörer, Maunder).

Even longer cycles or variations are plausible, and there is evidence that periods of cyclic behaviour alternate with times of constant, very low activity (e.g. Maunder minimum). In the course of a 11-years cycle, solar output is highest when the Sun is covered with sunspots since the regions around the spots (faculae, plages) actually emit more energy than when sunspots are absent. During the times of sunspot minima, solar output is much less variable. (See Figure 1.4.)

At the current point of knowledge, it is unclear, how far other stars match the Sun's role model.

Solar-type (luminosity class V) stars exhibit the same long-term cycles in their photospheric output as originally discovered from the chromospheric Ca II H & K emission (Baliunas & Soon 1995; Gray et al. 1996). However, this photosphere–chromosphere correlation cannot be reproduced for evolved G and K stars (see Choi et al. 1995). Long-term changes in the mean brightness of RS CVn stars (see §1.1.5) are, hence, not a straightforward tool for investigating spot cycles similar to the Sun's 11-year cycle. RS CVn stars are – in opposition to the Sun – very active, heavily spotted and *evolved*. It would not be too surprising, if they would differ from the solar analogon in another point: their magnetic cycle behaviour. Several factors could turn the balance: **(1)** RS CVn stars might not exhibit such a strict cyclic behaviour; **(2)** their long-term cycles might be of relatively small amplitude and masked by short-term irregularities; **(3)** their cycles might not be regular showing a replicating length (even the Sun's cycle length varies by 10–20%); **(4)** their cycle periods might be much longer than those found for solar-type stars (which amount to 7 – 21 years according to Baliunas & Soon 1995).

The Mt Wilson Ca II H & K survey of solar-like stars, started by Wilson in 1966 (e.g. Wilson 1978), is the most well-known attempt to find correlations between the lengths of activity cycles and other physical parameters. Two classes of long-term activity records were found in solar-type stars: cyclic and low-/non-variable (Baliunas et al. 1995, see Fig. 1.5), thereby confirming the well-known picture from the Sun. Radick et al. (1998), investigating Sun-like stars, show that young, active stars tend to become fainter at the time of cycle maximum (i.e. increased HK emission) while older stars (and also the Sun) tend to become brighter. A simple interpretation of this behaviour is that the long-term variability of young

stars is spot-dominated, whereas for the older stars is faculae-dominated. On the other hand, short-term photometric and chromospheric emission variations are almost always anti-correlated, like on the Sun. This may indicate that Sun-like stars, both younger and older, tend to organise their surface magnetic activity into active regions broadly similar to those seen on the Sun.

From what we know from our Sun, we would expect such an activity cycle to be accompanied by a spot cycle. Several groups began long-term Doppler-imaging studies (see §1.3) on a few selected active stars (that usually consist of one or a few images per year, i.e. per observing season). Among these stars are HR 1099, AB Dor, LQ Hya, II Peg, IM Peg, CM Cam, HD 199178, V410 Tau, ER Vul and, of course, EI Eri. All of them are active stars and most of them are close binaries with their rotation period usually spinned up by tidal forces. However, so far only one star, HR 1099 (Vogt & Hatzes 1996), has been observed over a sufficiently long time span to cover a complete activity cycle with Doppler maps.

EI Eri obviously exhibits cyclic behaviour, as seen in the photometric long-term data (Fig. 1.7). The cycle's length, however, is a source of on-going consideration. Within the first 16 years of photospheric observations, EI Eri gave the impression of a cycle of similar length to the solar cycle: Strassmeier et al. (1997) calculated a length of 11 ± 1 years. However, observations in the following years did not confirm this cycle as they did not meet the anticipated decline of brightness. Berdyugina & Tuominen (1998) estimated a 9-year periodicity from the positions of active regions. They did not discuss a possible change in the level of spottedness itself, though. Oláh et al. (2000) favoured a length of 16.2 years on a time base of 18.5 years and quote a significant remaining period of 2.4 years. Adding four more years of data, the preferred cycle length is now back to 12.2 years. The previously found 2.4 years short cycle is confirmed (see Olah & Strassmeier 2002).

It is not yet clear how far stellar cycles resemble the solar cycle. After each solar 11-year cycle, the polarity of the magnetic field changes. If such a polarity inversion is indeed present for stars such as EI Eri, we would expect it to change the morphology of the polar spot which might decay and reemerge as a new cycle begins. Cyclic behaviour is strongly related to differential rotation as the α effect, the source of the solar magnetic field, seems to be unable to produce an oscillating dynamo without differential rotation (see §1.1.2).

1.1.4 Differential rotation and meridional flows

Differential rotation is one of the basic ingredients invoked to explain the generation of the solar magnetic field due to its ability to transform a large-scale poloidal field into a stronger toroidal component. The details of this general principle are far from being understood. It is therefore a major aim for stellar differential rotation measurements to evaluate how stellar activity is connected to differential rotation.

We know from our Sun that its surface – as seen from the rotational rates of spots on different latitudes – does not rotate solidly but differentially, with higher surface features rotating slower than the equatorial area (a review on differential rotation can be found in Ruediger 1989). The rotation law at the photospheric level can be expressed by

$$\Omega = \Omega_0 + \beta \sin^2 \phi + \gamma \sin^4 \phi \ , \tag{1.1}$$

where Ω is the angular velocity at latitude ϕ, Ω_0 is the equatorial angular velocity and β and γ define the differential rate. In many solar studies, γ is set to 0 since the latitudinal coverage of the sunspots is quite small. In stellar studies, γ is never used. The differential rotation itself is described by

$$\alpha = \frac{\Omega_0 - \Omega_p}{\Omega_0} \ , \tag{1.2}$$

where Ω_p is the polar angular velocity. Solar studies yield $\alpha = 0.15 - 0.21$ and $\Omega_0 = 2.879 - 2.972\mu\,\mathrm{rads}^{-1}$ for different types of sunspots and $\alpha \approx 0.285$ and $\Omega_0 = 2.972 - 2.974\mu\,\mathrm{rads}^{-1}$ for supergranules. Small spots on the Sun rotate faster than larger ones and young faster than old ones, while sunspots rotate generally slower at the begin of the solar cycle and faster at the end of the cycle (Komm et al. 1993). It has been suggested that the rotation rate of a spot corresponds to the rotation rate at the anchor depth of the spot (e.g. Rhodes et al. 1990; Tuominen & Virtanen 1988), with a deeper anchor depth for young sunspots and an more shallow depth for old ones (Zappala & Zuccarello 1991).

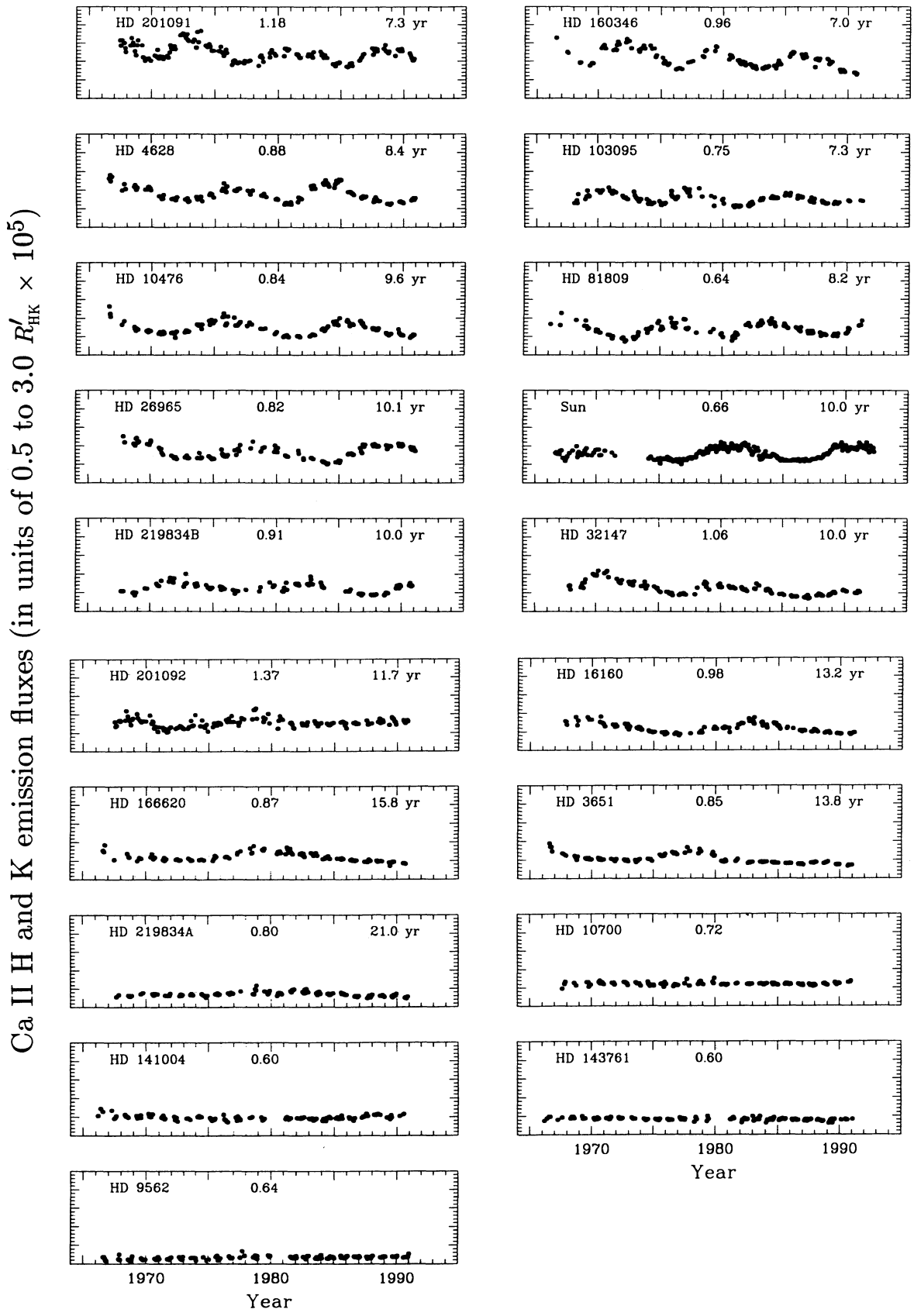

Figure 1.5: Chromospheric Ca II H & K fluxes for the Sun and 18 solar-type stars. The three numbers in each panel denote the HD number, $B - V$ photometric index and the activity-cycle length. From Baliunas & Soon (1995).

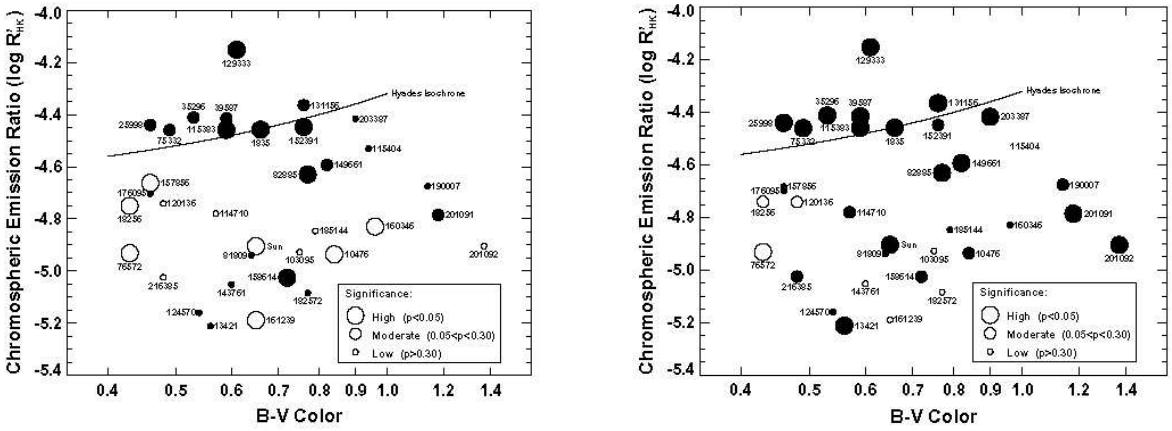

Figure 1.6: Correlation between photospheric brightness variation and HK emission variation, displayed on activity-colour axes. **Left.** Long-term variation. **Right.** Short-term variation. Filled circles denote stars that become fainter as their HK emission increases, open circles are stars that become brighter. (From Radick et al. 1998).

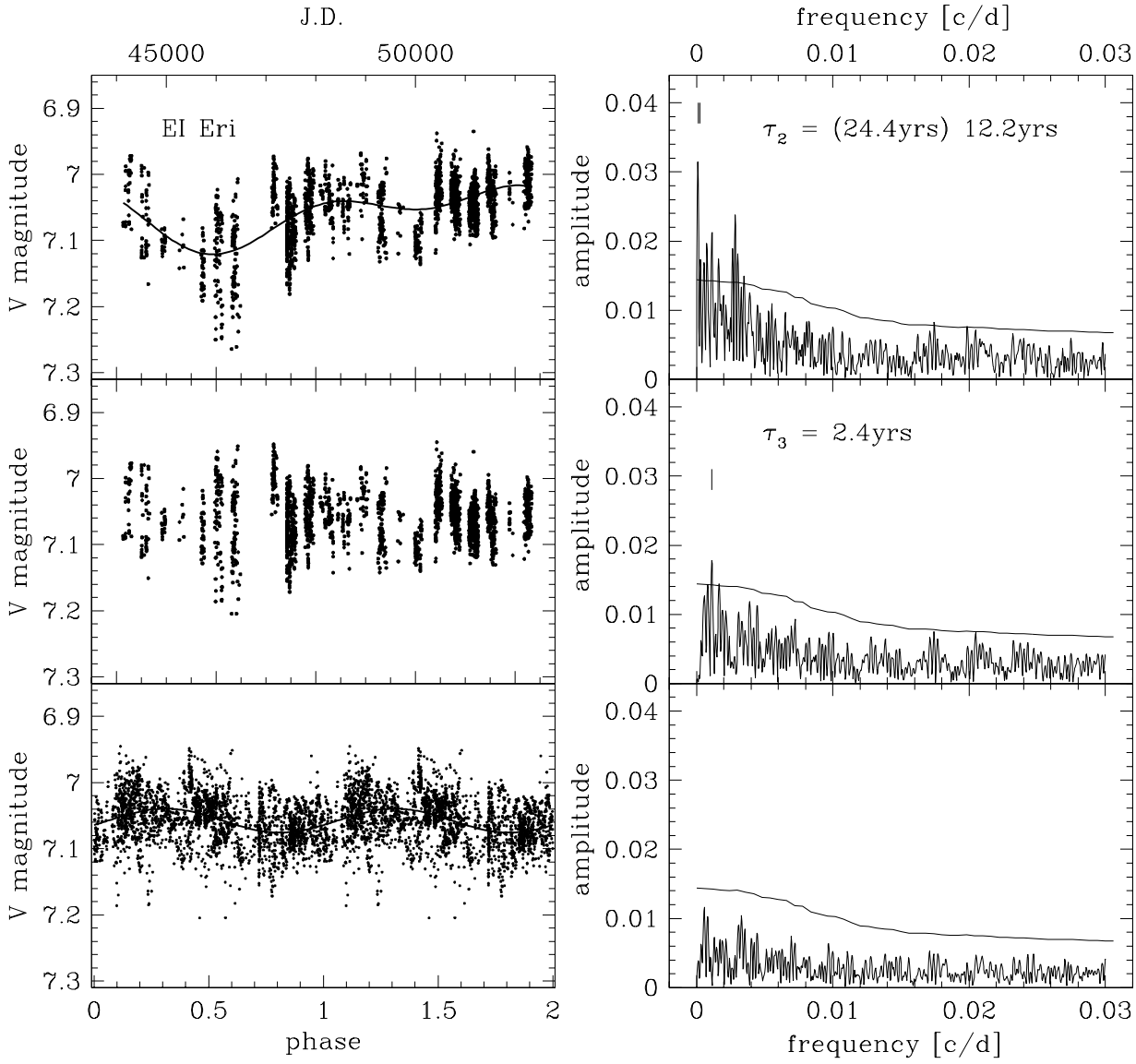

Figure 1.7: Long-term photometric observations of EI Eri from Olah & Strassmeier (2002).

Stellar differential rotation on cool stars can be studied by means of long-term photometry, from the periodic modulation of the Ca II H & K emission or making use of the Doppler imaging technique (see Collier Cameron 2002). As pointed out by Petit et al. (2002), differential-rotation parameters can be recovered reliably as long as the total data set spans at least four percent of the time for the equator to lap the pole by approximately one complete cycle. However, the method of comparing successive Doppler images faces some problems as pointed out by Petit et al. (2004a) and, therefore, has to be accomplished by additional indicators (see §5.3). Differential rotation rates have been estimated for the following RS CVn stars (for a more comprehensive list of differential-rotation detections for active late-type stars, see Strassmeier 2003):

1. II Peg: $\alpha = -0.05$ - $+0.015$, Henry et al. (1995); Rodonò et al. (2000); Weber (2004)
2. IM Peg: $\alpha = -0.03$, Weber (2004)
3. UX Arietis: $\alpha = -0.02$, Vogt & Hatzes (1991)
4. HU Vir: $\alpha = -0.011$ - $+0.006$, Strassmeier (1994); Vogt et al. (1999a); Henry et al. (1995); Strassmeier & Bartus (2000)
5. HR 1099: $\alpha = -0.004$, Vogt et al. (1999b)[1]
6. UZ Lib: $\alpha = -0.0026$, Oláh et al. (2003)
7. EI Eridani: $\alpha = +0.002$, Hatzes & Vogt (1992)
8. RT Lac: $\alpha \approx +0.003$, Lanza et al. (2002)
9. IL Hya: $\alpha = +0.004$, Weber & Strassmeier (1998)
10. RS CVn: $\alpha = +0.01$ - $+0.04$, Rodono et al. (1995)
11. HR 7275: $\alpha = +0.022$ - $+0.04$, Strassmeier et al. (1994)
12. σ Gem: $\alpha = +0.038$, Henry et al. (1995)
13. λ And: $\alpha = +0.04$, Henry et al. (1995)
14. V1149 Ori: $\alpha = +0.08$, Hall et al. (1991)
15. KU Peg: $\alpha = +0.09$ - $+0.34$, Weber & Strassmeier (2001)
16. V815 Her: $\alpha = +0.184$, Jetsu et al. (2000).

Obviously, most of the investigated RS CVn stars show weak solar-type differential rotation. Hall (1991) found that differential rotation is weaker in more rapidly rotating stars. The theoretical turbulence models by Kitchatinov & Rüdiger (1999) show that the absolute value of the surface differential rotation decreases initially as the rotation period decreases from the solar value but changes to a slight increase for periods of a few days. They predict that the differential rotation on giant stars is much larger than on dwarf stars. The orientation of the differential rotation is solar-like for all their models. Although anti-solar differential rotation has previously been noted to alter the line profiles in a similar way as a large polar cap, Hatzes et al. (1996) concluded that this would require an unreasonably strong differential rotation.

Meridional flow – the flow of material along meridian lines from the equator towards the poles at the surface and from the poles to the equator deep inside – must also play an important role in a magnetic dynamo (Choudhuri et al. 1995). At the solar surface, this flow rate is slow with about $20\,\mathrm{m\,s^{-1}}$, but the return flow towards the equator deep inside the Sun (where the density is much higher) must be even slower: about 1 to $2\,\mathrm{m\,s^{-1}}$. Such a slow return flow carries material from the polar regions to the equator in about 20 years – a rate that is very similar to that of the sunspot activity bands seen in the butterfly diagram (see Rüdiger & Elstner 2002). Anti-solar differential rotation, as found in some RS CVn stars, might indicate anti-solar meridional circulation, i.e. directed towards the equator at the surface and vice-versa at the bottom of the convection zones. This waits to be confirmed by observational results. (For contradicting results on KU Peg, see Weber & Strassmeier 2001.)

[1] For a contradicting result, see Petit et al. (2004b).

1.1.5 "Unveil thyself!"[2] – RS Canum Venaticorum stars

The type of stars that we are focusing on – as they supply us with ideal candidates for this kind of investigation – are called RS Canum Venaticorum stars, or short RS CVn stars. RS CVn stars are close but detached, chromospherically active binary stars that rotate synchronously due to tidal forces. They thereby present "normal" stars that are spinned up in rotation. It is characteristic of RS CVn binaries (see Fekel et al. 1986) to show periodic light variations that cannot be attributed to pulsation, eclipses or ellipticity – thereby resembling changing or rotating activity features. Their enhanced emission can be detected over a wide range of the spectral domain, especially in the Ca II H & K lines which usually exhibit strong emission in their line cores. The more active component is an evolved F, G or K star (subgiant or giant). The projected equatorial rotational velocities of those RS CVn stars that have been Doppler imaged ranges from 17 to 117 $\mathrm{km\,s^{-1}}$, their rotational periods from 0.6 to 25 days. Their photometric light curves often exhibit long-term variations that are possibly cyclic as well as wave-like distortions on shorter time scales that migrate towards decreasing orbital phase and that have variable depths of the primary minimum. The activity phenomena observed in these systems are attributed to the presence of magnetic fields generated by a dynamo process, and their fast rotation is believed to be responsible for the high activity level found on these stars. As such, these stars are valuable laboratories to study "the Sun in action".

1.2 Polar spots

Two decades of surface imaging (see §1.3) provided us with a striking fact: Obviously, it is a common characteristic of very active stars to have giant starspots on their rotational poles. For many years, however, polar spots were a doubted phenomenon ...

1.2.1 "Is it phantom? Is it reality?"[3]

Critics pointed out that Doppler imaging is based on periodic variations in spectral line profiles, while a polar spot just causes a flat-bottomed "filled-in" line-profile shape. Many mechanism were proposed holding against the reality of polar spots: The in-filling or deformation of the photospheric lines could be caused by an overlying chromospheric temperature rise (Byrne 1992; Unruh & Collier Cameron 1997), by differential rotation, limb brightening, gravity darkening or by problems with the radiative transfer calculations. However, high-latitude features have since then been found by many researchers on various stars applying a variety of techniques, and polar spots are now a generally accepted feature.

From a phenomenological point of view, facts in favour of polar spots are:

- If the flat-bottomed spectral line profiles are due to a stellar atmospheric effect rather than the presence of a cool polar spot, then it would show up as a *time-independent symmetric* effect (as for example a circular polar cap or equatorial ring). The opposite is true for many RS CVn stars, including EI Eri. (See Tuominen et al. 2002 for a "polar" spot that is clearly detached from the star's rotational axis.)
- We *do not* see a large polar spot on *all* RS CVn stars (eg. σ Gem, Hatzes 1993).
- Some RS CVn stars do show a polar spot at a particular time and none at some other time (eg. LQ Hya).
- RS CVn stars show an inclination dependence of the line-core flattening in a way that low inclination stars have the most flattened line cores (Hatzes et al. 1996). This cannot be explained satisfactorily by any uniform atmospheric effect.

One important effect, though, that can erroneously cause a polar spot is an underestimation of the spectral flux contribution from the unspotted companion star. Failure to properly remove the flux contribution

[2] Goethe, Faust I, Night
[3] Goethe, Faust I, Study

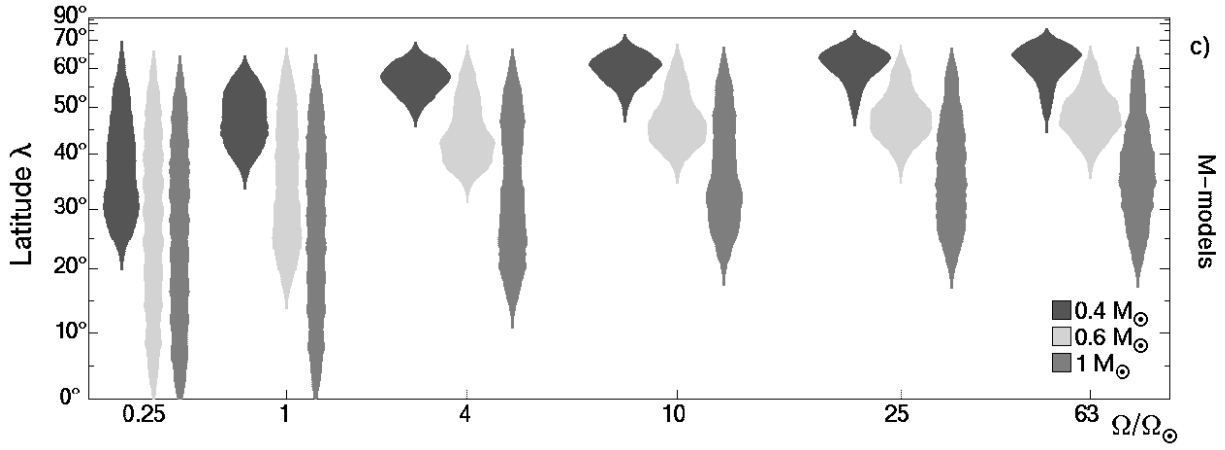

Figure 1.8: Flux-emergence simulations for ZAMS stars with different mass and rotational velocity; from Granzer et al. (2000). The axis of abscissae gives increasing rotation, the ordinate plots stellar latitude. The grey areas represent the spot-probability function, a normalised measure of probability of starspot formation as a function of stellar latitude. The probability rises as the appropriate area widens.

of the secondary component from the composite spectrum will cause the spectral lines of the primary to appear more shallow than they actually are. Too shallow lines can then be interpreted as an axisymmetric polar cap (see Aarum 1999).

1.2.2 The kernel of the brute: Flux tube deflection

Out of a sample of about 65 stars that have been Doppler mapped so far (about 40% of which are RS CVn-type stars), 97% have high-latitude and/or polar spots at least at one epoch, and as many as ∼60% have spots covering the rotational pole. Only 6% show no high-latitude/polar spot at least at one epoch (Strassmeier 2002). All of them are rapid rotators (which is an intrinsic requirement for Doppler imaging). In clear contrast, the Sun does not show any spots above a latitude of 50°.

It is generally believed that the rapid rotation is responsible for the high activity level and the high level of large spots. However, investigating the sample of surface mapped stars, it is not (yet) possible to identify any stellar parameter (like rotational velocity, rotational period or stellar radius) as a key ingredient for the latitudinal distribution of starspots (see Strassmeier 2001, Fig. 2). Binarity as such is also not crucial to the formation of polar spots. The list of polar spotted stars also includes young, rapidly rotating main-sequence stars (like the K0 V star AB Dor; e.g. Collier Cameron et al. 1999), two Pleiade stars (K0 V + K4 V; Stout-Batalha & Vogt 1999), single FK Comae stars, young T Tauri stars and W UMa contact systems. We therefore conclude, that the occurence of polar/high-latitude spots is also not correlated to target class. The only property in common for stars with polar spots is the rapid rotation and the therefore enhanced activity level.

Using very basic theoretical assumptions on stellar activity, Schuessler & Solanki (1992) already concluded that rotational rate is the key ingredient to explain polar spots. In a more elaborate study, Granzer et al. (2000) applied a thin flux-tube approximation to model the ascent of magnetic flux from the overshoot region to the star's surface. A flux tube, amplified in the overshoot region by dynamo action, is exposed to a small disturbance. The disturbance eventually grows and leaps out of the overshoot region into the convective envelope, where the growth of the disturbance is exponentially amplified by the superadiabatic stratification until it evolves into a rising loop. There are basically two scenarios leading to polar spots (see Fig. 3 in Granzer et al. 2000): **(1)** In a rapidly-rotating sun-like star (with a large radiative core), the Coriolis force may deflect rising flux tubes to high latitudes while the main part of the flux tube still remains anchored in the overshoot layer. (Fig. 1.8 shows the resulting spot distribution.[4]) **(2)** In a rapidly-

[4] Note that there are no simulations for evolving/evolved stars at the moment, only for ZAMS stars. However, these

rotating cooler star (with very small radiative core), magnetic tension lifts the previously anchored part of a flux tube along the overshoot layer towards the rotational axis where the entire loop detaches and rises, governed only by buoyancy forces, either to equatorial or to polar latitudes. Intermediate spot emergence, in this case, is unlikely. — Problems of these two approaches are: **(add 1)** Rotation may deflect rising flux to higher latitudes, but not to the polar cap. **(add 2)** Maintaining a continuous high polar-cap flux is difficult if there is a clear activity cycle with a migrating dynamo wave. Therefore, it is important for the observational astronomer to look out for spot occurence as a function of latitude and to investigate its dependence on a possible activity cycle as well as the long-term stability of a polar cap, if existent.

1.3 Doppler imaging

The existence of cool spots on stars other than the Sun, first discovered by photometric means, is now well accepted. However, photometric observations do not reveal detailed information about latitudinal structures on a star's surface. As spacially resolved images of our neighbouring star's surfaces are reserved to future observers (Freytag et al. 2002; Wittkowski et al. 2002; Carpenter et al. 2004), an indirect method has to be applied. By fitting the distortions in Doppler-broadened photospheric absorption-line profiles, two-dimensional surface images can be derived. This technique – named *Doppler Imaging* – has proved to be a very valuable tool for investigating cool spots. By using the relation between wavelength position across an absorption line and spatial position across the stellar disk we can derive an indirect image of a star's surface, usually using maximum entropy or Tikhonov regularisation to work around the nonuniqueness of the solutions. A set of model parameters (V_r, $T_{\rm eff}$, i, $v \sin i$) is determined in advance by independent means, and is then being improved using the goodness of fit (χ^2) from Doppler imaging in a way that a number of Doppler images are produced varying one variable over a certain range. The value (and the Doppler image) that yields the lowest χ^2 is chosen (or interpolated via graphing χ^2 versus the relevant parameter and finding the minimum; see Rice 1970; Rice & Wehlau 1990). An alternative to the use of χ^2 minimisation to select the optimum value of a parameter was first employed by Collier-Cameron & Unruh (1994) who selected the value on the basis of minimum spot area. Photometric data from the same epoch (if existent) are fitted simultaneously with the spectroscopic data: the photometric and spectroscopic χ^2 are added together with a variable weight to produce a single overall χ^2 that is accessed by the regularisation algorithm.

The requirements for Doppler imaging are fairly stringent: In order to avoid phase gaps (which result in artifacts in the surface map) the observations need to be well distributed over a rotation cycle. Furthermore one needs high quality spectra (S/N $\geq$ 200) at fairly high resolution (approx. $\geq$ 30-40,000), the star must be a rapid rotator ($v \sin i$ between 20 and 100 $km\ s^{-1}$) and the inclination of the rotation axis should be within 30 and 70°.

The first application of Doppler imaging to high-quality spectroscopic data of an RS CVn system was that of Vogt & Penrod (1983). They imaged the RS CVn system HR 1099 (though without regularisation) and found a large polar spot. Since then, a number of rapidly-rotating stars including RS CVn binaries, single giants, main sequence and young T Tauri stars have been mapped in temperature distribution, whereas Ap stars have been mapped in chemical abundance. The technique of Doppler imaging has revealed the existence of cool spots on stars other than the Sun (e.g. Strassmeier et al. 1991; Strassmeier 1994, 1996; Vogt & Hatzes 1991; Collier-Cameron & Unruh 1994; Kürster et al. 1994). In contradiction to what is seen on the Sun, a large numer of the mapped late-type stars contain a polar spot, and almost all show near-polar spots or high-latitude spot activity (for a review see Strassmeier 2002). Some stars, like EI Eridani, even exhibit huge polar caps that seem to be present at all times. Its nature and origin are a point of ongoing discussions. On the Sun, typical spot lifetimes do not exceed two solar rotations. This might also be true for others stars, and EI Eri seems to correspond to this image.

Spot lifetimes, differential rotation, meridional flows and magnetic mapping techniques are matters of ongoing efforts. A major problem we face today with conventional Doppler imaging is the urge to link hundreds of maps from dozens of stars to other stellar parameters, and the quest for proper parameterisation, i.e. quantitative analysis of surface maps.

simulations clearly point out the possible role of the coriolis forces on the spots' latitude.

Chapter 2

Observations & Data Reduction

> "Farewell! Dear Sun, as you go to bed, farewell!
> Now the glittering stars shimmer golden.
> How close am I to you, stars in the heavens,
> We travel far and wide through this world,
> You are always for us a faithful guide."
>
> *Schubert, Swansong, Farewell*

> "Please do not attempt to pet or feed any wild animal no matter how friendly. Skunks are rather numerous. Although generally tolerant of astronomers, they do not like to be approached. It is easy to stumble on one at night. To avoid such unpleasant consequences, we require that you carry a flashlight (for detection, not defense). A flashlight will also aid you in spotting other nighttime road hazards such as rattlesnakes. They usually rattle first, but not always."
>
> *Kitt Peak User Handbook*

Our spectroscopic data were obtained from several different observing facilities and observing campaigns, respectively:

- KPNO Coudé feed telescope (four visitor observing runs),
- NSO McMath-Pierce telescope (synoptic program and one visitor observing run),
- MUSICOS 98 campaign (joint observing run of seven observatories).

KPNO (Kitt Peak National Observatory) and NSO (National Solar Observatory) are Divisions of the National Optical Astronomy Observatories (NOAO), which is operated by the Association of Universities for Research in Astronomy, Inc. (AURA) under cooperative agreement with the National Science Foundation (NSF). Both, KPNO and NSO, hold observing facilities at Kitt Peak, outside of Tucson in Southern Arizona, which were used extensively for this research project.

MUSICOS (for MUlti-SIte COntinuous Spectroscopy) is an international project for obtaining high-resolution spectra of a single target for several days continuously. To do this, high-resolution spectrographs are used on several 2m-class telescopes well distributed around the world during an joint observing run. Such a *MUSICOS campaign* is organised every two years, and several stellar targets are selected for each campaign. EI Eri participated in November/December 1998 during the MUSICOS 98 campaign.

The following applies to all data: HJD is the heliocentric Julian date, corrected for the mid-point of an observation. Δt denotes the integration time. All data are phased with the orbital period derived in chapter 3.2. See Table 2.1 on page 17 for a detailed list of all observing facilities that contributed data for this research project.

2.1 Kitt Peak National Observatory (KPNO)

The KPNO (Kitt Peak National Observatory) data were obtained with the Coudé feed telescope (0.9m effective telescope diameter). For the 1994 run (March 4 – 18; hereafter: "CF94") and the 1995 run (Feb. 22 – March 7; "CF95") we applied the 800 × 800 TI-5 CCD chip (15μ pixels), grating A, camera 5, the long collimator, the blue corrector and a 280 μm slit giving a resolving power ($\lambda/\Delta\lambda$) of 36 000 at a wavelength of 6420 Å (the FWHM of an unblended Th-Ar comparison lamp line was about 1.7 pixel; dispersion was 0.1 px/Å). The useful wavelength range of the resulting spectra is 80 Å. For the 1996 run (Jan. 11 – 25; "CF96") we used the then new 1000 × 3000 pixel Ford CCD (F3KB chip, 15μ pixels; two pixels each were binned), with an otherwise identical spectrograph set: camera 5, grating A and the long collimator. F3KB enables a much larger wavelength region (∼320 Å from λ6335 to λ6655) but at a somewhat lower spectral dispersion of ≈ 0.105 Å per pixel. The resolving power is 24 000 at 6420 Å as measured by the larger FWHM of a Th-Ar line of about 2.6 pixel. We achieved a signal-to-noise ratio of ≈300:1. An additional observing run primarily dedicated to EI Eridani was undertaken in winter 1997/98 (Dec. 26 – Jan. 15; "CF97"). This time, we employed the TI-5 chip again, seeking the better resolution. The FWHM of a Th-Ar line turned out to be about 2.0 pixel and the resolving power consequently about 30 000. The spectrograph configuration was the same as above.

With the integration time of 2700 – 3600 s, we achieved a signal-to-noise ratio of up to 300–400:1. The spectrum covers ≈ 320 Å from λ6335 to λ6655.

Figure 2.1: The Coudé feed telescope on top of the spectrograph of the 2.1m. In the background (left) you can see the top of the McMath tower. This is Kitt Peak in southern Arizona.

A typical night of observations includes 20–40 biases, 10–20 flat-field images, and 2–3 integrations of a thorium-argon hollow cathode lamp for establishing the wavelength scale, at least one at the beginning and one at the end of each night. Additionally, at least one observation of a radial velocity standard star (see chapter 3.2) was taken per night. Neither the TI CCD nor the F3KB CCD show discernible signs of fringing at the wavelength of our observations. Consequently, no attempts were made to correct for it (other than the standard flat-field division).

Data reduction was done using the NOAO/IRAF software package and followed our standard procedure as described in Weber & Strassmeier (1998) which includes bias subtraction, flat fielding and optimal aperture extraction. All spectra were checked for narrow telluric water lines. These lines can be blended with Doppler imaging lines and produce misleading artifacts in the surface maps. The spectra of a rapidly rotating ($v \sin i \approx 300$ km s^{-1}) hot B-star revealed these telluric lines originating in the terrestric atmosphere and were compared with the spectra of EI Eri. Fortunately, in most cases no blend of a telluric line with

a Doppler imaging line occurred, and no corrections were applied to the line profiles. The only exception are a few spectra from the 97 run where a small telluric line hits the 6430Å line in several cases. These were either corrected by subtracting a hot B-star spectrum or, if no satisfactory result was achieved by this method, expelled from our sample of spectra.

Special care was exercised during the continuum fitting process. A low-order polynomial was sufficient to find a satisfactory continuum solution for all CF spectra. The observing logs for the KPNO runs are listed in Table A.21 – A.24 (see page 131).

2.2 National Solar Observatory (NSO)

The National Solar Observatory (NSO) operates an observing facility at Kitt Peak in Arizona, including the McMath-Pierce solar telescope at an elevation of 2096m. The McMath-Pierce (or just McMath) comprises three telescopes in one (main, east and west auxiliary) which can be used concurrently or independently. It is intended for solar research, but night-time observation is possible, too, in conjunction with the high-resolving stellar spectrograph. The main telescope, which was used for our observations, has an effective mirror size of 1.52m and an impressive focal length of 82.62m (f-ratio 54).

Figure 2.2: The McMath-Pierce telescope at sunset, seen from the Coudé feed. They are located on Kitt Peak, southern Arizona.

Our data were obtained on the one hand during a **regular visitor observing run** covering 70 nights (from November 1, 1996, to January 8, 1997; hereafter: "M96"), and, on the other hand from 1988 till 1995, participating in the synoptic nighttime program (which is described in chapter 6.1). The 58 spectra from the 70 nights long '96 observing run were taken using the 4.6m vertical Czerny-Turner stellar spectrograph (Smith & Jaksha 1984) with the Milton-Roy grating #1 and the 105-mm transfer lens together with the 800 × 800 TI-4 CCD camera (15μ pixels) at a dispersion of 0.118 Å/pixel. The mean FWHM of Thorium-Argon emission lines was around 2 pixels. At the beginning of an observing night, we aimed at an value of 1.5 pixels which was reached in many cases. However, during an observing night, it would typically drift between 1.6 and 2.2 pixels. We finally adopted 1.9 pixels as typical, "average" value, corresponding to a resolving power of ∼29 000 (varying between 27 000 and 32 000). The spectra were generally (except the first week, 01/11–08/11, where integrations were taken in one shot) recorded in a sequence of 3 × 15 minutes exposures and added up later performing cosmic ray removal, the integration time of the combined spectra was mostly between 1200 and 3600 s. The observations cover the wavelength range of about 45 Å

from 6410 to 6460 Å and include three lines suitable for Doppler imaging: Fe 6411, Fe 6430 and Ca 6439. The average signal-to-noise ratio is ≈150:1. Data reduction was done using the NOAO/IRAF software package in the same way as for the KPNO coudé feed data (see above). Usually, 20 flat-field exposures with a Tungsten lamp were taken at the beginning and at the end of each night, about three exposures of a Thorium-Argon reference lamp and at least one observation of the IAU radial velocity standard star α Ari (K2 III, $v_r = 14.51 \pm 0.11 \mathrm{km\,s^{-1}}$; Scarfe et al. 1990) were taken each night. Table A.20 on page 130 gives the observing log and the radial velocities. The 58 spectra cover altogether 35.4 consecutive stellar rotations.

The second part of the NSO observations were part of the **synoptic night-time program** at the McMath-Pierce telescope during the years 1988 till 1995. The same 800 × 800 TI-4 was applied in conjunction with the Milton-Roy (B&L) grating #1 but with a significantly better dispersion of 0.096 and an average FWHM of a comparison lamp emission line of 1.6 Å/px, thus increasing the resolution to R=42 000, giving an effective wavelength resolution of 0.15 Å (see Strassmeier et al. 1991). For wavelength calibration, a Th-Ne comparison lamp was used. The signal-to-noise ratio of the NSO synoptic spectra reaches in most cases 200–300:1. The observations are summarised in Table 6.1 (page 83). Observing logs and RVs are given in Tables A.1–A.19 (p.123–p.130).

2.3 MUSICOS campaign 1998

MUSICOS stands for MUlti-SIte COntinuous Spectroscopy and is an international observing campaign spanning a number of high resolution spectrometers coupled to telescopes of the 2m class, well distributed around the world, that aims at achieving continuous spectroscopic observations of dedicated stellar objects. The fifth MUSICOS campaign took place from November 22 to December 11, 1998. It involved seven northern and southern observing sites and provided continuous data for six scientific programs. More details about the MUSICOS 98 campaign and the results can be found in chapter 5.

2.4 Observational requirements for mapping EI Eri

For Doppler imaging it is important to obtain high signal-to-noise ratios (S/N $\geq$ 200) at moderate to high resolution ($\lambda/\Delta\lambda \approx$ 30–40,000). The wavelength region around 6420 Å provides up to four relatively unblended lines usable for Doppler imaging : Ca I 6439, Fe I 6430, Fe I 6411, and Fe I 6393 and were therefore chosen for the single-order spectrographs available at the McMath and CF telescope.

EI Eri's unfortunate rotational period is, amounting to 1.945 days, almost an integer multiple of the day/night cycle. As a consequence, one ideally needs 20 nights of continuous observations from a single observing site in order to achieve perfect phase coverage. In practice, 14 consecutive nights are sufficient to give a good-quality Doppler image. However, it is still possible to obtain Doppler maps from even shorter observing periods, but extended phase gaps bring artifacts or reduce structural information in the surface images (see section 4.2.5).

In order to reduce the risk of cosmic ray hits, one can decide to split one observation and take a series of short 10- or 15-min exposures which are later combined as appropriate.

Resolution for Doppler imaging

Due to the stars rotation, the integration length of a single observation is not arbitrary. While one integration is being taken, the star rotates and the spot pattern is shifted. This leads to a smearing of the surface information embedded in the line profile, resulting in a less resolved Doppler map. Therefore, the integration time as well as the possibility to sum up consecutive images (for increasing signal/noise) is limited. Generally speaking, rotational smearing for a single observation should, ideally, not exceed 5 degrees of the stellar surface or 1 – 2 percent of the rotation period. For EI Eri, this would limit one observation to about 40 minutes. However, at diminished observing conditions, one has to ponder upon whether stopping observation

Table 2.1: Observing facilities and overview of the observations

Site	Acronym	Date	HJD (24+)	n [a]	Detector	Disp. [Å/px]	ThAr FWHM [px]	$\lambda/\Delta\lambda$ [Å]	Observer [b]
NSO	NSOsyn	1988, Nov 16 – 1995, Dec 28	47481.9 – 50079.9	98	TI-4	0.096	1.6	42 000	PA, TT
	M96	1996, Nov 01 – 1996, Jan 08	50388.9 – 50457.8	58	TI-4	0.118	1.9	29 000	MW, TT, AW, KGS
KPNO	CF94	1994, Mar 05 – 1994, Mar 15	49416.6 – 49426.6	3	TI-5	0.106	1.7	36 000	KGS
	CF95	1995, Feb 21 – 1995, Mar 06	49770.6 – 49783.6	5	TI-5	0.106	1.7	36 000	AW, KGS
	CF96	1996, Jan 10 – 1996, Jan 24	50093.6 – 50107.8	24	F3KB	0.104	2.6	24 000	AW, KGS
	CF97	1997, Dec 27 – 1997, Jan 15	50809.6 – 50828.9	57	TI-5	0.1055	2.0	30 000	AW
MUSICOS		1998, Nov 21 – 1998, Dec 13	51139.4 – 51159.6	95	various				various; see §5

[a] ... Number of spectra
[b] ... Observers: KGS = Klaus G. Strassmeier, AW = Albert Washuettl,
MW = Michael Weber, TT = Trudy Tilleman, PA = Paul Avellar

Table 2.2: EI Eridani on the Vienna APTs. Status: April 2004.
Note that T7 is further on continuing observations of EI Eri.

	Wolfgang (T6)	Amadeus (T7)
comparison star	HD 25852	HD 25852
check star	HD 26584	HD 26584
1st observation	JD 2450711 / 1997-09-20	JD 2450395 / 1996-11-08
last observation	JD 2451094 / 1998-10-08	JD 2453057 / 2004-02-21
N(picked)	303	2348
N(success)	252	1660
N(used)	b:208/y:206	V:1355/I:1303
abort rate [%]	16.8	29.3
Variable − comparison star, minimum − maximum value:		
Δb (T6) / ΔV (T7)	-0.926 − -1.025	-0.734 − -0.881
Δy (T6) / ΔI (T7)	-0.760 − -0.839	-0.494 − -0.617

after 40 minutes and reading out a low S/N spectrum or accepting a little phase smearing for an acceptable S/N level.

Let's have a dedicated look at the spatial resolution aimed at: The time resolution of consecutive spectra was 2700 – 3600 s corresponding to a spot motion of 6 – 8° in longitude on the central meridian of the stellar surface or 5.2 – 6.9 km s^{-1} (0.11 – 0.15 Å) in the spectral line profile. This is still within one resolution element across the broadened line profile: With a typical resolving power of 24 – 36 000 ($\lambda/\Delta\lambda$), we achieve 8 – 12 resolution elements across the stellar disk, which corresponds to a velocity resolution of 8.3 – 12.5 km s^{-1} (0.18 – 0.27 Å) and a spatial resolution along the equator at the stellar meridian of approximately 10–14°. The orbital smearing accounts to 2.7 – 3.6 km s^{-1} (0.06 – 0.08 Å). We therefore extended our integration limit to 60 minutes.

2.5 Photometric observations

Photometric data were provided by the Wolfgang (T6) and Amadeus (T7) 0.75m Automatic Photoelectric Telescopes (see Granzer et al. 2001) of the University of Vienna twin APT at Washington Camp (previously, before summer 1996, on Mt. Hopkins) in southern Arizona. Both telescopes are part of the Fairborn Observatory in the Sonoran desert near Tucson, Arizona (Strassmeier et al. 1997).[1] Each observation of EI Eridani consists of two blocks – one each for V and I (T7) / b and y (T6) – of one bright navigation-star (Nav), two sky, two check- (Ck), four comparison- (C) and three variable-star measurements in the following order: Nav-CK-Sky-C-V-C-V-C-V-C-Sky-CK. Integration time of a single measurement is 10 seconds (T7). So, "one" observation takes $2 \times 12 \times 10 = 240$ seconds plus telescope movement. The JD identified with a final photometric value is the medium time of both observation blocks. Note that the specific observation time of a V value precedes the given JD while I values lose by about (up to) 120 seconds.

The measurements were made differentially with respect to HD 25852 as the comparison star and HD 26584 as check star. We applied a statistical procedure to eliminate all datapoints with an standard deviation greater than $\pm 0\overset{\text{m}}{.}02$. Datapoints that deviated from the rest by 2σ were taken out manually (the remaining number is listed as "N(used)" in Table 2.2). By these means, about 28% of the datapoints were expelled. All VRI photometry from Amadeus was transformed to match the Johnson-Cousins $V(RI)_C$ system as described below. In addition, older photometric observations back to 1980 were used from the literature (see Strassmeier et al. 1997, Table 5).

The APT began nightly observation of EI Eri with T7 on November 8, 1996 (JD 2450395) in I_C and V and with T6 on September 20, 1997 (JD 2450711) in b and y. Up to April 2004, we obtained about 1355

[1] See http://www.aip.de/groups/activity/APT/

Table 2.3: Photometric values of the comparison (HD 25852) and check star (HD 26584). Earlier on, HD 26409 was also used as comp/check star. All available measurements are compared. Entries in **bold face** are the best values and were used in the further investigation.

	HD 26409 (37 Eri)	HD 25852	HD 26584
spectral type	G8 III [g]	K0 [g]	G5 [g]
α [2000]	$04^h10^m22\overset{s}{.}5$	$04^h05^m30\overset{s}{.}6$	$04^h11^m56\overset{s}{.}1$
δ [2000]	$-6°55'25\overset{''}{.}9$	$-7°35'50\overset{''}{.}0$	$-8°50'14\overset{''}{.}9$
U	$7\overset{m}{.}05$ [a]	$9\overset{m}{.}62$	
B	$6\overset{m}{.}367$ [g]	$8\overset{m}{.}82$ [g]	$7\overset{m}{.}389$ [g]
	$6\overset{m}{.}38$ [a]	$8\overset{m}{.}84$	
V	$5\overset{m}{.}449$ [g]	$7\overset{m}{.}81$ [g]	$6\overset{m}{.}453$ [g]
	$5\overset{m}{.}44$ [a]	$7\overset{m}{.}84 \pm 0\overset{m}{.}01$ [b]	
	$\mathbf{5\overset{m}{.}44 \pm 0\overset{m}{.}01}$ [b]	$\mathbf{7\overset{m}{.}84 \pm 0\overset{m}{.}01}$ [c]	
	$5\overset{m}{.}448$	$7\overset{m}{.}84$ [e]	
	$5\overset{m}{.}44$ [d]	$7\overset{m}{.}83$ [d]	$6\overset{m}{.}45$ [d]
		$7\overset{m}{.}83$ [f]	
R_C		$\mathbf{7\overset{m}{.}30}$ [f]	
I_C		$\mathbf{6\overset{m}{.}80}$ [f]	
R_J	$4\overset{m}{.}70$ (2) [a]		
I_J	$4\overset{m}{.}30$ (2) [a]		
$U-B$	$0\overset{m}{.}67 \pm 0\overset{m}{.}01$ [b]	$0\overset{m}{.}80 \pm 0\overset{m}{.}01$ [b]	
		$0\overset{m}{.}79 \pm 0\overset{m}{.}01$ [c]	
$B-V$	$0\overset{m}{.}94 \pm 0\overset{m}{.}01$ [b]	$1\overset{m}{.}01 \pm 0\overset{m}{.}01$ [b]	
		$\mathbf{1\overset{m}{.}02 \pm 0\overset{m}{.}01}$ [c]	
	$\mathbf{0\overset{m}{.}941 \pm 0\overset{m}{.}002}$ [d]	$1\overset{m}{.}018 \pm 0\overset{m}{.}017$ [d]	$\mathbf{0\overset{m}{.}950 \pm 0\overset{m}{.}008}$ [d]
$V-R_C$		$0\overset{m}{.}54 \pm 0\overset{m}{.}01$ [c]	
$V-I_C$		$\mathbf{1\overset{m}{.}03 \pm 0\overset{m}{.}01}$ [c]	
	$0\overset{m}{.}94 \pm 0\overset{m}{.}04$ [d]	$0\overset{m}{.}99 \pm 0\overset{m}{.}01$ [d]	$0\overset{m}{.}94 \pm 0\overset{m}{.}01$ [d]
Chk − Cmp (95-96)[e]		$\Delta U = -2\overset{m}{.}581 \pm 0\overset{m}{.}011$	
		$\Delta B = -2\overset{m}{.}465 \pm 0\overset{m}{.}005$	
		$\Delta V = -2\overset{m}{.}392 \pm 0\overset{m}{.}006$	

[a] ... Hooten et al. (1989)
[b] ... Rodono & Cutispoto (1992)
[c] ... Cutispoto (1995)
[d] ... Hipparcos, ESA (1997)
[e] ... Bartus 2002, priv. comm.
[f] ... /chianti/apt/T7/STRASSMEIER/reduced/master/EI_Eri_Cp.joh(V-I)
[g] ... Simbad database

useful data points in V, 1303 in I and about 200 in b and y (see Tab. 2.2). The brightest observation of the APT T7 in V was on JD 2452261.6 and amounted to $\Delta V = -0\overset{\mathrm{m}}{.}881 \pm 0\overset{\mathrm{m}}{.}008$ which translates to $V_{\max} = 6\overset{\mathrm{m}}{.}949 \pm 0\overset{\mathrm{m}}{.}013$ when adding the comparison star ($V' = 7\overset{\mathrm{m}}{.}83 \pm 0\overset{\mathrm{m}}{.}01$).[2] Brightest ΔI_C was $-0\overset{\mathrm{m}}{.}617 \pm 0\overset{\mathrm{m}}{.}003$ at JD 2452261.6. Adding $I'_C = 6\overset{\mathrm{m}}{.}80$ gives $I_C = 6\overset{\mathrm{m}}{.}183 \pm 0\overset{\mathrm{m}}{.}014$.[3] Data from former epochs were also used; they are summarised in Strassmeier et al. (1997, Table 5). Investigating all available photometric data (of more than 20 years), we find that the brightest observations of EI Eri in V were at December 18, 2001, (JD 2452261.6) with $V = 6\overset{\mathrm{m}}{.}949 \pm 0\overset{\mathrm{m}}{.}013$ (see above), at October 6, 1992, (JD 2448902) with $V = 6\overset{\mathrm{m}}{.}968$, at 1987.82 with $V = 6\overset{\mathrm{m}}{.}960 \pm 0\overset{\mathrm{m}}{.}004$ and at 1980.11 with $V = 6.963$. Thus, we adopt $6\overset{\mathrm{m}}{.}949$ as the "least spotted" V brightness.

The maximum brightness values obtained here will be used in § 3.3.4 for calculating the absolute visual magnitude.

[2] The notation ΔV refers to $V_{\mathrm{obj}} - V_{\mathrm{cmp}}$, here written as $V - V'$. $\gg\ '\ \ll$ denotes the comparison star.

[3] In case one has only I'_J available, translation to I_C is more sophisticated. Calculate $(V - I_C)$ first:

$$(V - I_C) = \Delta(V - I_C) + (V' - I'_C) \tag{2.1}$$

where $\Delta(V - I_C)$ is $(\Delta V - \Delta I_C)$, and $(V' - I'_C)$ needs to be translated from $(V' - I'_J)$ first. This is done indirectly using the comparison star's V', I'_J and R'_J values:

$$\begin{aligned}(V' - R'_C) &= 0.63(V' - R'_J) + 0.07\\ (R'_C - I'_C) &= 0.978(R'_J - I'_J) - 0.012\end{aligned} \tag{2.2}$$

(taken from Taylor 1986). Adding the two resulting values gives $(V' - I'_C)$ which is put into equation 2.1. Adding V now results in $-I_C$.

Chapter 3

EI Eridani

"Thou great star! What would be thy happiness if thou hadst not those for whom thou shinest!"

Nietzsche, Thus Spake Zarathustra

"Here Phaethon lies; his father's car he tried –
Though proved too weak, he greatly daring died."

Ovid, Methamorphoses, II

The long, winding, sprawling constellation of Eridanus, the river, has been identified variously as the rivers Tigris, Euphrates, Po, Nile, Ebro, Rhine and Rhone, and Homer referred to it as an "Ocean Stream" which circled the earth. In the first place, the river Eridanus is named after the river-god who was the son of Oceanus and Tethys. It is said by some to be the one famous river whose path was changed by Herakles in order to clean the stable of king Augeias – one of Herakles' famous twelve missions. Not surprising for one of the mightiest rivers of the ancient world, Eridanus is – with a size of 1138 square degrees – the sixth largest and – spanning almost 50 degrees in right ascension and over 2 h in declination – the second longest constellation on the night sky. Its brightest stars have arabic sounding names like Acamar, Angetenar, Zaurak, Zibal, Beid, Keid, Azha and Achernar ("river mouth" in arab). A total of 41 of its stars are brighter than 5th magnitude (Hoffleit & Warren 1995).

The river Eridanus is mentioned in the story of Phaethon, the mortal son of Helios, the Sun god, who had the task to conduct every day the cart of the Sun accross the skies. The young Phaethon desperately wanted to drive the sun chariot for one day – a task always undertaken by his father. In this desire, he was encouraged by his sisters and mother. His father refused to give his permission as he knew that Phaethon was not strong enough for such a task. However, after much pestering, he finally agreed. The two white horses were harnessed, Phaethon climbed aboard and took up the reins to drive the Sun across the heavens. At first, Phaethon was ecstatic as he made the ascent into the clear morning sky. He felt like a God, mighty and proud, but quickly it became clear that he was not strong enough to control the horses. At first they galloped so high in the sky that the earth far below was in danger of freezing, then they swept so close to the earth that it became scorched. Zeus had watched all this in growing anger. His patience finally snapped, and he threw a thunderbolt straight at the chariot (see Fig. 3.1). Phaethon was killed outright. His flaming body fell and landed in the sacred river Eridanus. For their foolishness in encouraging him in such an irresponsible adventure, his sisters were turned into poplar trees along the river bank, and their tears became amber in the rivers water (Ovidius Naso 8 A.D.).

The Naiads, water nymphs, buried Phaeton and carved upon his tomb: "Here Phaeton lies..." *Phaeton, who greatly failed, more greatly dared.* Alas, Ovids report does not shed any light on the exact location of Phaethon's tomb. Let us, for the course of this investigation, assume to find Phaethon's grave at the position of EI Eri and point our telescope there ...

Figure 3.1: "And far fell Phaethon with flaming hair; / as haply from the summer sky appears / a falling star, although it never drops / to startled earth. – Far distant from his home / the deep Eridanus received the lad / and bathed his foaming face." – The moment when Phaethon is striken by a thunderbolt from Zeus, as described by Ovidius Naso (8 A.D.), is captured in the painting "Phaeton" by Gustave Moreau (1878). The form of Phaethon is a great diagonal gash in the image, as his body falls from the sky. A nimbus of light surrounds Phaethon, indicating the rays of the sun. The chariot plummets as well, with the horses panicing, their legs pawing at the air. – The fall of Phaethon was a popular theme, common in Renaissance and Baroque painting, especially on ceilings in the later period, and comprises such famous painters as Peter Paul Rubens and Gaspare Diziani.

3.1 General parameters of EI Eri and history

EI Eridani = HD 26337 (G5 IV, $P_{\rm rot}$= 1.945 days, $V = 7\overset{\rm m}{.}1$) is a rapidly rotating ($v \sin i = 51$ km s^{-1}), active, non-eclipsing, single-lined spectroscopic binary and as such a typical RS CVn star (see §1.1.5). Ca II H & K emission – the classical fingerprint of magnetic activity – was first noted by Bidelman & MacConnell (1973) and confirmed later by Fekel (1980) who classified it as moderate in strength, class C on the qualitative emission scale by Hearnshaw (1979). Moderate Ca II H & K and Hα emission lines were also pointed out by Strassmeier et al. (1990) and Fernandez-Figueroa et al. (1994). Fekel et al. (1982) classified EI Eri as a single-lined RS CVn star when they detected its light variability, with an amplitude being almost $0\overset{\rm m}{.}2$ in V, a photometric period of $2\overset{\rm d}{.}038$ and an orbital period of $2\overset{\rm d}{.}044$. The light variability was later confirmed by Bopp et al. (1983). Consequently, Kholopov et al. (1985) assigned the new variable star designation "EI Eridani". Fekel et al. (1986) determined the orbital period to be $1\overset{\rm d}{.}9472$. Hall et al. (1987) detected a photometric period of 1.945 ± 0.005 days from UBV photometry, interpreted it as rotation period and concluded that the primary component rotates synchronously. Not surprisingly, the Hα line is, as in most RS CVn stars, in absorption but highly filled in with chromospheric emission (see Smith & Bopp 1982) and quite variable in strength (Fekel et al. 1986). More than likely, these variations are caused by rotational modulation of the chromospheric Hα emission, presumably due to evolving plage regions on the stellar surface moving in and out of sight. Fekel et al. (1987), Pallavicini et al. (1992) and Randich et al. (1993) reported the presence of moderate amounts of lithium.

EI Eri has been detected at microwave frequencies (Slee et al. 1988); in the infrared (at 12 μm, see Busso et al. 1988) and with IRAS (Infrared Astronomical Satellite; see Beichman et al. 1988); in the ultraviolet (Fekel et al. 1987 detected strong emission lines), with EUVE (Extreme Ultraviolet Explorer; e.g. Osten et al. 2002) and with IUE (International Ultraviolet Explorer; e.g. Cardini et al. 2003); at radio frequencies

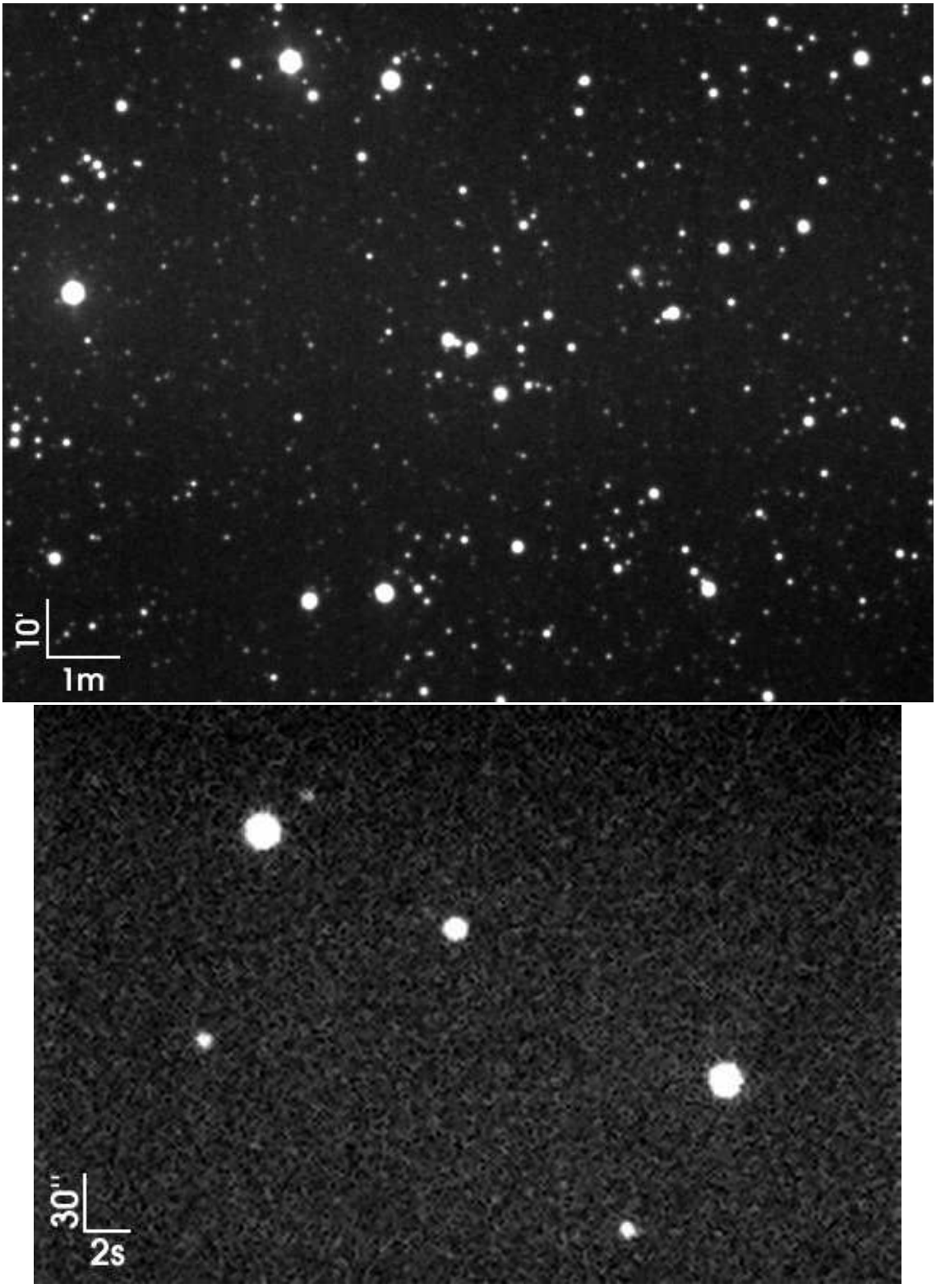

Figure 3.2: Sky image of EI Eri taken by J. Desteffani. Upper image: Taken on Feb. 13, 2004, in Cunter, canton Graubünden (Switzerland), with a ST-7 CCD and 50mm Konica camera lens, aperture 2.8, 140 images summed, exposure time 10 seconds each. EI Eri is in the very center, left star. The brightest star (at the top, left hand) is Beid (a.k.a. o_1 Eri, $4\overset{\mathrm{m}}{.}14$), the second brightest (close to the left border) is Keid (o_2 Eri, $4\overset{\mathrm{m}}{.}48$). — Lower image: Taken on February 18, 1998, in Brugg, canton Aargau, with a Meade LX-200 telescope and a ST-7 CCD, exposure time 15 seconds. EI Eri is the bright star in the left upper part. — See http://www.jogi.com/astro/sternwasi/ .

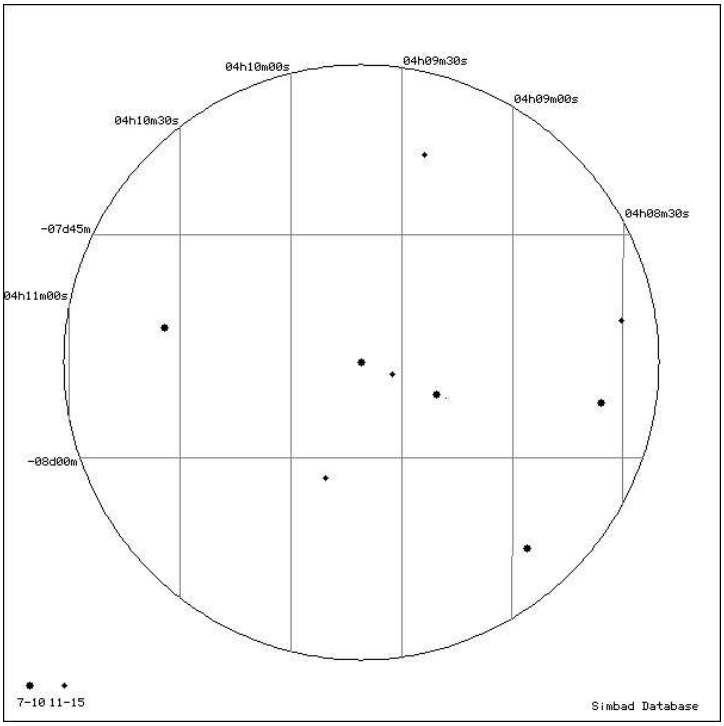

Figure 3.3: Sky plot around EI Eri; from Simbad (FK5, radius=20 arcmin, epoch and equinox = 2000.0)

(García-Sánchez et al. 2003; Fox et al. 1994; Mutel & Lestrade 1985); and at X-ray frequencies with the Einstein satellite (McDowell 1994) and with the ROSAT All-Sky Survey (Pounds et al. 1993; Drake et al. 1992).

Hall et al. (1987) already noted season-to-season changes in the photometric period (∼1%), in the light-curve amplitude ($0\overset{\mathrm{m}}{.}07$ – $0\overset{\mathrm{m}}{.}20$) and in the mean brightness (∼10%), likely indicating latitude and/or longitude changes of the location of the starspots. Strassmeier et al. (1989) report seasonal changes of the photometric period of 0.043 days. Rodono & Cutispoto (1992) suggest a possible cycle period of about 10 years. Strassmeier et al. (1997) summarised the first 16 years of photometric data and found a possible 11 ± 1 years cycle of the mean brightness. Based on this estimation, the current investigation proposed to Doppler image the full 11 years cycle. Continuation of photometric observations for the next two years disproved this period. However, using all available data, the proposed period is now back to 12.2 years. See §1.1.3 on page 6 for an extended discussion of the cycle length of EI Eri.

Several Doppler imaging studies have been carried out to map the photospheric spot distribution (see §4.1) while Donati et al. (1997) detected a clear Zeeman signature of the magnetic field of the primary star. The Zeeman signatures observed indicate that the field structure is not simply dipolar.

Figure 3.2 shows a sky image of EI Eri from Desteffani (2004). For a plot of the sky around EI Eri from Simbad (FK5) see Fig. 3.3; radius is 20 arcmin.

Table 3.1: "Who dares to call the child by its right name?" [1] – Names of EI Eridani

V* EI Eri	BD-08 801	CABS 35
CCABS 31	CMC 202464	CMC 130994
2E 943	2E 0407.2-0801	1ES 0407-08.0
EUVE J0409-07.8	2EUVE J0409-07.8	GC 5012
GJ 3264	GSC 05312-01791	HD 26337
[HFE83] 281	HIC 19431	HIP 19431
IRAS 04072-0801	N30 857	PPM 186606
RE J0409-075	RE J040939-075336	2RE J040940-075336
2RE J0409-075	1RXS J040940.8-075327	SAO 130994
SKY# 6350	TYC 5312 1791 1	uvby98 100026337 V
YZ 98 1031		

Table 3.2: "Where shall I, endless Nature, seize on thee?" [1]– Position of EI Eridani.

Parameter	Value	Reference
RA (2000)	$04^h09^m40\overset{s}{.}8932$	ESA (1997)
DEC (2000)	$-7°53'34\overset{''}{.}288$	ESA (1997)

Table 3.3: Original and improved orbital elements for EI Eri and suggestion for a possible third-body orbit. The original values are from Strassmeier (1990) except T_0 which is from Fekel et al. (1987). The "improved" values are from the binary solution without third component. After correction of the proposed tertiary orbit (listed in the very right column), several values of the (inner) binary solution change slightly: γ to $20.07 \pm 0.13\,\mathrm{km\,s^{-1}}$, K1 insignificantly to $26.79 \pm 0.18\,\mathrm{km\,s^{-1}}$ and the standard error (i.e. the standard deviation of the $O-C$ values) to $2.5\,\mathrm{km\,s^{-1}}$. — For the very right column ("third body"), the mass index "1" refers to the inner binary system, index 2 to the third body.

Orbital element	Original	Improved	Third body
P [days]	1.947227 ± 0.000008	1.9472324 ± 0.0000038	7000 ± 200
T_0 [HJD]	2 446 074.384	2 448 054.7109 ± 0.0005	2 442 000
γ [$\mathrm{km\,s^{-1}}$]	17.6 ± 0.2	21.64 ± 0.16	21.64
K_1 [$\mathrm{km\,s^{-1}}$]	27.4 ± 0.3	26.83 ± 0.23	4 ± 1
e (assumed)	0.0	0.0	0.0
$a_1 \sin i$ [km]	733000 ± 9000	718400 ± 6200	$3.9 \pm 1.0 \cdot 10^8$
f(M) [$\mathrm{M_\odot}$]	0.00415 ± 0.00015	0.00391 ± 0.00010	0.046 ± 0.035
M_1 [$\mathrm{M_\odot}$] [a]	–	1.25 ± 0.05	1.499 ± 0.070
M_2 [$\mathrm{M_\odot}$] [b]	–	0.249 ± 0.049	0.74 ± 0.66
K_2 [$\mathrm{km\,s^{-1}}$] [c]	–	135 ± 27	8 ± 7
$a_2 \sin i$ [km] [c]	–	$3.61 \pm 0.72 \cdot 10^6$	$7.8 \pm 7.2 \cdot 10^8$
a [km] [d]	–	$5.22 \pm 0.92 \cdot 10^6$	$1.41 \pm 0.88 \cdot 10^9$
Standard error of an observation of unit weight ($\mathrm{km\,s^{-1}}$)		3.2	

[a] ... estimated using evolutionary tracks; see §3.3.6.

[b] ... calculated using $f(\mathrm{M})$, assuming $i = 56.0 \pm 4.5°$.

[c] ... using the estimations of M_1 and M_2.

[d] ... assuming $i = 56.0 \pm 4.5°$.

[1] Goethe, Faust I, Night

3.2 Radial velocities and spectroscopic orbit

The Doppler imaging process requires an accurate correction of the orbital radial velocity variations from the spectral line profiles. Therefore, we recomputed the orbital elements with all our new radial velocities.

Radial velocities were determined from cross-correlations with spectra of a radial velocity standard star observed during the same night. Since EI Eri is a single-lined spectroscopic binary (SB1), only the radial velocity of the primary component can be measured, and no radial velocity information is available for the secondary star. The cross correlations were computed using IRAF's `fxcor` routine (see Fitzpatrick 1993), which fits a Gaussian to the cross-correlation function to determine the central shift. Several different IAU radial velocity standard stars were used (see Table 3.4).[2] Their radial velocities were, if possible, adopted from the work of Scarfe et al. (1990) as they are more precise than the IAU values. This means that most of the radial velocity values had to be corrected: The RV's from the observing runs CF94, CF95, M96 and CF97 and the RV's from Strassmeier (1990) and Fekel et al. (1987) were, originally, all measured using the IAU values (Pearce 1955). Therefore, we applied corrections for each RV value so that they now match the RV standard star velocities listed by Scarfe et al. (1990). (Table A.26 and Tables A.20–A.24 list the corrected RV values.)

We obtained altogether 354 new radial velocities for the primary component of EI Eri, 89 of which are from four dedicated KPNO/CF runs (March 1994, February 1995, January 1996, December 1997; see Tab. A.21–A.24 on page 131–132), 58 from one dedicated visitor observing run at NSO/McMath (Fall 1996; Tab. A.20, p. 130), 178 from the NSO synoptic night-time program (1988–1995; Tab. A.4–A.19, p. 124–130) and 29 from the MUSICOS 98 campaign. Additionally, 55 older radial velocities were found in the literature (see Table A.26): 27 from Fekel et al. (1987), 21 spectra from Strassmeier (1990), five from Gunn et al. (1996), and two from Donati et al. (1997). The former two used the standard star velocities from the International Astronomical Union's list of RV standard stars (Pearce 1955) and were, therefore, corrected to match the values by Scarfe et al. (1990). Gunn et al. (1996) used the RV standard star values from Pearce (1955) but does not unscramble which RV standard star was used for which spectrum. Therefore, the values could not be corrected. However, they were not used for calculating the orbital solution as they have too large error bars (up to $10\,\mathrm{km\,s^{-1}}$). The HJD values of the five RV measurements (as listed in Table A.26) were calculated using the T_0, P_{orb}, epoch and phase values listed by Gunn et al. (1996): HJD = 2 446 091.539 + 1.947227× (epoch + phase). Donati et al. (1997) do not mention which RV standard they used for their two radial velocity values. Fekel et al. (1987) lists a RV measurement without RVSS, observed at HJD 2444507.885, which is from a photographic plate from KPNO by Bernie Bopp. It was measured line by line vs. the comparison arc and has no RVSS. Fekel's observation from HJD 2445594.999 was measured with the RVSS α Ari (the RVSS "β Ari" listed in Fekel et al. 1987 is a typo; Fekel 2003). The star δ Aurigae was used once as radial velocity standard (in CF94 for HJD 2449416.619, see Table A.21). Wilson (1953) lists 8.2 ± 0.9 km s^{-1}, de Medeiros & Mayor (1999) measured 5.98 ± 1.97 km s^{-1} using the CORAVEL spectrometer. The value used for CF94 is 7.61 km s^{-1} (Strassmeier 1995).

From all available 409 RV values, the nine MUSICOS BXO values (see §5.2.2) and the five values by Gunn et al. (1996) (see above) were expelled from the sample. So altogether, 395 RVs were used to calculate the final orbit (presented in Tab. 3.3) using the formula

$$v_r = \gamma + K_1 \cos\left(2\pi \frac{\mathrm{HJD} - T_0}{P}\right) \quad . \tag{3.1}$$

3.2.1 Orbit calculation

Orbital elements were derived with the differential-correction program `sb1` of Barker et al. (1967), as modified and described by Fekel et al. (1999), in combination with the add-on scripts `sb1set` and `sb1go` which were built for convenient investigation of a large number of orbits. Table 3.3 lists the improved orbital

[2] Note that the IAU radial velocity standard stars α Tau and β Gem were found to be variable with $P = 643$ days / $K = 150$ m s^{-1} and $P = 558$ days / $K = 50$ m s^{-1}, respectively; see Hatzes & Cochran (1998, 1993). These amplitudes are, however, much smaller than the accuracy of our radial velocity measurements ($K \ll \sigma_{v_r}$) and are therefore neglected.

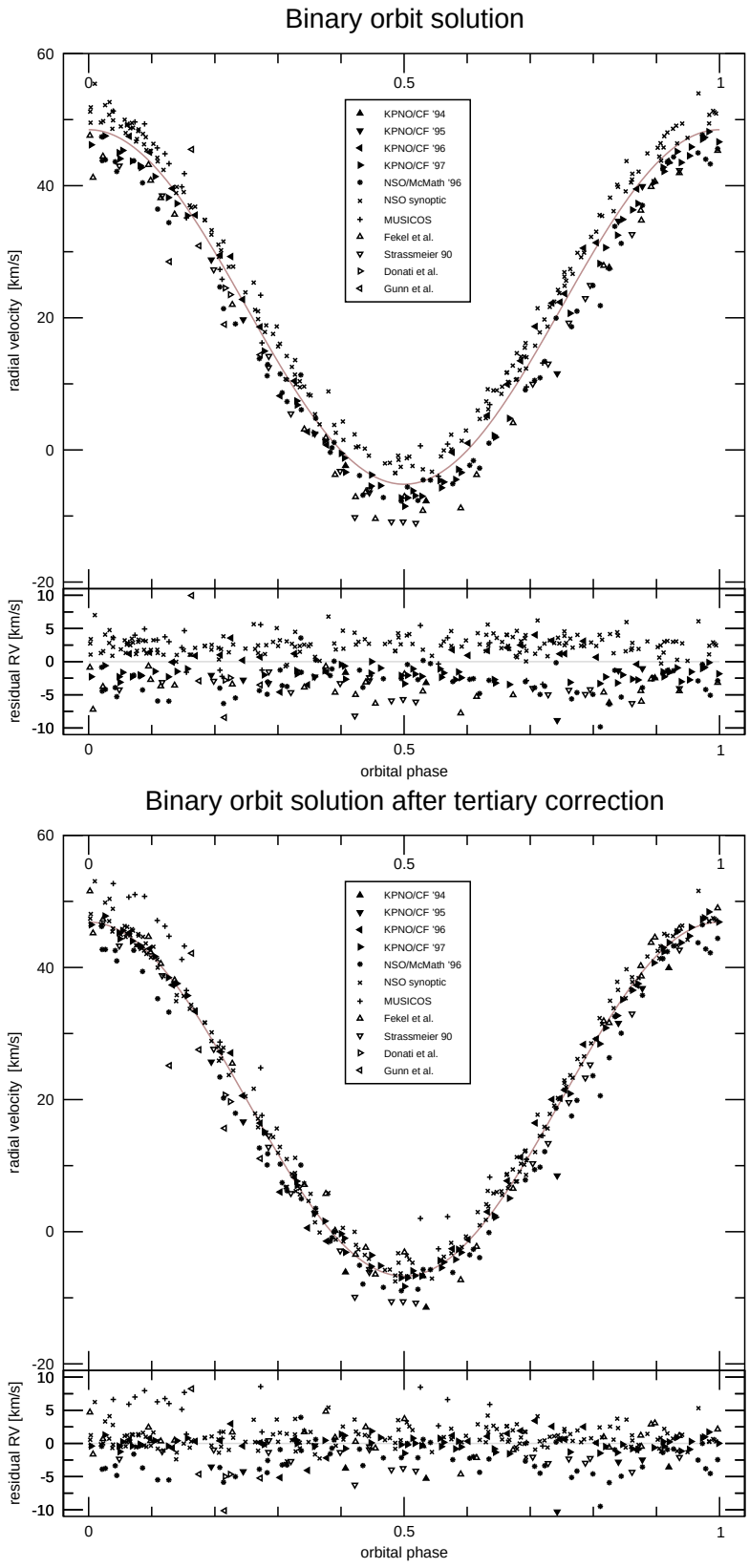

Figure 3.4: Observed and computed radial velocity curve for the binary solution. Upper panel: not taking into account the possible tertiary. Lower panel: after correction for the proposed tertiary. The line is the orbital solution from the elements in Table 3.3. The respective subpanels show the residual velocities. The standard error of an observation of unit weight (i.e. the standard deviation of all $O - C$ values) decreases from 3.2 to 2.5 $\mathrm{km\,s^{-1}}$.

Table 3.4: Radial velocity standard stars for our NSO, KPNO and MUSICOS observations (upper table) and for the observations found in the literature (lower table). The velocity values are from Scarfe et al. (1990) and Pearce (1955), respectively. 59 Ari and δ Aur are *not* IAU standard stars; their velocities are from Wilsons *General Catalogue of Stellar Radial Velocities*; see note at the end of the table. For details on the MUSICOS measurements see § 5.2.2.

Name	HD	v_r [km s^{-1}] IAU	σ_{v_r}	v_r [km s^{-1}] Scarfe	σ_{v_r}	NSO syn.	NSO 96	KPNO 94	KPNO 95	KPNO 96	KPNO 97	MUSICOS OHP	MUSICOS BXO	MUSICOS MSO
α Tau [a]	29139	54.1	0.1	54.25	0.08				*	*		*	*	
α Ari	12929	-14.3	0.2	-14.51	0.11		*				*			
β Gem [a]	62509	3.3	0.1	3.23	0.15					*	*			
16 Vir	107328	35.7	0.3	36.48	0.04			*	*	*	*			
33 Sex	92588	42.8	0.1	–	–								(*)	
β Lep	36079	-13.5	0.1	–	–									*
59 Ari [b]	20618	*-0.1*	?	–	–	*								
δ Aur [c]	40035	*7.61*	?	–	–			*						

[a] ... See footnote on page 26.

[b] ... Wilson (1953)

[c] ... Wilson (1953), de Medeiros & Mayor (1999)

Name	HD	v_r [km s^{-1}] IAU	σ_{v_r}	v_r [km s^{-1}] Scarfe	σ_{v_r}	Fekel et al. (1987)	Strassmeier (1990)	Gunn et al. (1996)
α Tau [a]	29139	54.1	0.1	54.25	0.08			*
α Ari	12929	-14.3	0.2	-14.51	0.11	*	*	
β Gem [a]	62509	3.3	0.1	3.23	0.15	*	*	
10 Tau	22484	27.9	0.1	27.95	0.19	*	*	
ι Psc	222368	5.3	0.2	5.60	0.16	*	*	*
γ Aql	186791	-2.1	0.2	-1.97	0.11			*

[a] ... See footnote on page 26.

elements from minimised O−C residuals. Our final elements converged at an eccentricity so close to zero that, in reference to the criteria adopted by Lucy & Sweeney (1971), a formal zero-eccentricity solution was adopted. The eccentricity of the least-squares elliptical orbit would amount to $e = 0.008 \pm 0.008$, so the formally correct value for e is zero within the error bars. Phases of all line profiles were then computed using revised ephemerises:

$$\mathrm{HJD} = 2\,448\,054.7109\,(5) + 1.9472324\,(38) \times E\ .$$

Orbital elements for EI Eridani were first derived by Fekel et al. (1987). They agree with our revised elements except for γ. As this could be a hint for a long-period third body, it will be discussed in §3.2.2. Donati et al. (1997) pointed out that the radial velocities they measured at two epochs (see Table A.26) are in strong disagreement with the ephemeris from Strassmeier (1990). Gunn et al. (1996) also report that their five radial velocities diverge significantly from the orbit suggested by Strassmeier (1990); they suspect the high rotational velocity to be responsible for the large discrepancies. As a matter of fact, Strassmeier's T_0 value for his orbital solution seems to be confused (possibly due to a typing mistake) as it does not give sensible results for his own radial velocities. Accordingly, Donati's radial velocity values are in perfect agreement with the previous ephemeris of Fekel et al. (1987). The same holds true for the five radial velocity values by Gunn et al. (1996). In Fig. 3.4, Donati's values show up as two open (non-filled) right-pointing triangles around phase 0.22.

3.2.2 EI Eri – a triple-star system?

By obtaining precise radial velocity measurements, more and more active close binary stars turn out to be members of triple systems, e.g. BY Dra (Zuckerman et al. 1997), XY UMa (Chochol et al. 1998), HU Vir (Fekel et al. 1999), RT Lac (Ibanoğlu et al. 2001), UX Ari (Duemmler & Aarum 2001). A thorough investigation of EI Eri's RV measurements reveals that the barycentric velocity γ has increased since the early observations in the 1980s by up to $8\,\mathrm{km\,s^{-1}}$ in the mid-1990ies. In order to examine whether the system is possibly a triple star, we calculate an orbit for several data subsets just varying the barycentric velocity γ and, for comparison, also the amplitude of the semi-major axis K_1.[3] The K_1 values are computed and shown for comparison, because a possible third body would only affect the barycentric velocity γ, not K_1. With the help of K_1, the internal error can be estimated. The results are shown in Figure 3.5 and Table 3.5. We notice γ variations larger than 3σ (which can also be recognised in the orbit plot in Fig. 3.4 (upper panel) by an up- or downward shift of RV data points from distinctive observing runs): The values vary between 15.7 and $26.7\,\mathrm{km\,s^{-1}}$ with an average error bar of $0.8\,\mathrm{km\,s^{-1}}$. It is seen that γ shows an obvious trend over the period of 20 years, which is not the case for K_1.

Assuming a third component as origin of this variation, there are two possible scenarios: First, a third star surrounding the binary system in a relatively close orbit with a period of around 94 days and an amplitude of the semi-major axis (of the inner binary system)K_{1-2} of around $2\,\mathrm{km\,s^{-1}}$. This is solely based on the M96 subsample variations outlined in Fig. 3.6c. The alternative would be a far orbit with a period of around 20 years and an amplitude K_{1-2} of $\approx 4\,\mathrm{km\,s^{-1}}$, leading to a f(M) of $0.046 \pm 0.035\,\mathrm{M}_\odot$ and a $a_{1-2}\sin i$ of $3.9 \pm 1.0 \cdot 10^8$ km (see Table 3.3, right column). Both values shrink in case of non-zero eccentricity. In §3.3.6 (page 44), I will discuss the mass of a potential tertiary.

3.2.3 Radial velocity standard star cross correlation

A possible explanation for long-term RV variations could be the use of different RV standard stars and the use of different instrumental configurations and reduction techniques. The radial velocity standard stars used for measuring the RV shifts are listed in Table 3.4. For the observing runs by Fekel et al. (1987), Strassmeier (1990) and our CF97 run, two of the three radial velocity standards used are identical. Though, γ differs by $4\,\mathrm{km\,s^{-1}}$ (with a mean deviation of $2\,\mathrm{km\,s^{-1}}$) which is about $10\,\sigma$. The NSO data, all taken with the same instrumental setup and the same RVSS (except M96) vary by $9\,\mathrm{km\,s^{-1}}$(mean deviation:

[3] Note that the γ and K_1 values are independent of each other (within a certain range), i.e. the resulting γ values are the same even if K_1 is fixed or varied.

Table 3.5: Variations of the barycentric velocity γ and the semi-major axis K_1. Several sets are splitted into subsamples. (See Figure 3.5.) *all data* include additional data points from CF94 (3 data points), CF95 (5), Donati (2) and from the NSO synoptic run that were not sufficient for calculating a separate orbit. *eieri02* is not included in *all data*.

Data set	HJD	$n_{spectra}$	γ	σ_γ	K1	σ_{K1}
FEKEL	44179 – 46076	27	17.54	0.40	27.18	0.58
FEKEL A	44179 – 44627	9	17.27	3.06	27.48	1.23
FEKEL B	45356 – 45599	10	17.97	2.66	26.15	1.55
FEKEL C	45594 – 46076	12	15.71	2.77	29.14	1.92
KGS90	47150 – 47170	21	17.64	0.47	27.25	0.58
NSO eieri02	47481 – 47517	17	13.21	0.25	27.53	0.39
NSO ccd016	48187 – 48227	9	23.67	1.32	26.16	1.93
NSO ccd024	48271 – 48333	9	23.39	0.24	26.68	0.32
NSO ccd107	48536 – 48657	21	23.85	0.32	27.12	0.46
NSO ccd107 A	48571 – 48598	12	24.05	0.63	26.46	1.36
NSO ccd107 A	48630 – 48657	8	23.27	0.48	27.64	0.45
NSO data92	48909 – 48957	14	23.75	0.26	26.66	0.39
NSO nso94	49280 – 49295	8	25.25	0.38	26.94	0.79
NSO nso94:more1	49302 – 49330	7	26.22	2.00	24.93	3.36
NSO nso94:more3	49416 – 49443	21	25.15	0.25	26.49	0.34
NSO nso94:more3 A	49416 – 49429	11	24.90	0.81	28.44	0.52
NSO nso94:more3 B	49427 – 49440	10	25.66	1.15	26.80	1.58
NSO nso94:more3 C	49429 – 49443	10	26.71	0.68	20.88	2.08
NSO nso95:94oct	49643 – 49656	16	23.17	0.47	26.31	0.45
NSO nso95:94dec	49703 – 49720	21	25.18	0.08	26.07	0.16
NSO nso95:95mar	49776 – 49804	12	25.38	0.85	22.41	1.05
NSO nso95:95nov	50029 – 50053	15	24.36	0.56	27.19	0.62
M96	50388 – 50457	58	18.45	0.25	25.73	0.35
M96 A	50388 – 50408	21	19.88	0.84	25.21	1.28
M96 B	50399 – 50417	19	18.34	0.69	26.41	0.43
M96 C	50409 – 50426	17	17.84	0.61	25.54	0.52
M96 D	50418 – 50437	17	17.60	0.34	24.04	0.68
M96 E	50428 – 50447	13	18.71	0.89	23.49	1.53
M96 F	50438 – 50457	12	19.58	0.90	26.57	0.54
CF96	50093 – 50107	24	21.85	0.46	27.09	0.90
CF97	50809 – 50828	57	19.53	0.12	26.82	0.14
CF97 A	50809 – 50814	20	19.24	0.45	27.14	0.34
CF97 B	50815 – 50822	19	19.40	0.46	26.72	0.26
CF97 C	50823 – 50828	18	19.50	0.33	26.69	0.14
CF97 1	50820 – 50828	29	19.62	0.22	26.82	0.13
CF97 2	50809 – 50820	29	19.15	0.38	26.90	0.32
MUSICOS	51141 – 51151	31	23.40	1.35	26.19	1.30
all data	44179 – 51151	409	21.64	0.16	26.83	0.23

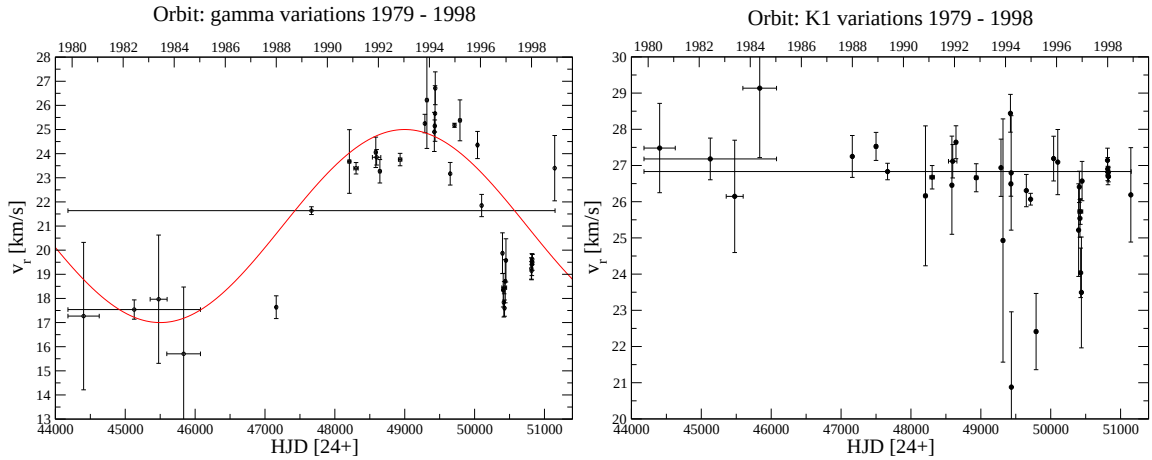

Figure 3.5: Variations of the barycentric velocity γ (left) and, for comparison, of the semi-major axis K1. The bars in the axis of abscissae (x) denote the time span of the data used for calculating the orbit. The bars in the axis of ordinates (y) are the error bars of the respective γ values. The line shows a suggestion for a tertiary orbit. (See Table 3.5)

2–3 km s^{-1}). At the same time, however, K_1 varies by a similar amount. Fig. 3.6 shows the results from a cross correlation of all radial velocity standard stars used (NSO, KPNO and MUSICOS). The observing blocks show a mean standard deviation of 0.82 km s^{-1}, the mean RV values of the blocks exhibit a standard deviation of 1.69 km s^{-1} which is 2.1 σ. Only the observing blocks CF96 (3.2σ), CF97 (5.6σ) and MUSICOS (3.6σ) deviate more than 2 σ. During the same period, γ varies on average by 7 σ. I conclude that the γ variations are not due to stochastic variations of the radial velocity standard stars (as caused by, e.g., different instrumental setups).

3.2.4 Further fragmentation of several subsamples

We now take the subsamples used for the orbit calculations and split them into subsubsamples. The results are shown in Fig. 3.7a-d. For comparison, the respective K_1 variations are shown in Fig. 3.7e-h. The subsamples from the M96 run (Fig. 3.7c) – all taken and reduced consecutively with the same instrumental configuration, using only one specific RV standard – exhibit a distinctive and steady change, suggesting a short period component (about 94 days). For comparison, we split the M96 data into alternative subsamples that are not consecutive in time and calculate their orbits (shown in Tab. 3.6). Their γ values also exhibit comparable deviations: the standard deviation of the alternative subsample orbits [a-n] is about 0.5 km s^{-1}, the deviation of the time-consecutive subsample orbits [A-F] marginally larger: 0.9 km s^{-1}, still leaving open the short-period third-body explanation. However, the same behaviour is seen in K1, thereby indicating the size of the typical error. If the γ variations of M96 are real, we would expect only γ, not K_1, to be influenced; and we would expect only the time-consecutive series of M96 to show a steady variation of γ, not the arbitrary subsamples (a-n). From this evaluation, we conclude that the γ variations of the M96 subsamples are statistically not significant, ruling out the short-period tertiary.

3.2.5 Radial velocity residuals

We now take the (observed-minus-computed) RV residuals of the orbit solution of the primary-secondary system presented in Fig. 3.4 and perform a period search on them to see if we can confirm any of the proposed periods. Figure 3.9 shows the result: No clear and outstanding peak is found in the range 20 days $\leq P \leq$ 1000 days. However, several weak periods are visible. The strongest are 6667 (0.000150), 2950 (0.000339), 1626 (0.000615), 301 (0.00332), 216 (0.00463), 203 (0.00493), 130 (0.00769) and, surprisingly enough, 96 days (0.0104 c/d). So both, a long period of around 7000 days as well as a short period of 96 days are found, supporting likewise the short and long period component (§3.2.2). However, after pre-whitening, i.e. subtracting the f0=0.000150 c/d signal from the residual RVs, the power spectrum does not show any

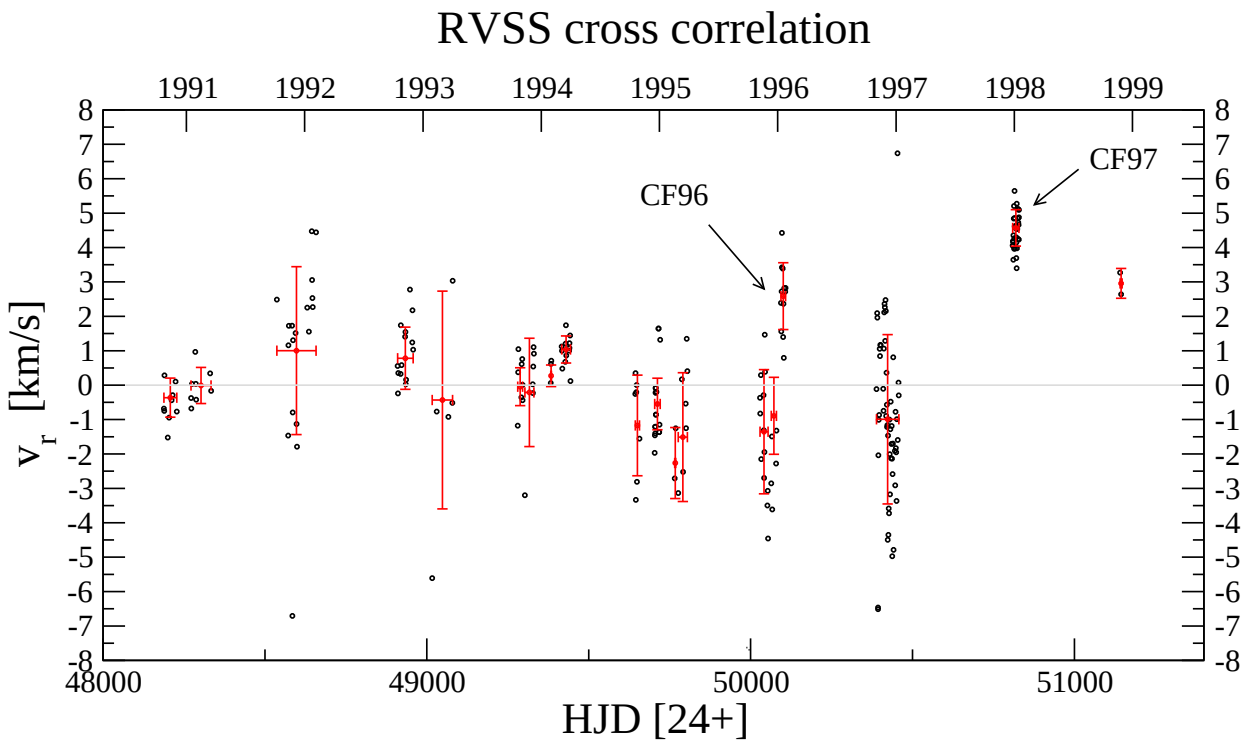

Figure 3.6: Cross correlation of all used radial velocity standard star spectra. The dots are the radial-velocity offsets for all individual RV standard stars. The dots with bars are the mean RV value for each observing block (corresponding to the suborbits in Fig. 3.5); the bars in the axis of abscissae (x) denote the time span of the respective observing block, the bars in the axis of ordinates (y) are the standard deviations of the RV values of the respective observing block.

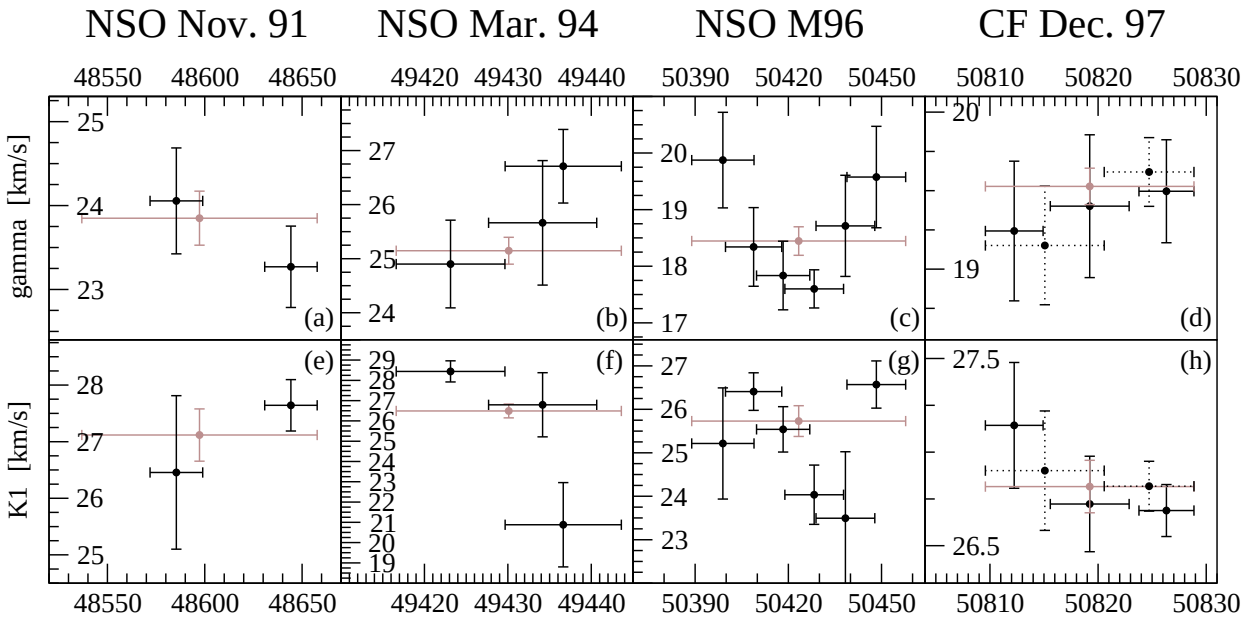

Figure 3.7: Variations of the barycentric velocity γ for four data subsamples and, for comparison, of the semi-major axis K_1. The bars in the axis of abscissae (x) denote the time span of the data used for calculating the orbit. The bars in the axis of ordinates (y) are the error bars of the respective γ values. (See Table 3.5)

Table 3.6: Test for the M96 RV variations: Alternative subsample segmentation. The subsamples are not arranged consecutively like in Tab. 3.5 but cover the same time span; every second/third/fourth/fifth RV value from the complete M96 sample was used for the subsamples a-b/c-e/f-i/j-n (with varying starting RV value). The mask denotes which RV value from M96, starting with the first one, was used ("1") or expelled ("0") and is repeated till the last RV value of M96. Statistics for several subsamples are appended including the subsamples A–F from Tab. 3.5.

Data set	mask	$n_{spectra}$	γ	σ_γ	K1	σ_{K1}
M96 a	01	29	17.919	0.386	25.549	0.556
M96 b	10	29	18.759	0.326	25.586	0.478
M96 c	001	19	18.555	0.332	25.019	0.499
M96 d	100	20	18.098	0.661	25.854	0.841
M96 e	010	19	18.424	0.440	25.870	0.620
M96 f	0001	14	17.551	0.538	26.910	0.781
M96 g	1000	15	19.047	0.495	26.631	0.874
M96 h	0100	15	18.023	0.440	24.414	0.675
M96 i	0010	14	18.752	0.440	24.950	0.528
M96 j	00001	11	19.355	1.050	25.081	2.008
M96 k	10000	12	18.126	0.493	25.814	0.726
M96 l	01000	12	17.824	1.033	25.411	0.974
M96 m	00100	12	17.558	0.692	26.226	0.608
M96 n	00010	11	18.286	0.443	25.710	0.644

block	n	γ				K_1			
		mean	std.dev.	min	max	mean	std.dev.	min	max
M96 [a-n]	14	18.306	**0.540**	17.551	19.355	25.645	**0.669**	24.414	26.910
M96 [c-h]	6	18.283	**0.513**	17.551	19.047	25.783	**0.944**	24.414	26.910
M96 [A-F]	6	18.657	**0.919**	17.599	19.875	25.211	**1.243**	23.494	26.570
NSOsyn	11	24.488	**0.992**	23.167	26.219	26.087	**1.369**	22.413	27.191

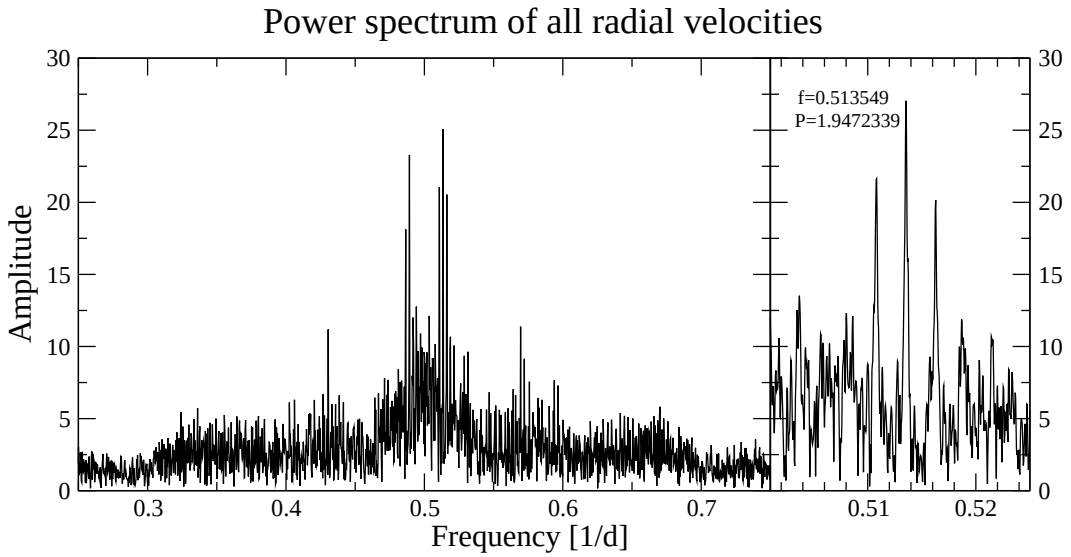

Figure 3.8: Power spectrum of all available radial velocities. The right panel is an enlargement of the region around 0.51^{-1}. Calculations provided by Oláh (2004).

distinct period any more (see Fig. 3.9 grey/dashed line). The other way around, when subtracting any of the other periods, the 6667 d period remains intact. This means that the 6667 days period is the only signal present in the residual data. The next two peaks can be explained as the second and third peak $2f_0$ and $4f_0$ of the 6667d period, the other ones come from the structure of the window function. Note that this period is very close to the total length of the data sample and therefore insecure.

3.2.6 Orbital period variations

RS CVn systems are known to show cyclic changes of the orbital period with amplitudes of the order of $\Delta P/P \approx 10^{-5}$ with time scales typically around 40–50 years. Two mechanism can account for such a period change: A third body, orbiting around the center of mass of the active binary star, changes its distance from us periodically and thereby also the times of minima (light-time effect). Secondly, a connection between the orbital period changes and the magnetic cycles was suggested (e.g. Hall 1990). This effect has been noticed also in other than RS CVn binaries, e.g. Algols containing an evolved component (Hall 1989). Preliminary models to account for the connection between magnetic activity and orbital period modulation have been presented by Lanza & Rodonò (1999). They propose that the orbital period modulation can be explained as coupling of the binary orbit to changes in the gravitational quadrupole moment of the magnetically active star in the system as it goes through an activity cycle. Rodono et al. (1995) found that the mean length of the starspot cycle is half that of the orbital period changes for the prototype active binary star RS CVn. A similar result was found by Lanza et al. (1998) for AR Lac (see also Ibanoğlu et al. 2001).

As EI Eri is an evolved star exhibiting a long-term activity cycle and possibly contains a third component, both effects can be expected to affect EI Eri's orbital period. In fact, the $O-C$ diagram suggests a possible variation with a period of around 20 years (see Fig. 3.10). If the variation seen is due to a third body, we would expect the $O-C$ values to exhibit positive signs (phase maximum appears earlier) at $\varphi = 0$ (which corresponds to the epoch 1997 in Fig. 3.5a), when the barycenter of the binary is most distant. Negative signs would be expected to peak at $\varphi = 0.5$ (1988). However, as seen in Fig. 3.10, the opposite is the case. Therefore, the suggested orbital period variations do not support the tertiary hypothesis, but could be caused by a magnetic activity cycle (see §1.1.3). A definite conclusion concerning the orbital period variations can not be drawn from the current data sample.

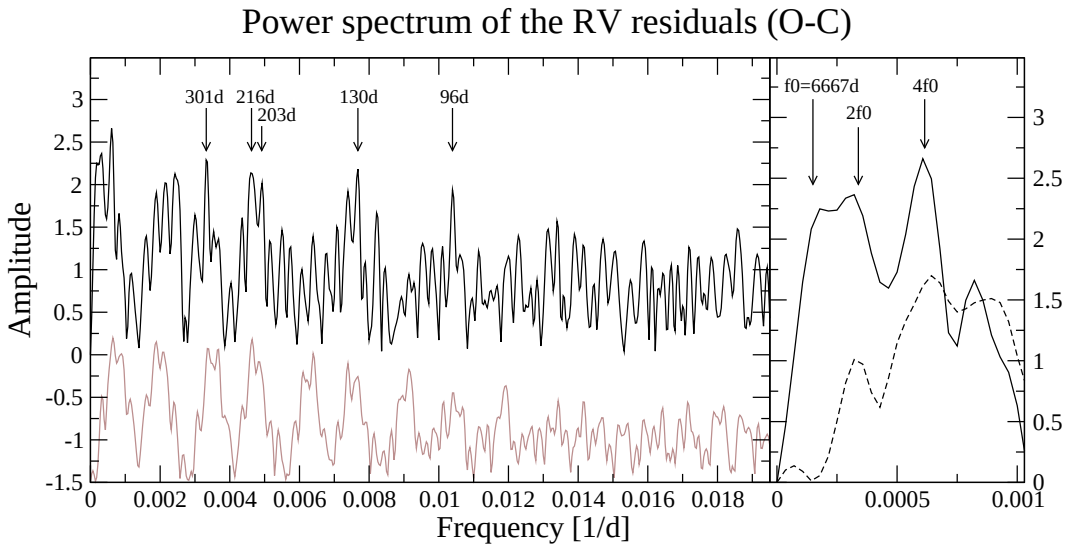

Figure 3.9: Power spectrum of the observed-minus-computed radial-velocity residuals from the orbital solution presented in Figure 3.4. The right panel is an enlargement of the area around 0.0005 d^{-1}. Also shown are the residuals after further subtraction of the 6667 d period (left panel: grey line, shifted in Y by -0.15 for better viewing; right panel: dashed line): the peak at 6667 d disappeared as well as all other peaks. Calculations provided by Oláh (2004).

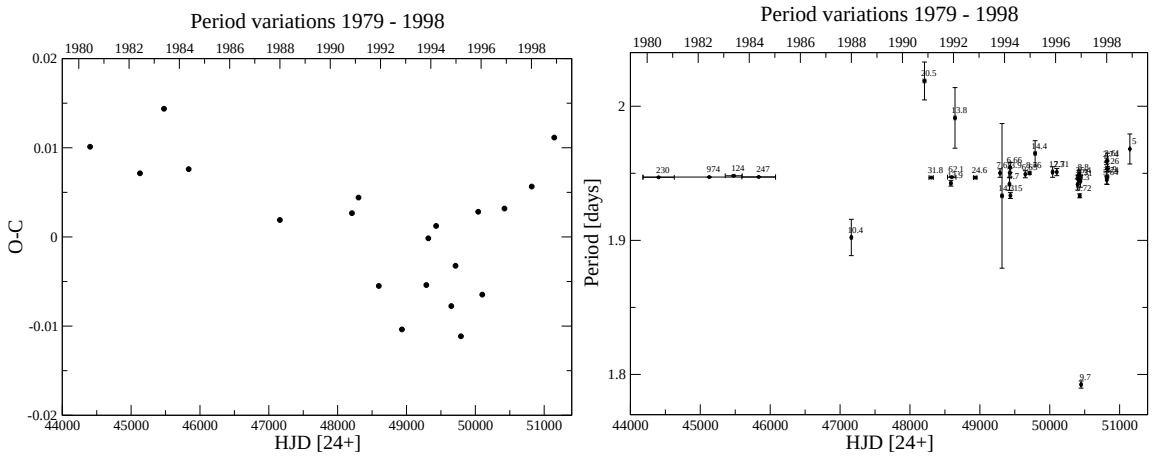

Figure 3.10: Variations of the orbital period. **(a)** The variations are actually seen in the phase-zero point (T0) and plotted as O–C values (observed minus computed phase zero-point for each epoch). We see a possible modulation with a period of about 20 years. The extrema are found at around JD 45000 and JD 49500. For comparison, **(b)** shows the period for each epoch. The bars in the axis of abscissae denote the timespan of the data used for calculating the orbit. The annotation numbers give the number of rotations for each data point. No evident drift is seen in the right panel.

3.2.7 Conclusion

We observe a long-period variation in the barycentric velocity γ of the binary system that is possibly cyclic. After all, an instrumental origin cannot be definitely ruled out. However, a thorough investigation of the orbit solutions of the individual observing runs and their RV standard stars could not explain those variations other than by a third component. Therefore, a stellar origin is favoured. The proposed long-term period is also supported by the O–C RV residuals. The observed orbital period variations, however, do not support the tertiary hypothesis but could also be caused by a magnetic activity cycle. A short-period option of 94 days, corresponding to a 80 Jupiter mass brown dwarf, did not gain sufficient confirmation and is therefore dropped. I suggest a cycle period of around 7000 days (19 years) and an amplitude of $4\,\mathrm{km\,s^{-1}}$ and interpret it as a third-body induced motion. The third component would thereby surround the known binary system in a wide orbit. Corresponding values for the tertiary mass and the orbital parameters of the binary–tertiary system are quoted (see end of §3.3.6 and Tab. 3.3). However, the plausibility of the suggested tertiary cannot be asserted unless a recurrence is observed or higher-quality RV measurements are available that give a more distinctive RV curve.

We may close this section with the warning of a philosopher: "Let us be on our guard against supposing that anything so methodical as the cyclic motions of our neighboring stars applies generally and throughout the universe; indeed a glance at the Milky Way induces doubt as to whether there are not many cruder and more contradictory motions there, and even stars with continuous, rectilinearly gravitating orbits, and the like. The astral arrangement in which we live is an exception..." (Nietzsche 1882).

3.3 Astrophysical parameters

Since the knowledge of the precise stellar parameters is very important to obtain reliable Doppler images, an extented parameter study was applied. Table 3.7 gives an overview of most important astrophysical parameters of EI Eri. Previously known and improved parameters are listed. The subsequent sections will address a thorough investigation of each parameter (see *comments* in Tab. 3.7). All available data, including those from the literature (see §A.3), were used.

3.3.1 Photometric and orbital period

Strassmeier et al. (1997) give photometric periods for epochs from 91/92 to 95/96 ranging from 1.9352 ± 0.0009 days to 1.9456 ± 0.0028 days and a long-term average of 1.952717 ± 0.000031 days for the time range 1980 – 1996. This value is also derived by Olah & Strassmeier (2002) using an even larger time base of 22.5 years, see Fig. 3.11). The orbital period of 1.9472324 days gained with `sb1` (§3.2.1) is supported by the periodogram of all radial velocities supported by Oláh (2004), see Fig. 3.8.

Given the evolved state of the primary and the short orbital period, it is reasonable to assume synchronised rotation (i.e. $P_{\mathrm{orb}} \equiv P_{\mathrm{rot}}$). In reality, EI Eri's photometric period differs from the spectroscopic orbital period by 0.00549 (3) days, i.e. 474 seconds, almost 8 minutes, or 2.8‰ which is about 180σ. Starspots on the surface of a rotating star can be used to determine the stellar rotation period and show up in the photometric variability. However, differential rotation makes the spot rotation rate become a function of spot latitude. Equally sized spots emerging at lower latitudes, which might rotate slightly faster or slower, will have a stronger impact on the photometric lightcurve than high-latitude or even polar spots. Additionally, stars with spot emergence at preferred latitudes can thereby mock a slightly deviating rotational period. However, as addresses in §5.3, EI Eri's differential rotation is oriented anti-solar, with the poles rotating faster than the orbitally synchronised equator. This would then cause a *shorter* photometric period. In fact, at the observing season 1998/99, EI Eri's photometric period *was* shorter than average (and also shorter than the orbital period), as seen in Fig. 3.12 (to be more precise, two out of three periods found during that season were shorter). However, a possible explanation for the photometric period variations found could be differential rotation.

Another possible cause for asynchronism is an eccentric orbit which can lead to pseudosynchronism (Hall 1986; Hut 1981): In a binary with an eccentric orbit, equilibrium is reached at a value of P_{rot} which is less

Table 3.7: Original and improved astrophysical parameters of El Eri. Orbital and photometric values are listed separately in Table 3.3 and 3.8.

Parameter	Unit	Original value	Reference	Improved value	Comment
Spectral type		G5 IV	Cutispoto (1995)	G5 IV + (M4-5 V)	[a]
$T_{\rm eff}$	K	5460	Strassmeier (1990)	5500±100	from § 3.3.2
	K	5600	O'Neal et al. (1998)	"	"
$T_{\rm spot}$	K	3600 ± 400	Strassmeier (1990)	3600	from § 3.3.2
	K	3700 ± 150	O'Neal et al. (1998)	"	"
$v \sin i$	$\rm km\,s^{-1}$	50	Fekel et al. (1986)	51 ± 0.5	from § 3.3.3
$P_{\rm orb}$	days	1.947227 (8)	Strassmeier (1990)	1.9472324 (38)	from § 3.2
$P_{\rm phot}$	days	1.945	Hall et al. (1987)	1.952717 (31)	see § 3.3.1
	days	1.9527	Olah et al. (2000, 2002)		"
	days	1.952717 (31)	Strassmeier et al. (1997)		", long-term average
M_V	mag	2.75	Fekel et al. (1987)	3.20 ±0.12	from § 3.3.4
L_1, L_2	$L_\odot$	–	–	4.60 ±0.35, (0.01–0.02)	from § 3.3.4, [a]
R_1, R_2	$\rm R_\odot$	≥ 1.9	Fekel et al. (1987)	2.37 ± 0.12, (0.3)	from § 3.3.4, [a]
M_1, M_2	$\rm M_\odot$	1.4–1.8, $\leq$ 1.0–1.3	Fekel et al. (1987)	1.25 ± 0.05, 0.249 ± 0.049	both from § 3.3.6
Inclination	°	$34 \leq i \leq 58$	Fekel et al. (1987)	56.0 ± 4.5	from § 3.3.5
Parallax	mas	17.80 ± 0.97	ESA (1997)		Hipparcos
Distance	pc	75	Fekel et al. (1987)	56.2 ± 3.1	from parallax
Angular diam.	mas	4–6	Wittkowski et al. (2002)	0.3921 ± 0.0006	from R_1 and dist.
Age	Gyr	–	–	4.8 ± 0.5	from § 3.3.6

[a] ... according to $M_2 = 0.249\,\rm M_\odot$ from §3.3.6 and the spectral type-luminosity tables in (Schmidt-Kaler 1982).

Table 3.8: Overview of photometric values of EI Eridani. All available measurements are compared. Entries in **bold face** are the best values and were used in the further investgation. However, all brightness and colour values of EI Eri are variable, so the "best" values are in fact the maximum values. (Note that $(B-V)_{\max}$ does not necessarily equal to $B_{\max} - V_{\max}$.)

EI Eri	Value	Reference
V	$6\overset{\text{m}}{.}95 - 7\overset{\text{m}}{.}1$	
$V_{\max}$	$\mathbf{6\overset{\text{m}}{.}949} \pm 0\overset{\text{m}}{.}013$	from § 2.5
$I_{C\,\max}$	$\mathbf{6\overset{\text{m}}{.}183} \pm 0\overset{\text{m}}{.}014$	from § 2.5
$U-B$	$0\overset{\text{m}}{.}14$	Lloyd-Evans & Koen (1987)
	$\mathbf{0\overset{\text{m}}{.}13}$	Cutispoto (1995) for $V_{\max} = 7\overset{\text{m}}{.}01$
$B-V$	$0\overset{\text{m}}{.}67$	Fekel et al. (1982)
	$0\overset{\text{m}}{.}684$	Fekel et al. (1986) from one observation ($V = 7\overset{\text{m}}{.}11$)
	$\mathbf{0\overset{\text{m}}{.}67}$	Cutispoto (1995) for $V_{\max} = 7\overset{\text{m}}{.}01$
	$0\overset{\text{m}}{.}712 \pm 0\overset{\text{m}}{.}007$	Hipparcos, ESA (1997) for $V = 7\overset{\text{m}}{.}03$
$V-R_J$	$0\overset{\text{m}}{.}611$	Fekel et al. (1986) from one observation ($V = 7\overset{\text{m}}{.}11$)
$V-R_C$	$0\overset{\text{m}}{.}455$	Fekel et al. (1986) transformed using formula 2.2
	$\mathbf{0\overset{\text{m}}{.}40}$	Cutispoto (1995) for $V_{\max} = 7\overset{\text{m}}{.}01$
$V-I_C$	$0\overset{\text{m}}{.}77$	Cutispoto (1995) for $V_{\max} = 7\overset{\text{m}}{.}01$
	$0\overset{\text{m}}{.}77 \pm 0\overset{\text{m}}{.}01$	Hipparcos, ESA (1997) for $V = 7\overset{\text{m}}{.}03$
$V_{\max} - I_{C\max}$	$\mathbf{-0\overset{\text{m}}{.}766} \pm 0\overset{\text{m}}{.}019$	from § 2.5
$R-I_J$	$0\overset{\text{m}}{.}390$	Fekel et al. (1986) from one observation ($V = 7\overset{\text{m}}{.}11$)
$R-I_C$	$0\overset{\text{m}}{.}369$	Fekel et al. (1986) transformed using formula 2.2
	$\mathbf{0\overset{\text{m}}{.}37}$	$(V-I_C) - (V-R_C)$ from Cutispoto (1995)

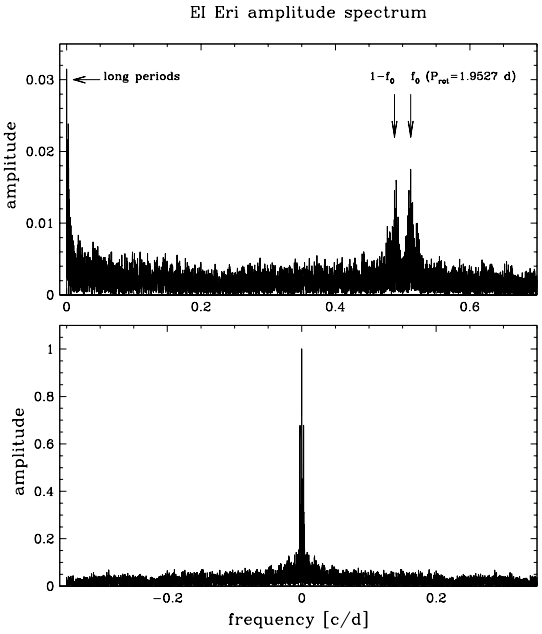

Figure 3.11: Photometric rotation period. From Oláh (2003), using the data from Olah & Strassmeier (2002), Fig. 2c.

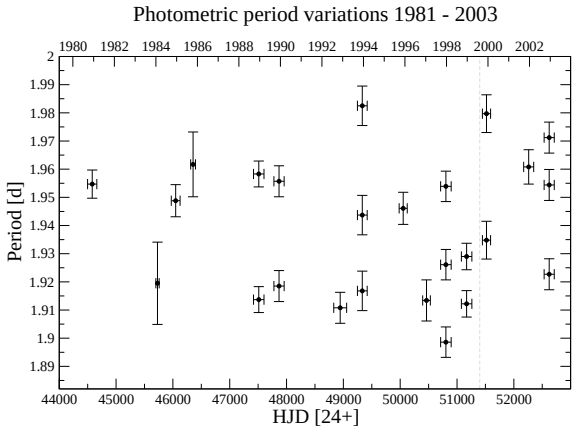

Figure 3.12: Photometric period variations. Calculation provided by Oláh (2004).

than $P_{\rm orb}$, the amount less being a function solely of the orbital eccentricity as given by Hut's equation 42. This can, hence, not account for the deviation found on EI Eri as $P_{\rm rot}$ is greater than $P_{\rm orb}$. Because the orbital solution presented in §3.2.1 sets an upper limit for the eccentricity of 0.015, any pseudosynchronism is thus greater or equal $P_{\rm orb}/1.00135 = 1.9446$ days. Therefore, some other mechanism must be responsible for the higher photometric period. Another cause for an increased period could be the expanding status of the class-IV evolving primary. Based on evolutionary tracks presented in Fig. 3.13, Granzer (2004) estimated that EI Eri's deceleration caused by conservation of angular momentum of the expanding subgiant amounts to ≈ 0.005 days within 1 Myr (at a radius growth of $\approx 0.001\,{\rm R}_\odot$, not taking into account the counteractive acceleration of the decelerating rotation due to tidal forces) – which is in the same order of magnitude as the divergence of the photometric and the orbital period.

3.3.2 Spectral type, $T_{\rm eff}$ and spot temperature

Bidelman & MacConnell (1973) classified EI Eri as G5 IV from objective-prism plates, Harlan (1974) characterises it as G2 IV-V. Abt (1986) assumed from photometric indices a "weak-lined" G5 V classification, while Cutispoto (1995) finds its colours consistent with a G5 IV + G0 V system. The classification of G5 IV is also favoured by Fekel et al. (1986) on the basis of high-resolution spectra. We adopt G5 IV as the most likely case.

Effective temperatures from photometric colours

The effective temperature of EI Eri can be estimated by comparing observed $U-B$, $B-V$, $V-R_C$ and $V-I_C$ colours (which are $0\overset{\rm m}{.}13$, $0\overset{\rm m}{.}67$, $0\overset{\rm m}{.}40$ and $0\overset{\rm m}{.}77$, respectively; see Table 3.8) to synthetic and empirical values from colour-temperature transformation lists. For EI Eri's $B-V$ value of $0\overset{\rm m}{.}67$, Flower (1996) lists a temperature of 5653 K. Comparing $B-V$ and $U-B$ with ATLAS-9 model atmospheres (Kurucz 1993)[4], we find our $U-B$ and $B-V$ values to be consistent with a temperature of $T_{\rm eff}$= 5500 K for metallicities between -0.5 and -1.0 dex which is required by the reconstruction of the line profiles (see §4.2). Solar abundances would yield a higher temperature by 250 K. $V-I_C$ ($0\overset{\rm m}{.}77$) and $V-R_C$ ($0\overset{\rm m}{.}40$) yield temperatures in-between 5500 and 5750 K. Schmidt-Kaler (1982) lists 5770 K for $B-V = 0\overset{\rm m}{.}68$ for luminosity class V. Randich et al. (1993) derived a $T_{\rm eff}$ of 5700 K using a spectrum synthesis analysis. Doppler imaging prefers a temperature of 5500 K (see §4.2).

Contribution from the secondary component

The above temperatures are formally for the combined EI Eri binary star. However, the system is completely dominated by the primary. No spectral lines from the secondary are seen which means that the continuum ratio must be larger than about a factor 10. According to our orbit, $M_2 = 0.249\,{\rm L}_\odot$ (see §3.3.6) which corresponds to a spectral type of M4-5 (assuming luminosity class V) and to $L_2 \approx 1\text{–}2 \cdot 10^{-2}\,{\rm L}_\odot$. Compared to the primary ($L_1 \approx 4.6\,{\rm L}_\odot$), the secondary contributes only 2–4‰ of the total light.

Spot temperature

The spot temperature was determined by Strassmeier (1990) using standardised V and R photometry and the Barnes-Evans relation (Barnes et al. 1978). He gives a temperature difference (star minus spot) of 1860 ± 400 K and, with $T_{\rm star} = 5460$ K, yields an effective spot temperature of 3600 ± 400 K which was also used by Hatzes & Vogt (1992). O'Neal et al. (1996) derived spot temperatures by using the 7055 and 8860 Å bands of the titanium oxide molecule and determined a value of $T_{\rm spot} = 3700 \pm 200$ K. They assumed a photospheric value of $T_{\rm phot} = 5600$ K and found the spot filling factor, f_s, to range from 15% to 38% for four epochs: Oct. 1989 (0.17-0.29), March 1990 (0.36-0.38), Feb. 1991 (0.15) and Feb. 1994 (0.29). This is significantly higher than the values presented by this project and than the values by Strassmeier (1990) which range between 6.4% and 10.3%. O'Neal et al. (1998) repeated his measurements and verified $T_{\rm spot} = 3700 \pm 150$ K and $0.26 \le f_s \le 0.36$ for data obtained in March 1992, $f_s \le 0.18$ for data from January 1995 and $f_s = 0.15$ for data from December 1995. Typical errors for f_s range from 0.04 to 0.08. Their spot filling factor tends to change significantly on short timescales, sometimes within only one rotation.

[4] see also ftp://ccp7.dur.ac.uk/ccp7/Atlas/colours/ubvm05k2.dat

3.3.3 $v \sin i$ and $R \sin i$

The projected equatorial velocity, $v \sin i$, was estimated by Fekel et al. (1986) to be 50 ± 3 km s^{-1}. Hatzes & Vogt (1992) and Donati et al. (1997) give 50 ± 1 km s^{-1} and 51 ± 1 km s^{-1}, respectively, which is confirmed by our Doppler imaging results to be 51 ± 0.5 km s^{-1} (see §4.2.4).

The minimum radius, $R \sin i$, in solar radii can be calculated using the equation

$$R \sin i = \frac{P_{\rm rot} \cdot v \sin i}{50.6} \tag{3.2}$$

where the rotational velocity is in km s^{-1} and the period is in days. The rotation period in days can be determined from photometric or spectroscopic (radial velocity) observations; we presume $P_{\rm rot} = P_{\rm orb} = 1.9472324 \pm 0.0000038$ and get $R \sin i = 1.963 \pm 0.019$ R$_\odot$.[5] Obviously, EI Eri's primary star is a subgiant rather than a dwarf, ruling out the luminosity class V suggested by Abt (1986).

3.3.4 Hipparcos-based absolute parameters: luminosity and radius

For solving the formulae used in this and the following sections and, most important, for incorporating correct error propagation, the php program `astro:calc` was written and made available on the World-WideWeb[6]. Appendix B.6 has more details about decent error calculation.

A trigonometric parallax of 17.80 ± 0.97 milli-arcsec was measured by the Hipparcos spacecraft (ESA 1997). This corresponds to a distance of 56.2 ± 3.1 pc. The brightest V magnitude of EI Eri corresponds to $6\overset{\rm m}{.}949$ (see § 2.5). Now, using

$$M_V = m_V - 5 \log R[pc] + 5 \tag{3.3}$$

we achieve the absolute visual magnitude which amounts to $M_V = 3\overset{\rm m}{.}20 \pm 0.12$. According to Flower (1996), the bolometric corrections for a subgiant with a temperature of $5500 \pm 100K$ is -0.139 ± 0.025.

$$M_{\rm bol} = M_V + BC \tag{3.4}$$

gives the bolometric magnitude which amounts to $M_{\rm bol} = 3\overset{\rm m}{.}06 \pm 0.08$. As we did not adopt an error for the brightest visual magnitude, the errors merely reflect the error of the parallax. However, if the brightest visual magnitude is smaller than $6\overset{\rm m}{.}9$, it does not affect the error of the stellar radius, but just the radius itself.

We now neglect interstellar absorption (as EI Eri is a nearby star) and calculate the luminosity (adopting a solar bolometric magnitude of $4\overset{\rm m}{.}72$) by using

$$L/L_\odot = 10^{\frac{4.72 - M_{\rm bol}}{2.5}} \tag{3.5}$$

Therefore, $L/L_\odot = 4.60 \pm 0.35$. Finally, applying the Stefan-Boltzmann law and assuming $T_\odot = 5777$ K and $T = 5500 \pm 100$ K,

$$R/R_\odot = \sqrt{L/L_\odot} \cdot (T/T_\odot)^{-2} \tag{3.6}$$

leads to the star's radius (independent of the inclination): $R/R_\odot = 2.37 \pm 0.12$ (consistent with the value of $R/R_\odot \geq 1.9$ from Fekel et al. 1987).

Derived using $\tan\left(\frac{\theta}{2}\right) = \frac{R/R_\odot}{\text{distance}} = \frac{2.37 \pm 0.12 \times 6.96\ 10^8}{56.2 \pm 3.1 \times 3.08568\ 10^{16}}$, EI Eri's radius corresponds to an angular diameter of $\theta = 0.3921 \pm 0.0006$ mas, in good agreement with the estimations from Wittkowski et al. (2002), which is twice the size of their proposed detection limit of 0.2 mas for starspot measurements with VLTI/AMBER.

[5] Compare: For $P_{\rm rot} = P_{\rm phot} = 1.9527 \pm 0.0001$, we get $R \sin i = 1.968 \pm 0.019$ R$_\odot$.
[6] http://wasi.ws/astro/calc/

3.3.5 Orbital inclination

Fekel et al. (1987) assume an upper limit for the mass of the secondary of $1.0 - 1.3\,\mathrm{M}_\odot$. Their estimation depends on the mass and assumed luminosity of the primary and is based on experiences of detecting the secondaries of other RS CVn binary stars in this wavelength region. Hence, they derive a lower limit for the inclination of $i \geq 34°$.[7] Since there is no photometric eclipse, we can assume $R_1 + R_2 < a\cos i$ which allows Fekel et al. (1987) to obtain an upper limit for the inclination of 58°. Therefore, they assume an inclination of $46° \pm 12°$(reading $36.5° \pm 21.5°$). This notation is misleading; it should be written as $34° \leq i \leq 58°$ (or actually $15° \leq i \leq 58°$), because the probability distribution of the inclination is equal within this range and zero outside (disregarding the error in the lower and upper limit).

We now repeat their estimation with our improved parameters. For a number of assumed primary masses, Table 3.9 lists several values of M_2 for different inclination angles using the mass function $f(\mathrm{M}) = (M_2 \sin i)^3 (M_1 + M_2)^{-2} = 0.00391\,\mathrm{M}_\odot$ (see App. B.2). For $i = 90°$, the resulting mass ratio (row 3) and semi-major axis (row 4; $a \sin i = a_1 \sin i\,(1 + M_1/M_2)$) – which are consequently the respective lower (M_2) and upper limits (M_1/M_2 and $a \sin i$) – are shown. Thereby, we conclude that for the chosen range of primary masses, the lower mass limit for the secondary is $M_2 \geq 0.17$. M_2 is again plotted for $i = 15°$, 20° and 30°, demonstrating the lower limit of the inclination as we assume the primary mass to be smaller than 1.0 – $1.3\,\mathrm{M}_\odot$. We can now take the value for the primary mass obtained in §3.3.6 (which was achieved merely using T_{eff} from §3.3.2 and L_1 from §3.3.4 which are both independent of the inclination), $M_1 = 1.25 \pm 0.05\,\mathrm{M}_\odot$, and get $M_2 \geq 0.202 \pm 0.008\,\mathrm{M}_\odot$, a maximum mass ratio of $M_1/M_2 \leq 6.18 \pm 0.25$ and an upper limit for the semi-major axis of $a \sin i \leq 5.16 \pm 0.25 \cdot 10^6$ km.

Now, using the eclipse-criterion $R_1 + R_2 < a\cos i$ (see App. B.3), our maximum value for $a \sin i$ and our value $R_1 = 2.368 \pm 0.124\,\mathrm{R}_\odot$ from §3.3.4, we achieve maximum values for the orbital inclination, i.e., $i \leq 71.6 \pm 2.0°$ for $R_2 = 0.1$ R$_\odot$, $i \leq 70.0 \pm 1.9°$ for $R_2 = 0.3$ R$_\odot$, $i \leq 69.5 \pm 1.9°$ for $R_2 = 0.5$ R$_\odot$ and $i \leq 67.5 \pm 1.9°$ for $R_2 = 0.7$ R$_\odot$. [8]

Using the equation $\sin i = (P_{\mathrm{rot}} \cdot v \sin i)/(50.6 \cdot R/\mathrm{R}_\odot)$, we can directly calculate the stellar inclination (see App. B.4). Taking the radius from above ($2.367 \pm 0.124\,\mathrm{R}_\odot$), the $v \sin i$ from Doppler imaging ($51.0 \pm 0.5\,\mathrm{km\,s^{-1}}$) and $P_{\mathrm{rot}} = 1.9472324 \pm 0.0000038$, we obtain $i = 56.0 \pm 4.5°$. Assuming the stellar rotational inclination to be perpendicular to the orbital plane, we adopt this as final inclination value.

3.3.6 Mass and evolutionary status

Fekel et al. (1987) estimated a mass of $1.4 \leq M/\mathrm{M}_\odot \leq 1.8$ for the primary and an upper limit for the secondary (for $i = 90°$) of $1.0 - 1.3\mathrm{M}_\odot$, depending on the mass and assumed luminosity of the primary. They suggested the secondary to be a late K or early M dwarf (since no evidence for a hot white dwarf companion is seen in the ultraviolet). According to Schmidt-Kaler (1982), the mass for a G5 IV star is around $1\,\mathrm{M}_\odot$.

With the relatively precise luminosity from §3.3.4 and the temperature from §3.3.2, we can locate EI Eri's primary star in the H-R diagram and compare its position with evolutionary tracks by Granzer (2003) and Schaller et al. (1992), see Fig. 3.13. The models by Granzer are identical with the ones presented in Granzer et al. (2000) but the calculations were extended to post-main sequence stars.[9] The result is shown in Fig. 3.13. The thick black lines are the post-main-sequence, the thin grey lines the pre-main-sequence tracks for masses of 1.0, 1.1, 1.2, (1.25,) 1.3, 1.5, 1.7 and 2.0 M$_\odot$ by Granzer (2003) with $Y = 0.277$ and $Z = 0.02$. The thin black lines are, for comparison, post-main-sequence tracks by Schaller et al. (1992) in

[7] Note that Fekel et al. (1987) accidently used $f(\mathrm{M}) = 0.041$ for their calculations instead of 0.0041 as listed in their paper. Accordingly, the values in their Table V are wrong. The correct inclination limits using their data values should read $15° \leq i \leq 58°$.

[8] $0.1 \leq R_2 \leq 0.7$ because we expect the secondary to be late K or M type.

[9] The stellar models were calculated by Thomas Granzer with an updated version of the stellar evolution code by Kippenhahn et al. (1967). Opacities of Alexander & Ferguson (1994) were used to complement the OPAL opacities by Iglesias & Rogers (1996) at the low-T/high-ρ end. The OPAL equation of state (Rogers et al. 1996) was used whenever applicable, otherwise the MHD equation of state (Mihalas et al. 1990) was adopted. Local mixing-length theory was used for modelling the convection zone. Comparing a model of a 1-M$_\odot$ star at an age of 4.6 Gyr with the present Sun confines the mixing-length parameter to $\alpha = 1.67$ and the initial helium abundance to $Y = 0.277$. Metallicity was set to $Z = 0.02$.

Table 3.9: For a number of assumed primary masses, the respective secondary masses M_2, mass ratios M_1/M_2 and semi-major axes $a \sin i$ are listed. These values are calculated under the assumption of $i = 90°$, thereby giving the upper limit for M_2, M_1/M_2 and $a \sin i$). For M_2, we additionally list its values calculated under the assumption of $i = 15, 20$ and $30°$, demonstrating the lower limit of the inclination. The radius gives another constraint for the upper limit of the inclination angle S(i) which was obtained using the eclipse criterion $R_1 + R_2 < a \cos i$ assuming $R_1 = 2.368\,\mathrm{R}_\odot$. For $M_1 = 1.25$, the respective errors are given. See §3.3.5.

M_1	1.00	1.10	1.15	1.20	1.25 ± 0.05	1.30	1.35	1.40	1.50	1.60	1.80	$\mathrm{M}_\odot$
M_2 $(i = 90°)$	≥ 0.18	0.19	0.19	0.20	0.202 ± 0.008	0.21	0.21	0.22	0.23	0.24	0.25	$\mathrm{M}_\odot$
M_1/M_2	≤ 5.70	5.90	6.00	6.10	6.188 ± 0.253	6.28	6.36	6.45	6.62	6.77	7.07	
$a \sin i$	≤ 4.81	4.97	5.03	5.10	5.164 ± 0.254	5.23	5.29	5.35	5.47	5.58	5.80	$10^6\,\mathrm{km}$
M_2 $(i = 15°)$	0.95	1.00	1.02	1.04	1.065 ± 0.038	1.09	1.11	1.13	1.17	1.21	1.29	$\mathrm{M}_\odot$
M_2 $(i = 20°)$	0.64	0.68	0.69	0.71	0.725 ± 0.027	0.74	0.76	0.77	0.80	0.83	0.89	$\mathrm{M}_\odot$
M_2 $(i = 30°)$	0.39	0.42	0.43	0.44	0.449 ± 0.017	0.46	0.47	0.48	0.50	0.52	0.56	$\mathrm{M}_\odot$
S(i) $(R_2 = 0.1\mathrm{R}_\odot)$	70.4	70.9	71.1	71.4	71.6 ± 2.0	71.8	72.0	72.2	72.6	72.9	73.5	°
S(i) $(R_2 = 0.3\mathrm{R}_\odot)$	68.9	69.5	69.7	70.0	70.2 ± 1.9	70.4	70.7	70.9	71.3	71.6	72.2	°
S(i) $(R_2 = 0.5\mathrm{R}_\odot)$	67.5	68.1	68.4	68.6	68.9 ± 1.9	69.1	69.3	69.6	70.0	70.3	71.0	°
S(i) $(R_2 = 0.7\mathrm{R}_\odot)$	66.1	66.7	67.0	67.3	67.5 ± 1.9	67.8	68.0	68.3	68.7	69.1	69.8	°

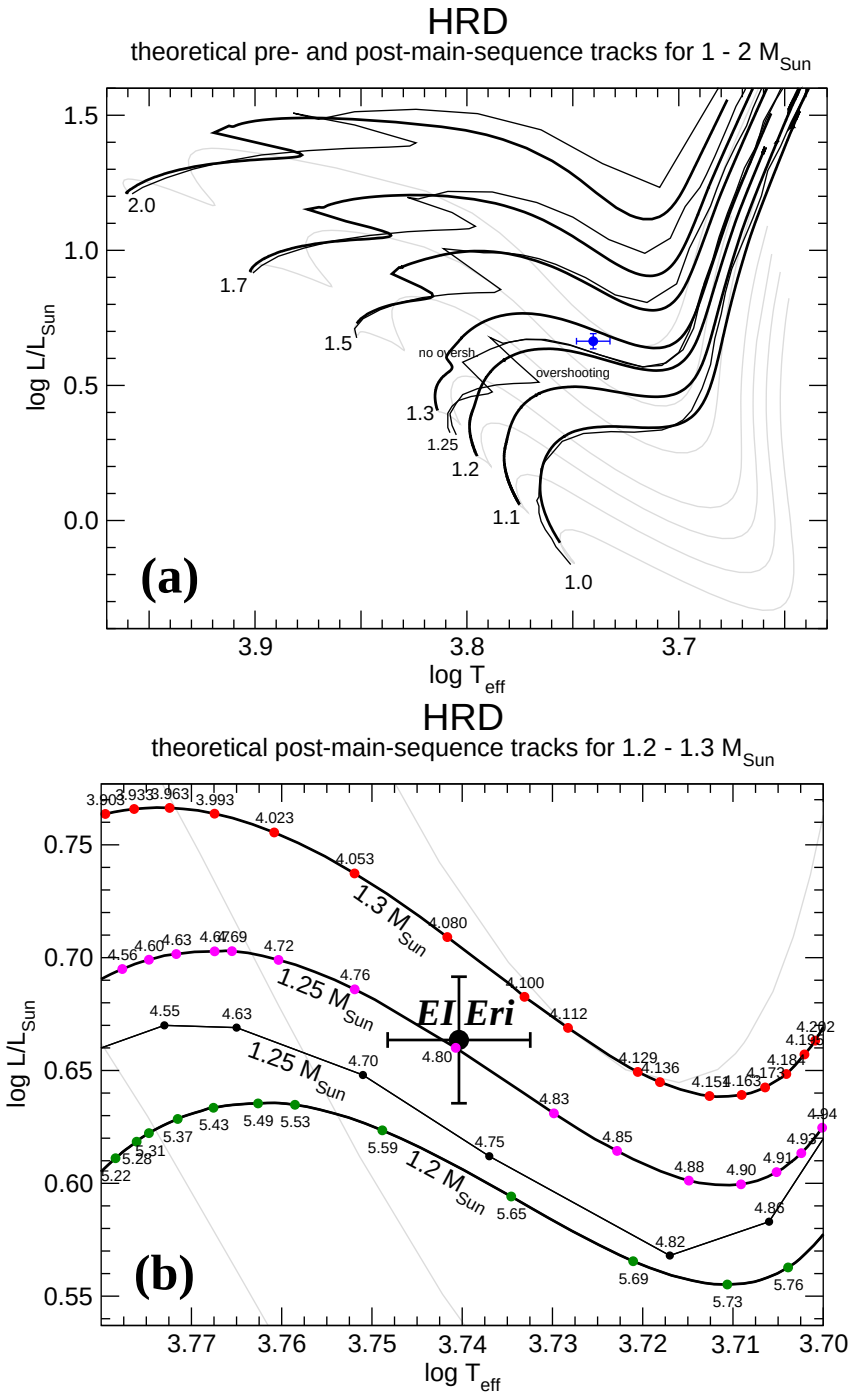

Figure 3.13: **(a)** Evolutionary tracks for post-main-sequence stars (thick black lines) and pre-main-sequence stars (thin grey lines) for masses of 1.0, 1.1, 1.2, 1.3, 1.5, 1.7 and 2.3 solar masses by Granzer (2003). In addition, post-main-sequence tracks for 1.0, 1.25, 1.5, 1.7 and 2.0 solar masses by Schaller et al. (1992) are shown as thin black lines. The position of EI Erdani is marked at $\log T_{\rm eff} = 3.7404 \pm 0.0079$ (5500 ± 100 K) and $\log L/\mathrm{L}_\odot = 0.664 \pm 0.028$ ($4.6 \pm 0.3\,\mathrm{L}_\odot$). **(b)** shows the central range of (a) but adding age along the evolutionary tracks (the values are Gyr) and an additional track for $M = 1.25\,\mathrm{M}_\odot$ by Granzer. The tracks suggest a primary mass of $M_1 = 1.25 \pm 0.05\,\mathrm{M}_\odot$ and an age of 4.8 ± 0.5 Gyr.

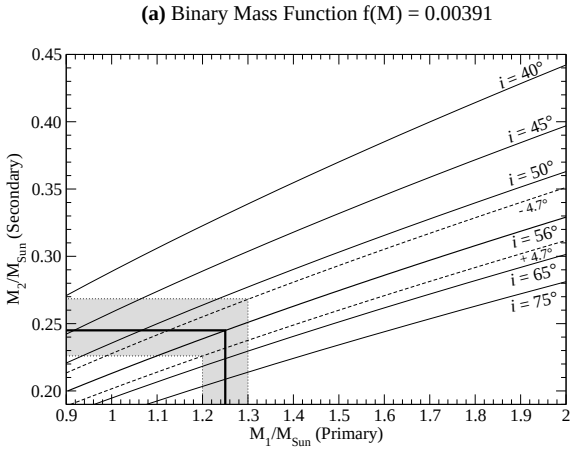

Figure 3.14: Relation between mass of primary and secondary star for f(M)=0.00391 (see §3.2.1) as a function of inclination. The thick black lines marks the mass of the primary star and the corresponding secondary mass. The grey shade indicates the error range.

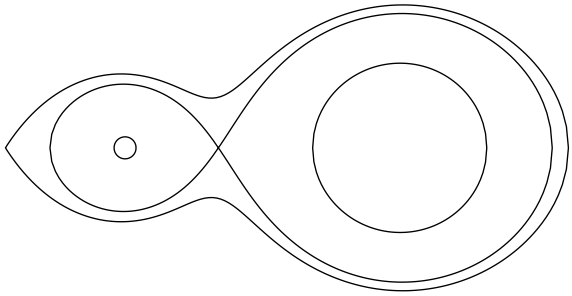

Figure 3.15: Critical Roche equipotentials of the EI Eri binary system, on the right side the primary star. The inner circles are the stellar surfaces, the other lines denote the inner and outer critical equipotentials, respectively. The primary fills $\approx 60\%$ of its Roche lobe and is close to spherical in shape.

steps of 1.0, 1.25, 1.5, 1.7 and 2.0 $M_\odot$ with $Y = 0.3$ and $Z = 0.02$; for Schaller et al. (1992), masses above 1.25 are with, those below without overshooting; for 1.25, both cases are shown. Figure 3.13b gives a detail of (a) but adding ages along the evolutionary tracks. In both diagrams, EI Eri's primary star is marked with the appropriate error bars. The tracks suggest a mass between 1.25 (Granzer) and 1.28 (Schaller) solar masses and an age between 4 and 5 Gyr for the primary. The difference between both models is probably due to the different initial helium abundance. We adopt a value of $M_1 = 1.25 \pm 0.05\,M_\odot$ for the primary and an age of 4.8 ± 0.5 Gyr from the Granzer tracks. These values are consistent within the errors with the models by Schaller et al.

We can now estimate the mass of the secondary component from the mass function $f(M) = (M_2 \sin i)^3 / (M_1+M_2)^2 = 0.00391 \pm 0.00010$ (achieved from the orbital solution in §3.2; see Table 3.3). Figure 3.14 shows the relation of M_1 and M_2 as a function of inclination. Assuming $i = 56\overset{\circ}{.}0 \pm 4\overset{\circ}{.}5$ (see §3.3.5), a presumed primary mass of $1.25 \pm 0.05\,M_\odot$ requires the mass of the secondary to be $0.249 \pm 0.049\,M_\odot$ corresponding to $K_2 = 134 \pm 27\,\mathrm{km\,s^{-1}}$and $a_2 \sin i = 3.61 \pm 0.72 \cdot 10^6$ km. (See Appendix B.2 for details on the calculation of M_2.)

From the combined mass for the binary system ($M_1 + M_2$) of $1.50 \pm 0.07\,M_\odot$, we can incorporate the mass function for the proposed binary/tertiary system (see §3.2.2, Table 3.3 on page 25) and repeat the above evaluation in order to estimate the tertiary mass M_3. A period of 7000 ± 200 days yields $M_3 = 0.74 \pm 0.66\,M_\odot$ corresponding to $K_3 = 8 \pm 7\,\mathrm{km\,s^{-1}}$ and $a_3 \sin i = 7.8 \pm 7.2 \cdot 10^7$ km (again for $i = 56\overset{\circ}{.}0 \pm 4\overset{\circ}{.}5$; for the results, see Table 3.3, very right column). The large errors are mainly due to the large error in the mass function of the binary–tertiary orbit which itself is mainly due to the large error in $K = 4 \pm 1\mathrm{km\,s^{-1}}$, the half-amplitude of the barycenter variation. The angular separation from the binary would then amount to 168 ± 2 mas. The problem of the possible tertiary component was discussed in §3.2.2ff.

3.3.7 Roche lobe and log g

The Roche-lobe radius is determined from the semi-major orbital axis and the mass ratio.[10] Assuming $M_1/M_2 = 1.25/0.249 = 5.10 \pm 0.05\,M_\odot$ and $a \sin i = a_1 \sin i + a_2 \sin i = 4.325 \pm 0.725 \cdot 10^6$ km, we can, using the formula from Eggleton (1983), calculate the Roche-lobe radii $R_{\mathrm{L},1} \sin i = (0.521 \pm 0.017)\, a \sin i = 3.24 \pm 0.56\,R_\odot$ and $R_{\mathrm{L},2} \sin i = (0.251 \pm 0.014)\, a \sin i = 1.56 \pm 0.28\,R_\odot$. Under the assumption of $i = 56\overset{\circ}{.}0 \pm 4\overset{\circ}{.}5$, this translates to $R_{\mathrm{L},1} = 3.91 \pm 0.67\,R_\odot$ and $R_{\mathrm{L},2} = 1.88 \pm 0.34\,R_\odot$ for the primary and the

[10] Correct error calculation for this section is enhanced by `astro:calc`, see http://wasi.ws/astro/calc/

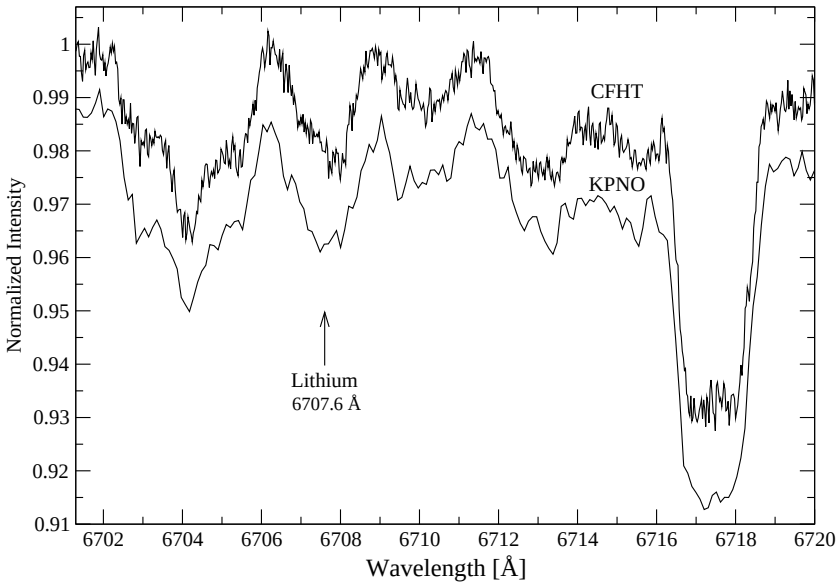

Figure 3.16: Lithium spectra from CFHT (top) and KPNO (bottom). The KPNO spectrum is, for better viewing, shifted in intensity by -0.01. Signal-to-noise is ≈ 550/330 (CFHT/KPNO), dispersion 0.027/0.103 Å, integration time 600/3600s.

secondary, respectively. The relative radius R/a of the primary is 0.378. This means that the primary ($R_1 = 2.37 \pm 0.12\,\mathrm{R}_\odot$) fills a large fraction of its Roche lobe ($61 \pm 10\%$) but is still significantly detached from its inner critical equipotential surface. The secondary with assumed $M_2 \approx 0.3\,\mathrm{M}_\odot$ fills about 20% of its Roche lobe. Appendix B.5 gives details on the calculation of the Roche lobe and its error. Figure 3.15 shows a graphical view of the binary system. Shown are the location of the stellar surfaces and the inner and outer critical equipotentials as obtained with the program BinaryMaker (Bradstreet 1993).

Using $i = 46°$, $M/\mathrm{M}_\odot = 1.6$ and $R/\mathrm{R}_\odot = 2.6$, O'Neal et al. (1996) determined $\log g$ to be ≈ 3.8 in consistency with $\log g = 3.75$ used by Hackman et al. (1991). Randich et al. (1993) determined a $\log g$ of 4.1 using spectrum synthesis analysis. Gray (1992) lists a $\log g$ of 4.46 for a G5 dwarf (V) and 3.3 for a G5 giant (III). Using the mass and radius of the primary and applying the relation

$$g = \frac{GM}{R^2}\ , \tag{3.7}$$

where G is the gravitational constant $6.6726{\cdot}10^{-8}\,\mathrm{cm^3\,g^{-1}\,s^{-2}}$, we can directly calculate $\log g$ to $3.786{\pm}0.068$ (where g is in $\mathrm{cm\,s^{-2}}$), in good agreement with previous claims.

3.3.8 Lithium abundance

Measurements of two spectra that show EI Eri in the lithium region (one from CF96 and one from an CFHT observing run in October 1997; see Fig. 3.16) give an equivalent width of $40 \pm 5\,\mathrm{m\AA}$ in good agreement with the value obtained by Fekel et al. (1987) of 36 mÅ. Comparing this to theoretical curves of growth from Pavlenko & Magazzu (1996), we derive a lithium abundance of $\log n(\mathrm{Li}) = 2.0$ for $T_{\mathrm{eff}} = 5500\,\mathrm{K}$ and $\log g = 3.5$–4.5, both LTE and non-LTE. However, if the equivalent width is reduced to 25 mÅ to account for blends, the abundance is still $\log n(\mathrm{Li}) = 1.75$. Randich et al. (1993) estimate $\log n(\mathrm{Li}) = 1.8$ using spectrum synthesis analysis.

Chapter 4

Doppler imaging: Tests and assumptions

"This book full of mystery,
Is it not ample company?
The stars' course then you'll understand
And Nature, teaching, will expand
The power of your soul, as when
One spirit to another speaks."

Goethe, Faust, Night

"I think my eyes are getting better. Instead of a big dark blur it's a big light blur."

Han Solo, Return of the Jedi

The *Doppler imaging* technique allows the reconstruction of the surface spot distribution of rapidly rotating stars by using the relation between wavelength position across an absorption line and spatial position across the stellar disk. The principle, idea, development and basic outlines of the technique of Doppler imaging were already described in §1.3. For the maps presented in this investigation, I primarily apply the Doppler-imaging code `TempMap` by John Rice – as described by Rice et al. (1989) and reviewed by Piskunov & Rice (1993), Rice (1996) and, most recently, by Rice (2002). For comparison only, the code `DOTS` by Andrew Collier-Cameron was applied (§4.3). `DOTS`'s general operation is identical to that of its predecessor `SSSIP` which is described in Collier Cameron (1992a), Collier Cameron et al. (1992) and Unruh et al. (1995). In chapter 4.3.1, `TempMap` and `DOTS` are described and compared in some more details.

4.1 Doppler imaging of EI Eri

With its large rotational velocity and an intermediate inclination, EI Eri is, as Fekel et al. (1987) already noted, an ideal candidate for *Doppler imaging*. Consequently, EI Eri has been a prime target since the first application of this technique to spotted late-type stars in 1982 (see my suggestion for a stamp "25 years of Doppler Imaging" in Figure 4.1). Doppler images of EI Eri can be found in Strassmeier (1990) (epoch 1987), Strassmeier et al. (1991) (epoch 1988; investigation of different DI techniques) and, for the 1984-87 period, in Hatzes & Vogt (1992). O'Neal et al. (1996) determined spot covering factors between 16% and 37%.

Observations of EI Eri have now been carried out for about two decades. Seven years of our long term synoptic observations of EI Eri with the McMath-Pierce telescope (1988-1995), one dedicated NSO/McMath visitor observing run in 1996, several dedicated KPNO/coudé feed visitor observing runs in 1995, 1996 and 1997 and participation in the MUSICOS 1998 observing campaign yield the following results: All surface maps of EI Eri show high-latitude spots surrounding or covering the rotational pole as also observed by

Hatzes & Vogt (1992), but in contradiction to what is seen on the Sun where spots occur only within $\pm 35°$ of the equator. This high-latitude/polar spot seems to be long-lived but changes its shape on comparatively short timescales (of the order of weeks). Spots along the stellar equator also occur, but their lifetimes tend to be relatively short and are not sufficiently well determined.

In one respect, EI Eri is less complicated to Doppler map than other RS CVn stars: It is a single-lined spectroscopic binary, and no correction for the contribution of the companion star has to be adopted (like in UX Ari; see Aarum Ulvås & Engvold 2003). However, the rotational period of 1.947 days makes it difficult to obtain spectral coverage for a complete rotational period, and ideally three weeks of observations from one particular observatory site are needed to provide good phase coverage for a Doppler image of EI Eridani.

Figure 4.1: (*left*) Austrian stamp "150 years Doppler principle" from 1992 and (*right*) suggestion for a stamp "25 years of Doppler Imaging".

4.2 TempMap: Input parameters and assumptions

There are **two groups of input parameters** for `TempMap`: those used for *calculating the theoretical local line profile* and those needed for *determining the temperature distribution on the star's surface* by comparing the calculated and the observed line profiles. The **first group** includes effective temperature $T_{\rm eff}$, gravity $\log g$, macro turbulence ζ_t and ζ_r (tangential and radial component), micro turbulence ξ, equatorial rotation velocity v_{eq}, stellar inclination i, abundances of chemical elements and atomic parameters (transition probability $\log gf$, lower excitation potential $\chi_{\rm low}$, atomic number, ionisation and wavelength) including blends. The parameters of the **second group** – used for calculating the temperature distribution – are spectroscopic and photometric data, regularisation method, smoothing parameter, number of iterations, weight of photometry, maximum temperature and a stepsize for the `TempMap` program.

4.2.1 Running `TempMap` – an overview

All these parameters are defined in the parameter file `tempmap.par` and in one of the input files which are the abundance file `abund.dat`, the atmosphere file `allatmos35.t5750`, the blend files (e.g. `ca1_6439.blend`) and the photometry file `photometry.dat`. The main input file (its name can be chosen arbitrarily) lists the filenames of the appropriate spectra (which are in text or fits format) including radial velocity shifts and is used by `extract2` together with the parameter file `period.par` (which lists orbital information) and the file `linelist.dat` (containing information about the spectral lines used for DI). The tool `extract2` (written by M. Weber) is used for preparing the data for extraction, adjusting remaining shifts and marking spectral regions which are to be cut later by `tmake2`. The extraction program `tmake2` (also by M. Weber) produces the final input file for `TempMap` (typically named `ca1_6439_s1_0.in`) using the blend file, the photometry file and the parameter files `tempmap.par` and `tmake2.par` which defines $\Delta\lambda$ and the number of points of the final spectra and a filter parameter for the fourier transformation; `tmake2.par` also lists the S/N ratio

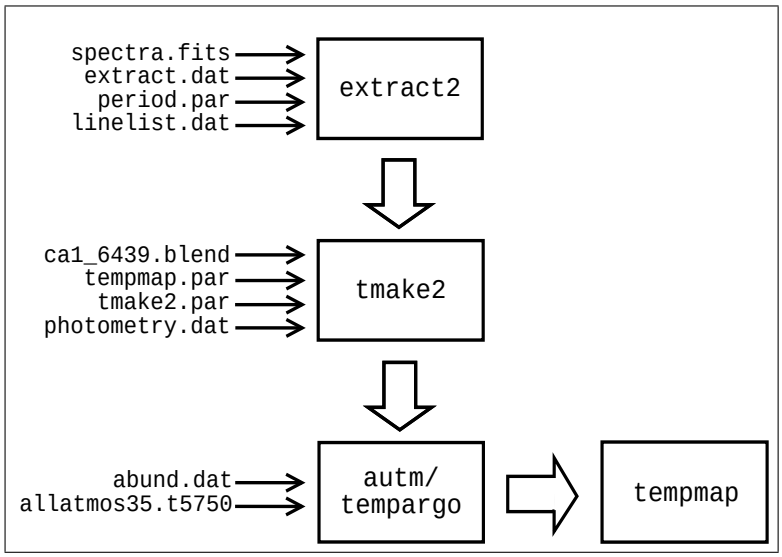

Figure 4.2: Flowchart: Input files involved for `TempMap`.

of the observed spectra and the FWHM of the instrumental profile. See Fig. 4.2 for a flowchart overview of the input files involved for `TempMap`. The final input file is then used together with the abundance and the allatmos file for running `TempMap`. This can be done by just entering the command or, more sophisticated, by the scripts `autm` and its add-on program `tempargo` [1]. The script `autm` allows to automatically submit an arbitrary number of tempmap jobs to the fastest currently available computers of the local linux cluster, being able to run as many jobs simultaneously as free CPU's are available.[2] The application program `tempargo` varies a specific tempmap parameter in a given range, creates the corresponding tempmap files, submits them to `autm` for simultaneous Doppler reconstruction and finally analyses and plots the resulting χ^2 distribution, which is most useful for fast and precise parameter evaluation.

Tuning the input parameters, `TempMap` turns out to be sensitive to the equatorial rotational velocity v_{eq}, abundances, transition probability $\log gf$, the number and intensity of blends, and to wavelength and intensity shifts of the individual spectral lines. It is slightly sensitive to inclination i, microturbulence ξ and temperature. However, `TempMap` does not allow to finetune micro and macro turbulences, stellar inclination, excitation potential $\chi_{\rm low}$, gravity $\log g$ and temperature, because the resulting line-profile fits and corresponding $\Sigma(O-C)$ values are (in a one-dimensional parameter evaluation) not influenced clearly enough to decide for the best input value of the relevant parameter. Values for these parameters were therefore chosen on the basis of evaluations presented in §3.3.

4.2.2 Radial velocity shifts

Due to the orbital movement of the binary star, the spectral lines of the primary are shifted according to orbital phase and radial-velocity corrections need to be applied. This can be done in several ways: (1) The individual line profiles can be shifted according to their *measured* radial velocity value. (2) The measured values can be used for calculating an orbit and the individual line profiles can then be shifted according to their *theoretical* radial velocity value. (3) A cross correlation between the individual line-profile wings is performed and the spectra are shifted accordingly. (4) The line profiles are shifted by hand and visual judgement.

The first method introduces a random error, the second method a systematical error corresponding to the inaccuracy of the orbit, the last method an arbitrary error – while the third method is almost too accurate:

[1] See http://www.aip.de/∼wasi/astro/autm/ for a detailed description of `autm` and `tempargo`.

[2] As of April 2004, there are 96 linux hosts with 110 CPU's available at the AIP, offering altogether about 230 GHz of calculating capacity.

Table 4.1: Specific parameters for TempMap

Parameter	Value
$P_{\rm phot} = P_{\rm rot}$	1.9472324
$T_{0,\rm phot} = T_{0,\rm rot}$	2448054.7109
γ	21.64 $\mathrm{km\,s^{-1}}$
K1	26.83 $\mathrm{km\,s^{-1}}$
e (eccentricity)	0 (adopted)
$T_{\rm phot}$	5500 K
$T_{\rm max}$	6000 K
$v \sin i$	51.0 $\mathrm{km\,s^{-1}}$
Inclination i	56.0°
$\log g$	3.5
Micro turbulence ξ	2.0 $\mathrm{km\,s^{-1}}$
Macro turbulence $\zeta_{\rm r} = \zeta_{\rm t}$	4.0 $\mathrm{km\,s^{-1}}$
Regularisation	Maximum Entropy
Stepsize	0.005
Smoothing parameter	5.0
Weight of phot. data	0.1
Number of iterations	15
Iteration number when phot. data come in	5
$\Delta\lambda$ of output spectra	0.08
Number of points $n_{\rm pts}$ in output spectra	43
$\log[Ca]$ abundance	−6.3 (0.6 dex below solar)
$\log[Fe]$ abundance	−5.5 (1.1 dex below solar)
FWHM of instrumental profile (CF/McMath/MUSICOS) [Å]	0.27 / 0.25 / various
Filter parameter (≥ FWHM of instr. prof.) [px]	4.0 / 3.5 (NSO syn./96 fall) 3.5 – 4.0 (KPNO CF) 16. (MUSICOS)

it even corrects for the spots situated in the line profile and thereby reduces the spottedness of the star. In order to minimise this effect, the cross correlation is only applied in the line wings where the influence of the spots is minor.

All these methods were applied and compared. The results were different depending on the quality (S/N) of the spectra. In fact, neither of the first three methods were sufficient for gaining good quality Doppler maps. In the end, the line profiles were shifted according to their measured radial velocities and then adopted by hand, as required.

4.2.3 Data preparation and mapping procedure

Once the data are ready reduced, the radial velocity shifts are measured, the orbit is determined and the stellar parameters are fixed, we mark the edges of each mapping line and extract the line profiles from each spectrum in the proper sequence, either sorted by orbital phase or chronologically.[3] At first, very high frequency noise (above the Nyquist frequency) is removed by using a filter value (`FILT`) which is based on the FWHM of the instrumental profile. For the Coudé Feed data we used 3.5–4.0 [pixel], for the McMath data 4.0. The next step is to remove the instrumental profile from each of the extracted profiles. This is done with a Gaussian approximation to the true instrumental profile where the average nightly FWHM of

[3] This choice does not influence the resulting map, but only the order in which the calculated and observed line profiles are plotted. For this investigation, we choose a chronological order since line profiles of similar phases can be differently shaped due to intermediate changes in the spot distribution (which seem to be typical for EI Eri; see §6.2) and can be spotted more easily.

Table 4.2: Line blends and atomic parameters.
The line printed in cursive with prefixed + is the respective mapping line.

Wavelength [Ångstrøm]	Atomic number	Transition probability $\log gf$	Excitation potential $\chi_{\rm low}$ [eV]	Ionisation level
6392.538	26	-4.00	2.279	1
6393.280	23	-1.16	2.115	1
+6393.602	*26*	*-1.50*	*2.43*	*1*
6394.237	57	-0.57	0.433	1
6395.113	23	-2.743	2.927	1
6395.153	27	-0.926	3.812	1
6410.822	22	-2.20	2.239	1
6410.926	22	-1.30	2.239	1
6411.445	22	+0.08	3.569	1
+6411.647	*26*	*-0.60*	*3.654*	*1*
6411.884	27	-2.20	2.542	1
6412.200	26	-3.70	2.453	1
6429.906	27	-2.35	2.137	1
6430.472	23	-0.70	1.955	1
+6430.844	*26*	*-2.20*	*2.176*	*1*
6431.623	23	-0.49	1.950	1
6431.994	28	-2.90	3.542	1
6432.680	26	-2.80	2.891	2
6437.640	63	-0.45	1.320	2
6437.703	14	-2.35	5.863	1
6438.088	23	-0.50	2.684	1
6438.755	26	-2.48	4.435	1
+6439.075	*20*	*0.470*	*2.526*	*1*
6439.554	26	-3.55	4.473	1
6440.566	14	-3.28	5.616	1
6440.971	25	-2.00	3.772	1

several weak lines from a Thorium-Argon comparison exposure is adopted as the FWHM of the instrumental profile (Coudé Feed: 0.27Å; McMath: 0.25Å). The code fits either relative or absolute colour variations in two photometric bandbasses simultaneously with fitting the line profiles. For the current investigation, I use relative photometry in the V (5500Å) and I_C (7900Å) bandbass for the KPNO 98 Jan. and the M96 data, and in the V (5500Å) and U (3650Å) bandbass for the KPNO 96 Jan. and the NSO 96 synoptic data. No photometry was available for the KPNO 95 Feb. data and the first $2\frac{1}{2}$ seasons of the NSO synoptic run.

The spectral line information together with the phot. data is now being feed into `TempMap`. The program is divided into two main sections: first part is the **computation of the local line profiles** from a solution of the equation of transfer from LTE model atmospheres using a grid of ten model atmospheres between 3500 and 5750 K in steps of 250 K and fixed $\log g$ (taken from the ATLAS-9 CD, Kurucz 1993). Wavelength-dependent limb darkening is implicitly accounted for during the disk integration. The 2nd part of the program is the iterated process of **solving the inverse problem** by using a regularisation function, either Tikhonov or Maximum Entropy. The latter was preferred; however, both methods yield very similar results.

A dump of the parameter files used for Doppler imaging is presented in the box on p. 51. The slanted text is not part of the respective parameter file but a comment specifying different values for different observations/instruments.

```
ALLATMOS35.T5750
ABUND: Ca -6.30; Fe -5.50

period.par:
PPHOT   1.9472324
TPHOT   2448054.7109
PORB    1.9472324
TORB    2448054.7109
GAMMA   18.97
K1      26.83
E       0.0
OMEGA   0.0

tempmap.par:
COMMENT    tempmap.par         ; TempMap Doppler imaging program
COMMENT___ version             ; V3
COMMENT___ ------ STELLAR VARS
TEFF       5500.               ;effective star temperature
INC        56.0                ;i [deg]
VSINI      51.0                ;projected rotational velocity [km/s]
MICROT      2.0                ;[km/s]
MACROTR     4.0                ;radial [km/s]
MACROTT     4.0                ;tangential [km/s]
RATIOMT     0.5
COMMENT    ------ PROGRAM PARS
TMAX       6000.               ;maximum temp. for TEMPMAP
MAXENTR    SE                  ;Reg: max entropy(SE) or smoothing (S)
STEPSIZE   0.005               ;stepsize of TEMPMAP program
ALPHA        1.0               ;smoothing param (0-5)
BETA         0.1               ;weight of photometric data
PHOTWT       1.0               ;photometric weight if no spectra aplicable
DELTAPH    180.0               ;angle betw. spectra to use PHOTWT
NITER         15               ;total number of iterations
NIPHOT         5               ;iteration number when photom. data comes in
PHOTDAT    photometry_%d.dat   ;photometry file
ABUND      abund.dat           ;element abundances
ATMOS      allatmos35.t5750    ;atmosphere

tmake2.par:
COMMENT___ tmake.par            ;TempMap util TMAKE
COMMENT___ version              ;V0.2  Jul.1998
DELTA      0.08                 ;delta lambda of spectra
NSPECTPTS  43                   ;number of pts in output spec
SN         250.0                ;Signal/Noise of spectra
FILT       3.5                  ;Filter parameter (FWHM of instr.profile) [px]
                                ;CF: 3.5, NSO: 3.5/4.0, MUSICOS: 16.0
IFWHM      0.27                 ;FWHM of instrumental profile [A/px]
                                ;CF: 0.27, NSO: 0.25, MUSICOS: 0.18
IPROF      0                    ;use IFWHM from image header? MUSICOS: 1
BELL       0.1                  ;Bell
PAD        0.1                  ;Pad
VERSION    3.1                  ;Tempmap version
HJD        1                    ;Use HJD instead of phase?
FALPH      0.0                  ;
```

4.2.4 Surfing through parameter spaces *or* The quest of automation

The success with the surface reconstruction depends on the accuracy with which the system parameters are known. Consequently, in order to verify or improve and also to demonstrate the correct input parameters, we produce a series of test reconstructions for the individual parameters, moving the relevant value through the parameter space. For these tests, it is reasonable to use the best quality data. Therefor, the data sets `CF96, CF97, NSO94dec` and `NSO95nov` were chosen. The plots in this section show, as a function of the respective value, the resulting normalised $\chi^2 = \sum(O-C)^2$ distribution (normalised by the particular minimum χ^2 value of each parameter) for several or all of these data sets. All four Doppler-imaging lines were processed in this way, but the high-quality lines λ6439 and λ6393 are the more crucial factor than the low-quality λ6430 line; in several cases, the most deviating lines were shaded in grey in order to emphasis the overall trend. For non-successful runs (like log g), only a part of the test sample is shown. The value used for Doppler imaging is indicated by an arrow. See Figures 4.3*ff*.

Stellar Inclination: We assume the orbital and the stellar inclination to be identical which is reasonable given the close and evolved status of the system.
Kürster (1993), Unruh & Collier Cameron (1995) and most recently Rice & Strassmeier (2000) have shown that the minimisation of χ^2 can be successfully used to constrain the inclination angle. (Of course, whether the best attainable fit to the data is also the correct one is debatable.) With Doppler imaging, we find an average minimum for the inclination angle at around $i \approx 40 \pm 10°$, see Figure 4.3a. The value favoured by Doppler imaging agrees with the orbital estimation by Fekel et al. (1987) of $15° \leq i \leq 58°$, while the improved value of $56 \pm 4°$ we derived in §3.3.5 is still on the low slope of the function. However, Doppler imaging is not sensitive enough to improve the value of the stellar inclination, but it does confirm the estimations discussed in §3.3. When applying the Doppler imaging technique, the surface spot distribution remains very similar even for a change of the inclination of about ±20° (see Vogt et al. 1987).

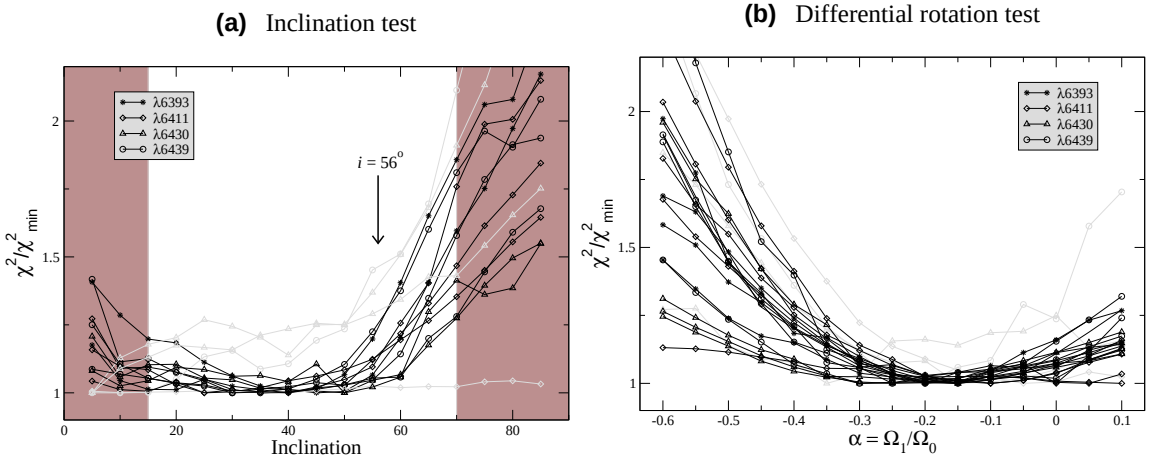

Figure 4.3: Normalised goodness of fit from Doppler imaging: as a function of **(a)** inclination and **(b)** the differential rotation parameter $\alpha = \Omega_1/\Omega_0$. The grey area in (a) marks the values below/above the lower/upper limit of 15 and 70°as estimated by Fekel et al. (1987) and improved in §3.3.5.

Differential rotation parameter: The differential rotation parameter $\alpha = \Omega_1/\Omega_0$ was recently introduced to the Doppler imaging code TempMap by M. Weber. As used here, it only takes into account the change in the line profile shape due to differential rotation and neglects the period variation of spots as a function of stellar latitude. As shown in §5, the MUSICOS data suggest a differential rotation of $\alpha = -0.27 \pm 0.15$. The value of -0.15 is supported by the χ^2 distribution when feeding a series for this parameter to TempMap. Fig. 4.3b shows the result which corresponds to an overall minimum at -0.17 ± 0.10 (implying all used lines, also those plotted in grey). As will be discussed in §5.3.3, a differential-rotation value of -0.15 – -0.2 can be assumed but needs further verification.

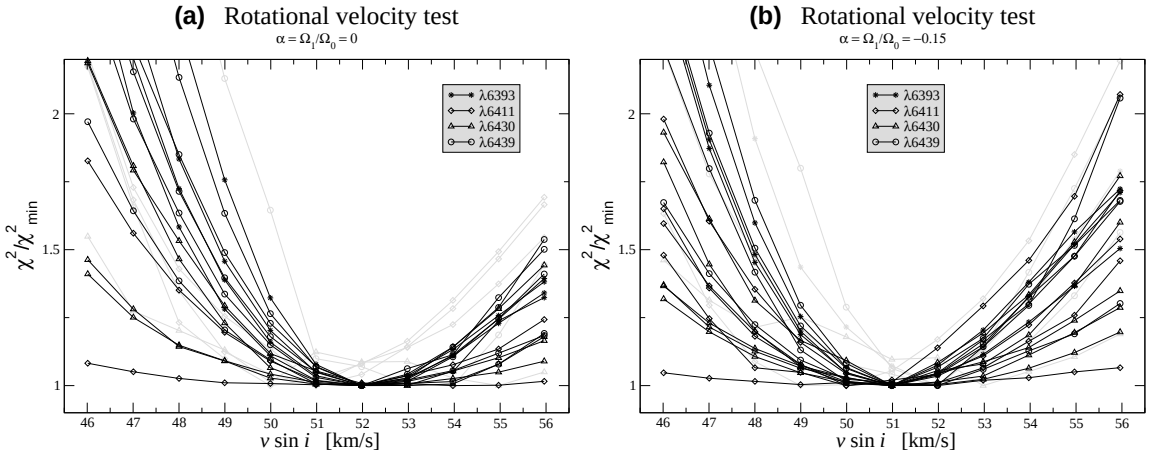

Figure 4.4: Normalised goodness of fit from Doppler imaging as a function of $v \sin i$ with a differential-rotation parameter of **(a)** $\alpha = 0$ and **(b)** $\alpha = -0.15$.

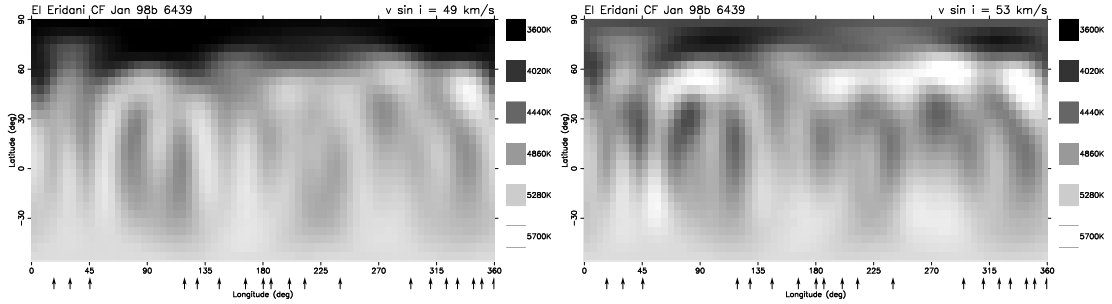

Figure 4.5: Doppler map of the CF98jan λ6439 line with $v \sin i = 49$ km s^{-1} (left) and 53 km s^{-1} (right).

Rotational velocity: The Doppler-imaging technique is very sensitive to the projected rotational velocity and provides better accuracy than any other method, as it takes into account the line deformation due to spots. Errors in the $v \sin i$ as small as 1-2 km s^{-1} can produce artefacts like a dark or bright band encircling the star near the equator (see Vogt et al. 1987). Fig. 4.5 shows two surface maps with a deviation from the final $v \sin i$ value of ± 2 km s^{-1}, one exhibiting an oversized polar cap, the other one a band of bright and dark low-latitude spots (between 30° and 50°). The normalised χ^2 distribution as a function of the rotational velocity $v_{\rm eq} \sin i$ is shown in Fig. 4.4a. It shows a minimum at 52 km s^{-1} which is slightly higher than the values denoted in the literature (see §3.3.3, page 40) and the value preferred when consulting the surface maps (see Fig. 4.5).

However, rerunning the test with a differential rotation parameter α of -0.15 (see above) relocates the minimum of the χ^2 function to 51 km s^{-1}. Additional tests with images of the λ6393, λ6411 and λ6439 line using `DOTS` (§4.3) lead to a value of 51.5 ± 0.5 km s^{-1}, not accounting for differential rotation (see Fig. 4.22). Note that the spot filling factor, the main characteristic in finding the best fit for `DOTS`, is extremely sensitive to the projected equatorial rotation velocity; see §4.3.4 for an additional constraint. — Finally, we adopt 51 ± 0.5 km s^{-1} as the most likely $v \sin i$ value.

Gravity and Temperature: Gravity ($\log g$) and effective temperature could not be successfully verified by this method. The results are shown in Fig. 4.6. A $\log g$ of 3.5 was chosen due to estimations presented in §3.3.7. Maps computed with $\log g = 3.0$ or 4.0 differ only by their average surface temperature being ≈ 40 K cooler and ≈ 70 K warmer, respectively. The surface distribution remains the same. The effective temperature was varied in steps of 100 K from 5000 to 6000 K. The resulting χ^2 values lie within less than 30 percent and do not show consistent trends. The minimum values of the χ^2 distribution gather at

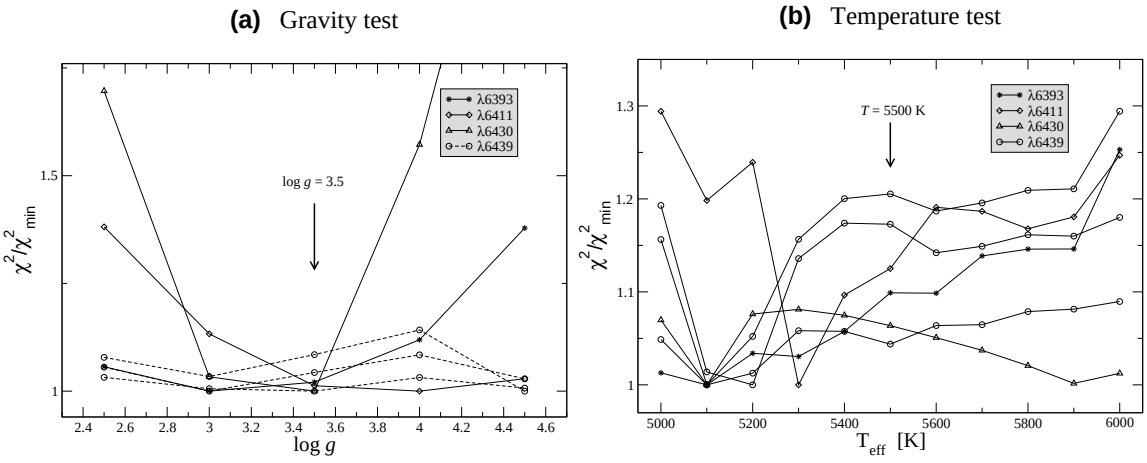

Figure 4.6: Normalised goodness of fit from Doppler imaging: as a function of (**a**) gravity (log g) and (**b**) effective temperature. Both distributions cannot be considered as significant.

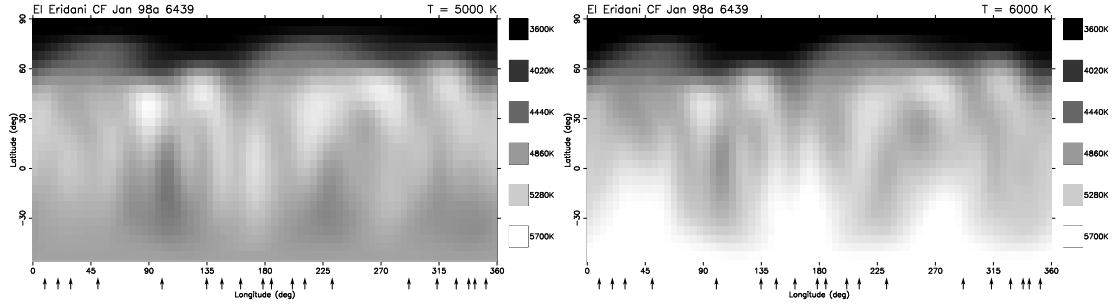

Figure 4.7: Doppler map of the CF98jan λ6439 line with T=5000K (left) and T=6000K (right).

5100 K. The corresponding maps, however, are filled with hot spots relative to the photospheric average. The surface *distribution* is unchanged even for values of 5000 and 6000 K (see Fig. 4.7), only the resulting average photospheric temperature changes. Finally, the temperature value was chosen based on estimations presented in §3.3.2.

Abundances: The element abundance of the relevant main mapping line shows, naturally, a strong influence on the line depth (equivalent width) and, consequently, on the line profile fits and the surface map. When varying the calcium abundance from -7.0 to -5.7, the surface distribution of the resulting map does not change significantly, but for decreasing values (smaller than -6.6), the polar spot grows significantly and reaches an expansion of down to 60° latitude at -7.0. On the other hand, `TempMap` cannot comply with the specified photospheric temperature of 5500 K until an abundance values beyond -6.2. For higher values (> -6.2), the excess flux cannot escape evenly through the photosphere and bright spots are produced. Figure 4.9 (left panel) shows the λ6439 map with $\log[Ca] = -6.0$ which complies with the χ^2 minimum value (Fig. 4.8a) but is dominated by bright spots. The right panel of Fig. 4.9 displays the respective calcium map with $\log[Ca] = -6.3$. The polar spot is at its minimum and no bright spots occur. Thus, the true abundance value (according to Doppler imaging) is likely to be between -6.2 and -6.5, and we finally adopted -6.3 (which is 0.6 dex below the solar value) as the most useful value for Doppler imaging.
The case of the iron abundance is more evident. Between -5.3 and -5.8, the Doppler imaging process renders reliable results. Higher values (> -5.3) lead to flux excess, values smaller than -6.0 to oversized polar caps. The χ^2 function (Fig. 4.8b) reaches its minimum at around $-5.5/-5.4$ which also yields the best Doppler maps. -5.5 (1.1 dex below solar) was adopted as final value.

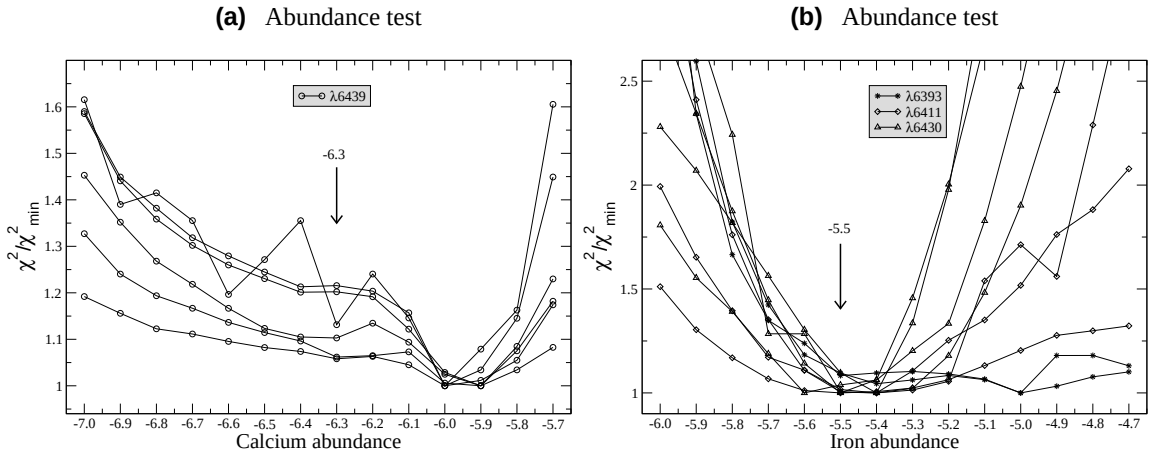

Figure 4.8: Normalised goodness of fit from Doppler imaging: as a function of (a) Calcium abundance and (b) Iron abundance.

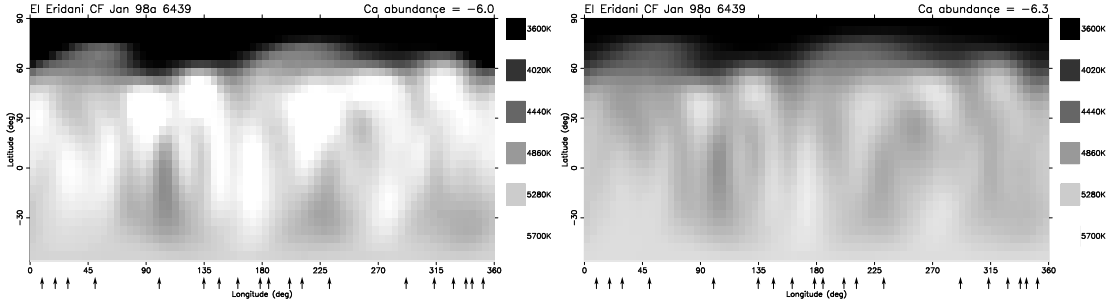

Figure 4.9: Doppler map of the λ6439 line with a calcium abundance of -6.00 (left) and -6.30 (right).

Macro and micro turbulence: Macro turbulence does not affect the equivalent width of a spectral line, and also the shape of the profile is just slightly influenced. The spot temperature slightly declines while macro turbulence increases. Overall, macro turbulence does not have any significant influence on our surface maps (see Fig. 4.10a). $2\,\mathrm{km\,s^{-1}}$ was chosen as standard value. Micro turbulence, on the other hand, does have a strong influence on the equivalent width. Accordingly, its χ^2 functions exhibit distinctive minima from two to three $\mathrm{km\,s^{-1}}$ with emphasis on $2\,\mathrm{km\,s^{-1}}$ (see Fig. 4.10b).

Line blends and transition probabilities: Unruh & Collier Cameron (1995) demonstrated that neglecting blends in the wings of the mapping line leads to spurious banding in the reconstructed image. If a blend is further away from the center of the mapping line, the artificial band shows up at higher latitudes. Consequently, one has to be very careful with including all known line blends for calculating the theoretical line profile, which requires knowledge of the correct line transition probabilities ($\log gf$) for each blend and the dominant mapping line of course. Table 4.2 is a list of the used blends including their atomic parameters. All mapping lines and their respective line blends were checked thoroughly with all the appropriate $\log gf$ values determined individually. For the difficult-to-map λ6430 line, the neighbouring lines Ca 6429.071, Ca 6430.127, Co 6430.290, Fe 6431.099, V 6431.809 and Ti 6432.121 were also taken into consideration but were expelled as they did not have any affect on the reconstructed line. The same holds true for λ6411's neighbours V 6410.416, Fe 6411.107, V 6411.276, Cr 6411.580 and Ti 6412.192. As an example, Fig. 4.11 shows the χ^2 distribution of the λ6439.075 and the λ6411.647 main mapping lines. A similar situation as for the abundance occurs: For the $\log gf$ λ6439.075 χ^2 minimum value (Fig. 4.11a), the map exhibits excess flux escaping in hot spots, while a slightly smaller value gives sensible results (Fig. 4.12). A value of $\log gf$ (λ6439.075) = 0.47 was adopted. The $\log gf$ λ6411.647 χ^2 minimum, on the other hand, occurs where the respective Doppler map is at its best (Fig. 4.11b).

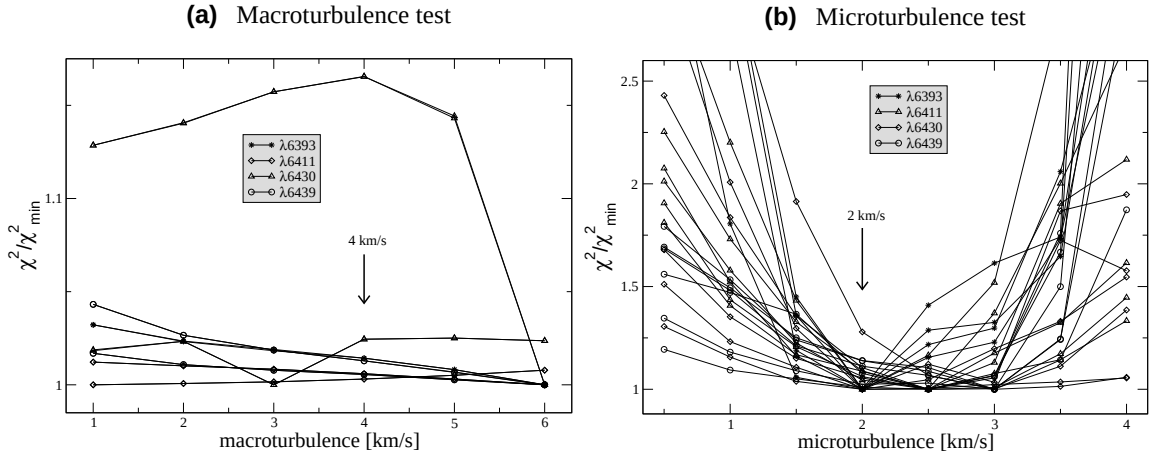

Figure 4.10: Normalised goodness of fit from Doppler imaging: as a function of **(a)** macro turbulence and **(b)** micro turbulence.

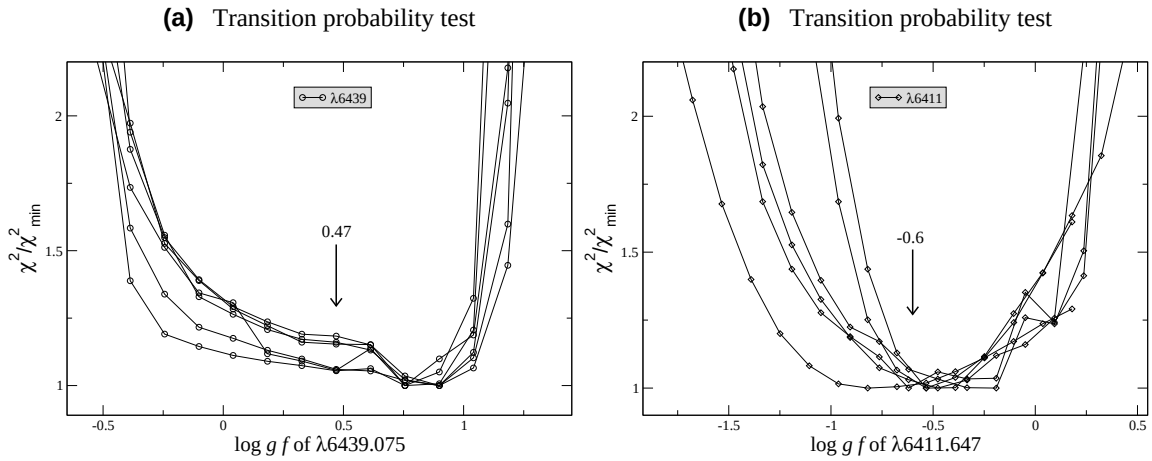

Figure 4.11: Normalised goodness of fit from Doppler imaging: as a function of transition probability ($\log gf$) for **(a)** the λ6439 and **(b)** the λ6411 line.

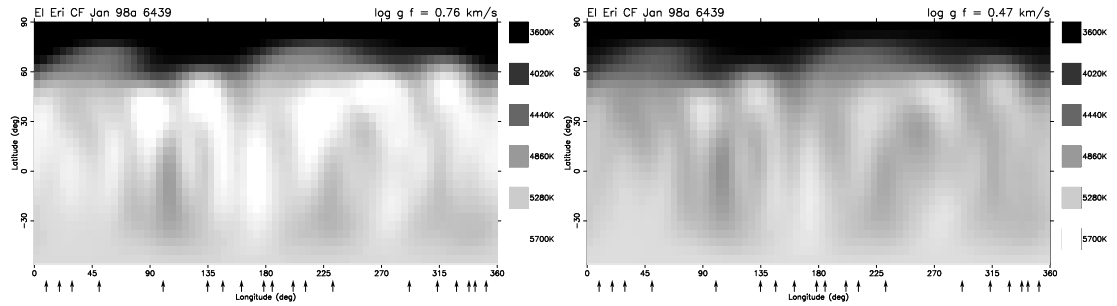

Figure 4.12: Doppler map of the λ6439 line with a transition probability ($\log gf$) of **(left)** 0.76, as suggested by the χ^2 minimum in Fig. 4.11a, and **(right)** 0.47, as suggested by myself.

Other parameters: The χ^2 function of the *rotational period* around the value determined in §3.2 is shown in Fig. 4.13. It comes without surprise that Doppler imaging is not a useful means in determining the correct rotational period. The period needs to be well defined before diving into Doppler tomography. As *regularisation method*, which imposes some type of smoothing constraint on the solution, a tikhonov (which sets constraints on the average mean square of gradient across the image) or maximum entropy approach is offered. Both approaches do not show much effect on the surface maps, and maximum entropy was preferred (see Piskunov et al. 1990). *Smoothing* can be used as a means of forcing TempMap to fit even smaller structures in the local line profile or to ignore fine structures (if they are assumed to be noise). The size and number of structural information in the surface map will thereby increase or decrease. Typical smoothing factor is 1. The *weight of photometry* was fixed to 0.1.

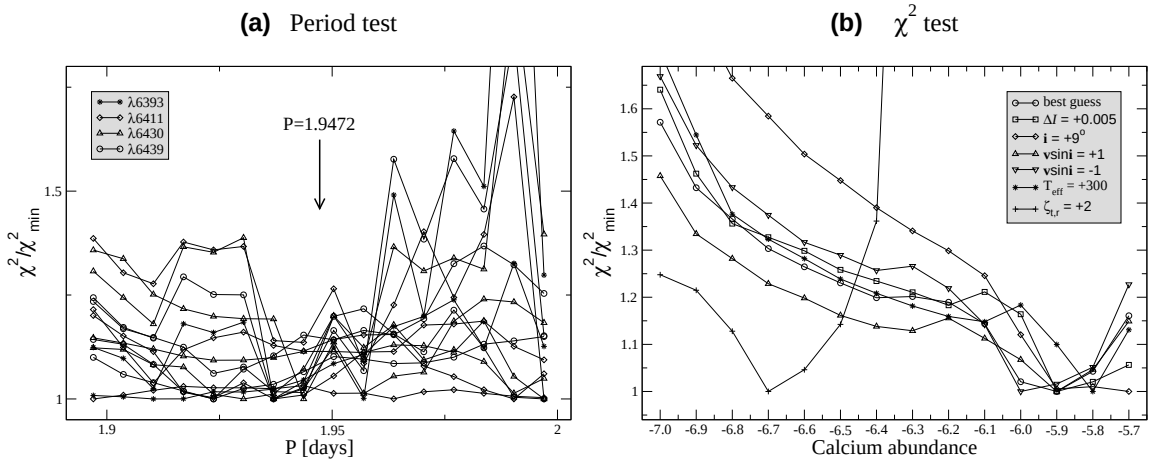

Figure 4.13: **(a)** Normalised goodness of fit from Doppler imaging as a function of stellar rotational period. **(b)** The χ^2 distribution of the calcium abundance as a function of various TempMap parameters.

The method of χ^2 minimisation as a measure of the correct parameter

Finetuning the input parameters by means of χ^2 minimisation is, in most cases, a difficult matter. Looking at a particular χ^2 distribution, the decision for the correct parameter value is not that straight forward and requires a certain amount of experience, which makes the automation of this process a tricky task: Some parameters have their correct value at the minimum of the χ^2 function (like ΔI, $\Delta\lambda$, the $\log gf$'s of the stronger line blends); some have it shifted with respect to their true χ^2 minimum (calcium abundance, sometimes $\log gf$); some have it typically at the slope of the χ^2 curve (inclination); for some parameters, the minimum is not followed by a new increase but a shallow or even plane gradient (e.g. the $\log gf$'s of some weak line blends); and for some parameters, their correct value is not resembled by the χ^2 distribution at all (macroturbulence, gravity). Moreover, the parameters are not independent of each other (see Fig. 4.13b) and local χ^2 minima might obscure the absolute minimum behind the next distribution hill. However, a certain degree of automation seems to be feasible if there are several spectral lines available. The χ^2 distribution of a single line can be misleading even if the overall χ^2 characteristic for a specific parameter is unique (see the grey shaded lines in Fig. 4.4). Overall, if the characteristic behaviour of specific parameters is taken into account, a χ^2 statistic over a large number of spectral lines can, being part of an automatic evaluation process, result in the correct values for a considerable number of parameters. For the current investigation though, the preceding tests were accomplished by making use of `tempargo` which still leaves the user to decide which value to choose.

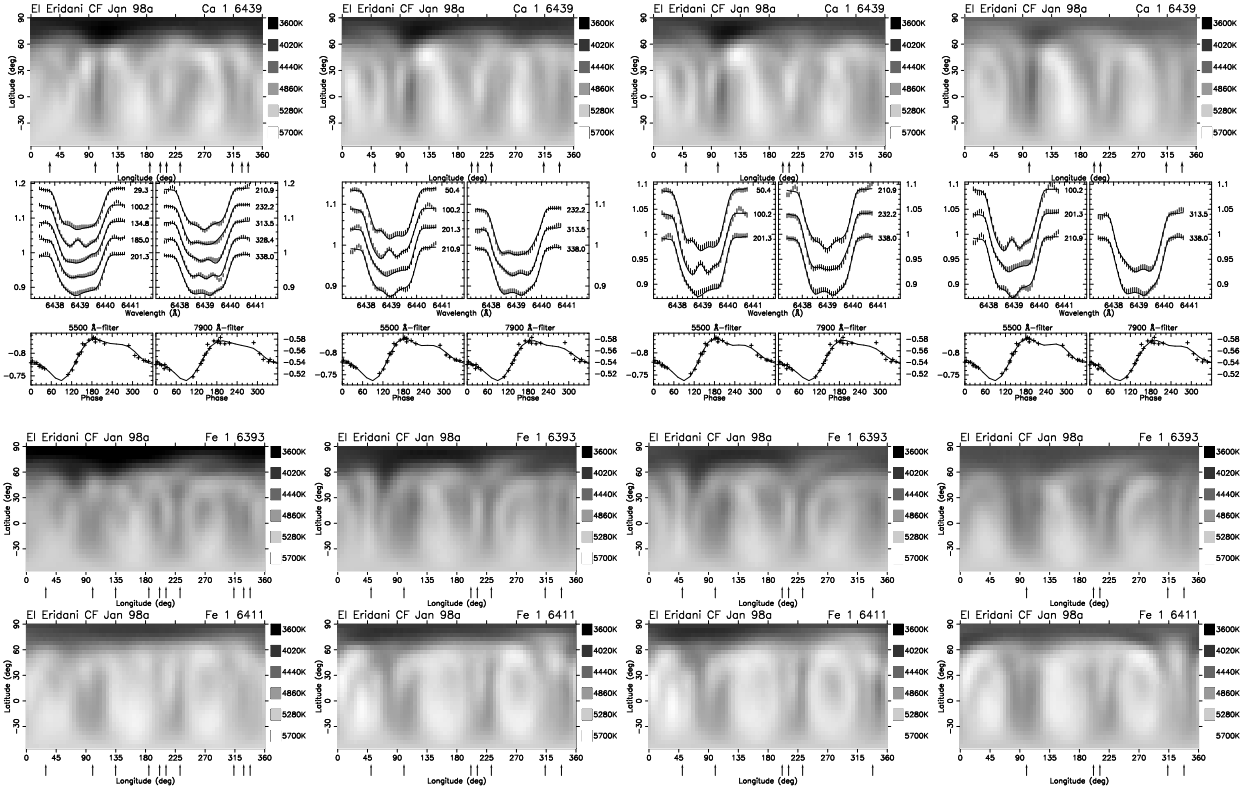

Figure 4.14: Doppler images from CF97dec with likewise decreasing number of spectra and increasing phase gaps (from left to right; see arrows below maps).

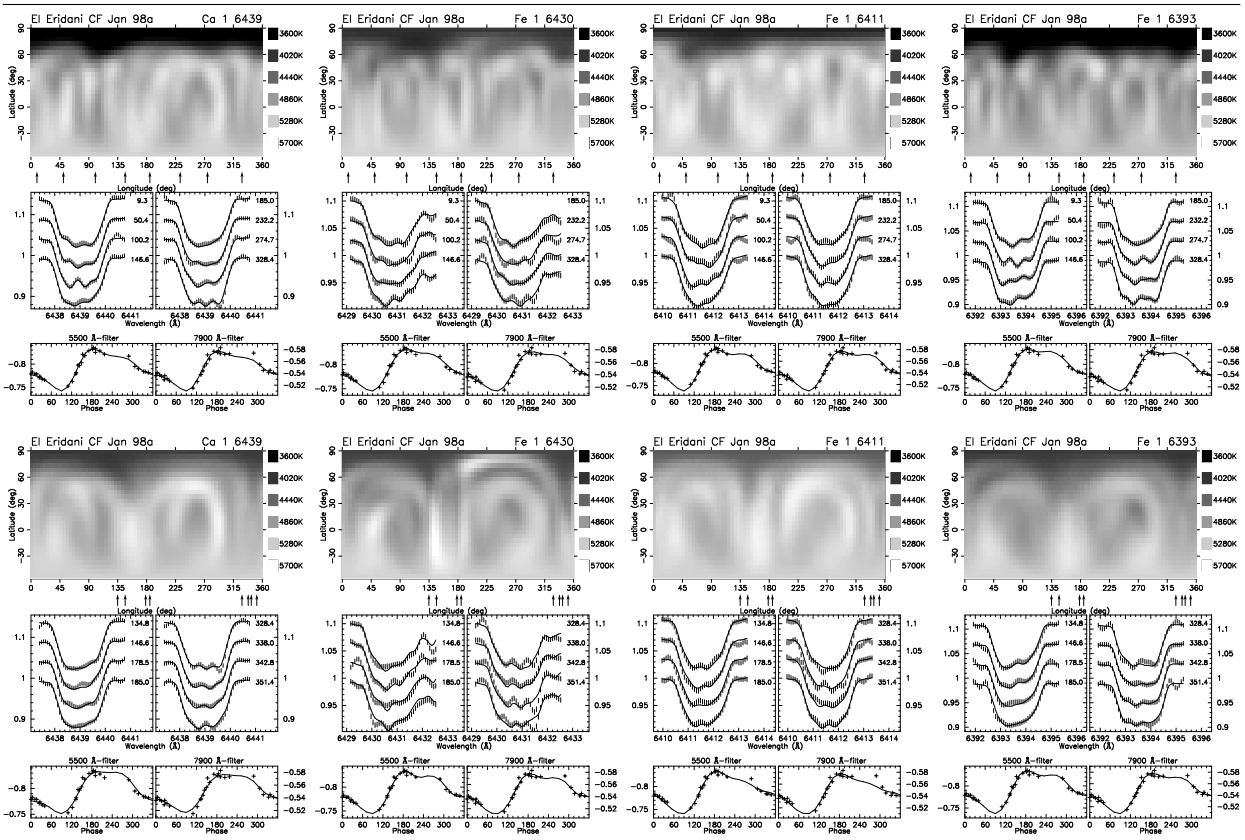

Figure 4.15: Doppler images from CF97dec with same number of spectra but good phase coverage (top) and bad phase coverage (bottom; see arrows below maps).

4.2.5 Windmills and phase gaps – a battle

A test was performed on the problem of phase gaps to see how the surface maps behave when large gaps occur. Figure 4.14 has the results. Presented are the spectral lines λ6439, λ6393 and λ6411 of the CF97dec run. (The low quality line λ6430 is omitted.) For each line, a series of four maps is plotted with likewise decreasing number of spectra and, consequently, increasing phase gaps (the associated theoretical and observed line profiles are only plotted for the λ6439 line). The arrows below the maps indicate the phase values of the observations. The original surface maps using all spectra of this block are shown in Fig. 6.22 on page 104. The corresponding average and maximum phase gaps are (starting with the complete map of Fig. 6.22 and continuing with Figure 4.14 from left to right), preceded by the number of spectra: 19/19°/60°, 10/36°/81°, 7/51°/101°, 6/60°/106° and 5/72°/122° (number of spectra / average gap / maximum gap). It is seen with gratification, that the structure of the surface maps does not change significantly. However, the distinctness of the polar cap abates, i.e. the temperature steps up. On its course to a smaller number of spectra with larger phase gaps, the average temperature rises for the λ6439 line from 4908 to 5031 K, the maximum temperature changes by 100 K while the minimum temperature increases by 700 K. For λ6393, the average steps from 4800 to 4870 K, the maximum decreases by 90 K while the minimum is enhanced by 600 K. The behaviour of the λ6411 and λ6430 maps is similar but less pronounced.

Figure 4.15 presents a different examination: Eight spectra of the same sample are chosen, one time with the spectra evenly distributed over phase (top; average/maximum phase gaps: 45°/54°), the other time focused around two rotational phases (bottom; av./max. phase gaps: 45°/143°). Now, we see a drastic decline of the surface structure as well as an overall temperature increase, again of the average and, more strongly, on the minimum temperature. Most conspicuous, the maps with good phase coverage but only eight spectra (top row) are almost identical to the complete map using 19 spectra (Fig. 6.22), in the case of the λ6393 line with slightly more pronounced structure.

We thereby conclude that a small number of spectra can, if evenly distributed over phase, still be sufficient for good-quality surface reconstructions while an inferior phase coverage dispels surface structure and can increase the minimum temperature. Unfortunately, we have a number of spectral observations from the NSO synoptic program that leaves us with possible Doppler maps comprised of very few spectra and housing significant holes in the phase coverage. Their credibility dwindles drastically in case of gaps exceeding 100°. However, we are left with the decision to use such a low-quality (or possibly even corrupted) Doppler map or to expel it and, thus, to have no surface map for that specific epoch at all. Subsuming, we can nothing but treat those surface maps exhibiting large phase gaps with reserve and scepticism and console ourselves with Mephistopheles' noteworthy inclination towards gaps, holes and the alike: "Once came a wanton dream to me. I saw therein a riven tree; It had a monstrous hole; 'Twas huge, yet I was pleased with it." (Goethe 1808)

4.3 Comparison DOTS – TempMap

4.3.1 Points in common and in contrast

The Doppler images presented in this section were generated using the Doppler imaging code TEMPMAP of Rice et al. (1989) and Collier Cameron's code for Doppler Tomography of stellar surfaces DOTS. For another comparison of different Doppler imaging codes on EI Eri, see Strassmeier et al. (1991).

The Doppler imaging program DOTS calculates a surface map as following: The star being imaged is assigned two effective temperatures, one for the photosphere and one for the spots. In this respect, DOTS differs from most other Doppler imaging codes including TempMap. The stellar surface is divided into a grid of pixels. A fraction f_i of the area of the ith pixel is occupied by spots, a fraction $1 - f_i$ contains clean photosphere of constant temperature (see Collier Cameron 1992), so each pixel can be described by a *spot filling factor* that gives the proportion of the respective pixel surface covered by spots. There is only one pre-defined spot temperature allowed, spots and clean photosphere coexist within a single pixel. Therefore, DOTS does

not allow bright spots to develop.

The surface area of a given pixel and the foreshortening angle at which it is viewed at any observed rotation phase depends on the surface geometry of the star. `DOTS` acknowledges a spherical or a rotationally-flattened Roche equipotential configuration. `TempMap`, up to the version used for this investigation, does not offer this choice and uses a spherical geometry.

`DOTS` does not calculate the synthetic line profiles itself but uses three-dimensional lookup tables of specific intensities as function of effective temperature, wavelength and foreshortening angle. It then uses linear interpolation to determine the local spectral intensities. The lookup tables are calculated either using model atmospheres (ATLAS 9) and applying a full spectral synthesis or an observed spectrum from an appropriate standard star of similar spectral type (template star; see Unruh & Collier Cameron 1995). The calculation of lookup tables takes into account the effects of continuum limb darkening, the center-to-limb variation in the line equivalent width, van der Waals damping and isotropic microturbulence by a radial-tangential model.

The goodness of the fit between the observed data and the synthetic data is measured using a mean square sum statistic where each point consists of a signal and an error. `TempMap` on the other hand uses the same weight for each data point. To choose one of the infinite number of possible solutions, a Maximum Entropy function is imposed. `TempMap` alternatively allows a Tikhonov reconstruction (see Piskunov et al. 1990; Piskunov & Rice 1993; Collier Cameron 1992a,b). At the signal-to-noise ratio of our EI Eri spectra of ∼300:1, we found no differences between the two regularisation functionals (see also Strassmeier et al. 1991). Using `DOTS` we then follow the procedure described in Collier-Cameron & Unruh (1994) to find the best fit. This involves minimising the χ^2 value as well as the spot covering fraction in the reconstructed image. It is crucial to the fitting procedure to decide when the data are fitted sufficiently and when they are being overfitted. At some point when decreasing the χ^2 value, the spot coverage fraction starts to increase more steeply as more and more noise is fitted. This is when the fitting process is to be stopped. The strong dependence of the spot filling factor when the χ^2 of the solution is pushed lower was already mentioned by Collier Cameron (1995). The reason for this behaviour is that the code, using the Maximum Entropy regularisation, starts to overfit the line profiles. Once a critical χ^2 is passed, spurious features on the surface are produced. Therefore, the fitting process has to be stopped at the critical χ^2 value. `TempMap` is not prone to this effect as the very high frequency noise is being removed prior to the reconstruction process, and `TempMap` stops automatically if no further improvement can be achieved. Usually, a number of 15 iterations is favoured.

`DOTS` can be applied in a single star or in a binary mode. In the first case, one needs to correct the orbital Doppler shifts of the primary spectrum before the data are fed into `DOTS`. Running in binary mode, `DOTS` requires input of the orbital elements and then shifts each (non-corrected) spectrum depending on its orbital phase.

`TempMap` treats the image pixel values as bolometric surface fluxes. This allows the surface flux to vary continuously over the surface of the star. During the reconstruction, spots brighter than the photospheric default value can develop and the temperature of dark spots is not fixed either. Stellar surface images produced with `TempMap` therefore show temperature values instead of filling factor.

With `TempMap`, we first calculate the local line profiles using a grid of model atmospheres with temperatures in steps of 250 K and fixed $\log g = 3.5$ (taken from the ATLAS-9 CD, Kurucz 1993). We then convolve the line profiles with the macroturbulence function and the instrumental profile (which are both not taken into account by `DOTS`). The line profile shape is assumed to be the same at different temperatures.

Both the `DOTS` and the `TempMap` code have the capability to solve light curves in two colours at once, simultaneously with spectral-line profile information. The version of `TempMap` used for this investigation can only handle one spectral region at a time. Maps from different lines can be averaged afterwards. `DOTS` can handle three spectral regions at a time but rather reconstructs three independent images which are then averaged at the end.

For a more detailed description of `TempMap` see Rice (2002) and references therein, for `DOTS` see Collier Cameron (1997) and Collier Cameron et al. (1992).

Table 4.3: Specific parameters for DOTS

Parameter	Value
$T_{\rm phot}$	5500 K
$T_{\rm spot}$	3600 K
$\log g$	4.0
Micro turbulence $\xi_{\rm r} = \xi_{\rm t}$	1.5 $\rm km\,s^{-1}$
van der Waals damping $[Ca]$	0.7
van der Waals damping $[Fe]$	0.4
limb darkening coefficient	0.6
relative He/H abundance	0.098
$n_{\rm pts}$ in output spectra	23
weight of phot. data	0.0 / 0.2
number of iterations	40
system mass ratio	0.261
primary polar radius R_p	2.75 $\rm R_\odot$

4.3.2 Applying DOTS to the CF96jan and M96 data sets

For DOTS a spot temperature of 3600 K was employed as determined by Strassmeier (1990) by using standardised V and R photometry and the Barnes-Evans relation (see §3.3.2). TempMap chooses the lowest spot temperature automatically. In fact, it turned out to be around 3500 K. Table 4.3 shows the specific parameters used for DOTS. A linear bolometric limb-darkening law is assumed with a limb-darkening coefficient of 0.6. The neglect of blends produces artificial structure in the surface maps. Therefore, we also applied the spectrum of a template star, scaled according to a linear limb-darkening law to produce lookup tables that can be compared with the observations. The results are, however, very similar.

The data from CF96jan and M96 were supplied to DOTS. The results are shown in Fig. 4.16 and 4.19. The four lines of the CF96jan run show all a polar cap tilted towards 30° longitude and a few small low-latitude spots. The appropriate line profiles, observed and calculated, are presented in Fig. 4.18, the corresponding TempMap results can be found in Fig. 6.20 on page 103. The TempMap maps show a polar cap with an extension at around 70° and a somewhat larger number of low-latitude features. The λ6439 map as calculated by DOTS and TempMap, respectively, is compared in more details in Fig. 4.17. The shape and size of the polar spot is well reconstructed with both codes while there is some agreement as well as disagreement within the low-latitude and equatorial features. During the M96 run, as described in §6.2.1, we obtained 70 nights of observations and therefore splitted the whole data sample into eight subsamples of three weeks and overlapping by two weeks each (see §6.2.1). Fig. 4.19 has the time-series of surface maps, reconstructed by DOTS (the eighth map is corrupted and therefore not shown). None of the low-latitude features are recovered in two consecutive, non-overlapping maps (like in 1–4–7). Thus, they are either not real or come and go too quickly to be detected again in the next Doppler image without spectral overlap. See §6.2.1 for the corresponding TempMap results.

4.3.3 Block segmentation and binary version

Four more tests were applied: **(1)** Splitting the CF96jan λ6439 data into two consecutive blocks and thereby reducing the number of spectra and increasing the phase gaps for each block (Fig. 4.20). The polar cap remains the same in size and orientation (tilted towards 0–30° with an extension at 210–240°. The second week's image shows only one low-latitude spot but is otherwise basically identical to the first week's image. **(2)** The binary version of DOTS was applied which automatically corrects the line-profile shifts caused by the orbital movement (see §4.3.1) and also takes into account non-spherical geometry. The results are almost identical as demonstrated in Fig. 4.21. **(3)** The projected rotational velocity $vsini$ and **(4)** the impact of photometric data on the surface maps was inspected and is described in the following subsections.

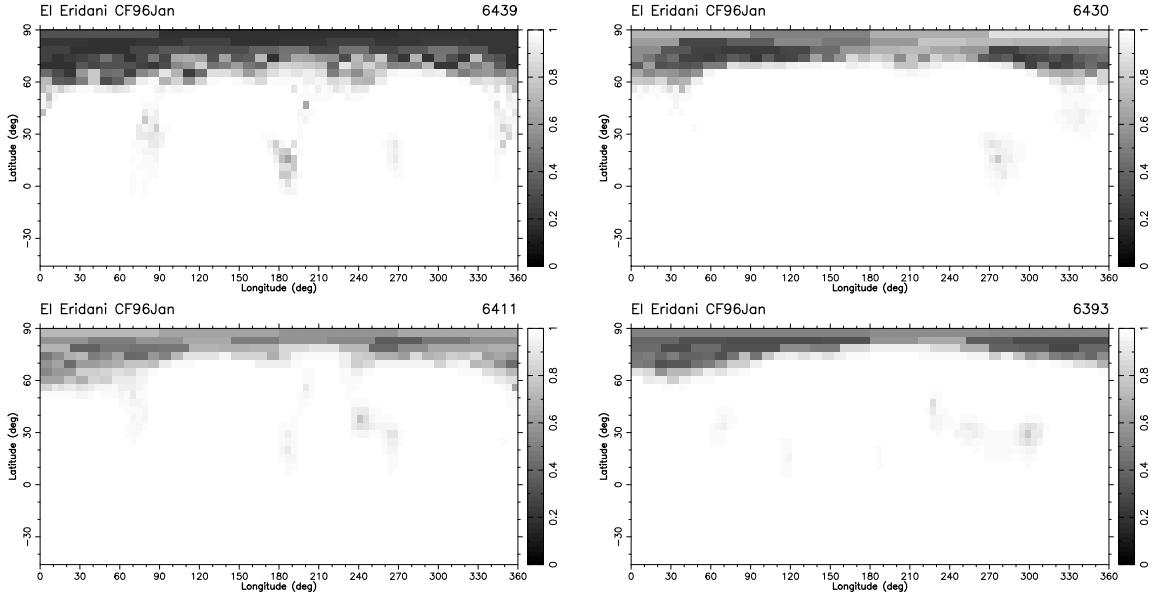

Figure 4.16: Doppler images from January 96 generated with DOTS: λ6439 (**a**; upper left), λ6430 (**b**; upper right), λ6411 (**c**; lower left), and λ6393 (**d**; lower right). The corresponding line profiles are plotted in Figure 4.18. See Fig. 6.20 on page 103 for the corresponding TempMap results. The λ6439 line is explicitly compared in Fig. 4.17.

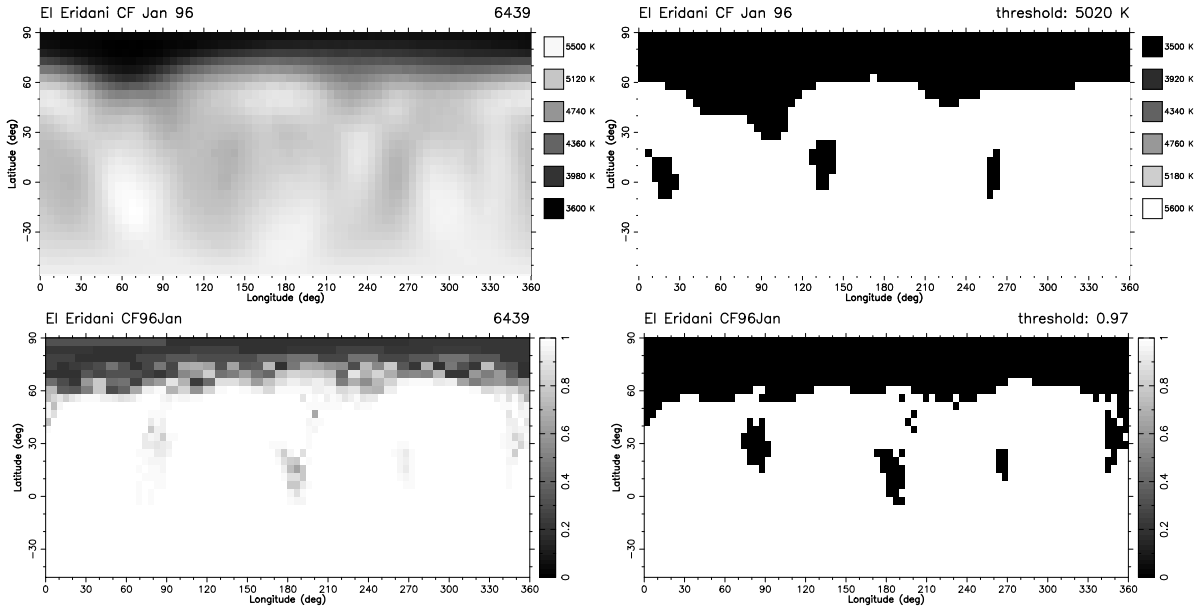

Figure 4.17: Comparison of two different Doppler imaging codes: Doppler images of EI Eridani from January 1996 produced with TEMPMAP (upper left; the same as Fig. 6.20, very left map) and DOTS (lower left). The right column shows the same maps but plotted with a threshold value.

Figure 4.18: Observed (crosses) and computed (solid line) line profiles for the maps presented in Figure 4.16.

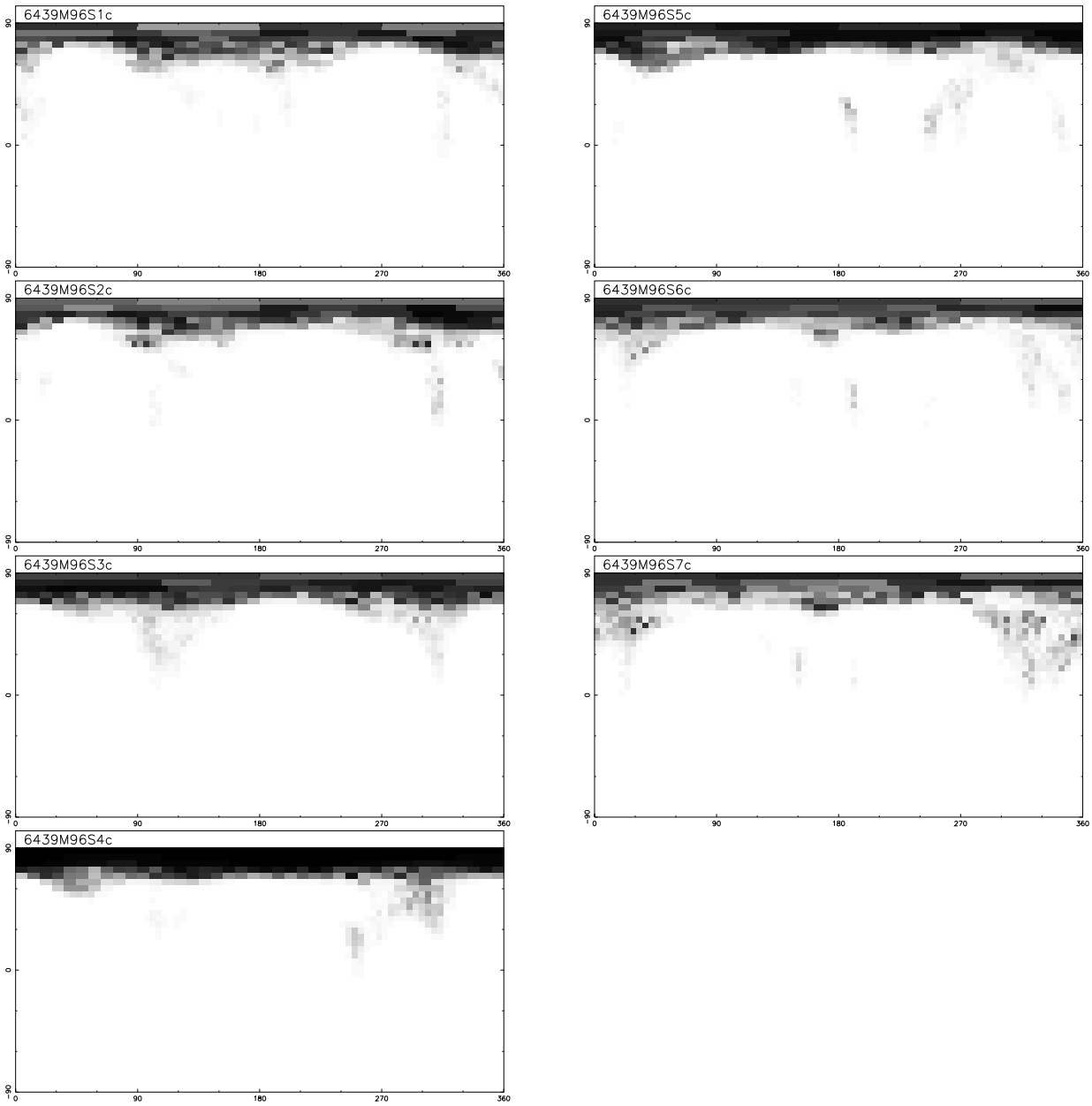

Figure 4.19: Time series of Doppler images of EI Eri from M96 (CaI 6439Å). (a) Observations from week 1 - 3 were used for this map. (b) Observations from week 2 - 4 *and so forth*, so there is a spectral overlap between three images each.

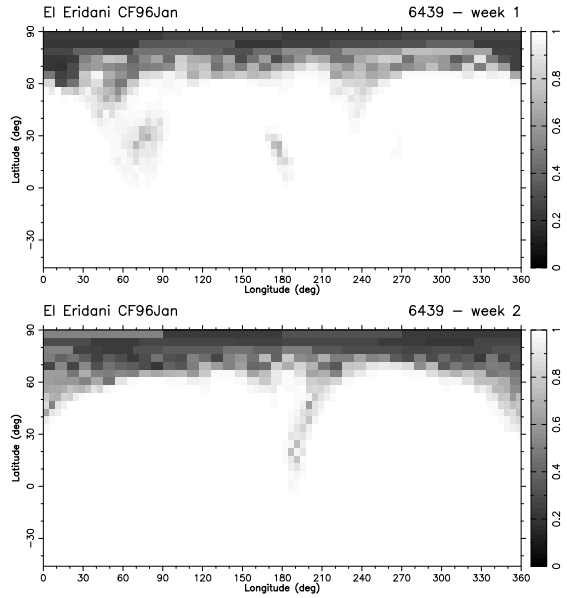

Figure 4.20: Doppler map of the λ6439 line (Jan. 96), where the two weeks of observations were splitted into two parts. The upper image shows the map gained with the spectra from the first week, the lower one represents the observed spectra from the second week.

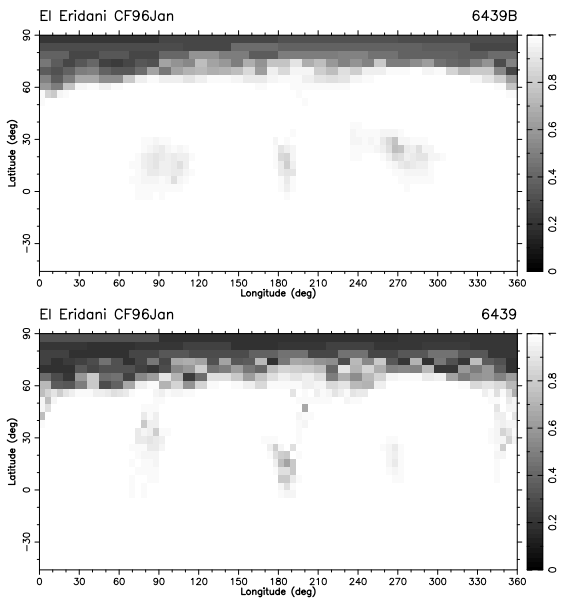

Figure 4.21: Two maps (from January 96) of the λ6439 line: The upper one was gained with the single star mode of DOTS after correcting the radial velocity shifts of the spectra and is the same as Fig. 4.16a (but calculated with less iterations); the lower one was produced using the binary star mode of DOTS (see §4.2.2).

4.3.4 The sensitivity of DI to the stellar rotational velocity

Since the Doppler imaging technique is very sensitive to the rotational velocity $v \sin i$, it can be used to determine this parameter with higher accuracy (as already done in §4.2.4 using TempMap, see Fig. 4.4 on page 53). As we know, artefacts in the surface map can easily develop when stellar parameters are wrong or inaccurate. Using DOTS, we therefore aim to minimise *both* the χ^2 value *and* the spot covering fraction which gives a more thorough constraint on the value of the respective parameter. The sensitivity to the $v \sin i$ value can thereby be advanced towards $0.5\,\mathrm{km\,s^{-1}}$, as demonstrated in Fig. 4.22. Note that a possible deformation of the local line profile due to differential rotation is not being accounted for by DOTS. The influence of a presumed α value of -0.15 (see page 4.2.4) already caused our best-value estimation for $v \sin i$, as enforced by χ^2 minimisation, to decline from 52 to $51\,\mathrm{km\,s^{-1}}$. We therefore stick to a final value of $51.0 \pm 0.5\mathrm{km\,s^{-1}}$.

4.3.5 The photometric impact on the Doppler images

The importance of photometric data for the surface image reconstruction as an additional constraint for the location, size and shape of the spots is well established. Introducing light-curve fitting to the surface-map reconstruction with DOTS (with a weighting of 0.8 for spectroscopy) leads to a large low-latitude spot that is not present at all in the spectroscopic data (Fig. 4.23b, lower left – as compared to Fig. 4.23a, upper left). Calculating a surface map from photometric data alone shows the same low-latitude feature and, as expected from photometry, no polar spot (Fig. 4.23c, upper right).

However, generating a fake light curve from the purely spectroscopic surface image in Fig. 4.23a and reconstructing a surface image with this fake light curve (instead of the observed light curve) shows the same low-latitude feature (Fig. 4.23d, lower right; less pronounced than in Fig. 4.23c). This means that the purely spectroscopic surface map sufficiently explains the photometric fit, while the photometric fit does not coincide with any feature in the more constrained line profiles. The photometric fit itself, which cannot

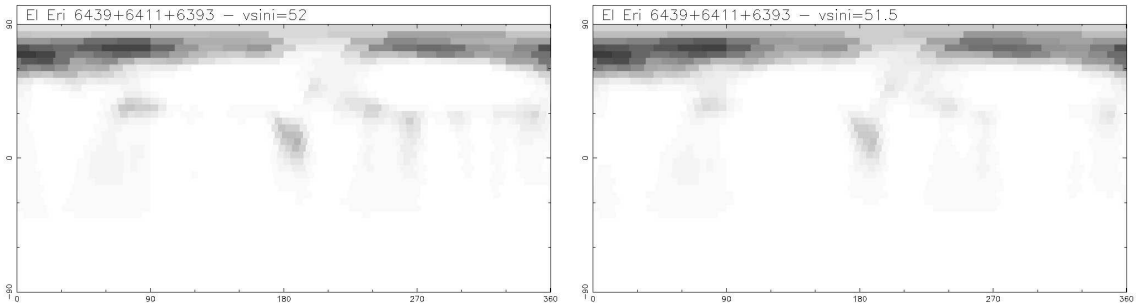

Figure 4.22: Reconstructed images (DOTS) demonstrating the sensitivity for the $v \sin i$ value when combining three different lines. The fractional spot coverage improves from 0.0372 (left panel with $v \sin i = 52.0$ km s^{-1}) to 0.0365 (right panel with $v \sin i = 51.5$ km s^{-1}).

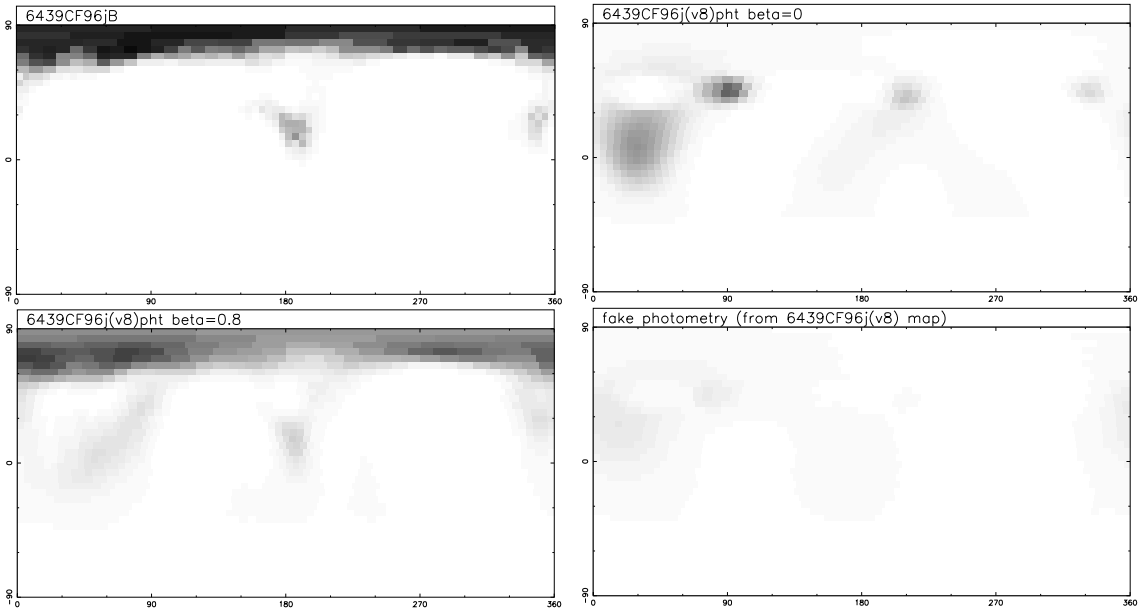

Figure 4.23: **(a)** upper left: Doppler image of El Eri from January 1996 (Ca I 6439Å, stopped ten iterations earlier than the corresponding maps in the previous Figures). **(b)** lower left: the same as (a) but including photometry. **(c)** upper right: For this reconstruction we used the photometric data alone and set the weighting for spectroscopy (beta) to 0. **(d)** Same as (c), but here we used the fake light curve generated from (a) instead of the observed light curve. – As one can see, the purely spectroscopic surface map sufficiently explains the photometric fit, while the photometric fit does not coincide with any feature in the more constrained line profiles. Yet another confirmation of the existence of the polar spot. (See text.)

"make use" of a polar feature, is not able to explain the spot distribution as seen in the line profiles, thereby endorsing the existence of a polar spot.

For Fig. 4.23b, the overall shape of the observed light curve is indeed reproduced, but the amplitude of the predicted light variations is too small. The reason is that the largest impacts on profile and light curve variation originate from different latitudes. The photometric light curve is particularly sensitive to low-latitude structure but less to structure above latitudes which are significantly higher than the inclination of the star, as structure above this limit is constantly in view and the rotational modulation introduced by it to the photometric light curve is due to foreshortening effects at high limb angles alone. The purely spectroscopic images on the other hand have relatively poor latitude discrimination around the stellar equator. Therefore, predicting a photometric light curve from spectroscopic data leads to a smaller amplitude and to less distinct low-latitude features – which is seen when comparing the maps achieved with and without photometry (Fig. 4.23 a and b, upper left and lower left).

Chapter 5

Short-term spot behaviour: The MUSICOS 98 campaign

"That the sun will rise tomorrow, is an hypothesis; and that means that we do not **know** whether it will rise."

Wittgenstein, Tractatus Logico-Philosophicus 6.36311

"The night is long that never finds the day."

Shakespeare, Macbeth

Variability studies on stars are often hampered by the fact (i.e. the hypothesis) that an observing night is finite and the Sun will rise in the morning – and therefore, by the limited phase coverage that observers can achieve from a single observatory. This is especially true for EI Eridani with its crucial rotation period of 1.945 days. For a single-site observing run, one needs at least two weeks of observations in order to avoid significant phase gaps that would reduce the quality of the Doppler images. Unfortunately, the low-latitude spot distribution on EI Eri seems to change on timescales shorter than two weeks (see §6.2.1). "Clearly, a thorough study of the spot morphology and evolution on HD 26337 requires a multisite campaign, preferably from observatories widely spaced in terrestrial longitude.", as already noted by Hatzes & Vogt (1992).

MUSICOS stands for MUlti-SIte COntinuous Spectroscopy and aims to achieve high-resolution, multi-wavelength spectroscopic observations from many sites around the globe, so that uninterrupted phase coverage of selected objects can be obtained. It addresses research in asteroseismology, stellar surface structure (Doppler and Zeeman-Doppler imaging), chromospheric activity (rotational modulation, flares, microflares), circumstellar environments (variable stellar winds) and similar fields. MUSICOS was initiated in 1988 (Catala & Foing 1988). Major campaigns have taken place in 1989, 1992, 1994, 1996, 1998 and 2001. A review of the first three campaigns is presented by Catala (1998). Additional information can be found on the Internet[1].

The MUSICOS 1998 campaign involved seven northern and southern sites (see Fig. 5.1), 13 telescopes (mostly equipped with cross-dispersed echelle spectrographs) and nine spectrographs and took place from November 20 to December 14, 1998. The involved sites were Haute Provence, Pic du Midi, La Palma, South Africa, ESO La Silla, Brazil, Kitt Peak, Xinglong, Mt Stromlo, Catania, Caucasus SAO. A summary of the sites and instruments involved in the campaign, some of their most important characteristics and the number of spectra gained is listed in Table 5.1. At the time of the campaign, the spectrograph FEROS had its commissioning and contributed only a few spectra, whenever it was possible. All other sites were fully dedicated to the campaign.

The campaign was organised at ESTEC/ESA by Bernard Foing and Joana Oliveira. It provided data for six different scientific programs. Three non-radial pulsating early-type B stars, known to be multiperiodic,

[1] http://www.ucm.es/info/Astrof/users/dmg/musicos/MUSICOS.html

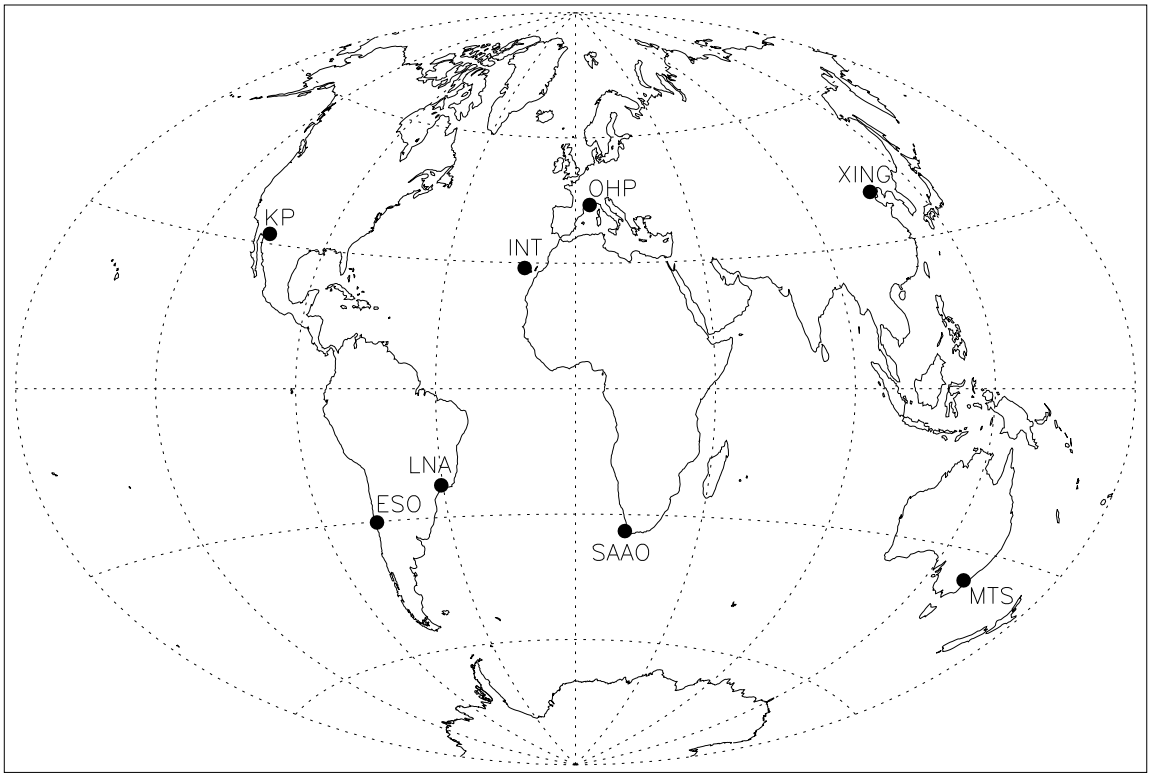

Figure 5.1: The sites involved in the MUSICOS 1998 campaign: INT, OHP, XING (BAO: Beijing Xinglong Observatory), KP (Kitt Peak), MTS (Mt. Stromlo), LNA, ESO and SAAO.

were monitored in order to determine unknown pulsation frequencies; the B star Omega Ori was observed in order to detect multi-periodic variations with time-scales ranging from 2 to 10 hours; the rapidly-rotating active binary stars EI Eridani and HR 1099 (García-Alvarez et al. 2003) were monitored to allow Doppler imaging of their surface photospheric spots, study differential rotation and spots lifetimes; the neutron star in Vela X1/HD77581 was observed to study the effects of non-radial pulsations and tidal forces on surface velocity fields of the supergiant companion; and the connection between stellar surface and wind structures was measured in three luminous supergiants. Although some sites suffered from snow and winds, the overall coverage was successful.

5.1 MUSICOS 98 and EI Eridani

My intention in participating in the MUSICOS 1998 campaign was to obtain two time-resolved Doppler images separated by about one week in order to look for differential rotation and other changes in the spot distribution (like polar shifts), and to pin down spot life times. As pointed out in §1.1.4, differential rotation is a key-ingredient for dynamo theories and therefore of high interest. Unfortunately, all Doppler images of EI Eri obtained to date (and obtainable at all) from a single observing site are "time-averaged" over about 10 rotation periods. Shorter-lived features are suppressed and smeared out in the reconstructions of EI Eri's surface which makes differential rotation measurements unfeasible. Considering the devastating effect of phase gaps on the surface maps, a Doppler image from a single site needs to be comprised of no less than 14 days of data, and the only solution for this dilemma is a multi-site campaign.

The presumed requirements for EI Eri were high signal-to-noise (S/N $\approx 200 - 300$) at moderate to high spectral resolution ($\lambda/\Delta\lambda \approx$ 30-40 000) gained in the classical wavelength region for Doppler imaging around

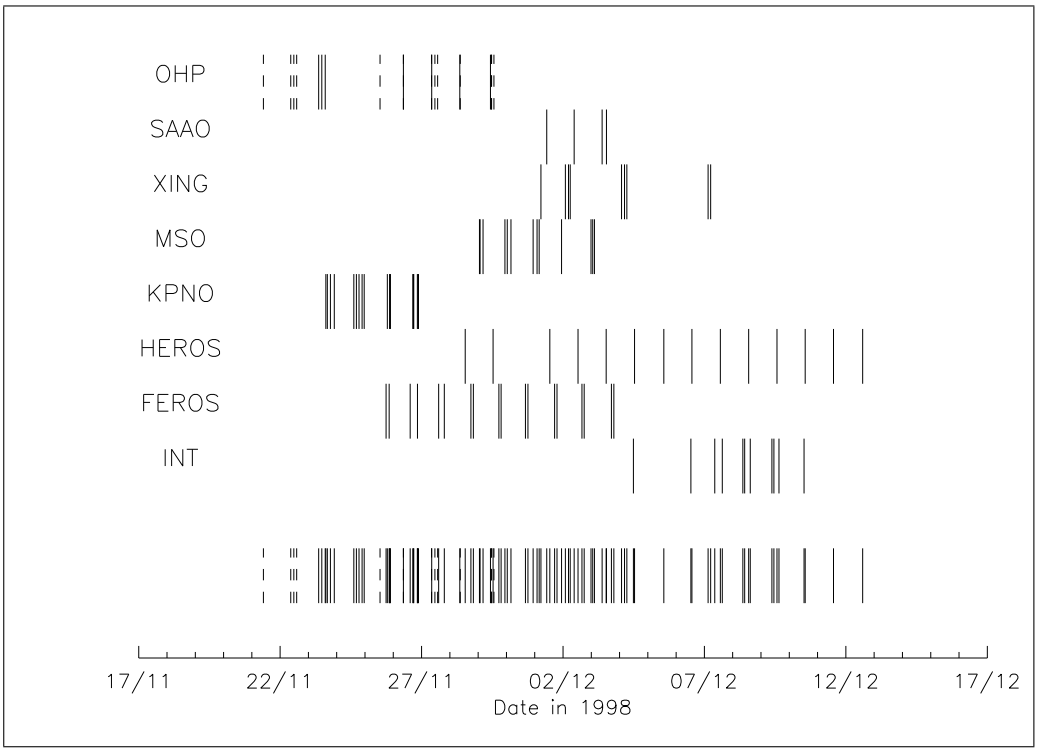

Figure 5.2: The time coverage of the EI Eri observations obtained during the MUSICOS 1998 campaign. The coverage of each site (indicated on the left) is shown, as well as the combined coverage of all sites (at the bottom of the figure). The dashed lines indicate spectra with wavelengths that could not be used for Doppler imaging.

6420 (± 50) Å. Two days of continuous observations with one exposure every two hours were proposed for achieving surface maps with ideal phase coverage. We requested two such observing blocks of two days each separated by about one week. Additionally, integrations of a fast-rotating B star for telluric-line correction and a RVSS were required. Co-investigators were Y. Unruh and K. G. Strassmeier. Simultaneous photometric observations were carried out with the Wolfgang-Amadeus twin Automatic Photoelectric Telescope (see §2.5).

5.2 The data

During the MUSICOS 1998 campaign, 122 high-resolution spectra of EI Eridani were obtained from seven different sites within a time span of 21 days (November 23 – December 13). Figure 5.2 shows the coverage of each site. At the bottom of the figure, the combined time coverage is displayed. The various observing sites made use of different spectrographs (Long Slit, Echelle) which leads to data sets of different quality (different wavelength ranges and spectral resolution; see Tab. 5.1). The data from SAAO, MSO, KPNO, ESO and INT were supplied as multi-aperture spectra. The ones from OHP and BXO came as one file per order. Unfortunately, only OHP193, BXO and MSO provided RVSS spectra, as required. For all other sites, no RV measurements were carried out as no precise zero-point is available (which would be essential for the triple star hypothesis, see §3.2.2).

A total of 95 of the spectra obtained with MUSICOS meet the classical wavelength region for Doppler imaging around 6420 (± 50) Å. A log of the observations including site, date, Heliocentric Julian date, exposure time, achieved signal-to-noise and – for OHP193, BXO and MSO – radial velocity is given in Table A.25. The four spectra from SAAO are of very poor quality and are, consequently, not used for Doppler imaging. One particular spectrum from MSO has a S/N of 25 and was expelled. After all, 90 spectra were taken into consideration for Doppler imaging.

Site	Abbr.	Telescope	Spectrograph	Number of nights	Resolving power	Resolution at λ6400 (FWHM of ThAr [px])	Number of orders	Wavelength range [nm]	Number of spectra	No. of spectra for DI
OHP, France	OHP152	1.5 m	Aurelie	6	22 000	–	1	652–672	13	0
	OHP193	1.9 m	Elodie/Ha	8	43 000	0.15	67	390–690	7	7
SAAO, S. Africa	SAAO	1.9 m	Giraffe	4	36 500	0.18	52	430–700	4sdf	0
Xinglong, China	BXO	2.2 m	Echelle	7	35 000	0.18	35	550–850	9	9
	–				43 000	0.15	24	397–700	0	0
Mt.Stromlo, Austr.	MSO	1.9 m	Echelle	5	35 000	0.18	43	480–680	13	12
Kitt Peak, USA	KPNO	0.9 m	Echelle	4	65 000	0.10	23	530–700	19	19
	–					–		390–490	0	0
ESO, Chile	ESO90	0.9 m	HEROS	15	20 000	0.32	33	580–865	14	14
	–					–	62	350–260	14	–
	ESO152	1.5 m	FEROS	9	48 000	0.13	35	368–855	18	18
LNA, Brazil	LNA	1.6 m	Coudé	0	60 000	0.11	1	663–672	0	0
INT, La Palma	INT	2.5 m	ESA-MUSICOS	7	35 000	0.18	58	400–680	11	11

Table 5.1: Sites and instruments involved in the MUSICOS 1998 campaign and some of their most important characteristics: resolving power, number of spectral orders, wavelength range, the number of nights allocated at each site and the instrument.

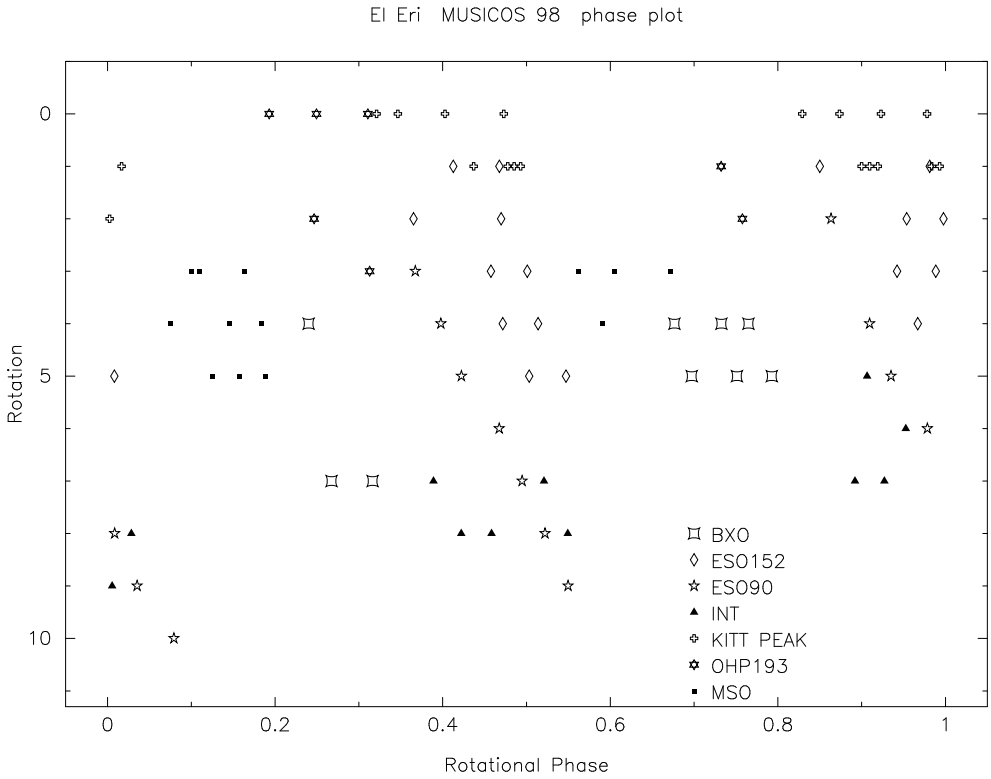

Figure 5.3: [Phase plot for the EI Eri observations obtained with the MUSICOS 1998 campaign.

5.2.1 Data reduction and preparation

The data were reduced using standard reduction procedures for echelle spectra using the IRAF NOAO packages: bias subtraction, flat-field correction using exposures of a tungsten lamp in order to remove pixel-to-pixel variations and the curvature of the blaze function, and wavelength calibration using spectra of a Thorium-Argon lamp. The spectra were normalised by applying a low-order polynomial or a cubic spline fit to the observed continuum. For OHP, ESO90 and BXO observations, the MIDAS[2] package was used.

The reduction of the data was supposed to be carried out by the individual observers. In fact, the data reduction was not done or not completed or did not meet the requirements for Doppler imaging in every particular. Only INT, ESO-HEROS and BXO/Xinglong were partly reduced (main targets only); all other spectra were reduced by David Garcia Alvarez and by myself. The spectra from the various observatories did not bear consistent image header keywords: some were missing, some were named differently. Consequently, important keyword parameters were standardised to the following names: UT, EXPTIME, DATE-OBS, RA, DEC and EPOCH.

5.2.2 Radial velocities

Radial velocity standard stars were only available for the data sets OHP193, BXO and MSO. The following RVSS were observed: HD 29139, HD 36079 and HD 92588. For a summary of the used RVSS see Table 3.4 on page 28. The data from Mount Stromlo Observatory (MSO) included two observations of the RVSS β Lep, a G5 III star with $r_v = 13.5 \pm 0.1$ (Pearce 1955), one on November 29 and one on December 3. Therefore, the spectra of EI Eri observed on November 30 were correlated with the RVSS observation from November 29, the ones from December 1 and 2 with the RVSS from December 3. As a test, the two spectra

[2] ESO-MIDAS is the acronym for the European Southern Observatory Munich Image Data Analysis System, which is developed and maintained by the European Southern Observatory

Site	Number of spectra	ADU (average)	S/N (average)	Wavelength range [Ångstrøm]	Order used for DI for line				Comments
					6393	6411	6430	6439	
OHP193	7	25000	180	6390 – 6459 (or62)					
SAAO	4	3000		?					
BXO	9	150	100	6379 – 6468 (or15)					
MSO	13	5000	80-90?	6323 – 6435 (or6), 6395 – 6507 (or5)	6	5	5	5	
KPNO	19	1600	60?	6332 – 6417 (or15), 6405 – 6491 (or16)	15	16	16	16	
ESO90	14			6354 – 6494 (px7400-8800)					
ESO152	18			6346 – 6496 (px94000-99000)					
INT	11		160?	6347 – 6445 (or53), 6422 – 6521 (or54)	53	53	53	54	

Table 5.2: Spectral range of the spectra used for Doppler imaging

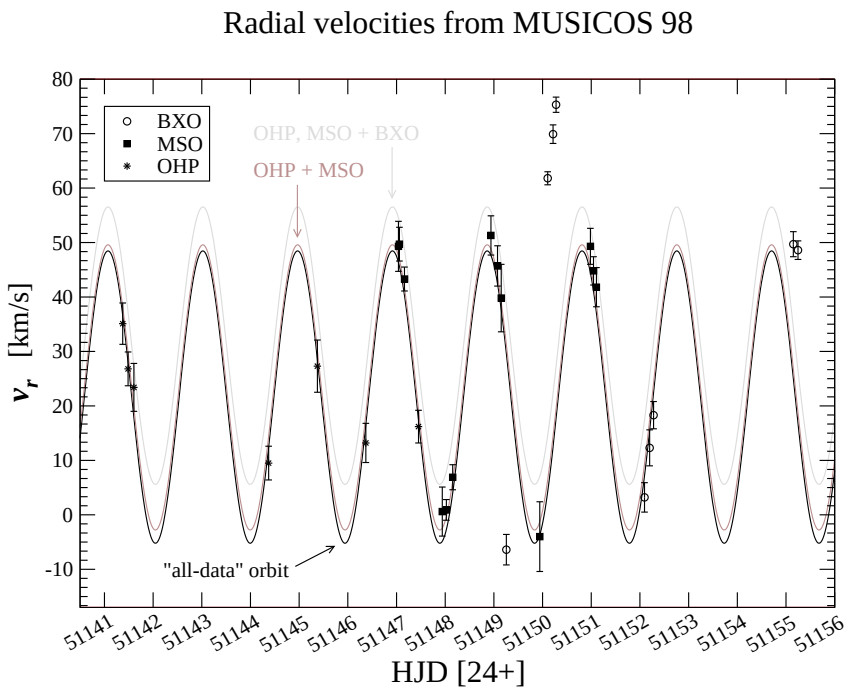

Figure 5.4: MUSICOS 98: radial velocities from OHP, MSO and BXO with superposed orbital solutions calculated with all available RV data (general orbit; black line; $\gamma = 21.6\,\mathrm{km\,s^{-1}}$; see §3.2), with all MUSICOS RVs (OHP, MSO and BXO; dark grey line; $\gamma = 31.1\,\mathrm{km\,s^{-1}}$) and with OHP and MSO only (light grey line; $\gamma = 23.4\,\mathrm{km\,s^{-1}}$). For an unknown reason, the BXO RVs are corrupted and were not used for the general orbit.

of β Lep were cross-correlated with each other and showed a difference of $0.17\,\mathrm{km\,s^{-1}}$ which is 20 times smaller than the average error of the RV measurements of EI Eri.

The data from BXO include two RVSS: HD 92588 = 33 Sex ($v_r = 42.8 \pm 0.1\,\mathrm{km\,s^{-1}}$; Pearce 1955) observed on December 1 and α Tau ($v_r = 54.25 \pm 0.08\,\mathrm{km\,s^{-1}}$; Scarfe et al. 1990) observed on December 2, 4 and 7, so for each spectrum of EI Eri, we have a RVSS observed during the same night.

OHP193 provided two observations of the RVSS α Tau ($v_r = 54.25 \pm 0.08\,\mathrm{km\,s^{-1}}$; Scarfe et al. 1990), one on November 23 and 26 each. Spectra of EI Eri from November 23 and 24 were cross-correlated with the RVSS spectrum from November 23, the ones from November 26 until 29 with the RVSS spectrum from November 26. The two RVSS spectra cross-correlated with each other show a difference of $0.7\,\mathrm{km\,s^{-1}}$ which is roughly the sixth part of the average error of the RV measurements of EI Eri ($\approx 4\,\mathrm{km\,s^{-1}}$).

The measured radial velocities from OHP, BXO and MSO were used for calculating orbital parameters. The results are shown in Fig. 5.4. Shown are the OHP, MSO and BXO RVs and three calculated orbits: one using all available RVs from all observing runs incl. KPNO and NSO (see §3.2; black line; $\gamma = 21.6\,\mathrm{km\,s^{-1}}$), one using the OHP, BXO and MSO values only (light grey line; $\gamma = 31.1\,\mathrm{km\,s^{-1}}$) and one with the OHP and MSO values only (dark grey line; $\gamma = 23.4\,\mathrm{km\,s^{-1}}$). The later one is almost similar to the "all data" orbit. The BXO values vary significantly from the projected orbit and are assumed to be corrupted. Consequently, the BXO radial velocities were not included in the orbit calculation in §3.2.1. The value of $\gamma = 23.4\,\mathrm{km\,s^{-1}}$ (OHP+MSO) was adopted as MUSICOS gamma velocity for §3.2.2 and, particularly, for Fig. 3.5.

5.3 Doppler imaging and differential rotation measurement

The same overall parameters as presented in § 4.2 were used for Doppler imaging. (The list of input parameters for Doppler imaging is outlined in the box on page 51.) Unfortunately, many MUSICOS spectra did not reach the desired quality. About half of all spectra exhibit low S/N of around 100 and even less

Block number	Number of spectra all[1]	6393	6411	6430	6439	Start - End in HJD (245+)	Epoch HJD	Duration [days]	Duration [$P_{\rm rot}$]
1	30				30	1141.376 - 1145.804	1143.590	4.43	2.28
2	23				21	1146.370 - 1149.785	1148.077	3.41	1.75
3	12				12	1150.106 - 1151.797	1150.951	1.69	0.87
4	17				15	1152.094 - 1156.633	1154.363	4.54	2.33
5	8				8	1157.400 - 1160.631	1159.015	3.23	1.66

Table 5.3: Block segmentation of the data for Doppler imaging – Version 1

Block number	Number of spectra all[1]	6393	6411	6430	6439	Start - End in HJD (245+)	Epoch HJD	Duration [days]	Duration [$P_{\rm rot}$]
1	19		17		17	1141.376 - 1144.373	1142.874	3.00	1.54
2	25		24		24	1144.598 - 1148.154	1146.376	3.56	1.83
3	14		12		13	1148.672 - 1150.667	1149.669	2.00	1.02
4	15		14		15	1150.747 - 1154.593	1152.670	3.85	1.98
5	15		15		12	1155.599 - 1160.631	1158.115	5.24	2.69

[1]... Two unused spectra are located between block 4 and 5.

Table 5.4: Block segmentation of the data for Doppler imaging – Version 2

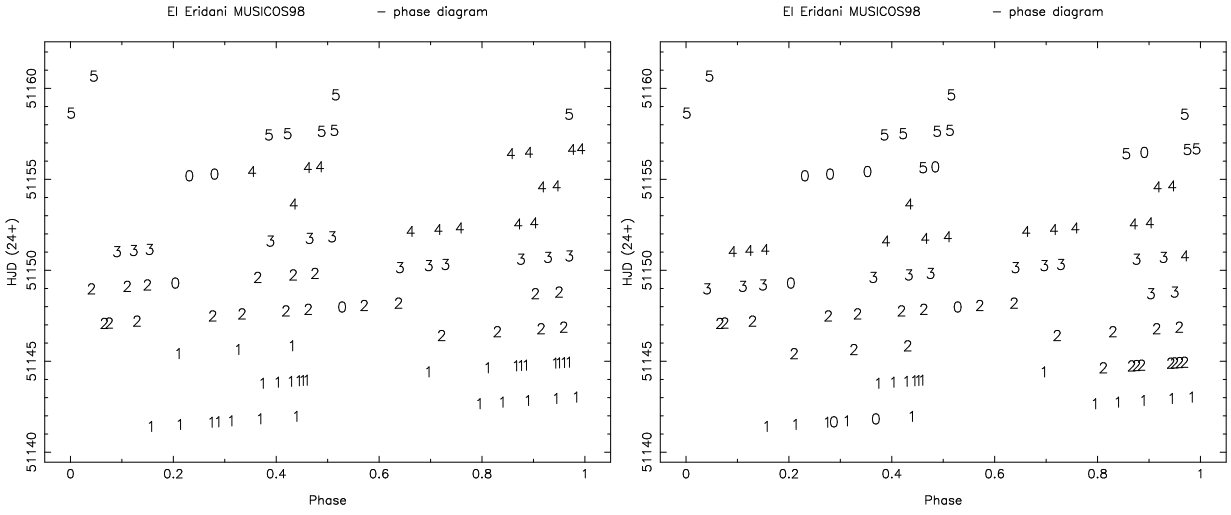

Figure 5.5: Phase plot incl. block segmentation for the λ6439 line, block segmentation: version 1 (left) and version 2 (right).

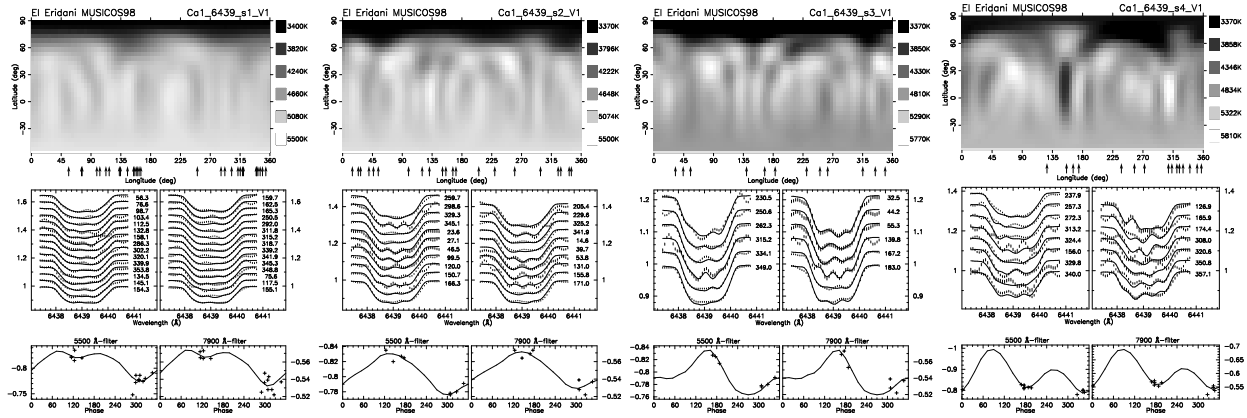

Figure 5.6: DI results for λ6439: Block 1-4 Version 1 corresponding to Fig. 5.5 (top left) and Table 5.3.

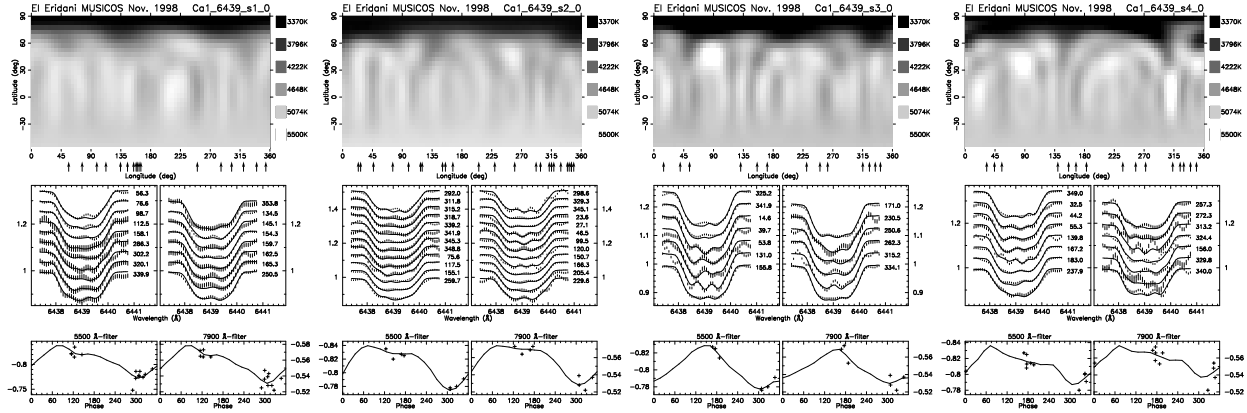

Figure 5.7: DI results for λ6439: Block 1-4 Version 2 corresponding to Fig. 5.5 (top right) and Table 5.4.

(see Table A.25). They can still be used for Doppler imaging, but not in all four mapping lines, and the quality of the surface maps suffers if too many low-S/N data are included. In the end, only the λ6439 and λ6411 lines gave satisfying results.

5.3.1 Doppler maps

The 90 MUSICOS spectra that were taken into consideration for Doppler imaging cover 20 days and were split into five blocks covering 2 to 5 days each, corresponding to 1 to 2.7 stellar rotations. For λ6439, two slightly different block segmentations were applied for comparison reasons (see Tables 5.3/5.4 and Figure 5.5). For λ6411, only the more evenly distributed block segmentation 2 was applied. A few spectra were not used due to poor S/N, cosmic-ray hits or redundant phase.

The best results were achieved with the λ6439 line. For block 1 – 3, we obtained reliable Doppler images (shown in Fig. 5.6 and 5.7), block 4 gives a reasonable Doppler map, while the spectra of block 5 are too noisy, and the resulting Doppler maps are not satisfying (and not shown). The λ6411 line was grouped in the same way as version two of λ6439's block segmentation. The first two blocks give satisfying results, while the spectra used for block 3 and 4 are quite noisy. Doppler imaging of these blocks is, however, still feasible. The resulting maps show a very similar spot distribution as the respective maps of the Calcium λ6439 line (version two). See Figure 5.7 and 5.8 for a comparison of the λ6439 and λ6411 Doppler maps. For testing the differential-rotation parameter α which was recently introduced to `TempMap` (see §4.2.4 and Fig. 4.3 on page 52), three different versions of `TempMap` were applied: The first one (3.0) does not include the differential-rotation parameter at all (and therefore overestimates the size of the polar spot), the second

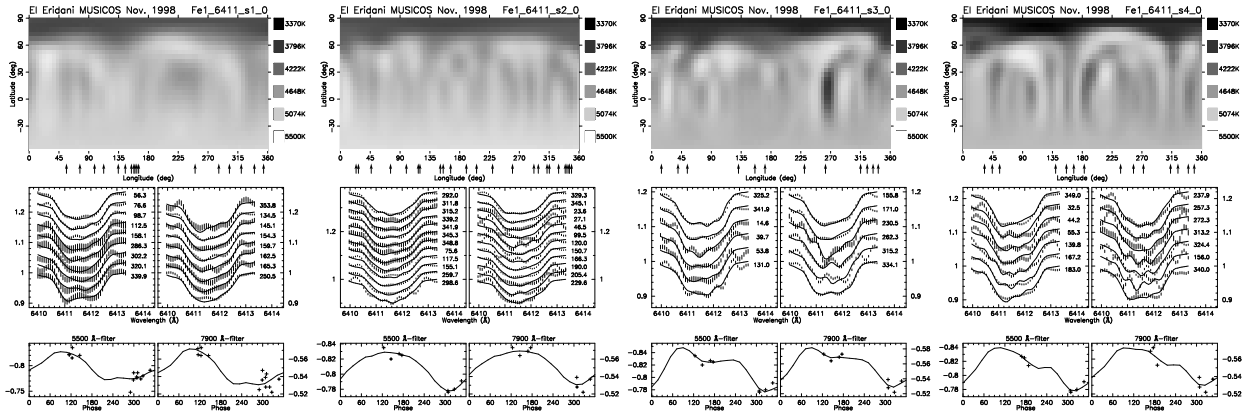

Figure 5.8: DI results for λ6411: Block 1-4 according to Fig. 5.5 (bottom) and Table 5.4.

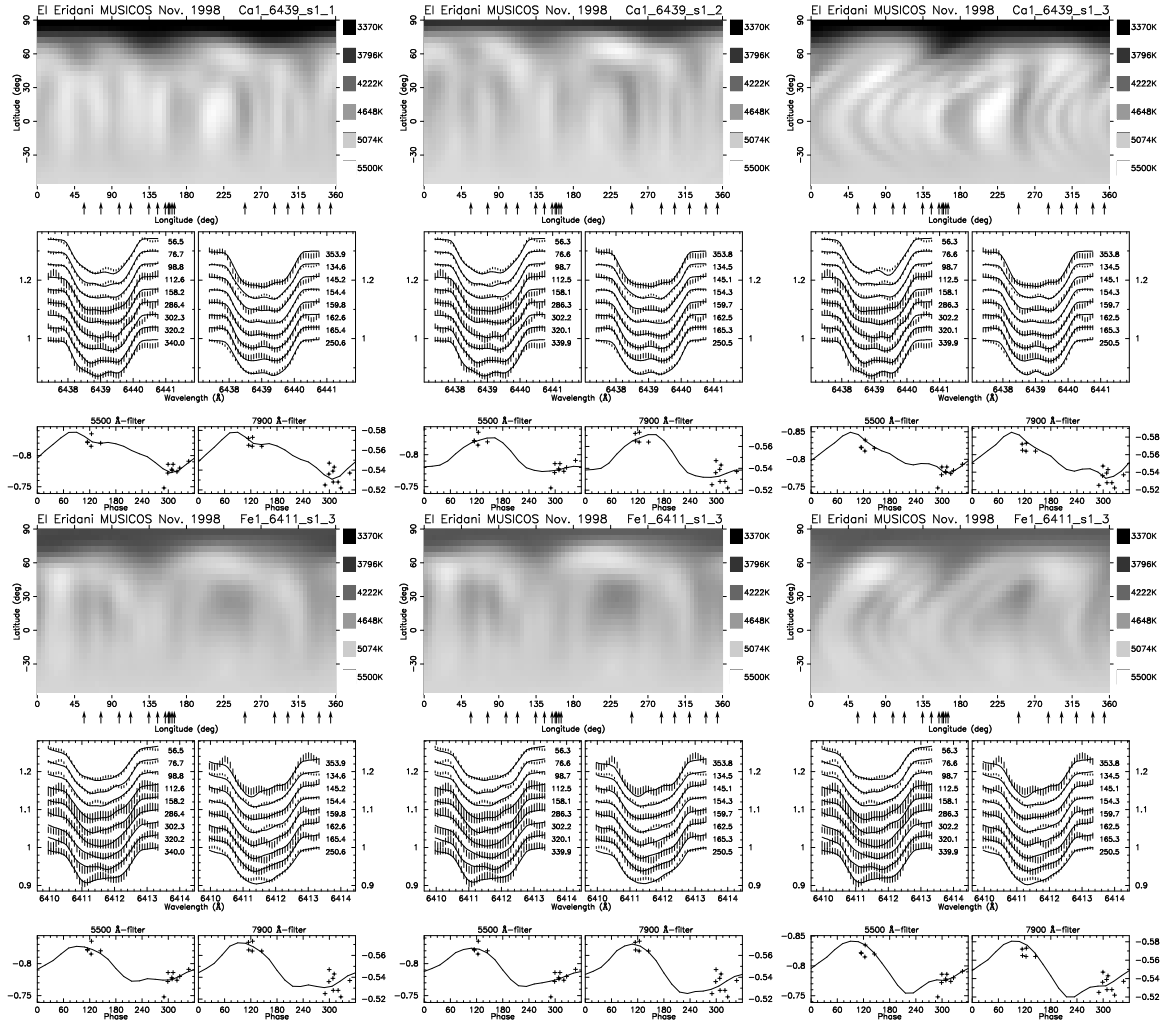

Figure 5.9: Testing three different TempMap versions (3.0, 3.1 and 3.2) using the λ6439 line block 1 (top) and λ6411 line block 1 (bottom): $\alpha = 0$ (left), $\alpha = -0.2$ (6439) / -0.15 (6411), only used for calculating shape of the line profile (middle), $\alpha = -0.2$ (6439) / -0.15 (6411), also accounts for P as a function of latitude.

one (3.1) uses α only for calculating the local line profiles (and exhibits a drastically reduced polar cap), the third `TempMap` version (3.2) additionally regards the period as a function of latitude. The results are shown in Fig. 5.9. The maps of `TempMap` 3.0 and 3.1 have an almost identical surface structure, but the polar cap is less distinct and, in the case of λ6439, smaller. `TempMap` 3.2 exhibits sinusoidally distorted structures. Obviously, the latitude dependence of the period is not embedded correctly and requires further programming efforts.

All achieved Doppler maps reflect the familiar image of EI Eri's surface: A polar spot of variable shape and a number of low-latitude spots that seem to change position and shape in timescales of a few days.

5.3.2 Differential rotation measurements

In order to reveal short-timescale drifts and differential rotation, two consecutive, independent Doppler maps are used. The star's latitudes are subdivided into slices of 5° width. Each latitude strip of the first image is then cross-correlated with the same strip of the second image. This way, the latitudinal cross-correlation functions (CCF) are assembled into a cross-correlation image (CCI). This technique was first applied by Donati & Collier Cameron (1997). For the cross-correlation calculations in this investigation, the tool `tempcor` by M. Weber was used in non-Fourier mode. A gaussian is then fitted to the central peak of the CCF, again for each latitude separately. Alternatively or for comparison, IRAF's `fxcor` task was used, doing a pixel correlation only (pixcor=yes). Both methods yield very similar results.

The pixel shift and the FWHM of the gaussian fit (for the error bars) are then used for computing a latitudinal-shift function. Finally, a least-square fit using a solar-type differential-rotation law ($\Omega(b) = \Omega_0 - \Omega_1 \sin^2 b$) was applied to this latitudinal-shift function (LSF) in order to get a quantitative measure of the differential rotation. Both block-segmentation versions for λ6439 were used. The resulting cross-correlation images including measured peaks and fits are shown in Fig. 5.11 and 5.12, while the resulting values of Ω_0, Ω_1, $\alpha = \Omega_1/\Omega_0$ and $1/\Omega_1$ are listed in Tab. 5.5 and 5.6. — For the former one **(block segm. 1)**, only the first three blocks were considered. Cross-correlation of any block with the low-quality block four did not give sensible results. For the cross-correlation image (CCI) 1–2 and 1–3, three possible LSFs (measurements and fits), for CCI 2–3, two possible LSFs could be defined. The corresponding α values come to -0.37, -0.34 and -0.15. The third LSF (right column in Fig. 5.11, corresponding to "Fit 2" in Tab. 5.5) is rather unlikely as (almost) all values of the LSF are smaller than the rotational period. The rotational period is rather expected to be around the mean of the LSF, as it is the case for version one and two. — For the latter one **(block segm. 2)**, the Doppler maps are of slightly better quality due to the more equal phase distribution, but the corresponding CCIs are, unfortunately, less distinct and thereby more difficult to measure. Fig. 5.12 (corresponding to the values in Tab. 5.6) has the results. The first row shows, for comparison, the CCI of block one with itself (left) and with block two (middle). Again, three LSFs were adopted for CCI 1–2 (second row) with the third one being rather unlikely (same reason as above). The corresponding values for the first two LSFs of CCI 1–2 are given in Table 5.6. The structure of CCI 2–3 (third row) does not provide an obvious path along which to fit the LSF. For comparison, the three different LSFs of CCI 1–2 are plotted. The first LSF of CCI 1–2 seems to fit CCI 2–3 best. CCI 1–3 suggests only one clear path for the LSF, shown in the fourth row, which is more similar to the second version of CCI 1–2 (this value is also listed Tab. 5.6). The decision for a specific LSF of CCI 1–4, 2–4 and 3–4 (shown in the fifth row) would be rather arbitrary. No measurements were applied for these images. The same is true for the CCIs of the λ6411 line. The sixth row shows the first three CCIs for λ6411. The last row of Tab. 5.6 gives an average of all three reasonable measurements. The resulting α value of -0.2 is comparable to the outcome of fit 2 of block segmentation 1 in Tab. 5.5.

Figure 5.10 shows the normalised goodness of fit from Doppler imaging as a function of the differential rotation parameter α for the λ6439 line. `TempMap` version 3.1 was used which introduces line profile distortion due to differential rotation. However, all latitudes are calculated with the same period. Block one to four are shown. Block one and three exhibit two minima: one at α = -0.15 – -0.20 and one at -0.4. Block two and four have one minimum at -0.25 – -0.30.

An α value of -0.2 to -0.35 (smaller than zero) means that the diff. rotation on EI Eri is anti-solar. $1/\Omega_1$ then evaluates to approx. 12 to 6 days denoting that the pole laps the equatorial region in 6 – 12 days.

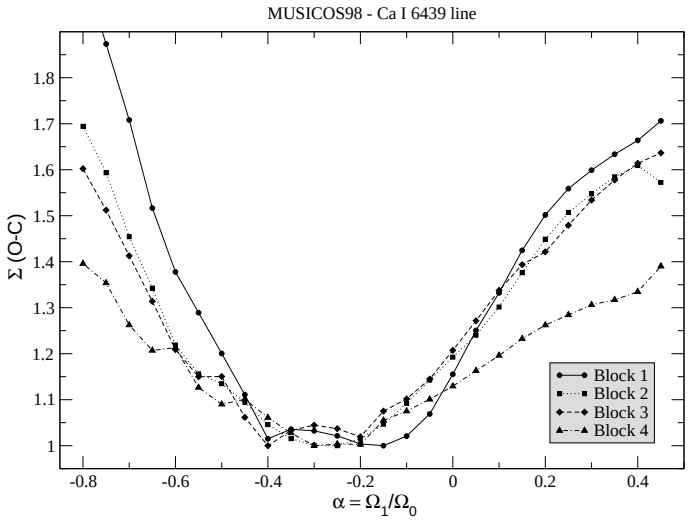

Figure 5.10: Normalised goodness of fit from Doppler imaging (λ6439-line) as a function of the differential rotation parameter $\alpha = \Omega_1/\Omega_0$.

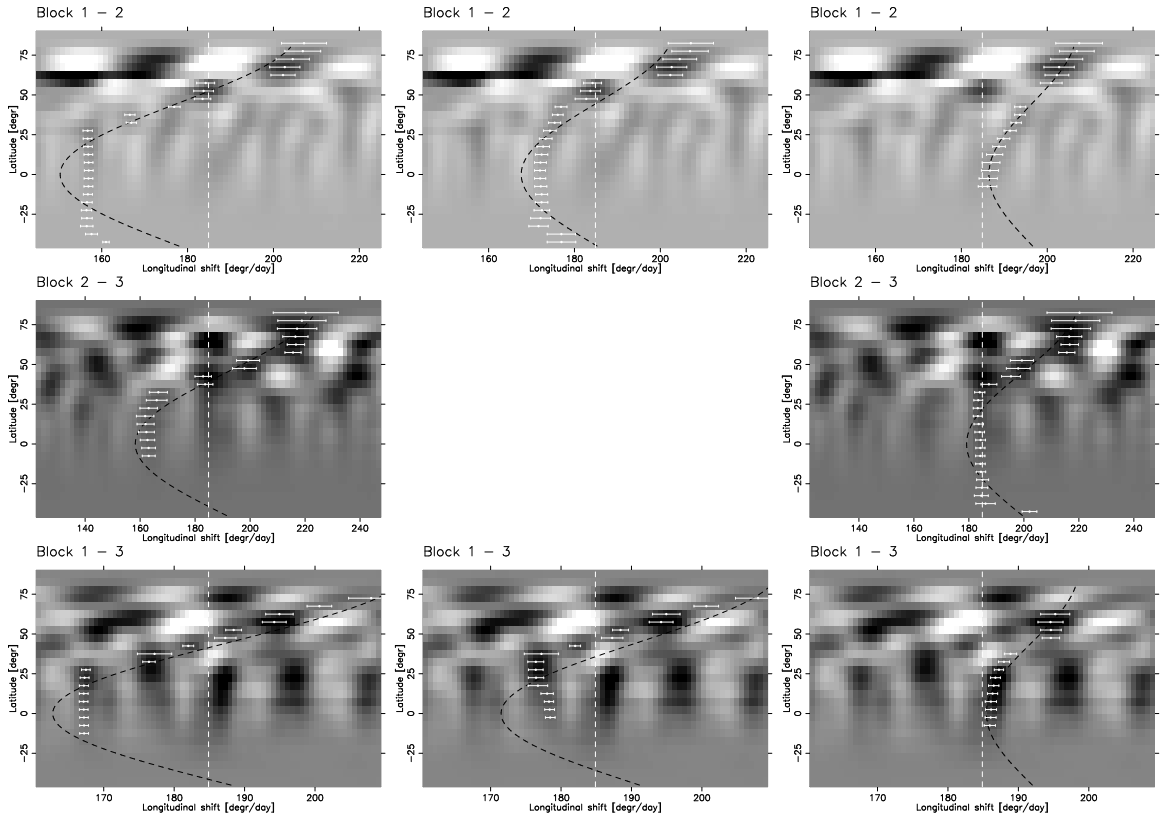

Figure 5.11: Cross-correlation images (CCI) of the first three consecutive Doppler maps shown in Fig. 5.6 (Calcium 6439 line, block segmentation version 1). Dark colour indicates good correlation. Additionally, the measured peaks of the correlation functions (with error bars), a least-square fit using a solar-type differential-rotation law and a white dashed line indicating the photometric/orbital rotation period is shown (see Table 5.5). **First row:** CCI for block 1–2 with three possible measurements/fits. **Second row:** CCI for block 2-3 with two possible measurements/fits. **Third row:** CCI for block 1–3 with three possible measurements/fits. Be aware that the scale in the axis of abscissae (x) varies for the different rows.

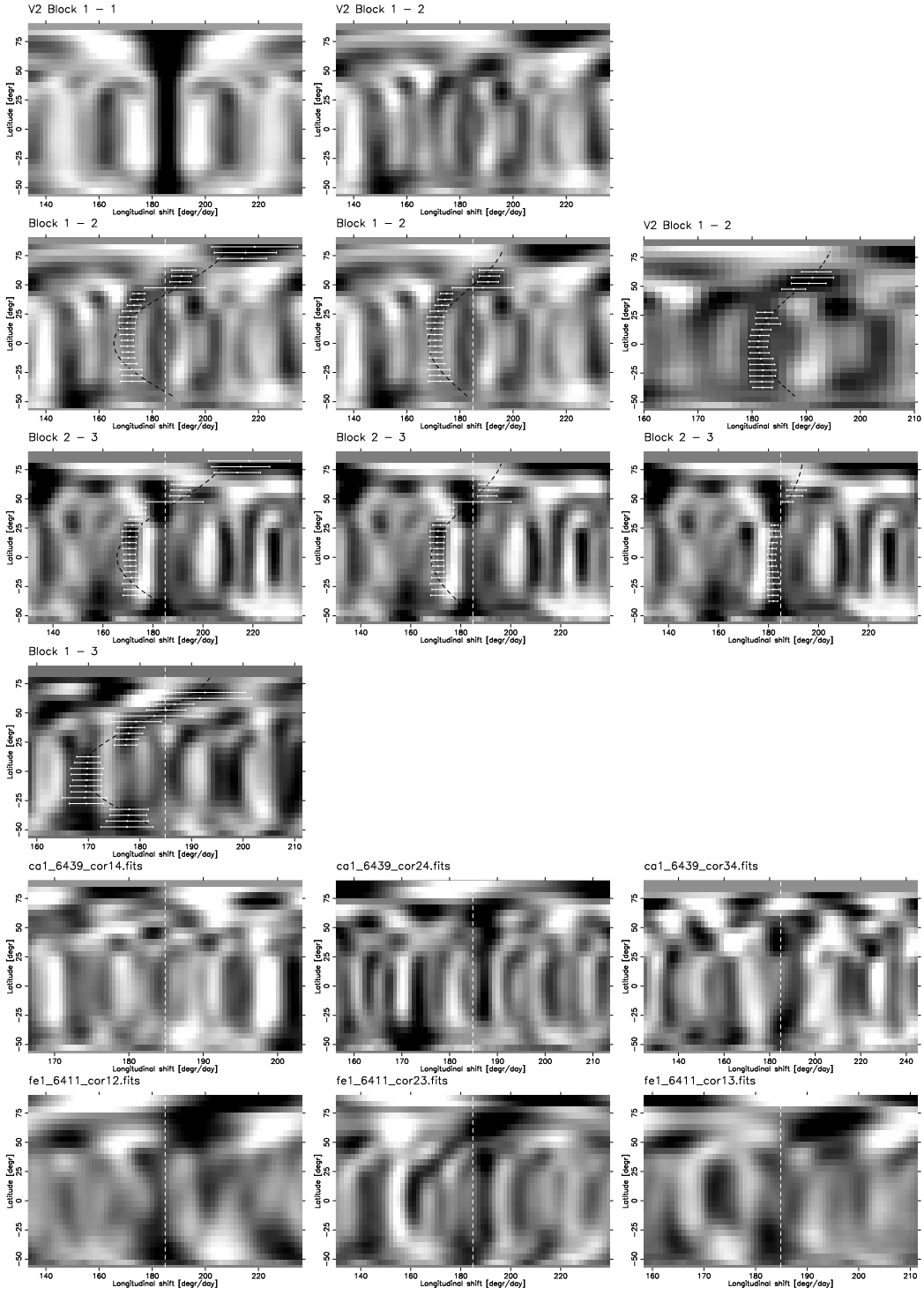

Figure 5.12: Cross-correlation image (CCI) of the first four consecutive Doppler maps shown in Fig. 5.7 (Calcium 6439 line, block segmentation version 2). Dark colour indicates good correlation. The filled white circles present the measured peaks of the correlation functions with error bars. The black dashed line shows a least-square fit using a solar-type differential-rotation law, the white dashed line indicates the photometric/orbital period. For the resulting values, see Table 5.6. **First row:** *Left:* Cross correlation of the Doppler map of block 1 with itself. No asymmetric structure is seen. *Middle:* Pure CCI of block 1–2 without overlying measurements/fits. **Second row:** CCI of block 1–2 with three possible measurements/fits. **Third row:** CCI of block 2–3. No latitudinal-shift function was measured. The plotted measurements/fits are taken from block 1–2 (second row) for comparison only. **Fourth row:** CCI of block 1–3 with measurements/fit. **Fifth row:** CCI of block 1–4, 2–4 and 3–4. **Sixth row:** CCI of block 1–2, 2–3 and 1–3 for the Fe λ6411 line.

Fit 1

Block	Ω_0 [°/day]	Ω_1 [°/day]	$\alpha = \Omega_1/\Omega_0$	$\lvert 1/\Omega_1 \rvert$ [days]
1–2	150.3	−55.4	−0.37	6.5
2–3	158.2	−66.4	−0.42	5.4
1–3	162.8	−50.7	−0.31	7.1
average	157.1±6.3	−57.5±8.1	−0.37±0.05	6.3±0.9

Fit 2

Block	Ω_0 [°/day]	Ω_1 [°/day]	$\alpha = \Omega_1/\Omega_0$	$\lvert 1/\Omega_1 \rvert$ [days]
1–2	167.6	−35.3	−0.21	10.2
2–3	—	—	—	—
1–3	171.5	−39.3	−0.23	9.2
average	169.5±2.7	−37.3±2.8	−0.22±0.01	9.7±0.7

Fit 3

Block	Ω_0 [°/day]	Ω_1 [°/day]	$\alpha = \Omega_1/\Omega_0$	$\lvert 1/\Omega_1 \rvert$ [days]
1–2	186.4	−20.4	−0.11	17.7
2–3	179.2	−40.6	−0.23	8.9
1–3	185.5	−13.1	−0.07	27.6
average	183.7±3.9	−24.7±14.3	−0.13±0.08	14.6±8.4

Table 5.5: Differential rotation of EI Eri (block segmentation 1) derived from the cross-correlations shown in Fig. 5.11 left (Fit 1), middle (Fit 2) and right column (Fit 3).

Block	Ω_0 [°/day]	Ω_1 [°/day]	$\alpha = \Omega_1/\Omega_0$	$\lvert 1/\Omega_1 \rvert$ [days]
1–2	165.6 / 168.1	−44.0 / −29.0	−0.27 / −0.17	8.2 / 12.4
2–3	–	–	–	–
1–3	168.7	−25.6	−0.15	14.1
average	167.5±1.6	−32.9±9.8	−0.20±0.06	11.6±3.0

Table 5.6: Differential rotation of EI Eri (block segmentation 2) derived from three cross-correlations shown in Fig. 5.12: The vales of block 1–2 correspond to Fig. 5.12's second row, left and middle image, while the values of block 1–3 correspond to to the left image in the fourth row of Fig. 5.12.

5.3.3 Discussion

All MUSICOS Doppler images from Nov/Dec 98 (Fig. 5.6, 5.7 and 5.8) show a very similar spot distribution. Some spots seem to decay, others seem to emerge or drift. Also, the shape of the polar spot changes significantly, while its size remains the same. The cross-correlated images suggest a differential surface rotation that is opposite to the solar case, i.e. the pole rotates faster than the equator (in contradiction to the results from Hatzes & Vogt 1992). However, the applied solar-like differential-rotation law obviously does not fully represent the measurements shown in Fig. 5.11/5.12. This is partly an intrinsic problem of the line-profile inversion technique (because spots near the stellar equator appear elongated in latitude due to the poor latitudinal information at the equator) and partly due to the insufficient quality of the Doppler maps. All in all, the α value resulting from the various cross correlations comes to -0.13 – -0.37 while $1/\Omega_1$, i.e. the time the pole laps the equatorial region, evaluates to 6 – 15 days.

How reliable are those values? Two major problems arise: the quality of the Doppler images and the influence of the polar spot on the local line profiles. **(1)** Unfortunately, the Doppler maps resulting from the MUSICOS 98 observations are of low quality, and it cannot be ultimately decided whether the cross-correlation patterns presented in this section can be assumed to be real. Nevertheless, the results comply with the minimum values of the χ^2 curves (normalised goodness of fit as a function of α) which amount to $\approx$ -0.27$\pm$0.15 (MUSICOS 98, λ6439, Fig. 5.10 on page 78) and -0.17$\pm$0.10 (several KPNO and NSO data sets, see Fig. 4.3 on page 52). **(2)** Another problem is introduced by the polar spot: As pointed out by Johns-Krull (1996), anti-solar differential rotation and polar spots have the same effect on photospheric line profiles, namely the core of the lines is not as deep as would otherwise be expected. Calculating the line profiles under the assumption of strong anti-solar differential rotation can, thereby, significantly reduce the polar feature (as seen in Fig. 5.9, top row, left and middle image), while neglecting anti-solar differential rotation – if existent – can mimic a polar cap (see also Reiners & Schmitt 2002).

After all, both approaches *per se* are not conclusive, but they do support each other, with both reproducing similar values. Therefore, I suggest a differential rotation on EI Eri of α = -0.15 – -0.2 but emphasise that this result has to be taken as preliminary, and further verification with better-quality data is needed. As to the MUSICOS 98 data, one alternative remains open: LSD, least-squares deconvolution – which allows to sum up thousands of spectral lines and thereby to boost the S/N – could be applied to these data (see Donati et al. 1997; Collier Cameron 2001). García-Alvarez et al. (2003) demonstrated the successfull application of LSD to the HR 1099 data, which are part of the same scientific program for MUSICOS 98 as EI Eri and comparable in quality to the EI Eri data. However, the technique of LSD is not applicable to the Doppler imaging code `TempMap`, so a different code like `DOTS` would have to be applied.

Anti-solar differential rotation may at first seem unreasonable from a theoretical standpoint. On the other hand, the strong levels of solar-like differential rotation which were predicted for rapidly rotating stars (and especially giants) by theoretical investigations (Kitchatinov & Rüdiger 1999; Kueker et al. 1993) are not observed (see the list on page 9), thereby indicating that our theoretical understanding of differential rotation is far from complete. So far, anti-solar differential rotation has been reported observationally on a few RS CVn stars (p.9) and some other stars (see Strassmeier 2003).

Differential rotation on close binaries with synchronised rotation, like EI Eri, is exposed to strong forces of tidal friction which might additionally weaken the differential rotation. Tides tend to synchronise (i.e. accelerate) rotation at all latitudes of the convective zone but are most pronounced at the stellar equator. However, Scharlemann (1982) points out that tides will not suppress or modify differential rotation, nor will it generate differential rotation on RS CVn stars.

Chapter 6

Long-term observations: NSO and KPNO data

> "The great new solar telescope at the Kitt Peak National Observatory in Arizona is a source of pride to this nation. The largest instrument for solar research in the world, it presents American astronomers with a unique tool for investigating the nearest of stars, our Sun. This project is of exceptional interest to all of our citizens..."
>
> *J. F. Kennedy, October 22, 1962*

> "If the star is still not there, first try moving in the Nord/South direction, then try East/West."
>
> *NSO-McMath Solar/Stellar Observations Guide*

Not only american astronomers are granted observing time at the McMath-Pierce telescope, and not always is the star not there. The McMath, looking much like the gnomon of an amazingly large sundial, was, at the day of opening, the world's largest and most sophisticated telescope for studying the Sun. It's tower rises 30 meters above the ground from which a shaft slants 60 meters to the ground where a tunnel continues an additional 90 meters into the mountain, with observing facilities, spectrographs, observers rooms etc. all located subterraneously. Being the only telescope that has won an architectural award, it still provides astronomers with highly resolved spectra from the Sun and stars.

6.1 NSO synoptic nighttime program

The old but useful McMath facility and its stellar spectrograph were already described in chapter 2.2. The McMath synoptic nighttime program was initiated by Smith & Giampapa (1987). Mr. Paul Avellar, later Ms. Trudy Tilleman, was the nighttime resident observer at the McMath telescope and obtained all the McMath synoptic data as part of a nighttime program open for the entire community on a peer-review basis. The program "Doppler imaging of EI Eridani" (P.I. K. G. Strassmeier) ran for seven years until the shutdown of the nighttime program at the end of 1995. The resulting spectra were reduced partly by the observer and largely by myself with IRAF using standard procedures as described in §2.

The NSO synoptic data were received from the observer in blocks named *eieri02, eieri03, ccd010, ccd016, ccd024, ccd106/107, data92, nso93, nso94* and *nso95*. For an overview of the NSO synoptic data see Table 6.1. All blocks, as received from NSO, contained a number of continuous spectra spanning one or two months and were, if possible, split into two groups. Most spectra were gained from end of October until middle of December and again from middle of January until February or March during the years 1988 till 1995. The first seven blocks with 10 – 20 spectra each allowed splitting into typically two groups, while the data from blocks *nso94* and *nso95* with about 40 and 80 spectra each included several subblocks spanning October to March and allowing three and five groups per season. Block *nso93* included some spectra from 1989 and 1992 (which could not be used due to data format errors) and six spectra from the 92/93 season spanning more than two months.

From Nov. 88 till Dec. 94, the dispersion axis runs along columns, from Feb. 95 on along lines. The wavelength range for the spectra from the NSO synoptic nighttime program ranges from λ6396 to λ6473Å, the resolution on the CCD is between 0.095 and 0.112Å/pixel, the instrumental resolution (FWHM of an ThNe line) 1.4 – 2.2 pixel. Ideally, when the focus is at its best, IFWHM for the convolution with `tmake2` would be set to 0.19 and FILT to 2.8 Å/px. In fact, the focus typically varies throughout the night, and IFWHM=0.25 and FILT=3.5–4.0 are more realistic values. Useful Doppler-imaging lines are λ6411, λ6430 and λ6439, the iron line λ6393 is not covered. Typically, there are something like 2 to 3 observations of EI Eri per week, so we have to combine several weeks of data to obtain one Doppler image with at least six spectra, and the phase gaps are usually high, ranging from 58° to 194° with 113° on average.

Table 6.1: Overview of the NSO synoptic observations. *HJD* gives the starting point of the first and last observation of the particular block. "*no. of spectra*" lists the number of observed spectra and, if different, separated by a slash the number of spectra used for Doppler mapping the λ6439 line. The column "*max. ph. gaps*" gives the maximum phase gap for the corresponding λ6439 Doppler map. The *number of rotations* denotes the time span from the beginning of the first till the end of the last observation used for DI of the particular block.

Directory	Pseudonym	Year	from – till	HJD [24+]	no. of spectra	max. ph.gap	no. of rotations
eieri02	**Nov. 88**	1988	Nov 16 – Nov 29	47481.86 – 47494.87	9	114.8	6.70
eieri02	**Dec. 88**	1988	Dec 13 – Dec 22	47508.90 – 47517.92	8	162.6	4.65
eieri03	**Jan. 89**	1989	Jan 12 – Jan 31	47538.82 – 47557.70	6	126.9	9.71
ccd010	**Nov/Dec89**	1989	Nov 9 – Dec 18	47839.91 – 47878.95	6	167.5	20.06
ccd010	**Jan. 90**	1990	Jan 7 – Jan 12	47898.78 – 47903.74	10	163.0	2.56
ccd010	*not used*	1990	Jan 21 – Feb 3	47912.81 – 47925.81	4	–	–
ccd016	**Nov. 90**	1990	Oct 23 – Dec 2	48187.91 – 48227.84	10	81.2	20.53
ccd024	**Jan. 91**	1991	Jan 15 – Jan 31	48271.80 – 48287.78	6	118.3	8.27
ccd024	*not used*	1991	Mar 8 – Mar 18	48323.74 – 48333.68	3	–	–
ccd106/7	*not used*	1991	Oct 7	48536.84	1	–	–
ccd106/7	**Nov. 91**	1991	Nov 11 – Dec 8	48571.88 – 48598.95	12	58.3	13.93
ccd107	**Jan. 92**	1992	Jan 9 – Jan 26	48630.80 – 48647.73	7	110.5	8.72
ccd107	*not used*	1992	Feb 5	48657.74	1	–	–
data92	**Oct. 92**	1992	Oct 14 – Oct 26	48909.82 – 48921.93	6	106.7	6.23
data92	**Nov. 92**	1992	Nov 6 – Dec 1	48932.99 – 48957.75	8	90.5	12.74
nso93	*not used*	1989	Dec 6 – Dec 15	47866.98 – 47875.78	2	–	–
nso93	*not used*	1992	Dec 2	48958.85	1	–	–
nso93	*not used*	1993	Jan 29 – Apr 2	49016.74 – 49079.67	6	–	(32.33)
nso94	**Oct. 93**	1993	Oct 20 – Nov 4	49280.93 – 49295.86	8/7	147.2	7.68
nso94:more1	*not used*	1993	Nov 11	49302.87	1	–	–
nso94:more1	**Dec. 93**	1993	Dec 5 – Dec 9	49326.88 – 49330.80	6	142.6	2.03
nso94:more2	*not used*	1994	Jan 30 – Feb 1	49382.71 – 49384.66	6	–	–
nso94:more3	**Mar 94**	1994	Mar 5 – Apr 1	49416.61 – 49443.60	21/17	65.8	13.86
nso95:94oct	**Oct 94**	1994	Oct 18 – Oct 31	49643.95 – 49656.87	16/12	146.7	6.66
nso95:94dec	**Dec 94**	1994	Dec 17 – Jan 3	49703.79 – 49720.84	21	68.3	8.77
nso95:95feb	*not used*	1995	Feb 17 – Feb 20	49765.67 – 49768.68	5	–	(1.55)
nso95:95mar	**Mar 95**	1995	Feb 28 – Mar 28	49776.65 – 49804.66	12/7	193.7	6.70
nso95:95oct	*not used*	1995	Oct 1 – Oct 2	49992.03 – 49992.89	3	–	–
nso95:95nov	**Nov 95**	1995	Nov 7 – Dec 2	50029.03 – 50053.81	15	74.7	12.73
nso95:95dec	**Dec 95**	1995	Dec 12 – Dec 28	50063.94 – 50079.90	5	114.7	8.22

Table 6.2: NSO synoptic data: Average dispersion and first pixel value. Column two (n_s) is the number of object spectra (EI Eri + RVSS), column three (n_d) the number of days per block.[2]

block	n_s	n_d	average dispersion	dispersion range	av. 1st pixel	range
ccd016	19	40	0.09603 ± 0.00182	0.09417 – 0.10075	6402.83 ± 1.34	6399.61 – 6404.35
ccd024	18	62	0.09603 ± 0.00005	0.09595 – 0.09613	6404.40 ± 0.46	6403.52 – 6405.00
ccd107	39	76	0.09597 ± 0.00067	0.09456 – 0.09724	6405.81 ± 2.34	6402.06 – 6409.21
data92	28	48	0.09530 ± 0.00120	0.09327 – 0.09636	6401.57 ± 0.68	6400.48 – 6402.58
nso93	11	63	0.09588 ± 0.00036	0.09527 – 0.09630	6401.45 ± 0.34	6401.23 – 6402.14
nso94	16	15	0.09688 ± 0.00018	0.09650 – 0.09713	6401.29 ± 0.58	6400.04 – 6402.04
nso94:more1	13	28	0.09627 ± 0.00013	0.09603 – 0.09639	6401.05 ± 0.40	6400.35 – 6401.66
nso94:more2	9	3	0.09629 ± 0.00016	0.09601 – 0.09644	6401.87 ± 0.46	6401.33 – 6402.40
nso94:more3	33	27	0.09630 ± 0.00007	0.09617 – 0.09647	6401.46 ± 0.53	6400.25 – 6402.33
nso95:94oct	23	13	0.09518 ± 0.00039	0.09468 – 0.09609	6401.58 ± 0.60	6400.41 – 6402.45
nso95:94dec	33	17	0.09527 ± 0.00039	0.09459 – 0.09613	6401.33 ± 0.70	6400.06 – 6402.19
nso95:95feb	7	3	0.11117 ± 0.00031	0.11092 – 0.11151	6395.88 ± 1.04	6394.77 – 6396.72
nso95:95mar	20	28	0.11248 ± 0.00071	0.11192 – 0.11413	6394.03 ± 0.80	6392.80 – 6395.10
nso95:95oct	5	1	0.11074 ± 0.00009	0.11060 – 0.11082	6394.88 ± 0.08	6394.81 – 6395.01
nso95:95nov	28	24	0.11060 ± 0.00004	0.11051 – 0.11068	6395.46 ± 0.74	6394.30 – 6396.53
nso95:95dec	10	16	0.11071 ± 0.00016	0.11058 – 0.11100	6395.74 ± 0.53	6395.01 – 6396.30
McMath 96	1080	69	0.11167 ± 0.00034	0.11100 – 0.11387	6398.99 ± 0.63	6397.89 – 6401.65

In the now following sections, the individual blocks, their data reduction and the corresponding Doppler images will be addressed. Observer of the first six blocks (until "ccd107"), although not mentioned in the image headers, was supposedly Paul Avellar.

6.1.1 Nov. – Dec. 1988 ("eieri02")

The block "eieri02" (Nov. and Dec. 1988) contains 17 spectra spread over a range of 36 days with a gap of 14 days right in the middle. Thus, it is reasonable to split the data into two blocks of 9 and 8 spectra each. Block one ranges then from November 16 to 29, 1988 (14 nights, 9 spectra), block two from December 13 to 22, 1988 (10 nights, 8 spectra).

All maps from both epochs show the usual picture of a single, clearly off-axis polar spot at around 45–90° longitude and a number of small low-latitude features. All three lines show similar results. The λ6439 from 1988 Nov was improved by setting the 6439.075 log gf from 0.47 to 0.07 and the 6438.755 log gf from -2.48 to -1.68. For 1988 Dec, a change for 6439.075 log gf to 0.27 did the trick. λ6430: for 1988 Nov and Dec, 6432.680 log gf was adjusted to -2.7; for 1988 Dec, 6430.844 was set to -2.2. No adjustments were applied for λ6411.

6.1.2 Jan. 1989 ("eieri03")

The block "eieri03" (Jan. 1989) contains 6 spectra. For λ6430, the reconstructed blue wing is too weak. The attempt to fix this misfit by varying the log gf values leads to a huge bright spot in the reconstructed images, so I decided on the less ideal line fits. The λ6411 line is close to the edge of the spectrum where the curve of the continuum is uncertain and difficult to fit. Thus, the λ6411 line of the 1989Jan NSO spectra is of poor quality and is not being used for DI.

Both blocks, "eieri02" and "eieri03", were already fully reduced but lacked any radial velocity information.

[2]The blocks *eieri02*, *eieri03* and *ccd010* are not listed as they were received in one-dimensional state and had been rebinned with fixed dispersion, so their individual dispersion information is not available.

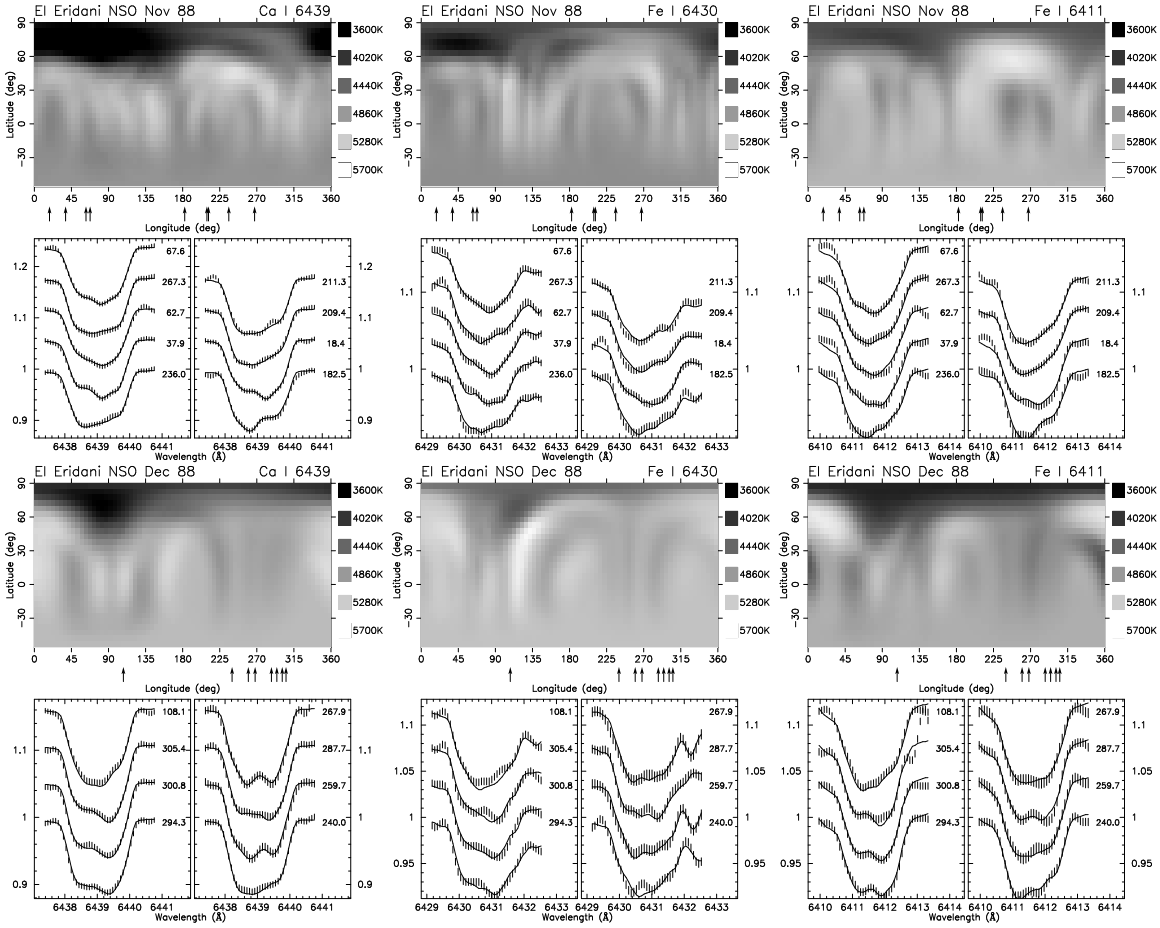

Figure 6.1: NSO eieri02: November 1988 and December 1988

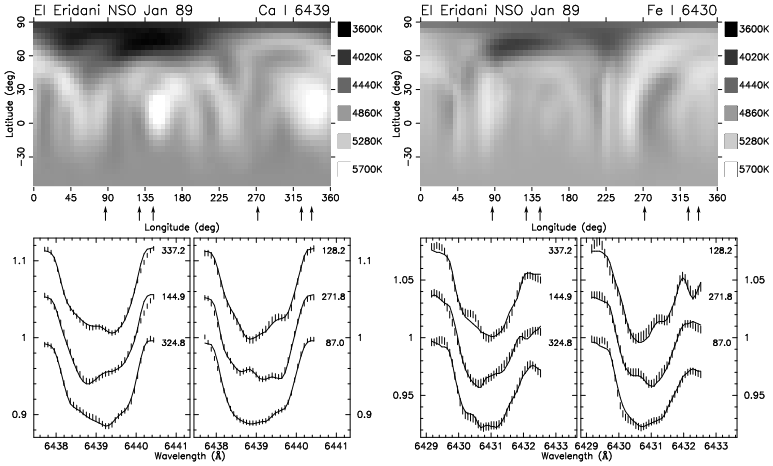

Figure 6.2: NSO eieri03: January 1989, λ6439 and λ6430

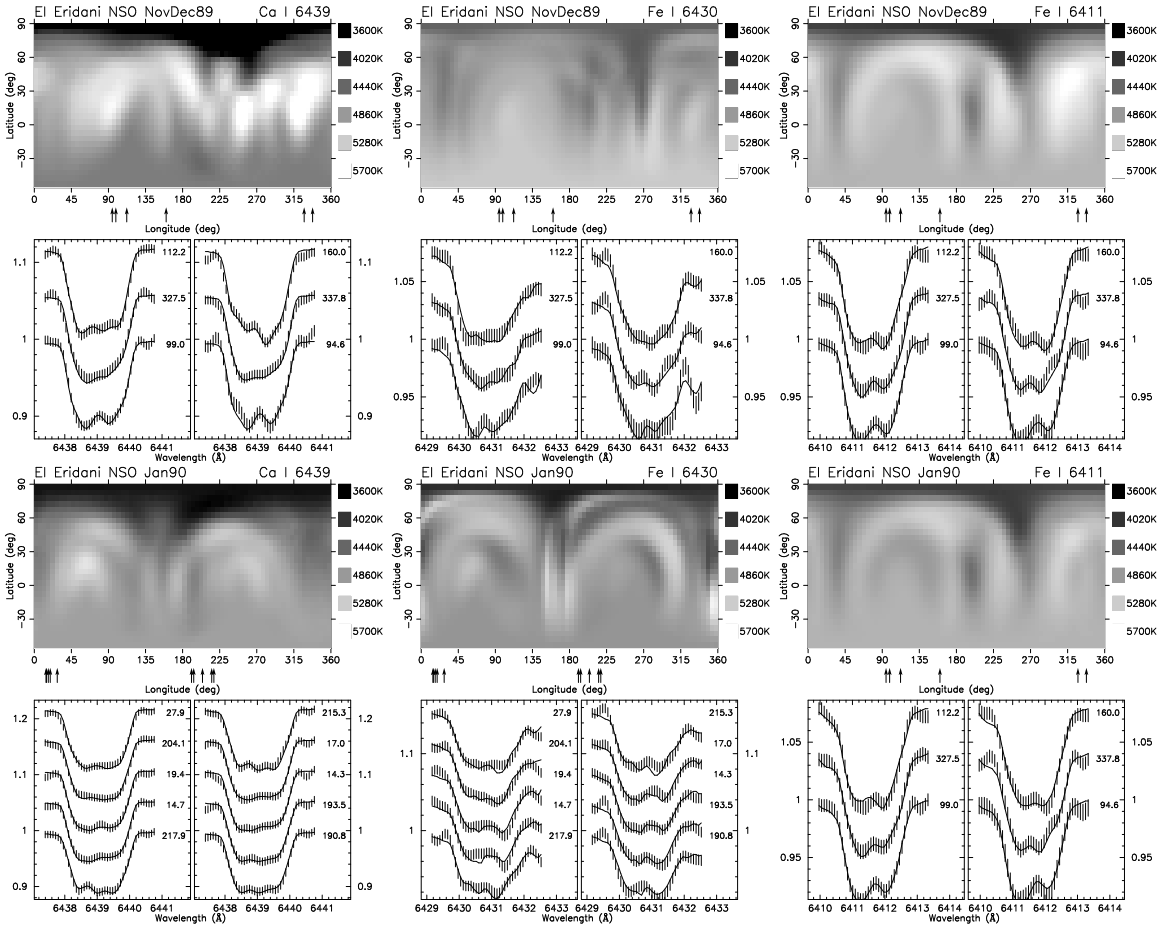

Figure 6.3: NSO ccd010: Nov./Dec. 1989 and January 1990

No radial velocity standard stars were available. Therefore, I shifted the spectral lines by hand with `extract2` und used the resulting velocity shifts as v_r's for Tables A.1 & A.2 and for calculating the orbit.

6.1.3 Nov. 1989 – Jan. 1990 ("ccd010")

The data in block "ccd010" were partly reduced: wavelength calibration, normalisation and radial velocity measurements were missing. Unfortunately, several of the required ThNe comparison spectra were missing, and no complete wavelength calibration could be applied to this block. Therefore, no radial velocity information from this block was used.

The block contains 20 spectra of EI Eri from November 9, 1989, to January 24, 1990. They were split into two groups, one from Nov. 9 to Dec. 18, the second from Jan. 7 to 12. Four more spectra from Jan. 21, Jan. 24 and Feb. 3 are too distant to join them with block two, and not sufficient for establishing an additional Doppler map. Moreover, they are of bad quality (low S/N and several critical cosmic ray hits).

λ6439: Excellent fits but hot spots in surface maps. For 1990 Jan, they could be strongly reduced by setting the Ca abundance from -6.3 to -6.7 (which did not help for 1989 Nov, so I sticked to the default value of -6.3).
λ6430: For 1989 Nov, $\log gf$ of 6432.68 was set to -2.75; for 1990 Jan, smoothing is 5 instead of 2.
λ6411: 1989 Nov: $\log gf$ of 6411.647 is -0.52.

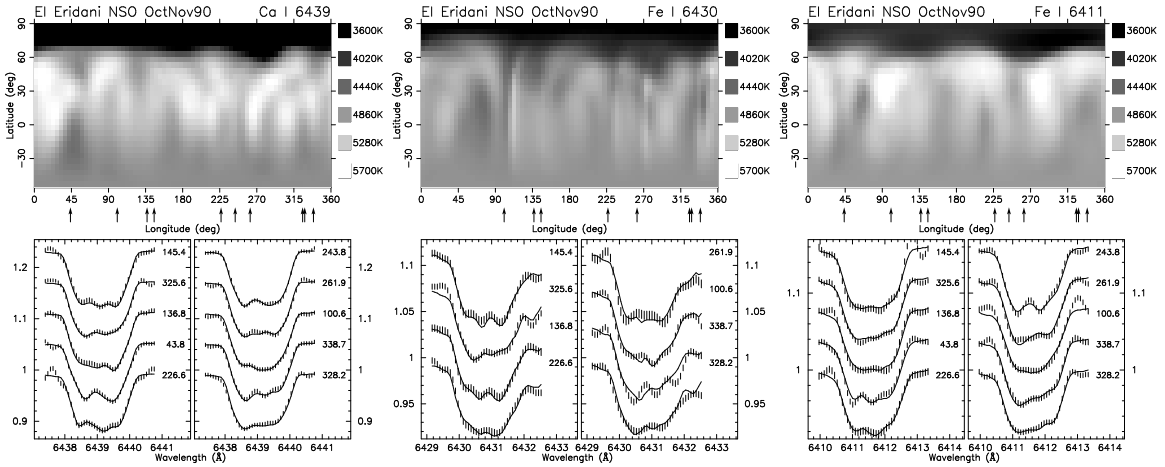

Figure 6.4: NSO ccd016: Nov. 1990

6.1.4 Nov. 1990 ("ccd016")

The data in block "ccd010" were partly reduced: wavelength calibration, normalisation and radial velocity measurements were missing. For each night, two comparison-lamp spectra (both after the object spectra) and one exposure of the RV star 59 Ari (G6 IV, v_r = -0.1 km s^{-1}; Wilson 1953) were taken, except for the night 03/11/90 where no radial velocity star is present. Cross-correlating the spectra of 59 Ari with each other gives deviations of 0.65 km s^{-1}, maximum is 1.3 km s^{-1}. Average dispersion of the 19 object spectra (ten EI Eri and nine RVSS) is 0.09603 ± 0.00182 Å/px [range: 0.09417–0.10075], average starting point (pixel 1) is 6402.83 ± 1.34 Å[range: 6399.61–6404.35].

Ten spectra of EI Eri are present, spread out over a period of 41 days, from October 23 to December 2, 1990, with three gaps of eight days each. All ten spectra were combined for one Doppler image.

This epoch again shows a huge polar cap, not symmetric but centered on the polar axis.
λ6439: warm/hot spots are present. The map is completely dominated by the polar cap which reaches down to 70 degrees on all longitudes. For λ6430, two spectra had to be omitted due to cosmic ray hits. It was reconstructed with a smoothing factor of 4 instead of 2. λ6411's $\log gf$ is -0.53 instead of -0.82.

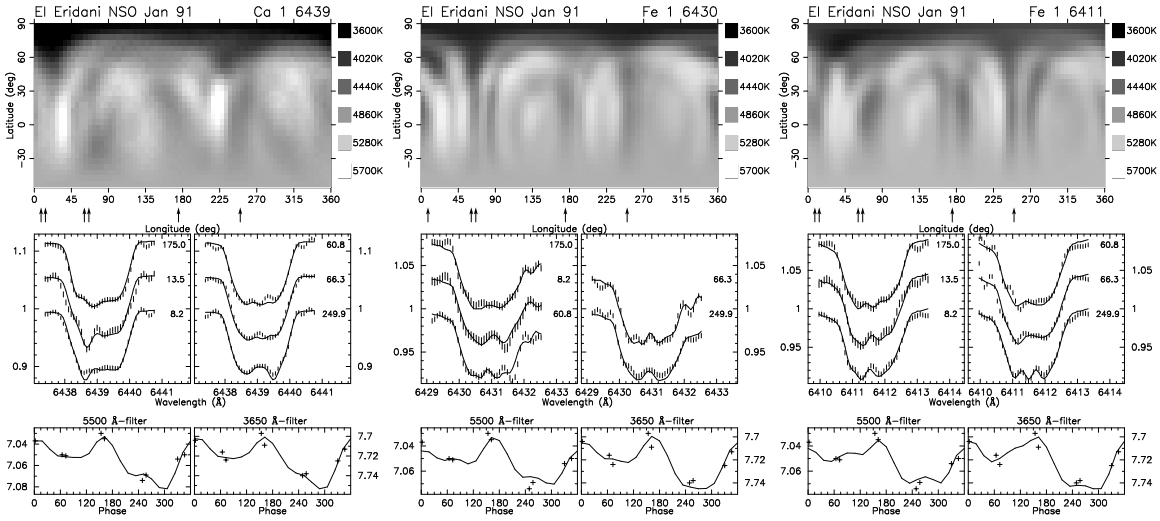

Figure 6.5: NSO ccd024: Jan. 1991

6.1.5 Jan. 1991 ("ccd024")

The data in block "ccd024" were again partly reduced: wavelength calibration, normalisation and radial velocity measurements were missing. For each night, we have two comparison-lamp spectra and one exposure of the RV star 59 Ari (G6 IV, v_r = -0.1 km s^{-1}; Wilson 1953). For the night 08/03/91, 59 Vir is listed as radial velocity star instead of 59 Ari – which is obviously a mistake as the respective image header lists the correct stellar position of 59 Ari. The radial velocity star spectra exhibit, cross-correlated with each other, an average/maximal deviation of 0.5/0.9 km s^{-1}. The 18 spectra (nine EI Eri and nine RVSS) have an average spectral resolution of 0.09603 ± 0.00005 ranging from 0.09595 to 0.096125 Å/px with starting points ranging from 6403.525 to 6405.003 Å(6404.40 ± 0.46 Å).

Best FWHM of a ThNe emission line is around 1.4 pixel, typical values are between 1.6 and 2.0. FILT for the convolution with `tmake2` was set to 3.5. Continuum was set using a cubic spline function in third order. Photometry is available from HJD 2448268.74 (12/01/91) to 2448293.67 (06/02/91), altogether 9 measurements. The first six spectra were observed in the second half of January and span 16 nights, the following three spectra are from March – they were omitted from the sample.

For λ6430, $\log gf$ was adjusted to -2.3, for λ6411, a $\log gf$ of -0.68 was applied.

6.1.6 Nov. 1991 / Jan. 1992 ("ccd107")

Block "ccd107" comprises 19 spectra ranging from October 7, 1991, to February 2, 1992, and concentrating on November and January. Each night pleases with a RVSS measurement and two comparison-lamp exposures, one taken before and one after the object spectra. Only bias and flat field correction, trimming and overscan correction was accomplished by the observer. For the 39 object spectra (21 EI Eri and 18 RVSS), the dispersion varies between 0.09456 and 0.09724 Å/px (average: 0.09597 ± 0.00067 Å/px), and the starting wavelength shifts kind of gradually from 6402.06 to 6409.21 Å (average: 6405.81 ± 2.34 Å). Dispersion axis is along columns (dispaxis=2). Best FWHM of a ThNe emission line is 1.3 pixel, typical values are between 1.6 and 2.4.

Nightly RV standard is again 59 Ari (G6 IV, v_r = -0.1 $\mathrm{km\,s^{-1}}$; Wilson 1953). The RVSS from 25/11/91 was named "α Ari", but again this seems to be a typing error as its stellar position (in the image header) agrees with the position of 59 Ari. The RVSS spectra were all cross-correlated with each other; the average divergence is $2.6\,\mathrm{km\,s^{-1}}$, the highest ones are $7.3\,\mathrm{km\,s^{-1}}$ (HJD 2448584.71 from 24/11/91) and $3.3\,\mathrm{km\,s^{-1}}$ (HJD 2448598.99 from 08/12/91). For the night 27/11/91, no RVSS is available. Cross-correlation with the preceding and the subsequent RVSS spectra (from night 26/11 and 04/12) yields 21.45 ± 1.98 and $21.43 \pm 2.62\,\mathrm{km\,s^{-1}}$; consequntly, $21.44 \pm 1.98\,\mathrm{km\,s^{-1}}$ was adopted for EI Eri's HJD 2448587.69 observation. Same problem for night 10/01/92: cross-correlation with the RVSS from 09/01 and 14/01 gives 9.41 ± 1.97 and $10.46 \pm 2.13\,\mathrm{km\,s^{-1}}$ for the HJD 2448631.73 spectrum of EI Eri; thus, $9.93 \pm 2.00\,\mathrm{km\,s^{-1}}$ was adopted.

Photometry is only available from JD 2448562.89 (02/11/91) to 2448568.88 (08/11/91), which precedes the spectroscopic data by about a week, and from JD 2448623.71 (02/01/92) to 2448657.69 (05/02/92).

For DI, the data were split into two blocks comprising the Nov./Dec. and the January data, respectively. The single spectrum from October and the one from February were expelled. The autumn block comprises 12 spectra spread over a period of 28 days $\hat{=}$ 14 rotations, the January block 18 days $\hat{=}$ 9 rotations. The λ6439 line gives reasonable results, λ6430 is acceptable, while λ6411 hits the edge of the CCD in several cases and is, therefore, unreliable.

6.1.7 Oct. 1992 / Nov. 1992 ("data92")

The data were not reduced by the observer. Data reduction was performed in the standard way as described in §2. The 20 spectra span the period 14/10 – 01/12 with a gap of 10 days at the end of October / beginning of November which naturally splits the data set into two groups, lasting 14/10 – 26/10 and 06/11 – 01/12. Each night comes again with a RVSS observation of 59 Ari and two comparison-lamp exposures picked up before and after the object spectra. Average dispersion for all 28 spectra is 0.09530 ± 0.00120 [0.09327–0.09636] with an average starting point of 6401.57 ± 0.68 [6400.48–6402.58]. This unusual high deviation of the average dispersion can be avoided by separating the spectra (taking out eight spectra from 06/11 till 09/11) and calculating the values again, this time for the two groups separately: average dispersion is now 0.09603 ± 0.00032 [0.09518–0.09636] (20 spectra) for all object spectra except the period 06/11 – 09/11 where it is 0.09349 ± 0.00016 [0.09327–0.09368] (eight spectra). Best FWHM of a ThNe emission line is around 1.5 pixel, typical values are between 1.6 and 2.2. Cross-correlation of the RVSS spectra with each other gives deviations of $0.93\,\mathrm{km\,s^{-1}}$ with a maximum of $1.8\,\mathrm{km\,s^{-1}}$. Photometry provides us with eight measurements from 05/10/92 till 01/11/92 ("Oct. 92") and 12 measurements from 04/11/92 till 03/12/92 ("Dec. 92"). Observer was Paul Avellar.

λ6430+6411: two spectra had to be taken out as they were too noisy.

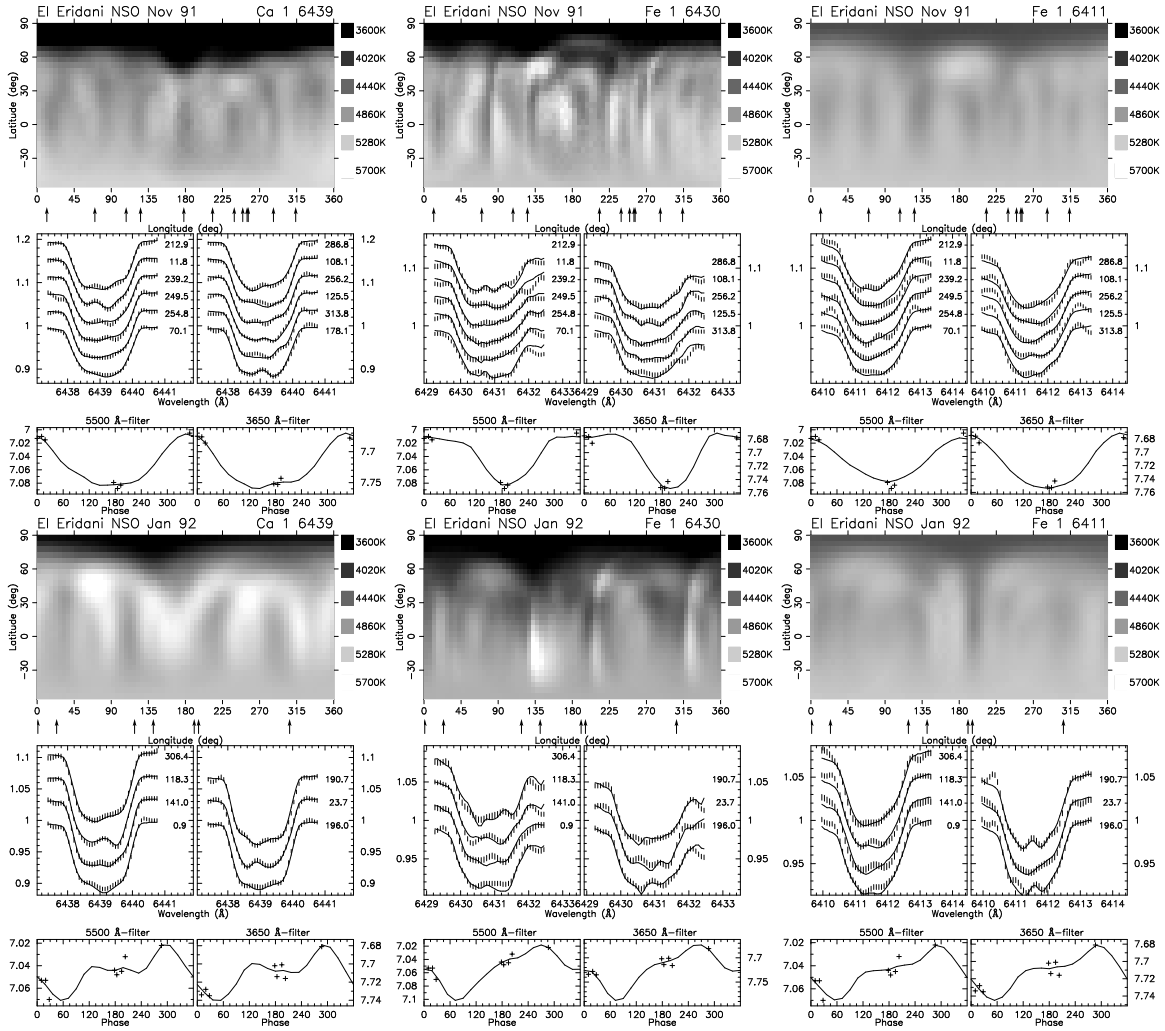

Figure 6.6: NSO ccd107: Nov. 1991 / Jan. 1992

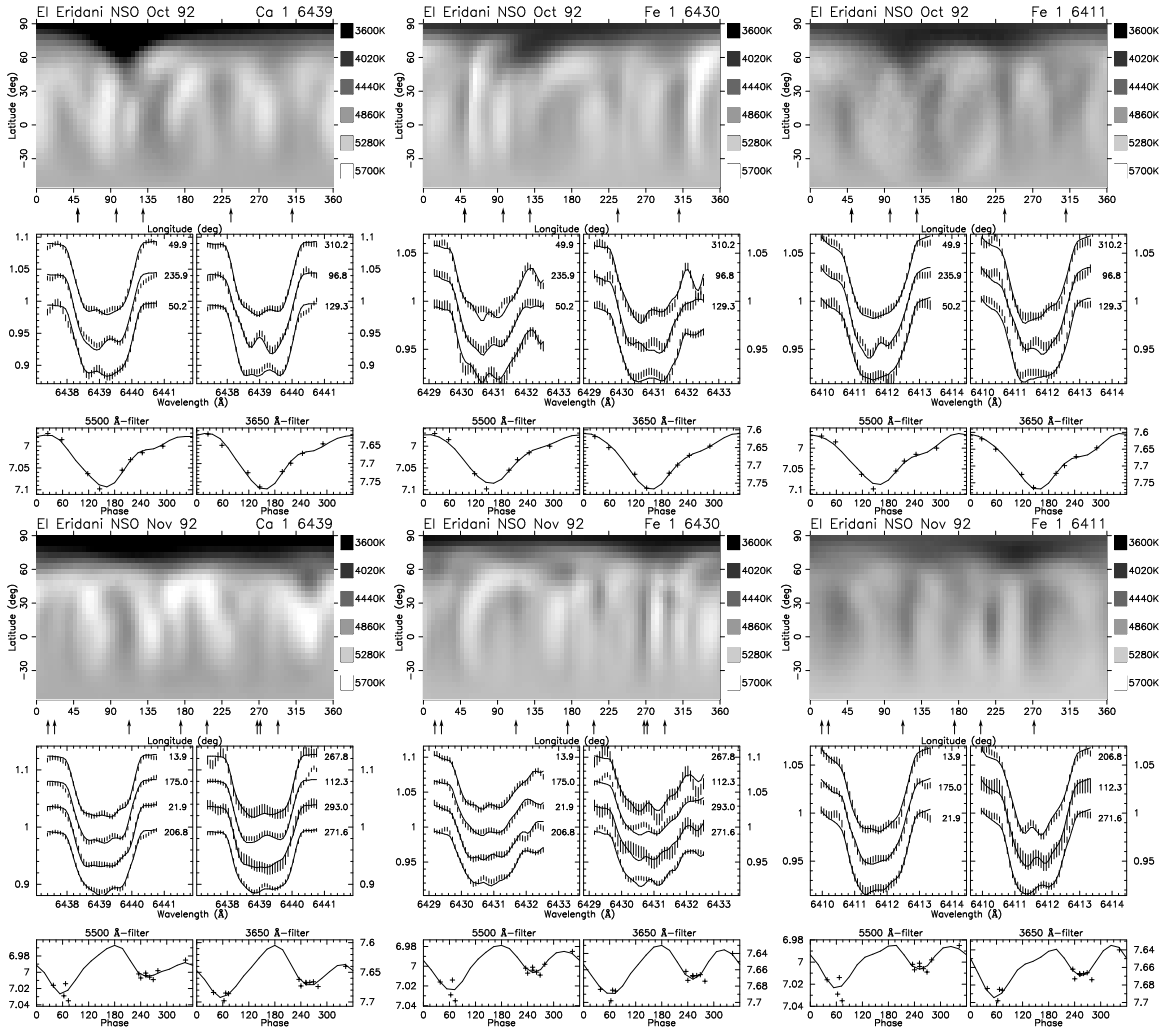

Figure 6.7: NSO data92: Nov. 1992. Top: with photometry; bottom: without; bottom right: first four spectra shifted down by one increment.

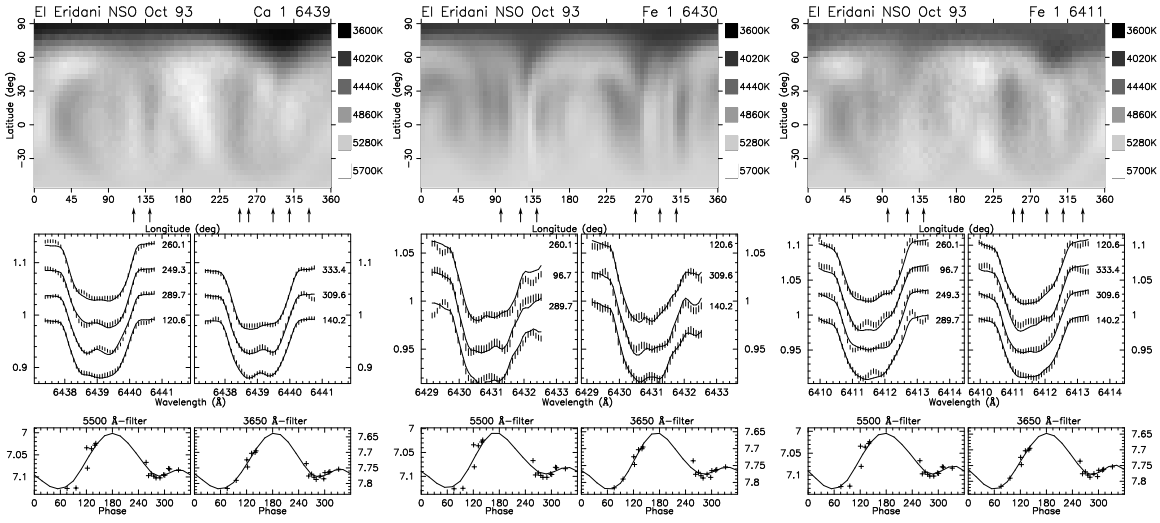

Figure 6.8: NSO nso94: Oct. 1993.

6.1.8 Mar. 1993 ("nso93")

The data were not reduced by the observer. Data reduction was performed in the standard way as described in §2. This block contains nine spectra of EI Eri: one from 06/12/89 and one from 15/12/89 (which were reassigned to *ccd010*), one from 02/12/92 (reassigned to *data92*), and six spectra from five nights, observed from January to April 93. Identification of the comparison integrations was not possible for the first three spectra. All nights except the first two from 1989 contain one observation of the RVSS 59 Ari. The RVSS from 2449016.70 (29/01/93) and 2449066.63 (20/03/93) were named 59 Vir but exhibit the stellar position of 59 Ari; consequently, they were treated as 59 Ari. The average dispersion is 0.09588 ± 0.00036 [0.09527–0.09630] for all 11 object spectra, starting point 6401.45 ± 0.34 [6401.23–6402.14]. Observer was Paul Avellar.

The spectra of this block were not used for Doppler imaging as they are spread out over a too wide range.

6.1.9 Oct. 1993 ("nso94")

The data were not reduced by the observer except bias combination, bias correction, trimming and oversize correction for the object spectra. This block contains 8 spectra spectra of EI Eri from seven nights spanning 16 days.

Trim data section was set by hand to [5:12,1:800]. All nights contain one observation of the RVSS 59 Ari. All but two nights include two comparison-lamp integrations, only one is available for the nights 20/10/93 and 01/11/93 each. The average dispersion is 0.09688 ± 0.00018 [0.09650–0.09713] for all 16 object spectra, starting point 6401.29 ± 0.58 [6400.04–6402.04]. Observer was again Paul Avellar. Best FWHM of a ThNe emission line is around 1.4 pixel, typical values are between 1.7 and 2.1. Cross-correlation of the RVSS spectra with each other gives deviations of $0.44\,\mathrm{km\,s^{-1}}$ with a maximum of $0.56\,\mathrm{km\,s^{-1}}$. 18 photometric measurements are available in the time frame of the seven spectroscopic spectra.

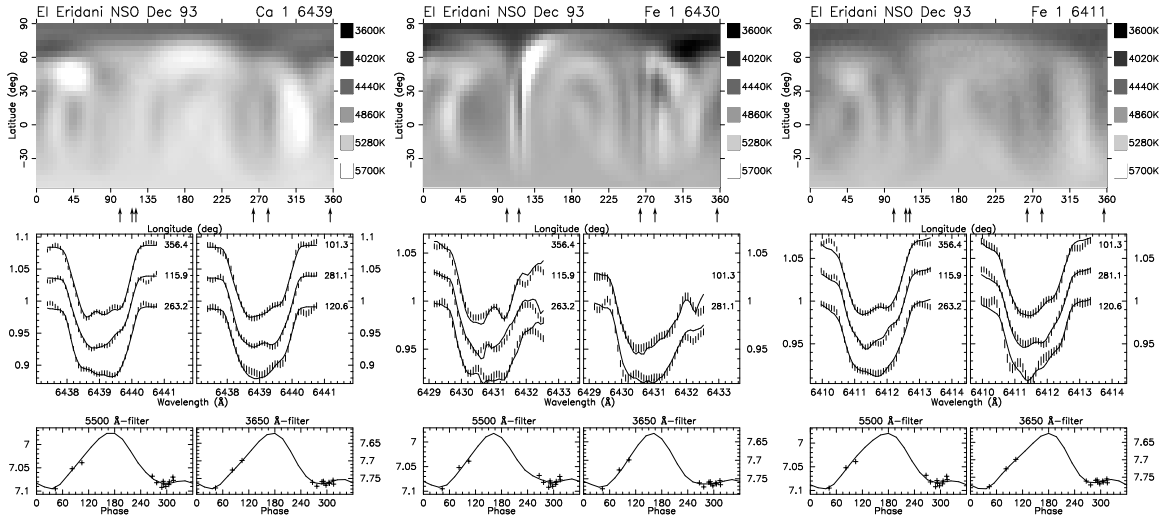

Figure 6.9: NSO nso94:more1: Dec. 1993.

6.1.10 Dec. 1993 ("nso94:more1")

The data were not reduced by the observer except bias combination, bias correction, trimming and oversize correction for the object spectra. This block contains six spectra of EI Eri, one from 11/11/93 and five from 05/12 till 09/12/93.

Trim data section was set by hand for each night indivudually by the observer and varied between [3:11,1:800] and [6:13,1:800]. All nights contain one observation of the RVSS 59 Ari. All but the last night (09/12/93, which provides only one comparison exposure) include two comparison-lamp integrations. The average dispersion is 0.09627 ± 0.00013 [0.09603–0.09639] for all 13 object spectra, starting point 6401.05 ± 0.40 [6400.35–6401.66]. Cross-correlation of the RVSS spectra with each other gives deviations of $0.74\,\mathrm{km\,s^{-1}}$ with a maximum of $0.87\,\mathrm{km\,s^{-1}}$. Photometry comprises 13 observations from 03/12 till 11/12/93. Observer was Trudy Tilleman.

6.1.11 Jan. 1994 ("nso94:more2")

The data were not reduced by the observer except bias combination, bias correction, trimming and oversize correction for the object spectra. This block contains six spectra of EI Eri observed during three nights from 30/01 till 01/02/94. All nights contain one observation of the RVSS 59 Ari and two comparison-lamp integrations. The average dispersion is 0.09629 ± 0.00016 [0.09601–0.09644] for all nine object spectra (six EI Eri and three RVSS), starting point 6401.87 ± 0.46 [6401.33–6402.40]. Cross-correlation of the three RVSS spectra with each other gives a mean deviation of $0.31\,\mathrm{km\,s^{-1}}$ with a maximum of $0.36\,\mathrm{km\,s^{-1}}$. Observer was Trudy Tilleman. The spectra of this block were not used for Doppler imaging due to the large phase gaps.

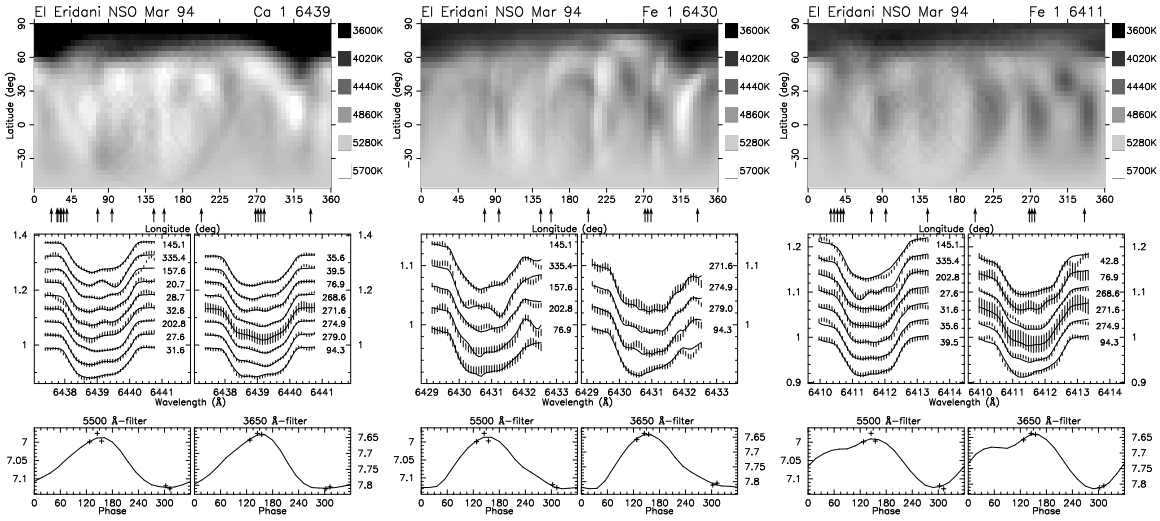

Figure 6.10: NSO nso94:more3: Mar. 1994.

6.1.12 Mar. 1994 ("nso94:more3")

The data were not reduced by the observer except bias combination, bias correction, trimming and oversize correction for all spectra. This block contains 21 spectra of EI Eri from eleven nights spread out from 05/03/94 till 01/04/94. Each night is equiped with one integration of the RVSS 59 Ari and ThNe comparison exposures. The average dispersion is 0.09630 ± 0.00007 [0.096175–0.096470] for all 33 object spectra (12 spectra of 59 Ari and 21 of EI Eri), starting point is 6401.46 ± 0.53 [6400.25–6402.33]. Cross-correlation of the RVSS spectra with each other gives deviations of $0.32\,\mathrm{km\,s^{-1}}$ with a maximum of $0.64\,\mathrm{km\,s^{-1}}$. Only five photometric observations are available, spanning 28/02/94 – 07/03/94. Observer was Trudy Tilleman. The λ6430 line is of very poor quality. Several spectra had to be expelled. Nevertheless, the shape of the polar cap resembles the λ6439 polar cap.

6.1.13 Oct. 1994 ("nso95:94oct")

The data were not reduced by the observer except bias combination, bias correction, trimming and oversize correction for all spectra. This block contains 16 spectra of EI Eri observed during seven nights from 18/10/94 till 31/10/94. Each night is equiped with at least two comparison-lamp exposures, embracing the object spectra, and one integration of the RVSS 59 Ari. Average dispersion is 0.09518 ± 0.00039 [0.09468–0.09609] for all 23 object spectra (7 spectra of 59 Ari and 16 of EI Eri), starting point is 6401.58 ± 0.60 [6400.41–6402.45]. Cross-correlation of the seven RVSS spectra with each other gives deviations of $1.57\,\mathrm{km\,s^{-1}}$ with a maximum of $1.89\,\mathrm{km\,s^{-1}}$. Only three photometric observations are available, on 18/10/94, 28/10/94 and 29/10/94. Observer was Trudy Tilleman.

6.1.14 Dec. 1994 ("nso95:94dec")

The data were not reduced by the observer except bias combination, bias correction, trimming and oversize correction for all spectra. This block contains 21 spectra of EI Eri observed during ten nights from 17/12/94 till 03/01/95. Each night contains at least two comparison-lamp exposures, at the beginning and end of the observing block, and one integration of the RVSS 59 Ari. Average dispersion is 0.09527 ± 0.00039 [0.09459–0.096125] for all 33 object spectra (12 spectra of 59 Ari and 21 of EI Eri), average starting point is 6401.33 ± 0.70 [6400.06–6402.19]. Cross-correlation of the 12 RVSS spectra with each other gives deviations of $0.74\,\mathrm{km\,s^{-1}}$ with a maximum of $1.54\,\mathrm{km\,s^{-1}}$. No photometric observations are available during the time of the spectroscopic observations (17/12/94–03/01/95), but four measurements were taken prior to the

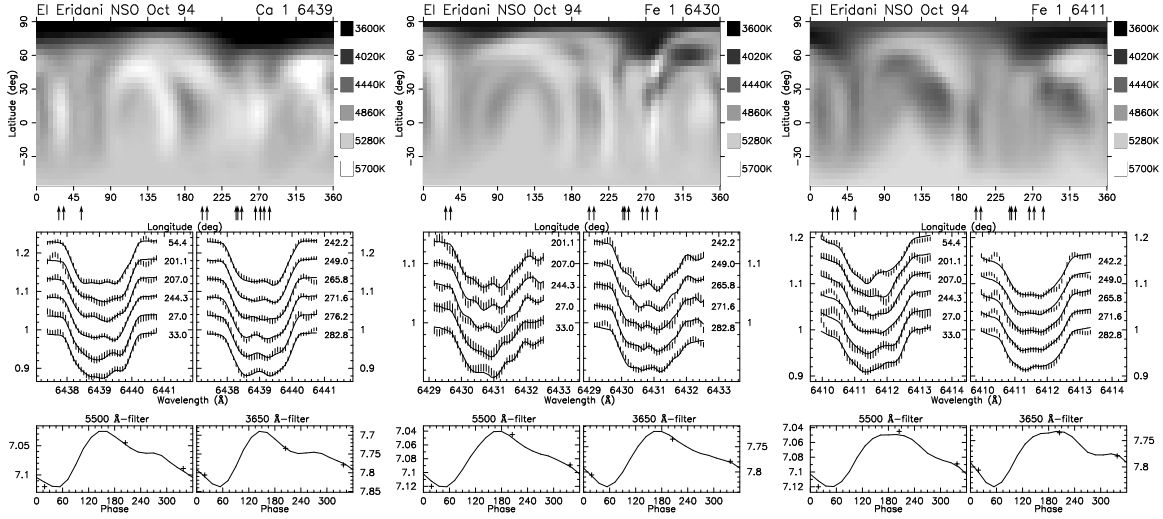

Figure 6.11: NSO nso95:94oct: Oct. 1994.

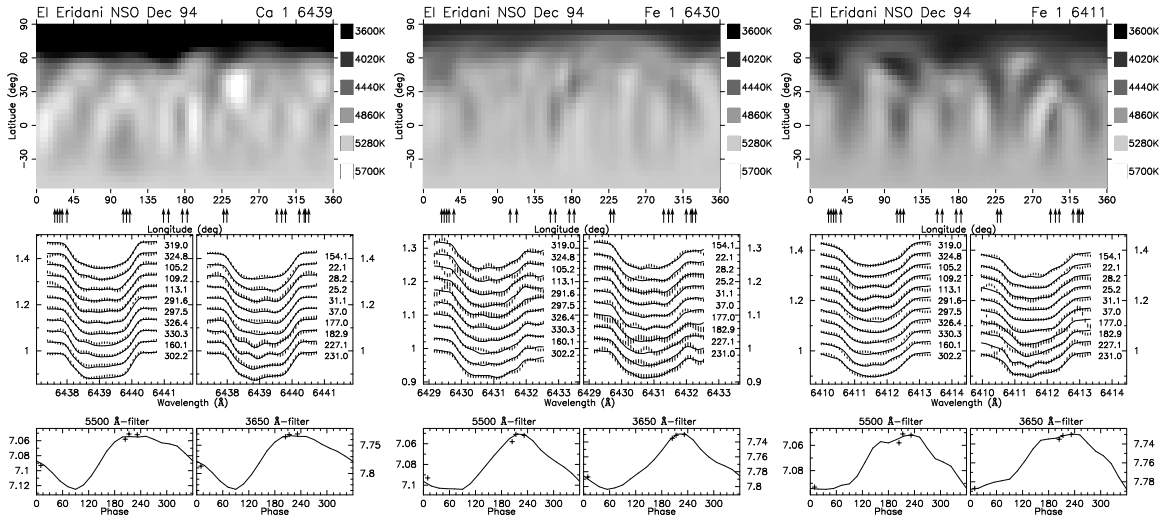

Figure 6.12: NSO nso95:94dec: Dec. 1994.

spectroscopic observations: one each on 07/12, 08/12, 13/12 and 15/12/94. Observer was Trudy Tilleman.

6.1.15 Feb. 1995 ("nso95:95feb")

The data were not reduced by the observer except bias combination, bias correction, trimming and oversize correction for all spectra. The dispersion axis runs along lines now. Bad pixel correction had to be applied for columns 277–278, 483–485 and 623–638 according to 6426.67–6426.79, 6449.58–6449.80 and 6465.14–6466.81 Å; no intensity information is available for those wavelengths; the respective values were linearly interpolated. This block contains five spectra of EI Eri observed during two nights (17/02/95 and 20/02/95). Each night contains two comparison-lamp exposures (at the beginning and end of the observing block) and one integration of the RVSS 59 Ari. Average dispersion is 0.11117±0.00031 [0.11092–0.11151] for all 7 object spectra (2 spectra of 59 Ari and 5 of EI Eri), average starting point is 6395.88 ± 1.04 [6394.77–6396.72]. Cross-correlation of the two RVSS spectra with each other gives a deviation of 1.77 km s^{-1}. Observer was Trudy Tilleman. These spectra were not used for Doppler imaging (not enough spectra; huge phase gaps).

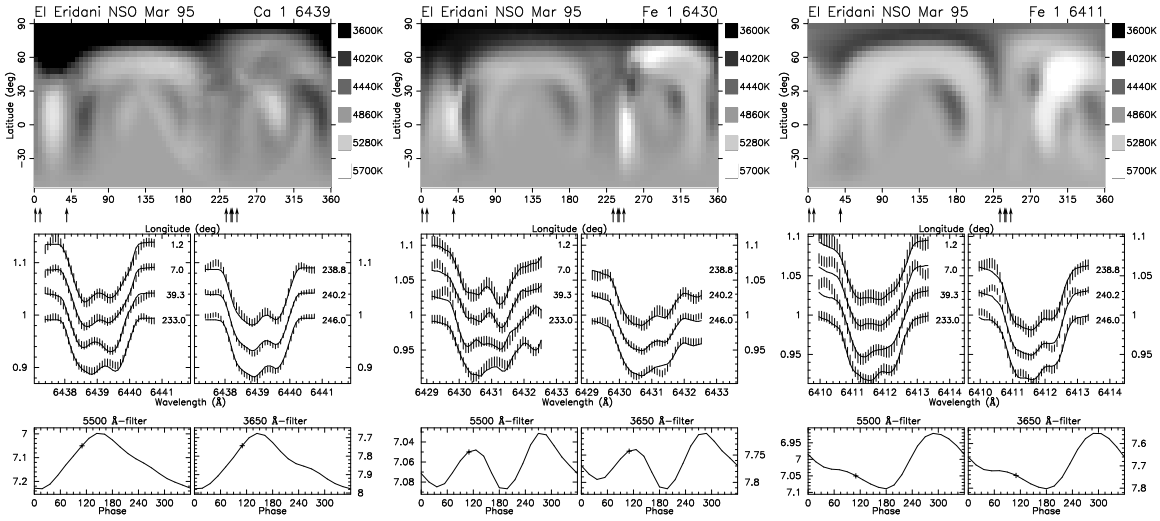

Figure 6.13: NSO nso95:95mar: March 1995.

6.1.16 Mar. 1995 ("nso95:95mar")

The data were not reduced by the observer except bias combination, bias correction, trimming and oversize correction for all spectra. Again, the dispersion axis runs along lines. Bad pixel correction had to be applied for columns 277–278, 483–485 and 623–638 corresponding to 6425.19–6425.30, 6448.36–6448.58 and 6464.11–6465.79 Å; no intensity information is available for those wavelengths; the respective values were linearly interpolated. This block contains 12 spectra of EI Eri observed during seven nights from 28/02/95 till 28/03/95. Each night contains at least two comparison-lamp exposures, at the beginning and end of the observing block, and one integration of the RVSS 59 Ari. Average dispersion is 0.11248 ± 0.00071 [0.11192–0.11413] for all 20 object spectra (8 spectra of 59 Ari and 12 of EI Eri), average starting point is 6394.03 ± 0.80 [6392.80–6395.10]. Best FWHM of a ThNe emission line is around 1.25 pixel, typical values are between 1.5 and 1.7. Cross-correlation of the eight RVSS spectra with each other gives deviations of $2.21\,\mathrm{km\,s^{-1}}$ with a maximum of $3.42\,\mathrm{km\,s^{-1}}$. Unfortunately, only one single photometric measurement is available between 2449701 and 2449982, namely on 2449751. Observer was Trudy Tilleman.

$\log gf$ for λ6439 was set to -0.03 in order to avoid huge white spots.

6.1.17 Oct. 1995 ("nso95:95oct")

The data were not reduced by the observer except bias combination, bias correction, trimming and oversize correction for all spectra. The dispersion axis runs along lines. Bad pixel correction had to be applied for columns 277–278, 483–485 and 623–638 corresponding to 6425.55–6425.67, 6448.37–6448.59 and 6463.87–6465.53 Å; no intensity information is available for those wavelengths; the respective values were linearly interpolated. This block contains three spectra of EI Eri observed during the two nights 01/10/95 and 02/10/95. Each night contains two comparison-lamp exposures, at the beginning and end of the observing block, and one integration of the RVSS 59 Ari. Average dispersion is 0.11074 ± 0.00009 [0.11060–0.11082] for all 5 object spectra (2 spectra of 59 Ari and 3 of EI Eri), average starting point is 6394.88 ± 0.08 [6394.81–6395.01]. Cross-correlation of the two RVSS spectra with each other gives a deviation of $0.3\,\mathrm{km\,s^{-1}}$. Observer was Trudy Tilleman. This block was not used for Doppler imaging.

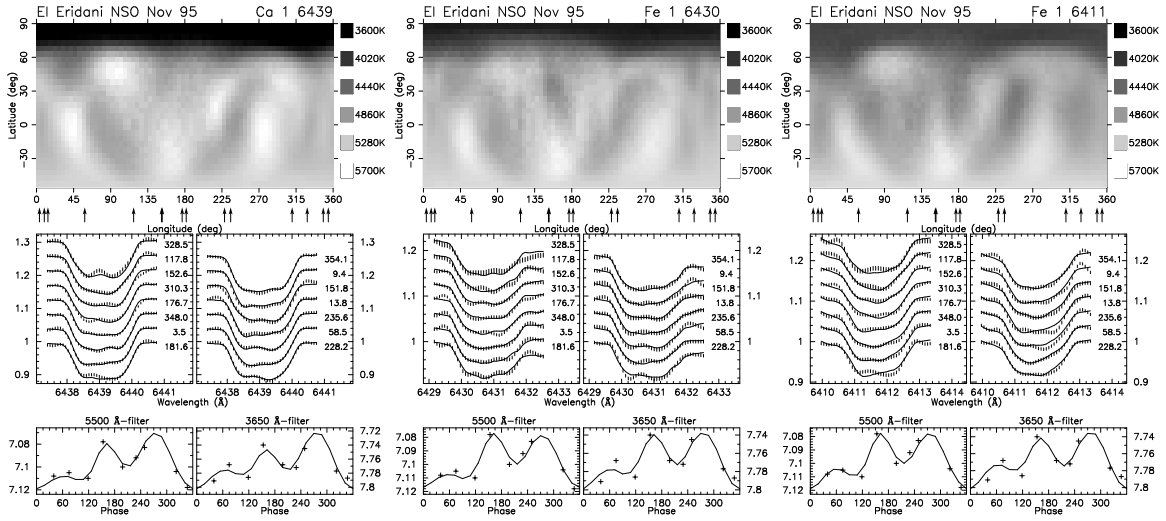

Figure 6.14: NSO nso95:95nov: Nov. 1995.

6.1.18 Nov. 1995 ("nso95:95nov")

The data were not reduced by the observer except bias combination, bias correction, trimming and oversize correction for all spectra. The dispersion axis runs along lines. Bad pixel correction had to be applied for columns 277–278, 483–485 and 623–638 corresponding to 6426.10–6426.21, 6448.88–6449.10 and 6464.36–6466.02 Å; no intensity information is available for those wavelengths; the respective values were linearly interpolated. This block contains 15 spectra of EI Eri observed during 13 nights from 07/11/95 till 02/12/95. Each night contains two comparison-lamp exposures, at the beginning and end of the observing block, and one integration of the RVSS 59 Ari. Average dispersion is 0.11060 ± 0.00004 [0.11051–0.11068] for all 28 object spectra (13 spectra of 59 Ari and 15 of EI Eri), average starting point is 6395.46 ± 0.74 [6394.30–6396.53]. Cross-correlation of the eight RVSS spectra with each other gives an average deviation of $1.85\,\mathrm{km\,s^{-1}}$ with a maximum of $3.26\,\mathrm{km\,s^{-1}}$. Nine photometric measurements are available from 2450025.95 till 2450056.87. Observer was Trudy Tilleman.

6.1.19 Dec. 1995 ("nso95:95dec")

The data were not reduced by the observer except bias combination, bias correction, trimming and oversize correction for all spectra. The dispersion axis runs along lines. Bad pixel correction had to be applied for columns 277–278, 483–485 and 623–638 corresponding to 6426.41–6426.52, 6449.21–6449.43 and 6464.71–6466.37 Å; no intensity information is available for those wavelengths; the respective values were linearly interpolated. This block contains five spectra of EI Eri from five different nights, spanning 12/12/95 till 28/12/95. Each night contains at least two comparison-lamp exposures, at the beginning and end of the observing block (except 28/12 which contains only one comparison-lamp exposure), and one integration of the RVSS 59 Ari. Average dispersion is 0.11071 ± 0.00016 [0.11058–0.11100] for all ten object spectra (five spectra of 59 Ari and five of EI Eri), average starting point is 6395.74 ± 0.53 [6395.01–6396.30]. Cross-correlation of the five RVSS spectra with each other gives an average deviation of $0.93\,\mathrm{km\,s^{-1}}$ with a maximum of $1.31\,\mathrm{km\,s^{-1}}$. Five photometric measurements are available between 2450055 and 2450078. Observer was Trudy Tilleman.

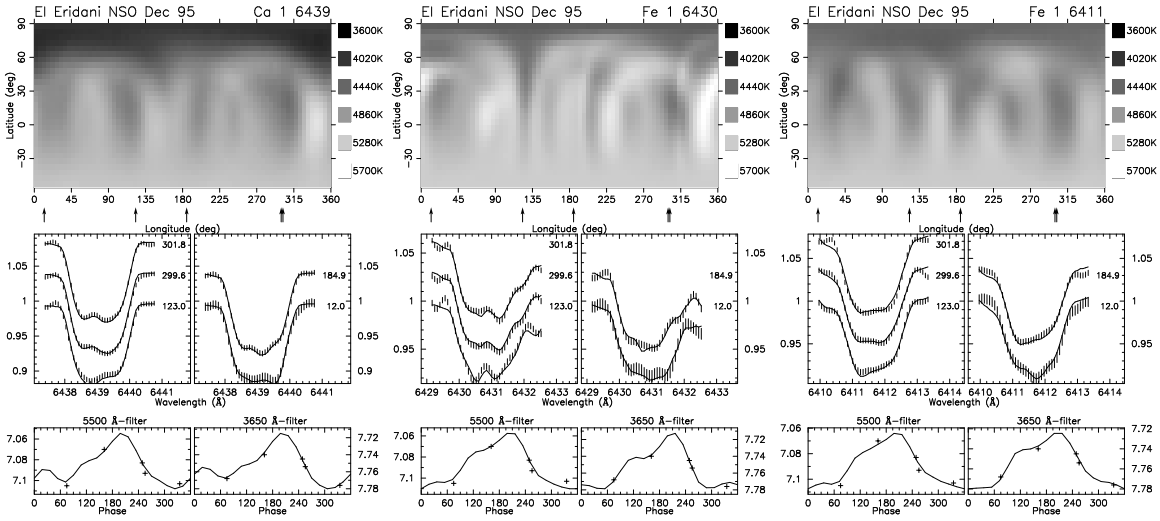

Figure 6.15: NSO nso95:95dec: Dec. 1995.

6.2 NSO visitor observing run

6.2.1 NSO 96 fall

In November/December 1996 we obtained 58 high S/N spectra during 70 nights of observations at the NSO/McMath telescope. This allows us to produce a timeseries of Doppler images. There are three lines of interest on the CCD chip: λ6411, λ6430 and λ6439. The λ6393 line is out of range. The 58 spectra can be split into three blocks of about 19 spectra each. The λ6411 line sits so close to the edge of the CCD chip that continuum fitting is very crucial and was done seperately for the λ6411 and the central (λ6430 and λ6439) region. Otherwise, a plain continuum cannot be achieved with a single fit for the whole spectral range.

Nevertheless, the λ6411 line could not be used for Doppler imaging as its quality is insufficient. Iron 6430 as well is too poor for gaining good-quality Doppler maps, the results are nevertheless shown in Fig. 6.18 but not used for the investigation in §7. However, λ6439 meets our expectations and is shown in Fig. 6.17.

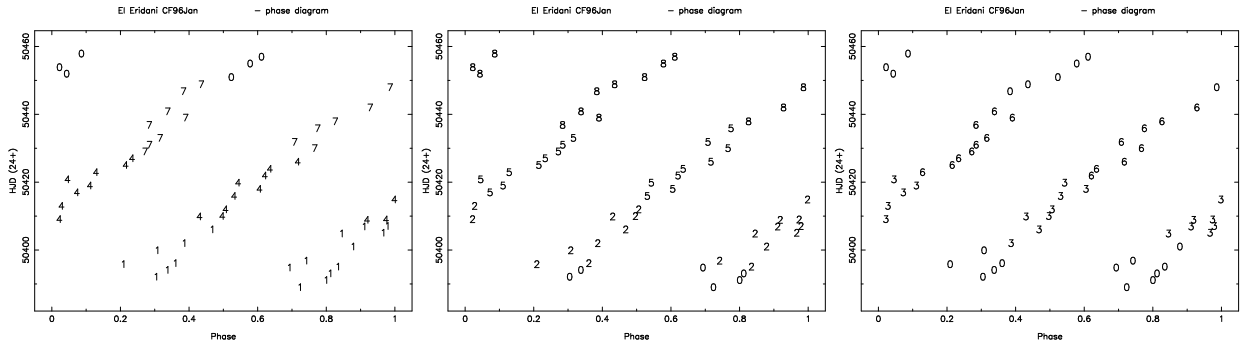

Figure 6.16: **a) − c)** Phase plots for the 1996 fall data (NSO). See text.

Three weeks of data are combined for one Doppler image in order to ensure good phase coverage (see Fig. 6.16a, numbers 1, 4 and 7). This results in three consecutive Doppler images that follow each other without overlap and without time gap between two maps (images a, d and g in Fig. 6.17, the three left ones). Neither the shape of the polar cap nor the number and position of low-latitude features can be reassembled in these three maps. On the other hand, the overall shape of the polar cap and several of the

Table 6.3: Block segmentation of the M96 data for Doppler imaging. The column *Overlap* shows the overlap of spectra of each block with the following one.

Block number	Start – End in HJD	Number of spectra	Overlap	Duration [days]	Duration [$P_{\rm rot}$]
1	2450388.903 – 2450406.925	18	61%	18	9.3
2	2450394.961 – 2450414.751	20	67%	20	10.2
3	2450401.877 – 2450420.685	20	62%	19	9.7
4	2450408.754 – 2450426.893	20	57%	18	9.3
5	2450415.789 – 2450435.736	18	79%	20	10.2
6	2450421.805 – 2450441.876	17	78%	20	10.3
7	2450428.914 – 2450448.706	14	62%	20	10.2
8	2450436.727 – 2450457.762	14	–	21	10.8

low-latitude spots seem to occur likewise in the respective maps of the λ6439 and the low-quality λ6430 reconstruction. Therefore, we can assume these features to be real and not artefacts of the reconstruction which result from low S/N data. This suggests that both the shape of the polar cap and the low-latitude spots are not only real but also vary on timescales much shorter than three weeks. Thus, the spots seen on our maps are averaged features that do not resemble the actual spot distribution on the star.

As a consequence, it was decided to further split the data into altogether eight overlapping blocks with three blocks overlapping each, shifting the starting point of each block by one week (see Table 6.3). Fig.6.16 has the phase plot: The numbers denote the respective block. Time starts at the bottom. Thereby, again three weeks of data are combined for one Doppler image. (Since, the blocks overlap, the phase plots in Fig. 6.16 are shown as three graphs. Block 1 covers the first three weeks, block 2 covers week 2–4 etc.) The results are shown in Fig. 6.17a-h for λ6439 and Fig. 6.18a-h for λ6411. The first image represents week 1 – 3, the second week 2 – 4 and so on. For a few spots (like the spot in map no.6 at 150 degrees longitude and +40 degrees latitude), it seems like we can follow the tracks of spots moving (in this case polewards), i.e. slightly changing its position, from one map to the next one. However, for this kind of investigation (with non time-resolved, overlapping maps), this drift-effect would show up in the same way both for drifting spots as well as spots decaying with a different spot emerging in the vicinity. It therefore cannot be concluded from the M96 images whether spot movements are concerned or not.

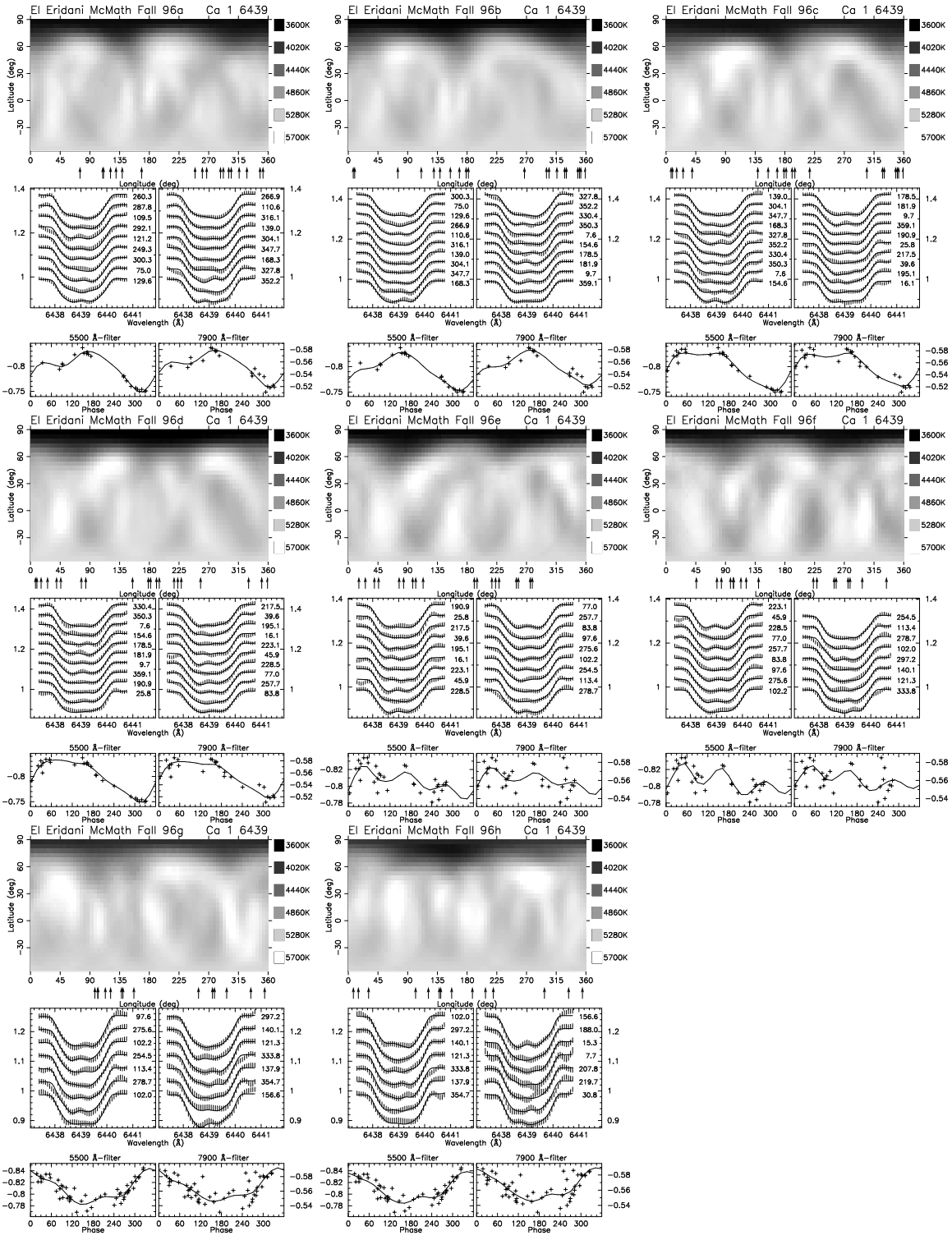

Figure 6.17: **a) - h)** Doppler Images from M96: λ6439 block 1 - 8.

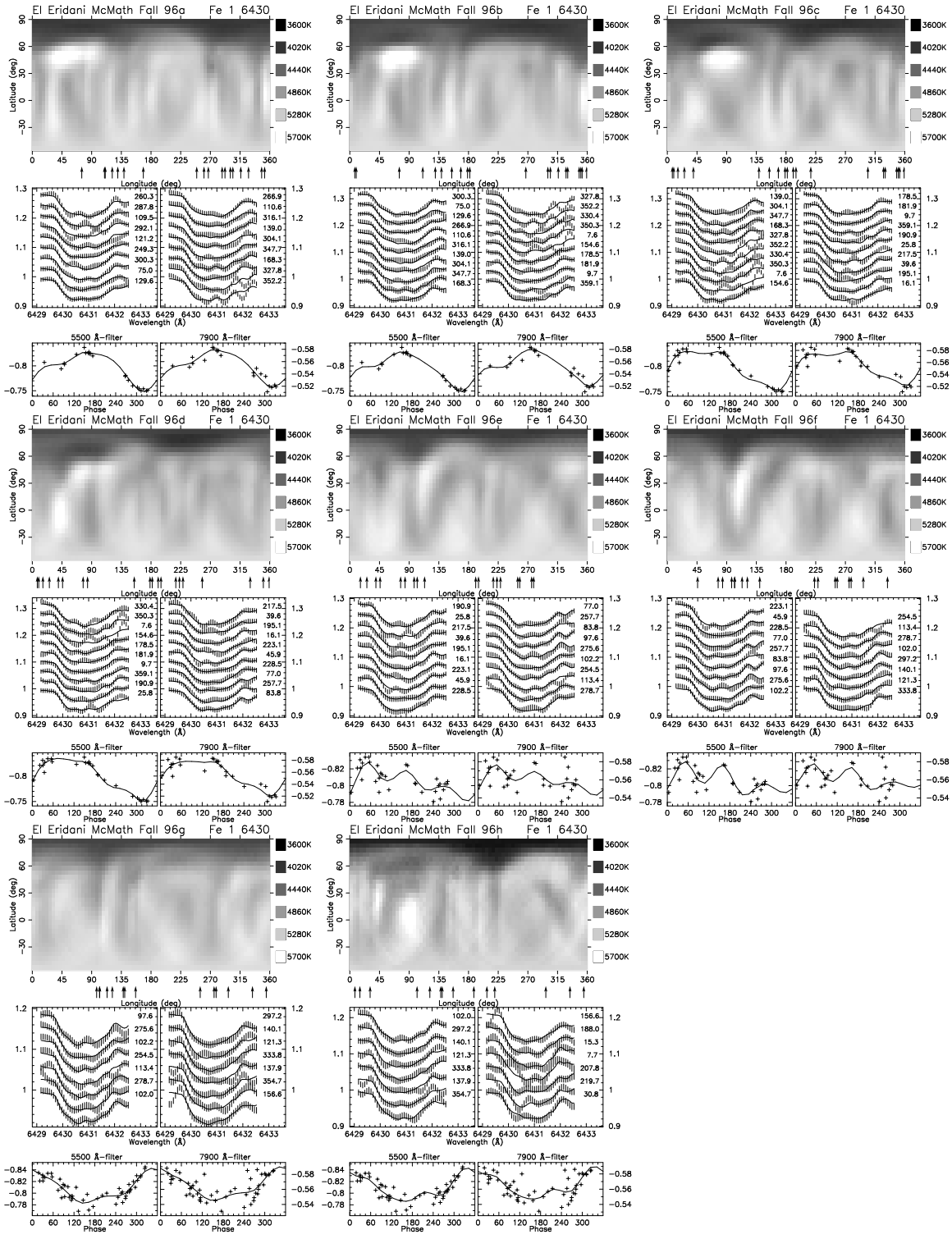

Figure 6.18: **a) - h)** Doppler Images from M96: λ6430 block 1 - 8.

6.3 KPNO visitor observing runs

In 1971, the Kitt Peak 2.1-m telescope coudé spectrograph was redesigned with its own telescopic optical system, making use of the replaced 1.6-m heliostat quartz mirror of the McMath-Pierce telescope. The 1.6m mirror was now used in an altazimuth mounting to feed starlight to a 0.9-m image-forming mirror mounted in a tower just south of the 2.1-m building. This allowed the coudé spectrograph to be operated independently of the main 2.1-m telescope from which was now called the coudé feed telescope. Amazingly enough, the coudé spectrograph in its new stand-alone mode is about as efficient as it was when used with the 2.1-m telescope due to its fewer number of reflections (AURA 1971).

Unfortunately, the coudé feed telescope has been closed to the public as a cost-cutting measure but before provided us with several two- to three-weeks observing runs which were also (but not only) used for observing Phaetons favourite, EI Eridani. Altogether four coudé feed observing runs were undertaken that provided data for this investigation, in March 1994, February 1995, January 1996 and December 1997 / January 1998. Three of them were successfull enough to allow for Doppler imaging.

During the March 1994 run, only three spectra of EI Eri were obtained which is definitely not sufficient for Doppler imaging. The 95 February and the 96 January run each provide one Doppler map, the 97 December run three simultaneous Doppler maps for the same epoch, resulting from three independent data sets taken during the same time period (as opposed to the NSO 96 run which yielded three consecutive Doppler maps for three different epochs). In all cases, the λ6439 Calcium-line turned out to be the most reliable of the four investigated Doppler imaging lines. For the three KPNO runs, the Iron lines λ6393, λ6411 and λ6430 were used as well.

6.3.1 KPNO 95 Feb

During the February 1995 observing run, we obtained no more than five spectra of EI Eridani due to bad weather conditions (see Table A.22). Consequently, the data exhibit huge phase gaps. The Doppler maps nevertheless turn out satisfactory for the λ6393, λ6411 and λ6439 line. The maps corresponding to these lines are quite similar. They all exhibit roundly blurred spots at the latitudes around 130 and 320°, where data gaps occur. This is a typical behaviour resulting from such wide gaps. λ6430 did not give reasonable fits. All four Doppler maps are shown in Fig. 6.19.

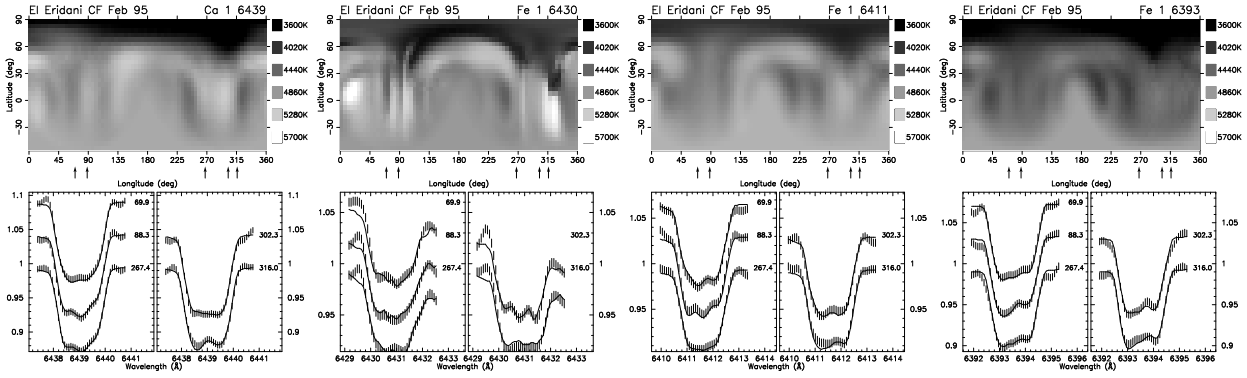

Figure 6.19: Doppler Images from 1995 February.

6.3.2 KPNO 96 Jan

The 24 spectra obtained in January 1996 were used for one single Doppler image with only small phase gaps around 180 and 360° of less then 70° each. The Doppler images are shown in Fig. 6.20. The data were also processed using `DOTS` and compared to the surface maps presented in this section, which were achieved with `TempMap`. See §4.3.2 for details.

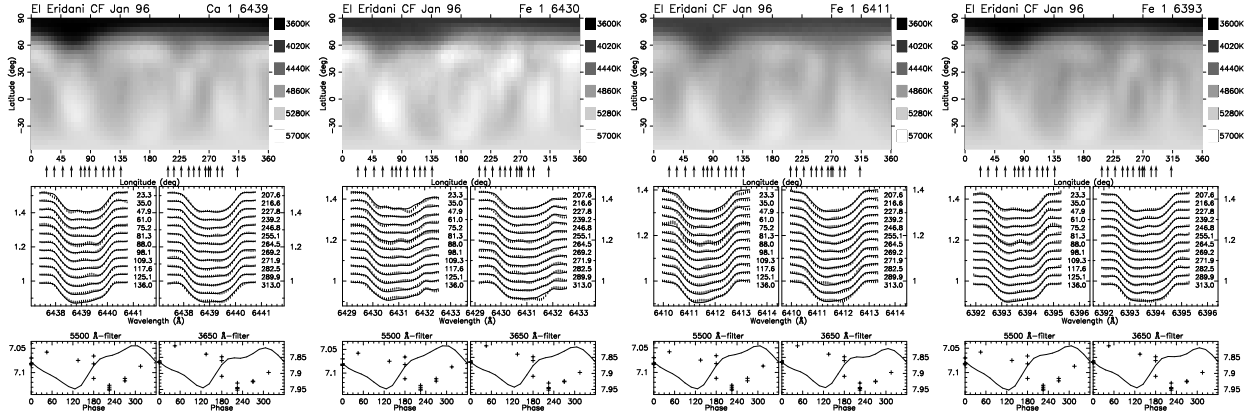

Figure 6.20: Doppler Images from 1996 January.

6.3.3 KPNO 97 Dec

About 20 spectra, evenly spread over the rotational period, are sufficient for a good-quality Doppler image. As we have 57 spectra from the 97 December run within a period of 19.3 days, I decided to split the data into three blocks in such a way that I optimised the splitting process for achieving a most uniform phase distribution of spectra over the rotational period for each block. The resulting phase plots are shown in Fig. 6.21, the corresponding Doppler images in Fig. 6.22-6.24. Table A.24 shows the observing log with the appropriate block numbers.

Most surface structures, high-latitude as well as low-latitude spots, are seen in a very similar configuration in the three independent maps (block 1 – 3), thereby confirming the quality of our Doppler images.

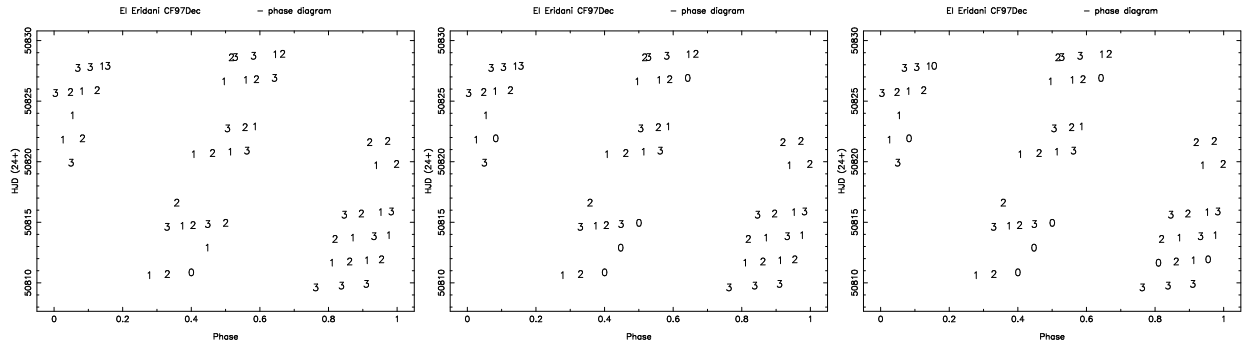

Figure 6.21: Phase plot for the CF 97 Dec data: λ6439 and λ6430 (left), λ6411 (middle) and λ6393 (right). The data were split into three different blocks (number 1–3; 0 refers to expelled spectra).

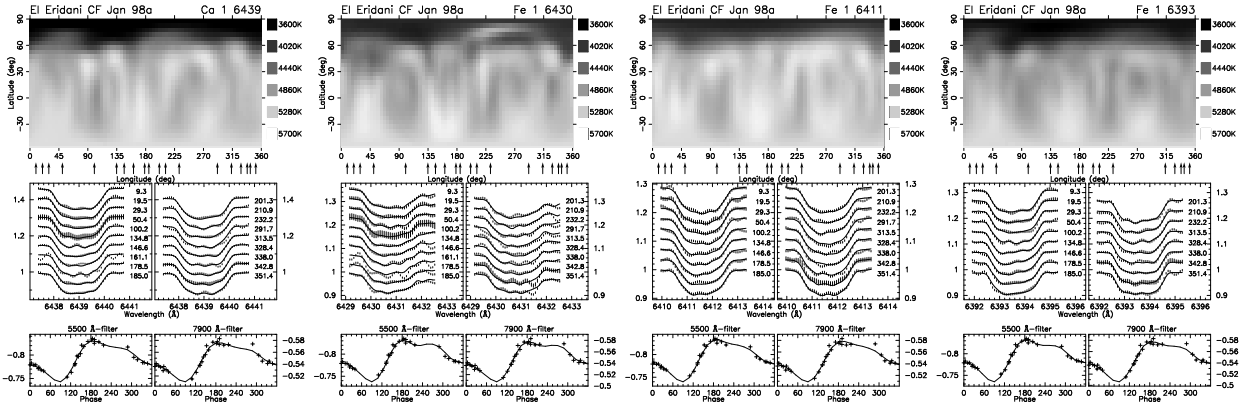

Figure 6.22: Doppler Images from 1997 December – Block 1

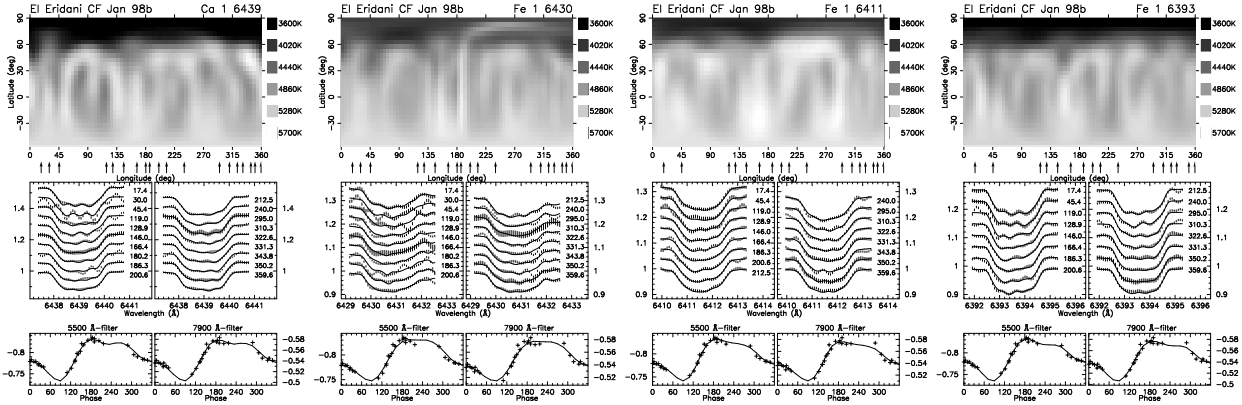

Figure 6.23: Doppler Images from 1997 December – Block 2

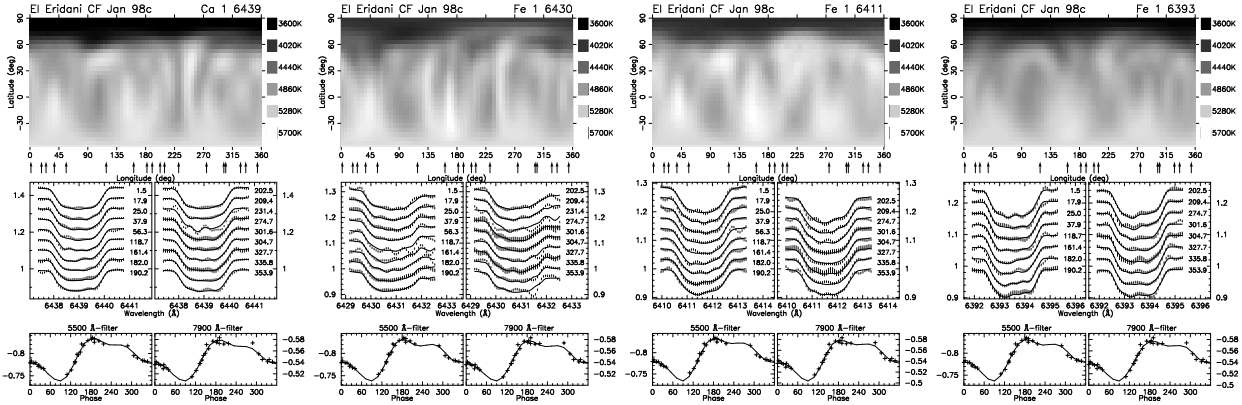

Figure 6.24: Doppler Images from 1997 December – Block 3

Chapter 7

Analysis of Doppler maps and conclusion

"Is it even so? Then I defy you, stars!"

Shakespeare, Romeo & Juliet

"Ah, God! how long is art! And soon it is we die."

Goethe, Faust, Night

For this investigation, data of EI Eridani were collected which span altogether about 20 years. Photometric observations were supplied by the Vienna twin-APTs and several preceding studies. Spectra from the NSO synoptic night-time program as well as spectra observed by myself and co-investigators at KPNO with the Coudé feed telescope, at NSO with the McMath-Pierce telescope and from the MUSICOS 98 campaign were gathered (see §2) and turned into a series of Doppler images spanning 11 years and comprising of about 100 surface maps (34 in λ6439, 30 in λ6430 and 25 in λ6411 and a few in λ6393) for up to 27 independent epochs (see §6 and §5). Mean distance between two independent maps is 141 days, minimum and maximum distance is 3 and 382 days. For tests and parameter evaluations, an estimated total number in the order of 10 000 maps were calculated, using up to 60 computers with 70 CPUs simultaneously, requiring a total computation time in the order of 100 days. Two different versions of the Doppler imaging code were applied (§4). A detailed differential-rotation study with the MUSICOS data was accomplished thereafter (§5). Incipiently, an extensive parameter study of the binary system was attained (§3). All final Doppler images are listed again in a comprehensive form on the following pages. They are followed by a detailed analysis of all maps and resolved by a discussion and summary section.

7.1 A thousand Doppler maps

Now what are we going to do with a thousand Doppler maps from a specific star? How are we to compare those results? Is it true, to speak with Goethe, that "one should not covet the stars, one should merely rejoice in their splendor", or can we make up means of quantitatively analysing our surface imagery? These questions are the matter of the current and final chapter, and they are also well-known to, e.g., Korhonen et al. (2004, FK Com, 24 maps from 1993 to 2003), Vogt et al. (1999a, HR 1099 = V711 Tau, 23 maps from 1981 to 1992), Berdyugina et al. (1998, II Peg, 9 maps from 1992 to 1996; and 2001, LQ Hya, 9 maps from 1993 to 1999), Oláh et al. (2002b, UZ Lib, 8 maps from 1994 to 2000) and others. Thereby, the problem arises of how to parameterise the information content of a Doppler image such that images from different epochs, different stars and desirably also from different Doppler-imaging codes can be compared with each other as well as with model predictions. This can also help to reveal small-scale variations on longer time-

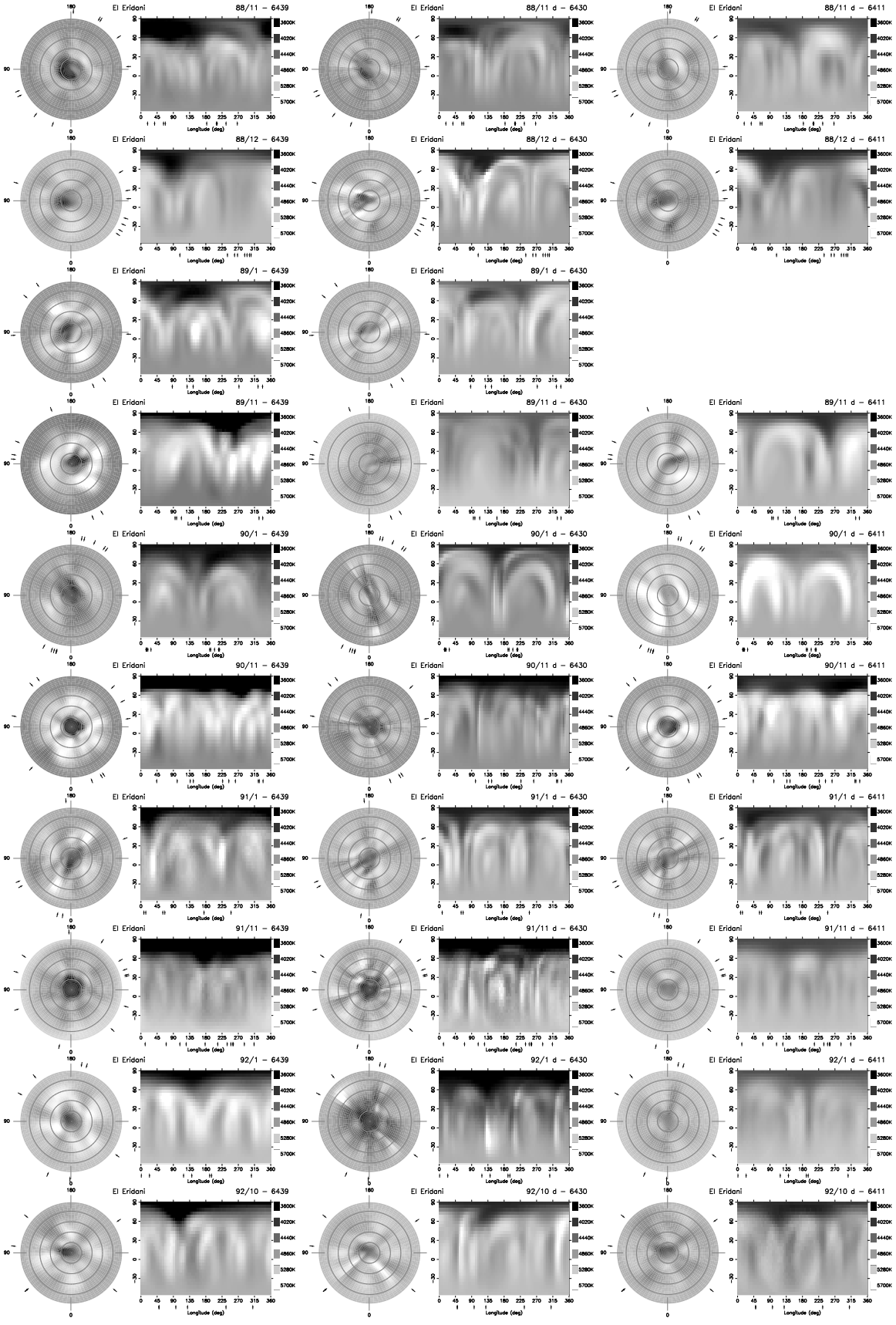

Figure 7.1: Comparison of all Doppler maps: Ca 6439, Fe 6430, Fe 6411

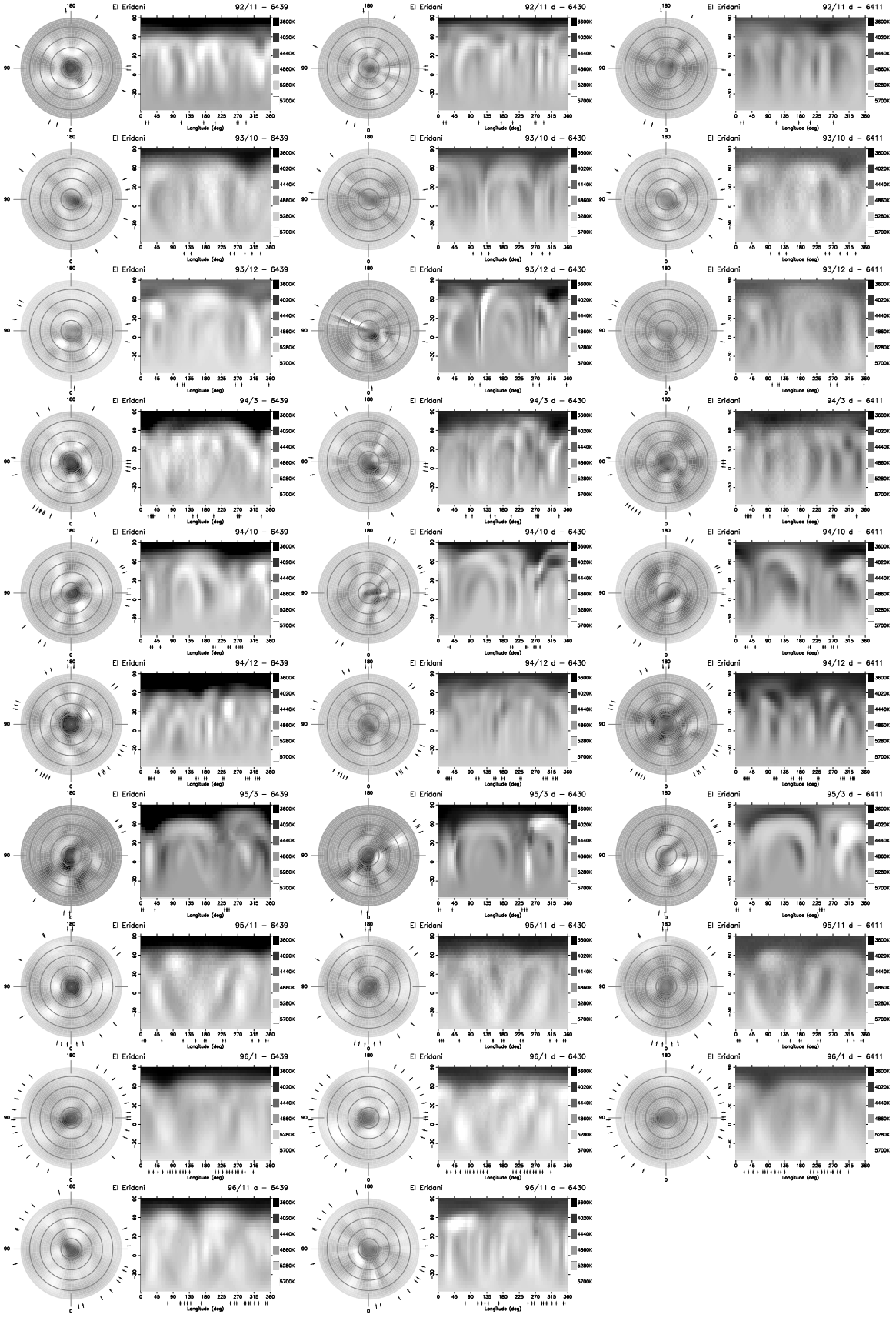

Figure 7.1: Comparison of all Doppler maps: Ca 6439, Fe 6430, Fe 6411 (continued)

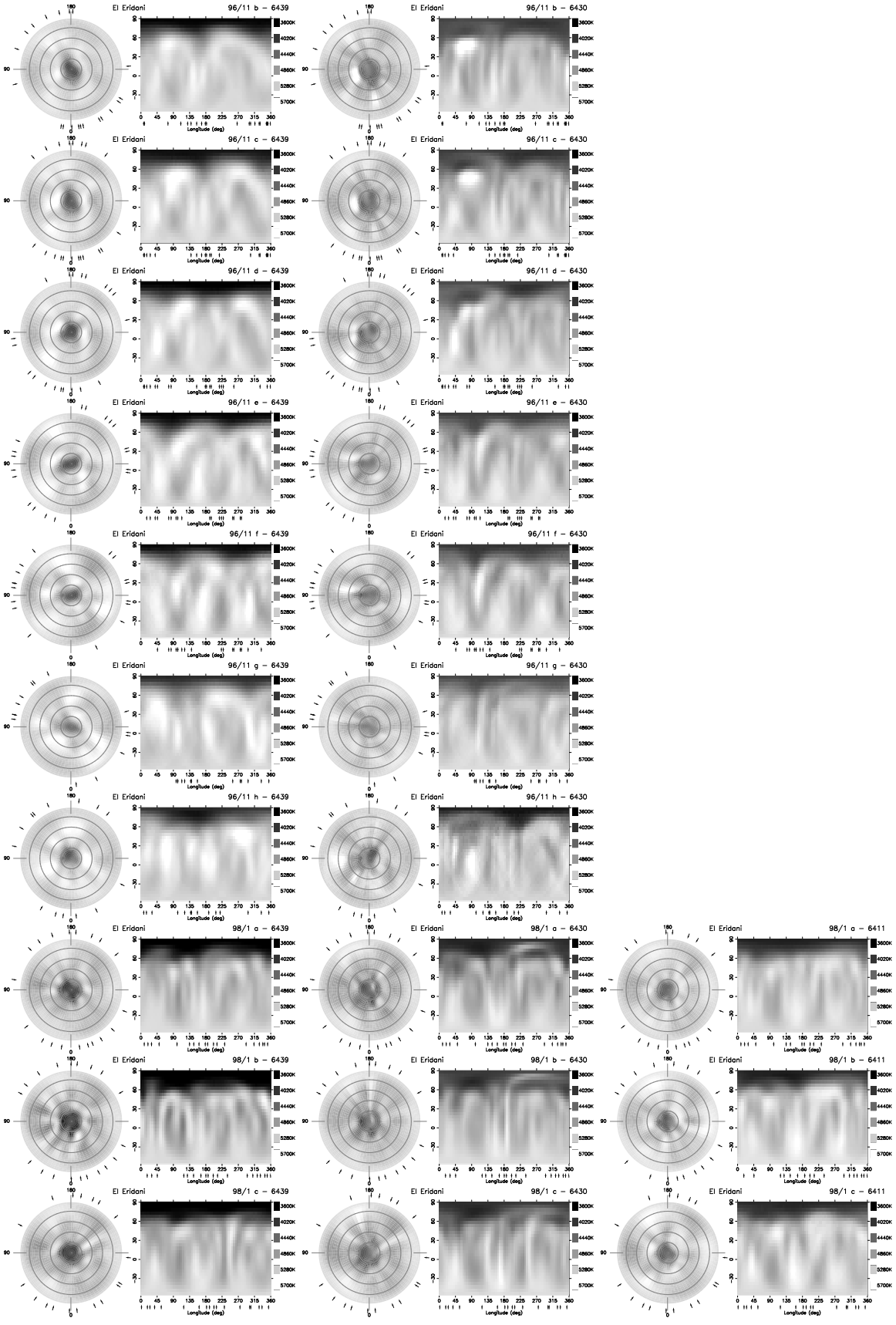

Figure 7.1: Comparison of all Doppler maps: Ca 6439, Fe 6430, Fe 6411 (continued)

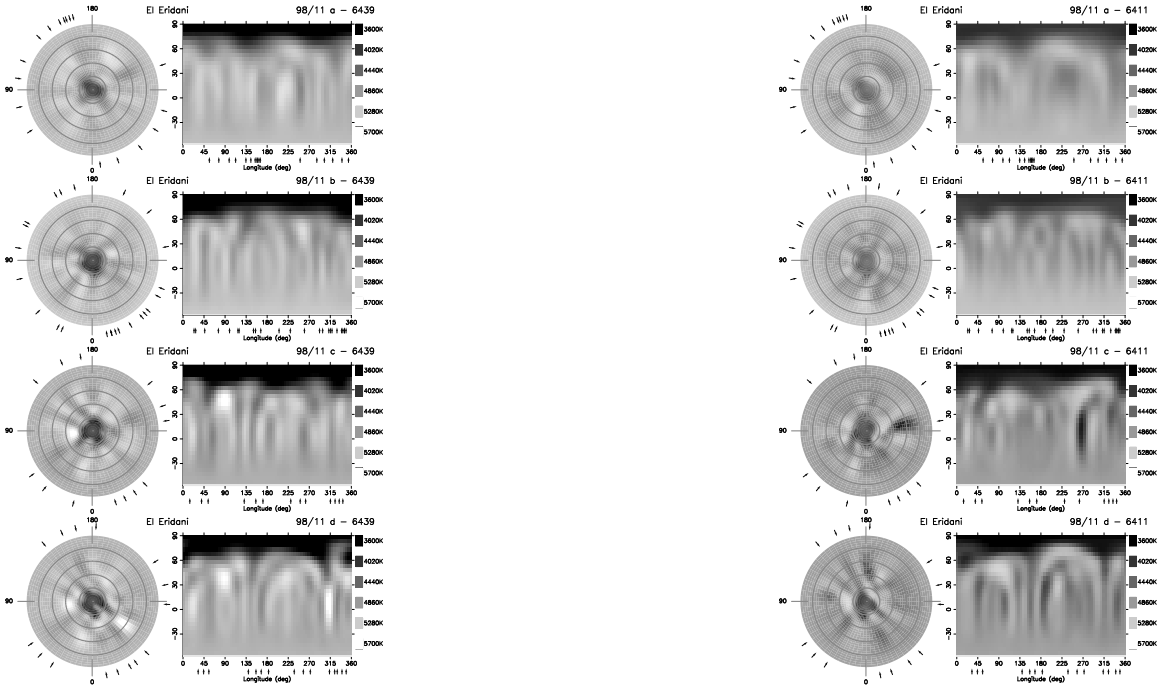

Figure 7.1: Comparison of all Doppler maps: Ca 6439, Fe 6430, Fe 6411 (continued)

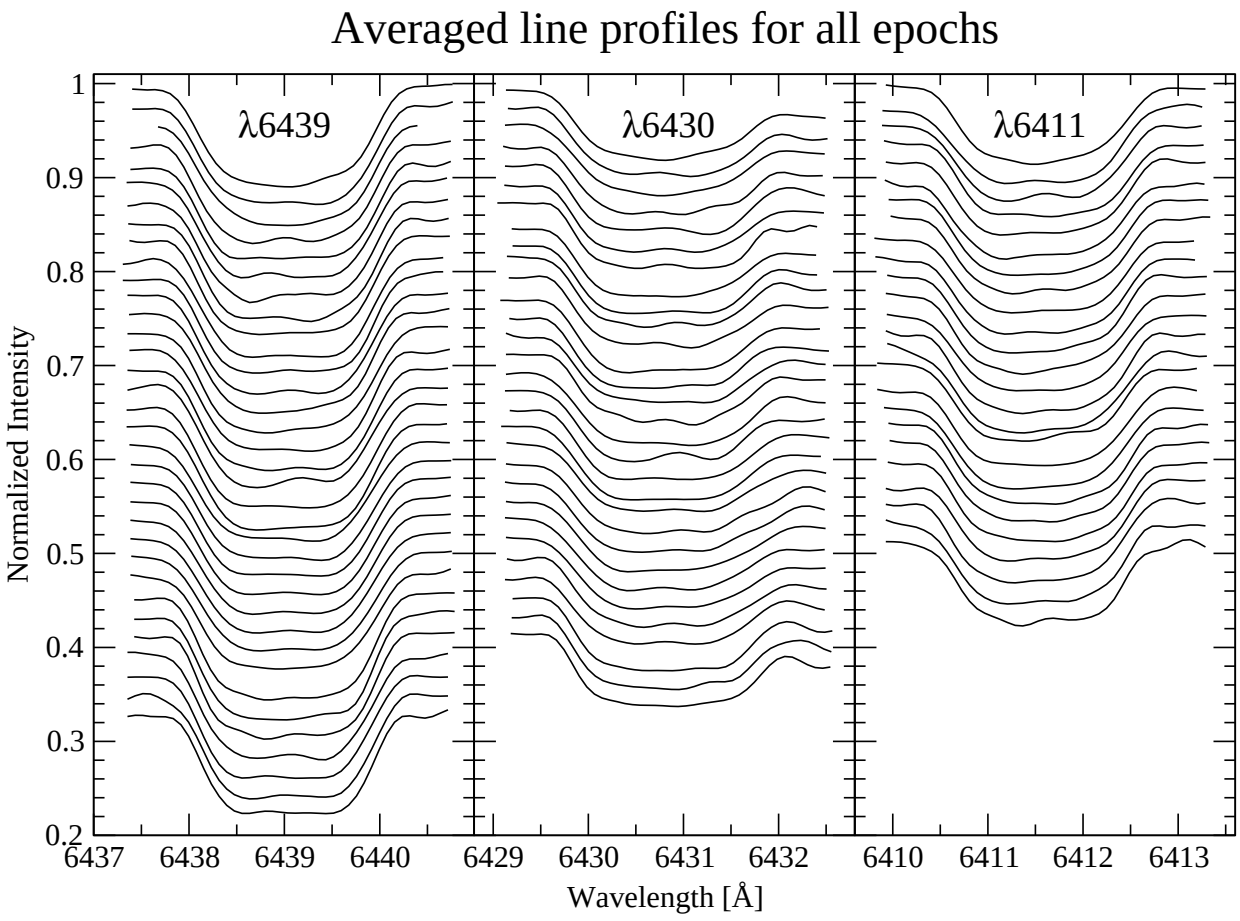

Figure 7.2: Averaged line profiles for all epochs. Each spectrum is shifted by -0.02 in intensity for better viewing. The averaged profiles are in the same order as the maps in Fig. 7.1, earliest epochs are on top (starting with 88/11).

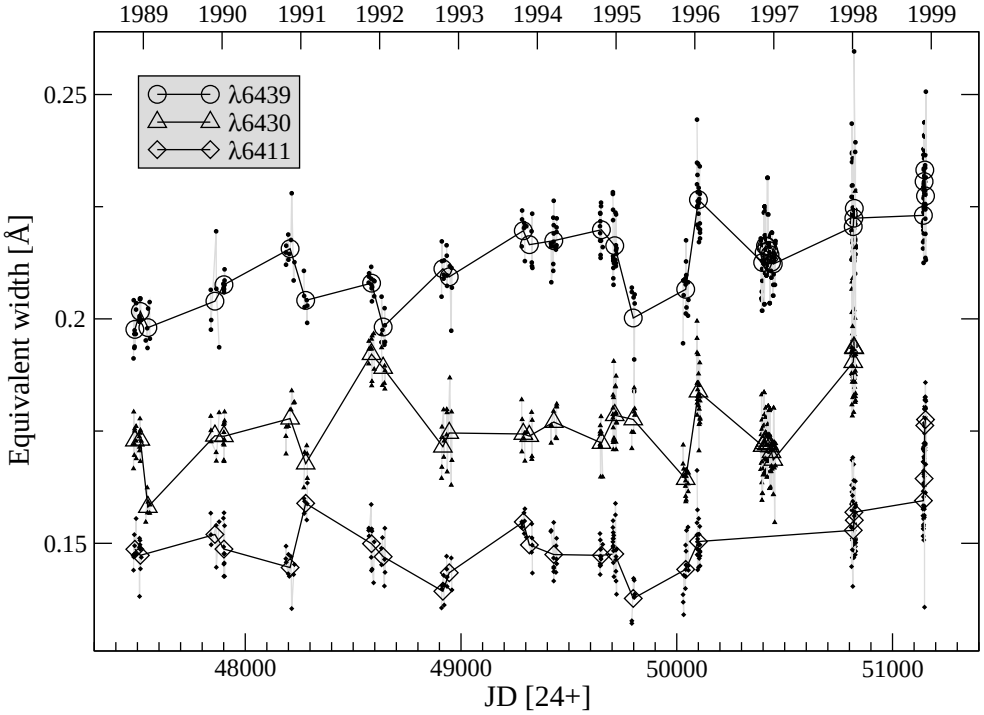

Figure 7.3: Equivalent widths for all epochs. The large open symbols are the mean values for the appropriate epochs/Doppler maps, the small symbols denote the individual spectra. The individual values of each block are connected by grey lines.

scales like a complete activity cycle – which might be hard to detect from a purely visual inspection of a large number of Doppler images.

The preceding pages list all achieved Doppler maps for comparison, one row per epoch, each displaying Ca I 6439, Fe I 6430 and Fe I 6411. Each map consists of a pole-on view (on the left side, with dark, solid circles drawn at equally spaced intervals of 30° down to a latitude of -30°) and a pseudo-Mercator projection (right side, from latitude -56° to +90°. The respective line profiles and fits and the corresponding light curves can be found in §5 and §6 where all maps are described in more details. The phases of the observations are marked by arrows around/below the maps. All maps are plotted with the same temperature scale ranging from 3600 to 5700 K.

For 89Jan and M96, no λ6411 maps are available; for 98Nov, λ6430 is missing. See chapters 5 and 6 for details on the individual Doppler maps. Note that the 96/11 maps overlap. Several surface maps exhibit large phase gaps and have to be considered with scepticism (see §4.2.5). Often, they exhibit spots that are elongated in latitude. In the pole-on plots, they seem to extend radially from the pole, sometimes accompanied by likewise elongated bright spots. See for example 91/1 λ6430/6411 or 93/12 λ6430. This is caused by the minor latitudinal resolution as compared to the longitudinal resolution.

All epochs exhibit a polar cap. In a few cases, the polar cap seems to be less distinct (i.e. higher temperature). However, this phenomenon is never resembled in all three spectral lines; see 90/1 in λ6411 or 93/10 in λ6430 and λ6411. Epoch 93/12 is the only case where the λ6439 map seems to decrease which is resembled in λ6411 but not in λ6430. However, the maps of this epoch exhibit a particularly poor phase coverage. As demonstrated in §4.2.5, large phase gaps can mock an increase in spot temperature. Therefore, this incident is neglected.

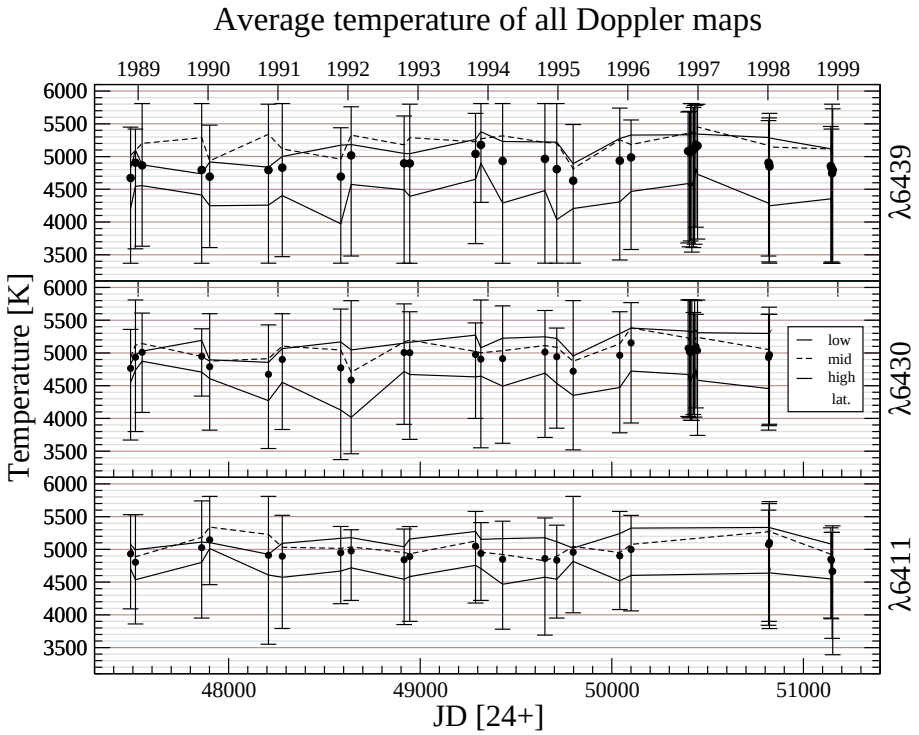

Figure 7.4: Temperature changes of all Doppler maps. Filled circles give the overall average of the respective map, bars denote the minimum and maximum temperature. The upper solid lines are the low-latitude averages (-55° – 0°), the dotted lines the mid-latitude averages (0° – 45°), and the lower solid lines the high-latitude averages (45° – 90°).

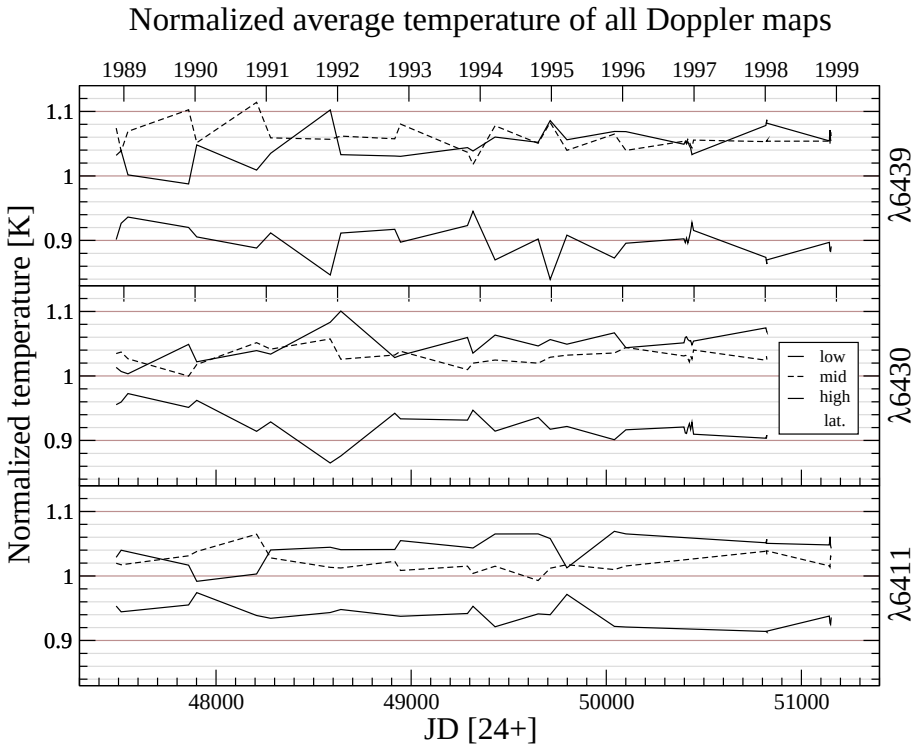

Figure 7.5: Temperature changes of all Doppler maps, normalised by average temperature. The lines denote the low-, mid- and high-latitude average.

7.2 Analysis and parameterisation of the Doppler maps

Apart from tagging preferred spot locations, simple visual inspection of the Doppler maps does not give further insights. Thus, we extract several parameters from the Doppler maps and carry out statistical evaluations to see if we can find any trends in the temperature distribution or even correlations with the proposed activity cycle (as displayed in Fig. 1.7 on page 8 and in Fig. 7.8).[1] Fig. 7.4 shows the progression of the average temperature for all Doppler maps (from 1989 till 1999), separated for each mapping line[2]: The filled circles are the overall temperature averages of the corresponding Doppler maps, the bars in the axis of ordinates denote the minimum and maximum temperature, the respective upper solid line is the temperature average of the low-latitude band, the dotted line of the mid-latitude band and the the lower solid line of the high-latitude band. The low/mid/high-latitude bands run from $-55°$ (smaller latitudes are not seen as they are tilted out of sight due to the stellar inclination) till 0°, from 0° till 45°, and from 45° till 90°. Variations are noticed but not resembled in all spectral lines. In particular, there seems to be a spot maximum (corresponding to a minimum in temperature) in the high-latitude band in 1992 and around 1995, seen in λ6439 and λ6430. Overall, no pronounced correlation with the photometric cycle (Fig. 7.8) is evident. Misfits in the line-profiles can lead to arbitrary variations in the overall temperature (e.g. caused by artificial hot spots). In order to account for possible misfits, the latitude-dependent temperature averages were normalised by the respective total average temperature. The results are shown in Fig. 7.5, again separated for each mapping line. More clearly, we now perceive the temperature decrease in high latitudes in 1992 (in the λ6439 and λ6430 line) which corresponds to an increase in the low-latitude band. As seen in Fig. 7.8 and, more clearly, in Fig. 1.7 (p. 8), in 1992 (JD 48700), EI Eri reached its photometric maximum. The normalised temperature distribution shows a similar but minor decrease/increase in the high/low-latitude band in 1995, three years later, but now only in the λ6439 line. Note that the photometric long-term observations of EI Eri yield a short-term period of 2.4 years beside the 12.2 years cycle (Fig. 1.7 middle panel). In 1998, a minor decrease/increase can be spotted in the λ6439 line.

Let us now inspect the star's spottedness as a function of time. For this purpose, we define a temperature threshold value and count the number of pixels on the star's surface with temperatures below this threshold and relate it to the total number of surface pixels in order to achieve percent values. Several options for defining a threshold are presented in Fig. 7.7 which displays three examples of temperature distributions of a single Doppler map (for the λ6439 line). First, the overall temperature average is established (which usually sits at the lower edge of the photospheric temperature domain). Its location is, however, so edged that, as a second threshold option, a reduction of the temperature average by a fixed value of 300 K seems advisable. Alternatively, we use the minimum value, increased by 500 K and an arbitrarily fixed value of 4000 K as threshold temperature. All temperature values smaller than the respective threshold temperature provide us with a fraction value which is translated to spottedness in percent. The results are shown in Fig. 7.6. Additionally, the average temperature distribution, divided by 100, is shown as grey line/circles. The average-temperature threshold is, as presumed, too close to the photospheric-temperature bulge and sometimes exhibits large increases (around 1990 which is not seen in any of the other curves), induced by photospheric values. In turn, the arbitrary value does not account for higher spot temperatures as occurring in the λ6411 map (it could be raised, though). The minimum temperature, increased by a specific value, seems to be valuable but sometimes exhibits large deviations which are not resembled in any of the other mapping lines. Overall, we conclude that the average temperature, decreased by a specific value (in this case 300 K, so that the threshold lies well between the photospheric- and the spot-temperature bulge), gives best results. Concentrating on the lower solid line with filled circles, we notice an increase in spottedness in 1992 in the λ6439 and, more distinctly, in the λ6430 map and another small increase in 1995, mainly in the λ6439 map. Compare these results with spot-filling factors derived from TiO band modelling: Solanki & Unruh (2004) list filling factors of EI Eri (as obtained from O'Neal et al. 1998) for the epochs 1992Mar (total 25% / minimum 11%), 1995Jan (13%/5%) and 1995Dec (13%/5%). These values coincide with the increase seen in λ6430 in 1992Jan as compared to 1995Jan/Dec but not to the same extent. However, this relation is not seen at all in λ6439 and λ6411. — Overall, no long-term trend is evident, above all no

[1] Analysis of Doppler maps and parameter extraction was carried out with the program `tempanal`, see http://www.aip.de/∼wasi/astro/tempanal/ .

[2] Doppler maps of the λ6393 line are omitted in the following inspections as there are only four maps of λ6393 available (one in 96/01 and three in 98/01).

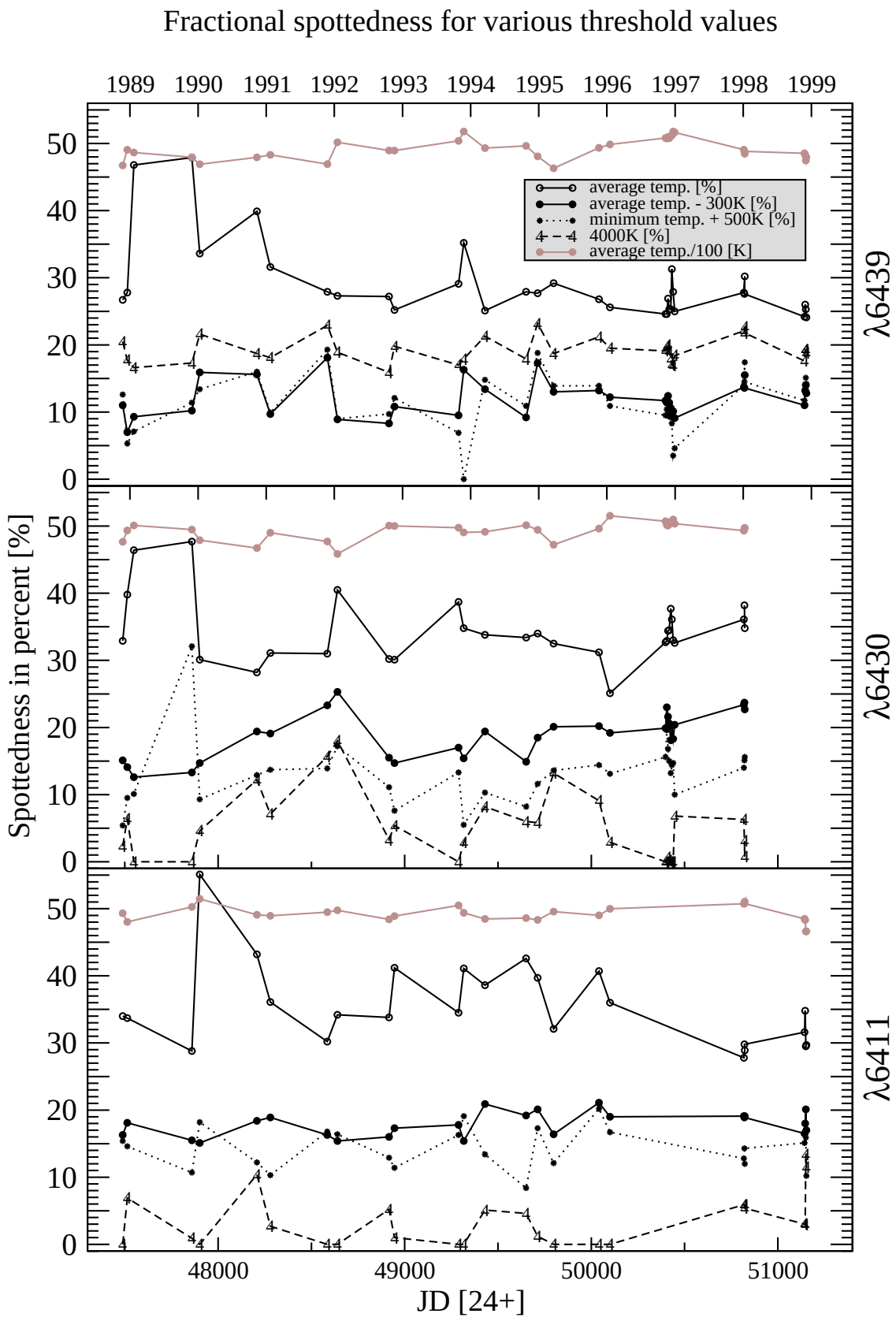

Figure 7.6: Fractional spottedness for all Doppler maps as a function of time. The solid black line with filled circles (av. temp. − 300 K) gives the best results.

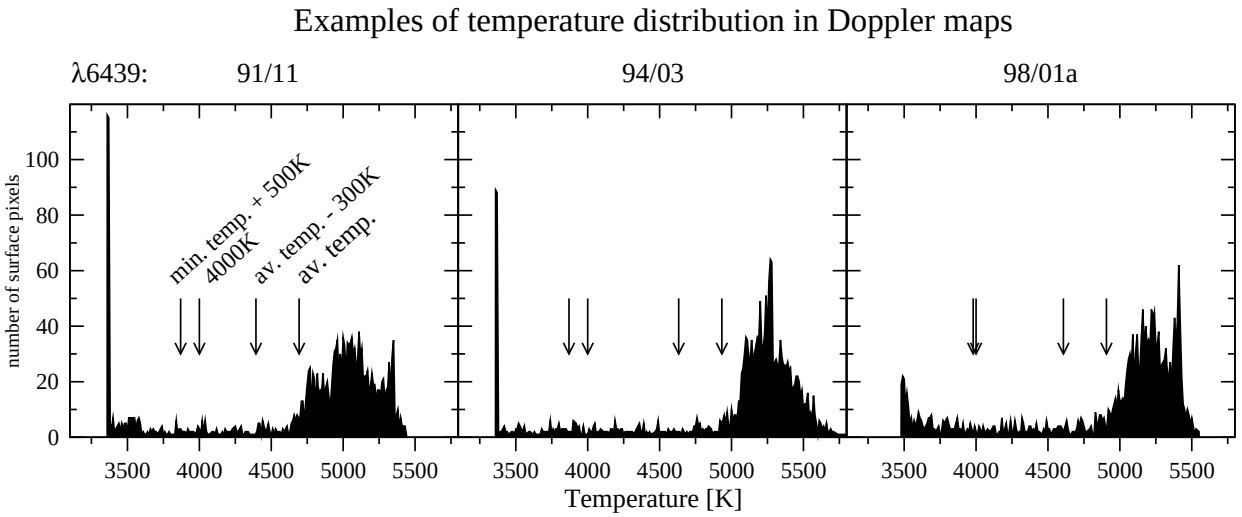

Figure 7.7: Examples of temperature distributions in Doppler maps. The arrows present several suggested definitions of a threshold value for calculating the fractional spottedness.

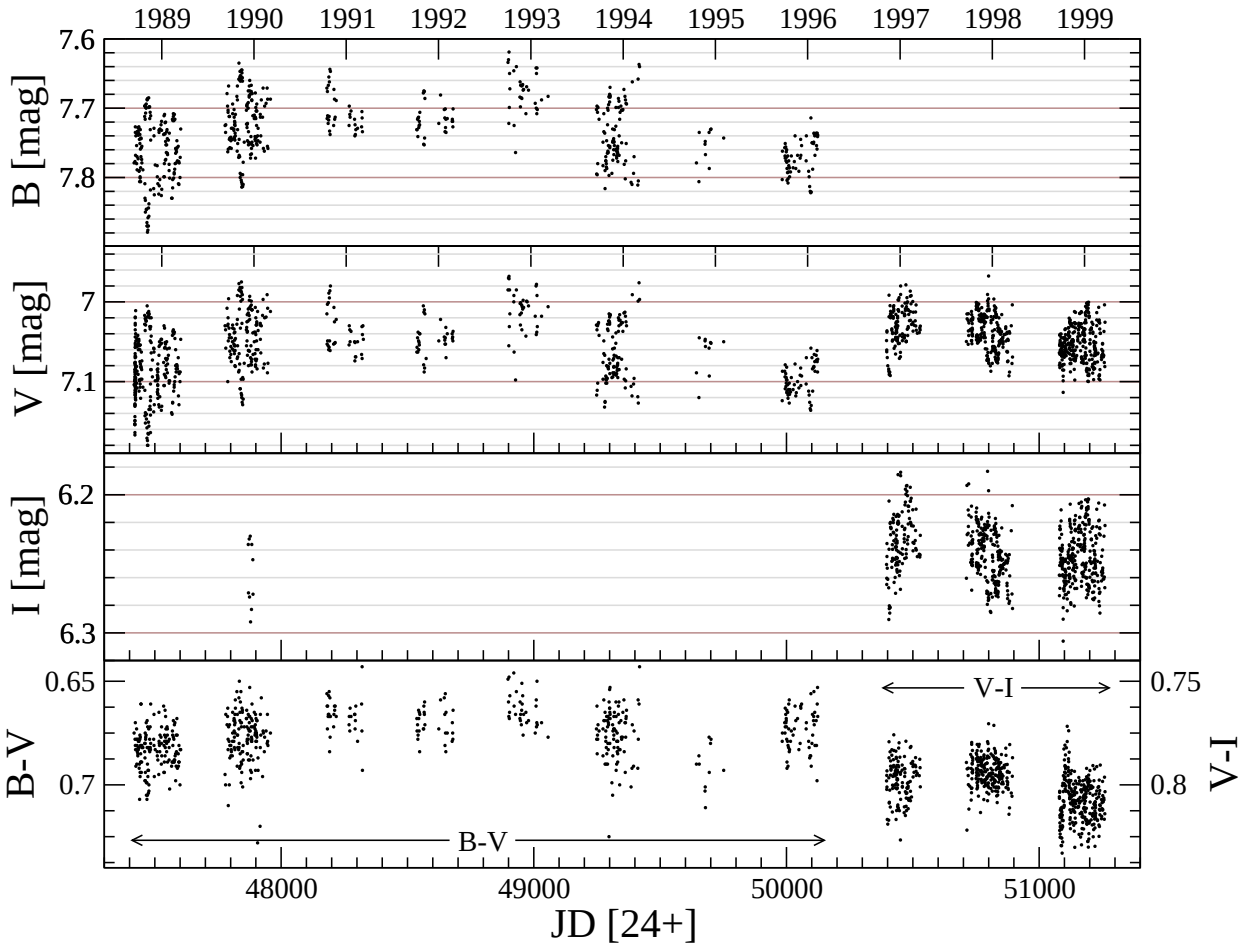

Figure 7.8: Photometric data for the timeframe of our Doppler maps. See Fig. 1.7 on page 8 for the complete data set.

correlation with the long-term cycle of 12.2 years is seen.

Fig. 7.9 shows, for all Doppler maps of the λ6439 line, the temperature distribution as a function of stellar longitude (left) and latitude (right). Starting from 1988/11 on top, each map is shifted by $-100\,\mathrm{K}$ for better viewing. It can be seen without further investigation that there are no obvious preferred longitudes. Overall, we cannot determine any preferred fixed surface positions of spots on EI Eridani (apart from the polar cap as such) which is also demonstrated by the "grande average Doppler maps", an average of all available Doppler maps from 1988 till 1998, separately for each spectral line (see Fig. 7.12, top panels). Does this implicate that there are no preferred longitudes at all? This would be in contradiction to what was published by Berdyugina & Tuominen (1998). They observed, by means of photometry, active longitudes which are not synchronised with the orbital motion and which shift by one orbital phase in about 2.7 years, switching primary and secondary minima after 9 years (flip-flop). Fig. 7.10 allows a more detailed look at the spot occurrences as a function of stellar longitude. The functions are the same as in Fig. 7.9 (left) but are plotted as two mirrored lines with their interspace filled in black, after normalisation by their respective maximum temperature ("spot-occurrence function"). A broad area thereby denotes a longitude with lower average temperature and therefore stronger spottedness. The uppermost panel shows the latitudinal locations of the strongest and second strongest polar appendages as inspected by eye. For the years 1989 till 1994, we see a possible correlation of the longitudinal occurrences of polar appendages, showing a systematic drift towards higher longitudes (i.e. later orbital phase), indicated by solid (primary maxima) and dotted (secondary maxima) grey lines. The shift amounts to 360° after about 3 years which is very similar to the 2.7 years found by Berdyugina & Tuominen (1998). Assuming a switch between primary and secondary minima to occur around 1994 (as proposed by Berdyugina & Tuominen 1998), we reverse the solid and dotted lines at 1994.4 in Fig. 7.10 (uppermost panel) and see that the continuation from 1994 onwards follows roughly this pattern. The active longitudes noticed in Fig. 7.10, uppermost panel, are not clearly resembled by the average-temperature functions shown in the lower panels of the same figure (which give an average of each longitude, from $-i$ to 90° latitude). Thus, I conclude that the longitudinal migration is mainly caused by the polar appendages. The latitude range of the polar appendages is also the most active area on EI Eri, as revealed by the long-term sigma maps (see below).

Fig. 7.11, right panel, shows the temperature averaged along latitudes. Clearly, the polar cap dominates the surface maps. Compare these results with the diagrams presented by Granzer et al. (2000), see Fig. 1.8 on page 11. They are similar only to Granzers $0.4\,\mathrm{M}_\odot$ cases, and no theoretically predicted spot-probability functions are available yet for giant stars (the results from Granzer et al. are for ZAMS stars). Obviously, more effort is required from the theoretical counterparts.

The bottom line of Fig. 7.12 shows the respective sigma maps of a combination of all maps from 1988–1998. Clearly, the most and strongest variations are found in the appendices of the polar cap at a latitude of 60° – 75°. Nevertheless, as demonstrated by the right panel in Fig. 7.11, the downreach of the polar cap remains very stable and ends, without exception, at 45° – 50°. The polar cap is present in all maps (unlike claimed from preliminary results by Washuettl & Strassmeier 2002). This finding is emphasised by the succession of averaged line profiles, one for each epoch/Doppler map, as presented in Fig. 7.2 on page 109. If the polar cap would diminish for any epoch, we would expect the respective line profiles to be more pointed, i.e. less shallow. While all averaged profiles are very homogeneous, a few deviate slightly in line depths. This behaviour is, however not followed in all three mapping lines simultaneously and is therefore assumed to be spurious. Fig. 7.3 on page 110 features the appropriate equivalent widths of all spectra (separated for each line) as well as the equivalent width of the respective average profiles. The only trend found in all three spectral lines is a minor decrease during the year 1995.

In fact, none of the extracted parameters exhibits a clear correlation *in all three mapping lines* within the proposed activity cycle. I assume (possibly with a few exceptions) most of the minor variations found in the various parameters (Fig. 7.3–7.11) to be spurious and caused by low-quality Doppler maps. In other words, I assume all of the extracted parameters to remain *basically* constant during the whole period of observations. The only obvious variation is the existence and migration of preferred active longitudes which gets support from photometric observations (Berdyugina & Tuominen 1998).

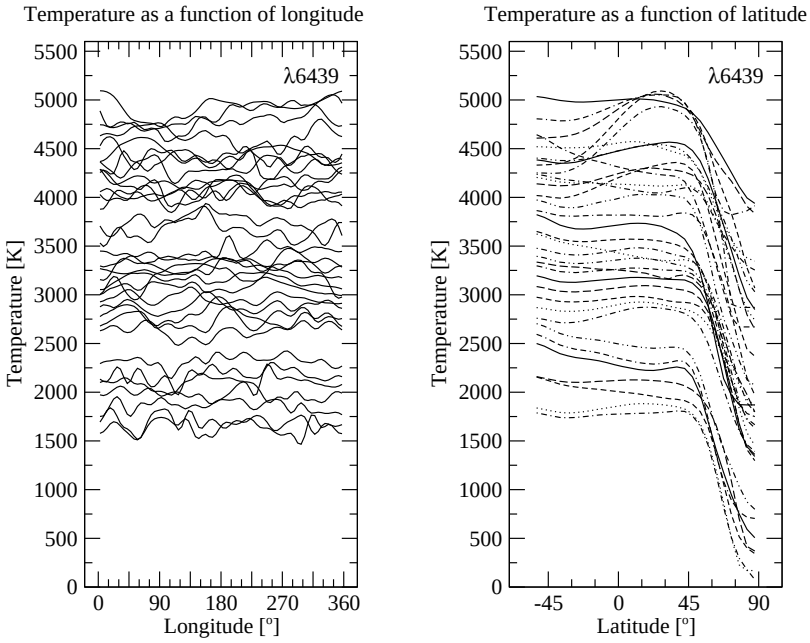

Figure 7.9: Temperature as a function of longitude (left) and latitude (right). Each function is shifted by $-100\,\mathrm{K}$ for better viewing. Earliest epochs are on top.

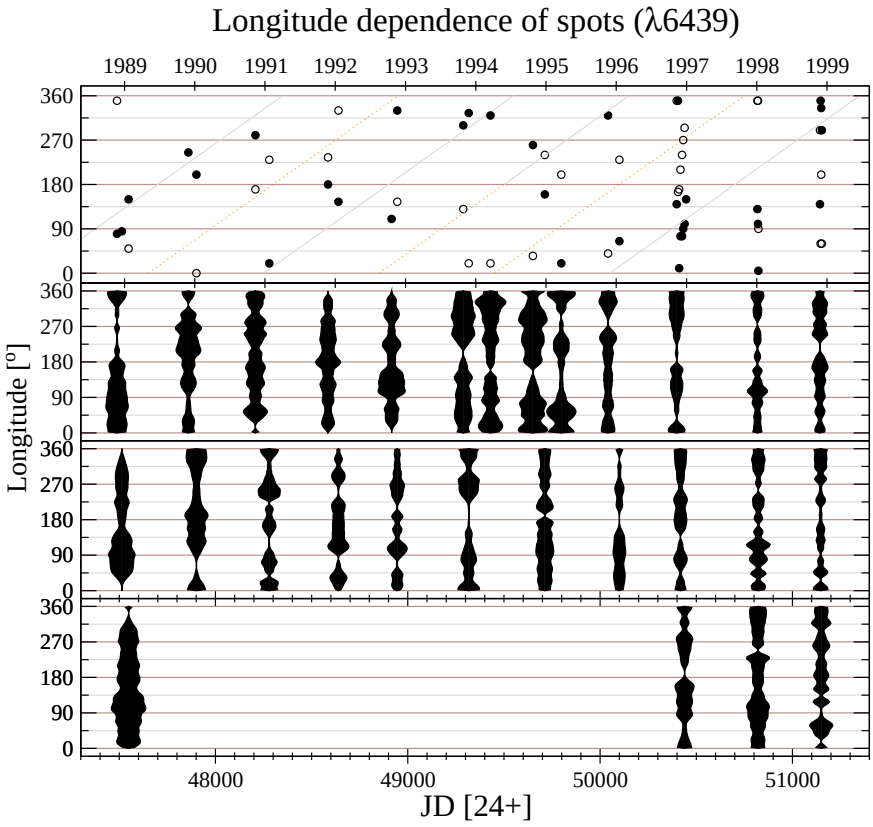

Figure 7.10: Longitudinal spot-occurrence functions. The black areas represent average temperature as a function of longitude, normalised by its respective maximum average temperature. A broader area denotes lower average temperature (corresponding to stronger spottedness) in the respective longitude. If an area would overlap with its antecessor, it is plotted in the subjacent panel. The uppermost panel gives the longitude of the strongest (filled circles) and second strongest (if existent; open circles) polar appendage for each map, as inspected by eye.

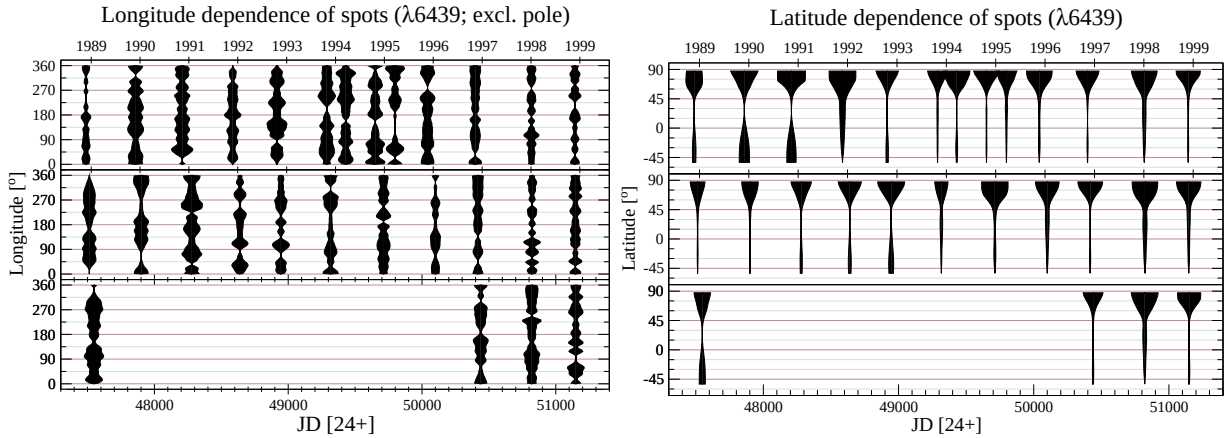

Figure 7.11: Spot-occurrence functions. The black areas mark averaged temperatures as a function of longitude excluding the polar region (left) and as a function of latitude (right). See Fig. 7.10 for description. — This display mode is, for the latitudinal case (right panel) most useful for comparing observational results with the theoretical diagrams (spot-probability functions) presented by Granzer et al. (2000), see Fig. 1.8 on page 11.

7.3 Discussion

We are now faced with the puzzling finding that the cyclic brightness variations as seen from photometric observations (exhibiting a period of roughly 12 years) are not resembled by our spectroscopic data – neither by any parameter extracted from Doppler maps nor by the "raw" spectroscopic mapping lines as such (EW). This is in contrast to the solar analogon which suggests that the total spottedness varies with the activity cycle. Thus, we are asked to explain either what exactly causes the long-term variations of the mean brightness and the change in the amplitude of the brightness variations seen at each epoch — or/and why are these variations not found in our Doppler maps.

Short-term variations

Let us focus on the amplitude of the short-term variations first: The amplitude varies such that at the begin of the photometric cycle minima in 1984/85 and 1995/96, the amplitude was smallest, turning largest right thereafter in 1984/85. However, a clear correlation with the long-term cycle is not seen (see Fig. 1.7, left upper panel, page 8). These short-term brightness variations are assumed to be caused by spots moving across the visible disk of the star – which is reasonable. However, differences in the amplitude of those variations do not necessarily reflect a larger or smaller number of spots or spottedness. They can also be a sign of a homogeneous or otherwise a concentrated spot distribution on the star's surface. However, the short-term brightness changes, if caused by spots, should be directly related to the longitude function (Fig. 7.10), and should therefore be seen therein. To be more precise, the brightness changes are only affected by those parts of the stellar surface that are not circumpolar. Therefore, we recreate the plot displaying the longitudinal spot-occurrence functions, but this time with the high latitudes ($90° - i$) excluded (see Fig. 7.11, left panel). However, a relationship with the brightness variation (Fig. 7.8) is still not seen. After all, for epochs with a small number of photometric data points, another problem could possibly be caused again by the disadvantageous rotational period of almost two days: most photometric data of EI Eri were collected by automatic telescopes which normally execute the same targets every night. This brings about a similar time of observation of a specific target for each night and, in the case of EI Eridani, a similar orbital epoch – which might, for a small data sample, mimic smaller photometric amplitudes.

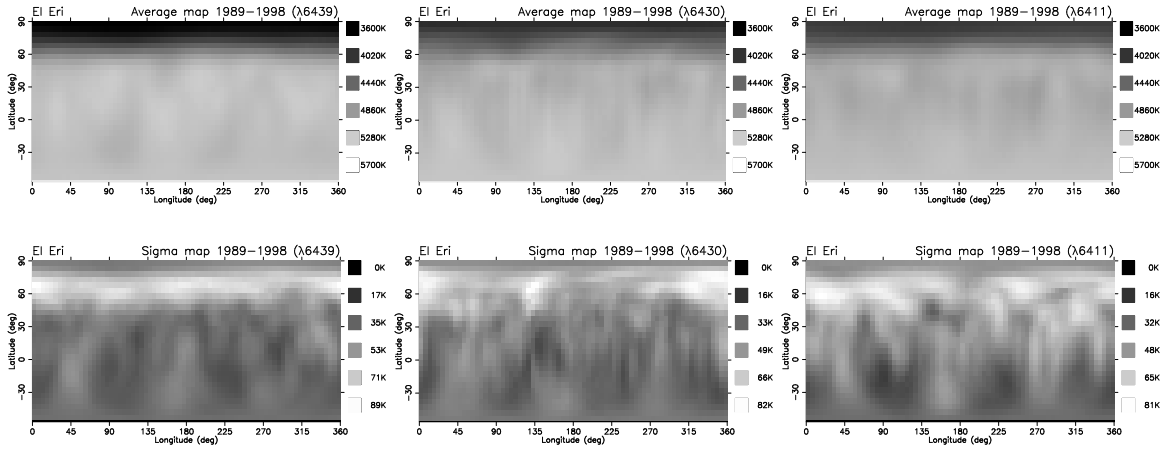

Figure 7.12: Top line: The "grande average Doppler maps" for 1988–1998. No fixed (in the orbital reference frame) preferred longitudes are seen. Bottom line: sigma maps for 1988–1998.

Long-term variations

On the other hand, why is the long-term variation of the mean photometric brightness not reflected by our Doppler maps? A decrease or increase in total brightness – if caused by a larger spottedness or, like on the Sun, by a higher faculae emission – should accordingly be reflected by the spottedness as extracted from the Doppler maps, and thereby also by the average temperature and the equivalent width. None of it is the case with EI Eri. One possible explanation is that the normalisation of the spectra (continuum fitting) could potentially adulterate the temperature span. Another one is the surface resolution limit for Doppler imaging. Possibly, the cyclic brightness variation is caused by a fluctuation of small, unresolved spots while the fractional coverage of large-scale spots remains basically constant. Doppler images do a good job in catching starspots that significantly modulate the line profile, but it is extremely difficult to detect a background of small starspots evenly distributed over the stellar surface. Solanki & Unruh (2004) found that even for heavily spotted (hypothetical) stars, a large fraction of the spots are smaller than the current resolution limit of Doppler images. Thus, it is possible that a substantial part of the spot coverage is not resembled by our measurements of fractional spottedness (as presented in Fig. 7.6). Spot covering fractions can also be derived from TiO band modelling – a method that does not suffer from the resolution limitation. It would therefore be essential to monitor and compare fractional spottedness as derived from DI with TiO filling factors. By this means, however, Berdyugina (2002) obtained filling factors for the RS CVn system II Peg that coincide with the corresponding Doppler images without requiring additional (unresolved) starspots. — As a final alternative, we could only assume that the long-term variation of the total mean brightness is not caused by the degree of spottedness. In this case, it would be questionable in what way the photometric cycle corresponds to a magnetic cycle.

The Sun

On the Sun, the solar cycle is visible not only in the visual brightness but also in many other observables including total irradiance, radio and total magnetic flux, Ca II H & K emission, in magnetic features like sunspots, and others (see Fig. 7.13). The sunspot number, though, is the most prominent one. Most indices vary roughly in phase with the sunspot number. However, the modulation amplitude varies widely between different indices. In visible light, the amplitude is marginal and vague, and most likely not obvious to a casual naked-eye observer.

The sunspot maximum correlates with a maximum in total irradiance/brightness, Ca II H & K core emission and total magnetic flux (Harvey & White 1999; Radick et al. 1998). Thus, the Sun is brighter during sunspot maximum which is caused by the dominating emission from faculae. This behaviour is also found on other old stars (Radick et al. 1998, see also §1.1.3). Both, the Sun and EI Eri, tend to become bluer as they

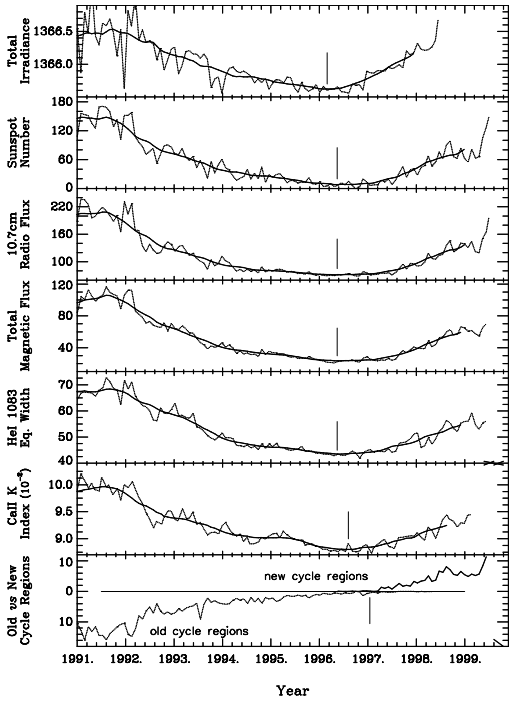

Figure 7.13: Variation in the total solar irradiance, sunspot number, 10.7 cm radio flux, total magnetic flux, He I 1083 nm equivalent width, Ca II K-index, and number of new- and old-cycle regions, through the minimum period between solar cycles 22 and 23. In the top six panels, the light-dotted curves show the averages, by Carrington rotation, of each index, while the heavy-dashed curves give a 15-rotation running mean of these data. The vertical bars provide the best estimate of the minimum for the particular index. (From Harvey & White 1999).

get brighter (in the course of the cycle), which suggests that EI Eri might exhibit a higher level of faculae emission during activity (i.e. photometric) maximum. On the Sun, however, the occurence of faculae is usually associated with spots.

A model presented by Solanki & Unruh (1998) indicates that the radiative properties of magnetic features on the solar surface (i.e. faculae and sunspots) provide the dominant contribution to irradiance variations on a solar-cycle time-scale – thereby suggesting that such features are responsible for the visual brightness variations on EI Eri. However, the total irradiance variations seem to be strongly dependant on the inclination angle of the star and, for the Sun, could increase by a factor exceeding 6 when viewed from a heliographic latitude of 60°(see Radick et al. 1998). Possibly, the variations in total spottedness on EI Eri are minute and not resolved by this investigation, but the accompanying faculae could have – as seen from an inclination angle, i.e. stellar latitude of 56° – an enhanced effect on the brightness and colour.

Other stars

The finding that the proposed activity cycle, i.e. the photometric cycle, does not resemble a corresponding spot or magnetic cycle might get support by results from other stars. Donati et al. (2003) presented long-term magnetic surface images for the young K0 dwarfs AB Doradus and LQ Hydrae and for the RS CVn-type K1 subgiant HR 1099 and found that large regions (with predominantly azimuthal magnetic fields) are continuously present at the surface of these stars. Long-term structural changes take place but reflect no more than the limited lifetime of the corresponding surface structures. An active longitude, as seen on EI Eri, is not confirmed on HR 1099. Further more, no clear secular change is detected in the axisymmetric component of the magnetic field and in particular, no global polarity switch was observed in the field ring pattern of HR 1099, nor in the high-latitude azimuthal field ring of AB Dor. Petit et al. (2004b) report that, on HR 1099, the small-scale brightness and magnetic patterns undergo major changes within a time-scale of 4-6 weeks, while the largest structures remain stable over several years.

Another case, the K2 IV RS CVn star II Peg, exhibits – like EI Eri – migrating active longitudes including the flip-flop phenomenon. However, the total spot area is approximately constant during this cycle. This means that II Peg's activity cycle is only expressed as the spot area evolution within the active longitudes, i.e. as a rearrangement of the nearly constant amount of the spot area (Berdyugina et al. 1999).

Vogt et al. (1999a), having observed HR 1099 for 11 years, suggest starspots to be stellar analogs of solar coronal hole structures and expect a dynamo cycle to be manifested by periodicity in the area of the polar spot – an expectation obviously not confirmed by EI Eridani.

Preferred longitudes

As pointed out in §7.2 (p.115), EI Eri seems to exhibit preferred longitudes that migrate within the orbital reference frame, supporting the finding from Berdyugina & Tuominen (1998). The time it takes for an active longitude to shift by one orbital phase (360°) is about 3 years which is close to the short-period cycle found by Olah & Strassmeier (2002). Compare this value to the proposed differential-rotation rate: If the values suggested in chapter 5 are real, the pole overlaps the equatorial spots in 10–15 days. Particularly, differential rotation then cannot account for the longitudinal migration of spots as suggested by the phase drift of the migrating photometric wave minimum – a result also found on HR 1099 (Vogt et al. 1999a). During the time the pole overlaps the equator (10–15 days), the preferred latitudes shift only by 3–5°. After one orbital rotation, this shift amounts to $\approx 0.65°$, while the shift of the polar region comes to 30–40° during the same time . Therefore, considering both a strong differential rotation and the existence of stable, preferred longitudes, the spots constituting the high-latitude appendages must either be very short lived (otherwise they would be moved out of the preferred longitudes by the faster rotating polar region) or they are anchored in a deeper layer that is not bound to the differentially rotating surface. Possibly, the appendages at the preferred longitudes (or perhaps all spots in the polar region) are the footprints of a strong dipole magnetic field that is firmly anchored to the synchronised deeper core of the star. The magnetic energy density of such a dipole could be stronger than the kinetic energy density of the differential shearing motions of the gas. This emergent dipole field would then dominate the gas motions at high latitudes, producing apparent synchronisation of the high-latitude features with the orbit.

Overall, active longitudes seem to be a common feature on active close-binary stars. Such a phenomenon has been noticed using the technique of Doppler imaging on, e.g., the active giant DM UMa (Hatzes 1995), on the two main-sequence components of σ^2 CrB (Strassmeier & Rice 2003), on the two pre-main sequence components of V824 Ara (Hatzes & Kürster 1999; Strassmeier & Rice 2000) and the active giant UZ Lib (Olah & Strassmeier 2002), as well as by long-term photometric analysis on, e.g., RT Lac (Çakırlı et al. 2003), UZ Lib (Oláh et al. 2002a) and on the RS CVn stars II Peg, σ Gem and HR 7275 (Berdyugina & Tuominen 1998). Holzwarth & Schüssler (2003) presented a numerical investigation for fast-rotating solar-like binaries which showed that, although the magnitude of tidal effects is rather small, they nevertheless lead to the formation of clusters of flux tube eruptions at preferred longitudes on opposite sides of the stars (synchronised with the orbital motion). This finding is supported by simplified theoretical calculations by Moss & Tuominen (1997) who showed that synchronised close late-type binaries can be expected to exhibit large-scale nonaxisymmetric magnetic fields with maxima at the longitudes corresponding to the two conjunctions (again locked within the orbital reference frame). None of these investigations can reproduce migrating active longitudes and the flip-flop phenomenon as seen on EI Eri. For a possible theoretical explanation of the flip-flop phenomenon on the single giant FK Com, see Elstner & Korhonen (2004).

7.4 Summary of results

The key results from the incipient parameter study can be summarised as follows:

- Improved orbital parameters were determined with HJD = 2,448,054.7109 + 1.9472324 × E, $\gamma = 21.6\,\mathrm{km\,s^{-1}}$, $K_1 = 26.8\,\mathrm{km\,s^{-1}}$.
- The barycenter velocity γ exhibits variations of about $8\,\mathrm{km\,s^{-1}}$. I interpret these variations as induced by a third stellar component and suggest an orbital solution for the tertiary component with a period of around 19 years.
- Using the parallax from Hipparcos, I achieve a luminosity of $4.6 \pm 0.3\,\mathrm{L_\odot}$ and a radius of $2.4 \pm 0.1\,\mathrm{R_\odot}$, independent from the inclination.
- The inclination is thereby found to be $i = 56.0 \pm 4.5°$.
- With the new parameters and using evolutionary tracks, the position of the primary in the HR diagram is located. It correlates to a mass of $1.25 \pm 0.05\,\mathrm{M_\odot}$ and an age of $4.8 \pm 0.5\,\mathrm{Gyr}$.
- Using the observed mass function of the inner binary and assuming $i_{\mathrm{orb}} \equiv i_*$, we derive the mass of the unseen secondary: $M_2 = 0.249 \pm 0.049$ corresponding to a M4-5 V star. Accordingly, the mass of the proposed tertiary is estimated to be $0.74 \pm 0.66\,\mathrm{M_\odot}$ (implying zero eccentricity).
- In the course of the proposed activity cycle (as seen from photometric data), EI Eri becomes bluer as it gets brighter.

The key results from the Doppler-imaging analysis are as follows:

- The general morphology of the spot pattern remains persistent for more than 10 years.
- The polar spot is long-lived but changes its size and shape on short time-scales (one week).
- The polar cap is present at all observed epochs along the photometric cycle; no decay and reemergence due to, e.g., a polarity inversion was spotted.
- The downreach of the polar cap is stable and ends, without exception, at 45° – 50°.
- The most active surface area is the latitude band between 60° and 75°; the appendages in this area seem to be responsible for the light variability and especially for the migrating active longitudes.
- Low latitude spots occur and decay on short time-scales (less than a week) and are much less pronounced.
- No static preferred longitudes locked to the orbital reference frame of the system are seen; the polar appendages do seem to appear on preferred longitudes, but drifting towards larger longitudes with respect to the line of centers in the binary ($\mathrm{P} \approx 3\,\mathrm{yr}$), thereby confirming the migrating active longitudes proposed by Berdyugina & Tuominen (1998).
- No correlation is seen between the photometric long-term cycle and any parameter extracted from spectra and Doppler maps; this includes EW, latitude and longitude function, average temperature and spottedness.
- Preliminary results from a cross-correlation analysis of consecutive Doppler maps suggest a differential rotation of $\alpha \approx$ -0.15 – -0.2. This equals the solar value but its direction is anti-solar, i.e. the pole rotates faster than the equator. This result needs further confirmation.

7.5 Outlook

Since the dawn of Doppler imaging in the early 1980ies, hundreds of Doppler maps were established for at least 65 different stars (see Strassmeier 2002) showing a large variety of spot configurations. It is, by now, doubtful what we still can learn from just another Doppler map or even just another Doppler imaged star, and merely phenomenological findings will no longer be a sufficient stimulus for observing time or publication. However, there *are* scientific questions yet to be addressed by means of Doppler imaging:

- Differential rotation and meridional flows are important key ingredients in dynamo theories. The most direct approach for measuring these phenomena is by means of Doppler imaging.
- Correlations of spot behaviour with other stellar parameters are yet to be established. This requires a large, statistically significant sample of stars and a quantitative analysis procedure of Doppler maps.
- From photometric and Ca II H & K observations, cyclic behaviour on active stars is now well established. Accordingly, long-term Doppler-imaging studies like the present one are an important means for exposing the accompanying spot characteristics of cyclic behaviour on stars, and thereby for broadening our understanding of the underlying processes. However, long-term Doppler imaging should preferably be supported by TiO modelling and Ca II H & K and Hα monitoring.
- Magnetic surface maps derived by Zemann Doppler imaging are required for detailed magneto-hydrodynamic modelling of stellar activity.

Inevitable requirements for long-term DI studies, as strengthened by the results of this thesis, are: high S/N (definitely not below 300), high spectral resolution and, above all, a permanent and consistent instrumental configuration. Clearly, continuous high-resolution spectra from a particular observing site that operates for many years without significant instrumental modifications will provide observations under the required stable conditions and with consistent quality — which is essential for comparing Doppler maps spanning complete activity cycles.
Furthermore, we clearly need more input from theory in order to compare our observational results with model predictions — as we have to keep in mind that a purely empirical description without explanatory theory does not provide real insights in the underlying physical processes.

Appendix A

Observing logs

"This star standeth in my heaven even in dark nights"[1], and it is therefore of little surprise that the list of observations presented here is longsome. Observing logs for all data used in this investigation, the ones from our own observing runs as well as the ones from the literature, are specified on the following pages. The tables list the Heliocentric Julian Date (HJD) at the midpoint of an observation, the date of observation in universal time (UT) and the starting time of the observation. It includes the exposure time (combined exposure time in case of combined images; actually, CCD dark time is used), the signal-to-noise ratio as estimated using `IRAF`'s `splot`, the airmass, the phase (computed with the ephemeris in §3.2.1; see also Table 4.1), the heliocentric radial velocity v_r in $\mathrm{km\,s^{-1}}$, the error of the radial velocity measurement σ_{v_r} im $\mathrm{km\,s^{-1}}$ and the RVSS ("RV Std"). The 97 Dec. log additionally lists the block number used for splitting the data into several blocks for Doppler imaging.

A.1 NSO and KPNO observations

The observing logs for the NSO synoptic program, for the visiting NSO run in 1996 and for all KPNO observing runs are listed here.

NSO 88 Nov / 88 Dec (eieri02)

Observations from Nov 16 – Dec 22, 1988

HJD	date	UT	t_{exp}	S/N	airmass	phase	v_r	σ_{v_r}	RV Std
2447481.85877934	16/11/88	7:59:26	3600	280	1.30	0.8121	22.92 (DI)	–	–
2447482.72595936	17/11/88	4:58:10	2400	240	1.85	0.2575	11.59 (DI)	–	–
2447485.78022403	20/11/88	6:10:16	3000	270	1.41	0.8260	24.96 (DI)	–	–
2447485.91420547	20/11/88	9:11:44	4500	270	1.44	0.8948	35.20 (DI)	–	–
2447486.78984068	21/11/88	6:30:09	2400	270	1.36	0.3445	-1.94 (DI)	–	–
2447486.92332404	21/11/88	9:42:22	2400	290	1.57	0.4130	-10.62 (DI)	–	–
2447492.77544820	27/11/88	6:09:29	2400	280	1.35	0.4184	-10.40 (DI)	–	–
2447493.80873462	28/11/88	6:57:26	2400	270	1.30	0.9490	38.34 (DI)	–	–
2447494.86839555	29/11/88	8:30:52	1500	250	1.42	0.4932	-14.11 (DI)	–	–
2447508.90138814	13/12/88	9:16:23	1800	290	2.02	0.6999	3.99 (DI)	–	–
2447509.78106126	14/12/88	6:19:56	2100	270	1.31	0.1516	30.67 (DI)	–	–
2447509.80592715	14/12/88	6:58:58	1800	280	1.35	0.1644	29.19 (DI)	–	–
2447511.78858361	16/12/88	6:29:06	2400	280	1.32	0.1826	24.80 (DI)	–	–
2447511.93134400	16/12/88	9:51:54	2509	200	2.80	0.2559	13.26 (DI)	–	–
2447513.77129171	18/12/88	6:09:19	1800	230	1.31	0.2008	20.90 (DI)	–	–

[1] Nietzsche, Thus Spake Zarathustra, Before Sunrise

2447513.92290565	18/12/88	9:45:09	2100	200	2.84	0.2787	8.24 (DI)	–	–
2447517.92410247	22/12/88	9:32:08	3900	250	2.91	0.3335	-0.36 (DI)	–	–

NSO 89 Jan (eieri03)

Observations from Jan 12 – Jan 31, 1989

HJD	date	UT	$t_{\rm exp}$	S/N	airmass	phase	v_r	σ_{v_r}	RV Std
2447538.81751973	12/01/89	7:02:58	3600	370	2.23	0.0633	46.11 (DI)	–	–
2447545.69961784	19/01/89	4:28:48	1815	340	1.36	0.5976	-6.03 (DI)	–	–
2447546.67373727	20/01/89	3:52:46	1680	330	1.32	0.0978	42.21 (DI)	–	–
2447549.68456430	23/01/89	4:07:42	1800	270	1.35	0.6440	-1.07 (DI)	–	–
2447556.69637278	30/01/89	4:18:02	2700	340	1.46	0.2449	19.06 (DI)	–	–
2447557.69618472	31/01/89	4:20:23	2400	380	1.48	0.7584	17.01 (DI)	–	–

NSO 89 Nov—Dec / 90 Jan (ccd010)

Observations from Nov 9, 1989, – Jan 24, 1990

HJD	date	UT	$t_{\rm exp}$	S/N	airmass	phase	v_r	σ_{v_r}	RV Std
2447839.90839991	09/11/89	9:18:30	2700	310	1.3	0.6883	–	–	–
2447840.69110908	10/11/89	4:08:05	2400	260	3.1	0.0903	–	–	–
2447841.92716837	11/11/89	9:47:59	2400	280	1.4	0.7250	–	–	–
2447864.96392067	04/12/89	10:43:33	2100	240	2.8	0.5556	–	–	–
2447865.94967414	05/12/89	10:20:34	2400	320	2.4	0.0618	–	–	–
2447878.94827398	18/12/89	10:14:10	3000	150	3.8	0.7372	–	–	–
2447898.78161089	07/01/90	6:20:44	2400	200	1.4	0.9226	–	–	–
2447899.77544479	08/01/90	6:14:27	2100	200	1.4	0.4330	–	–	–
2447900.77487947	09/01/90	6:16:14	1800	310	1.5	0.9463	–	–	–
2447900.80027108	09/01/90	6:50:18	2100	280	1.6	0.9593	–	–	–
2447901.64796707	10/01/90	3:18:34	1200	280	1.3	0.3946	–	–	–
2447901.66231884	10/01/90	3:39:14	1200	240	1.3	0.4020	–	–	–
2447902.73509105	11/01/90	5:24:08	1200	240	1.3	0.9529	–	–	–
2447902.74944197	11/01/90	5:44:48	1200	250	?	0.9603	–	–	–
2447903.72759042	12/01/90	5:13:26	1200	230	1.3	0.4626	–	–	–
2447903.74192943	12/01/90	5:34:05	1200	240	1.4	0.4700	–	–	–
2447912.81237266	21/01/90	7:09:33	1800	210	2.3	0.1281	–	–	–
2447915.68691188	24/01/90	4:11:10	1800	240	1.3	0.6043	–	–	–
2447925.76718365	03/02/90	6:02:58	2400	200	2.1	0.7810	–	–	–
2447925.81426603	03/02/90	7:08:16	2700	230	3.7	0.8052	–	–	–

NSO 90 Nov (ccd016)

Observations from Oct 23 – Dec 2, 1990

HJD	date	UT	$t_{\rm exp}$	S/N	airmass	phase	v_r	σ_{v_r}	RV Std
2448187.90907048	23/10/90	9:25:11	2100	280	1.30	0.4038	1.51	2.17	59 Ari
2448188.88383156	24/10/90	8:51:17	1800	350	1.32	0.9044	44.40	2.31	59 Ari
2448189.80971259	25/10/90	7:04:30	1800	280	1.61	0.3799	8.86	5.90	59 Ari
2448199.04278572	03/11/90	12:35:42	2280	320	2.64	0.1216	–	–	–

2448200.03172236	04/11/90	12:08:44	3600	240	2.23	0.6294	4.80	1.73	59 Ari
2448204.01902843	08/11/90	11:45:20	4200	370	2.13	0.6771	10.62	1.86	59 Ari
2448211.90627687	16/11/90	9:22:50	1800	330	1.42	0.7276	18.67	1.71	59 Ari
2448214.92815164	19/11/90	9:49:19	2400	310	1.55	0.2795	17.85	2.05	59 Ari
2448224.00487253	28/11/90	11:32:22	3300	300	3.76	0.9408	49.40	2.16	59 Ari
2448227.84227865	02/12/90	7:40:49	3000	340	1.34	0.9115	45.78	1.58	59 Ari

NSO 91 Jan (ccd024)

Observations from Jan 15 – Jan 31 / Mar 8, 1991. RVSS: 59 Ari

HJD	date	UT	$t_{\rm exp}$	S/N	airmass	phase	v_r	σ_{v_r}	RV Std
2448271.80021084	15/01/91	6:45:48	2700	300	2.03	0.4861	-3.45	1.82	59 Ari
2448272.87407843	16/01/91	8:29:47	3000	230	7.84	0.0376	48.61	3.50	59 Ari
2448274.79259064	18/01/91	6:35:09	2700	360	2.04	0.0228	49.77	1.64	59 Ari
2448284.81303141	28/01/91	7:05:44	2700	390	3.65	0.1688	36.82	2.16	59 Ari
2448286.79004258	30/01/91	6:15:22	4800	390	2.91	0.1841	34.83	1.70	59 Ari
2448287.78336189	31/01/91	6:30:52	1800	360	2.65	0.6942	14.03	1.66	59 Ari
2448323.74119835	08/03/91	5:41:46	946	110	10.7	0.1603	37.02	1.98	59 Ari
2448330.66309608	15/03/91	3:25:30	3900	350	2.74	0.7151	17.80	1.98	59 Ari
2448333.67863402	18/03/91	3:44:49	4200	280	4.13	0.2637	21.20	1.61	59 Ari

NSO 92 Jan (ccd107)

Observations from Jan 9 – Feb 5, 1992

HJD	date	UT	$t_{\rm exp}$	S/N	airmass	phase	v_r	σ_{v_r}	RV Std
2448536.84220564	07/10/91	7:47:36	2400	300	1.66	0.5982	2.94	1.89	59 Ari
2448571.87915138	11/11/91	8:38:51	2400	300	1.33	0.5915	1.38	2.01	59 Ari
2448572.73822549	12/11/91	5:18:24	2100	250	1.73	0.0326	50.73	1.69	59 Ari
2448573.96871468	13/11/91	10:50:17	2100	300	1.93	0.6645	10.30	1.62	59 Ari
2448583.76049664	23/11/91	5:45:24	2700	250	1.40	0.6931	12.33	1.67	59 Ari
2448583.78916548	23/11/91	6:36:41	1500	300	1.32	0.7078	15.78	1.58	59 Ari
2448584.73695026	24/11/91	5:14:00	2400	350	1.49	0.1946	(32.59)	(1.54)	59 Ari
2448585.90944273	25/11/91	9:27:24	1800	300	1.64	0.7967	32.25	2.12	59 Ari
2448586.88967786	26/11/91	8:58:57	1800	300	1.52	0.3001	15.67	1.84	59 Ari
2448587.69108233	27/11/91	4:12:59	1800	300	1.79	0.7117	21.44	1.98	59 Ari
2448594.77324122	04/12/91	5:56:27	3600	350	1.31	0.3487	8.40	2.08	59 Ari
2448597.73887879	07/12/91	5:17:04	2400	300	1.35	0.8717	42.13	1.96	59 Ari
2448598.95181001	08/12/91	10:11:14	3900	250	3.49	0.4946	-2.56	2.02	59 Ari
2448630.80189166	09/01/92	6:32:35	4500	300	1.83	0.8512	39.14	1.81	59 Ari
2448631.73144606	10/01/92	4:53:44	4200	375	1.38	0.3285	9.93	2.00	59 Ari
2448635.74885926	14/01/92	5:19:13	4200	300	1.50	0.3917	2.60	1.96	59 Ari
2448644.72706482	23/01/92	5:03:49	2400	375	1.51	0.0025	51.21	1.93	59 Ari
2448645.75364952	24/01/92	5:39:43	2700	350	1.74	0.5296	-2.93	1.79	59 Ari
2448646.79759322	25/01/92	6:43:07	2700	325	2.57	0.0658	48.68	2.17	59 Ari
2448647.72925336	26/01/92	4:49:49	4500	350	1.59	0.5442	-3.29	2.15	59 Ari
2448657.74044939	05/02/92	5:17:09	3300	325	2.01	0.6854	14.11	2.59	59 Ari

NSO 92 Oct / 92 Nov (data92)

Observations from Oct 14 – Dec 1, 1992

HJD	date	UT	$t_{\rm exp}$	S/N	airmass	phase	v_r	σ_{v_r}	RV Std
2448909.81574167	14/10/92	7:28:52	3300	350	1.72	0.1386	38.89	1.80	59 Ari
2448910.82189280	15/10/92	7:37:39	2700	320	1.64	0.6553	9.57	2.53	59 Ari
2448911.76449788	16/10/92	6:14:56	2100	220	2.47	0.1393	39.80	2.90	59 Ari
2448919.01267057	23/10/92	12:11:50	2520	280	1.79	0.8616	41.80	2.41	59 Ari
2448919.80544506	24/10/92	7:13:23	2400	250	1.58	0.2688	19.80	1.84	59 Ari
2448921.92832595	26/10/92	10:10:13	1920	320	1.35	0.3590	5.41	1.47	59 Ari
2448932.98758668	06/11/92	11:35:06	3000	300	1.96	0.0384	49.89	6.25	59 Ari
2448933.85932839	07/11/92	8:30:23	1800	350	1.30	0.4861	-3.52	1.40	59 Ari
2448934.97814509	08/11/92	11:21:27	2400	280	1.90	0.0607	49.12	1.87	59 Ari
2448935.97845108	09/11/92	11:21:52	4200	360	1.96	0.5744	2.31	1.53	59 Ari
2448947.99180786	21/11/92	11:40:59	4500	140	3.29	0.7439	24.23	1.72	59 Ari
2448954.93973981	28/11/92	10:26:05	3300	320	2.17	0.3120	10.72	1.07	59 Ari
2448955.91696006	29/11/92	9:53:18	2961	130	1.85	0.8138	35.42	1.97	59 Ari
2448957.74816912	01/12/92	5:50:17	3300	380	1.36	0.7542	26.90	1.76	59 Ari

NSO 93/94 (nso93)

Observations from January 29 – April 2, 1993

HJD	date	UT	$t_{\rm exp}$	S/N	airmass	phase	v_r	σ_{v_r}	RV Std
2447866.97849159	06/12/89	11:02:06	2400		5.46	0.5901	–	–	–
2447875.77605125	15/12/89	6:15:59	1800		1.32	0.1081	–	–	–
2448958.85377396	02/12/92	7:57:23	3000		1.43	0.3220	–	–	–
2449016.74254290	29/01/93	5:11:54	4200	300	1.81	0.0508	48.96	1.53	59 Ari
2449030.68296247	12/02/93	4:00:20	2700	350	1.61	0.2098	30.22	1.63	59 Ari
2449030.70657099	12/02/93	4:46:50	1200	250	1.83	0.2220	27.71	1.93	59 Ari
2449066.66889489	20/03/93	3:31:58	4200	250	3.88	0.6904	14.14	1.54	59 Ari
2449078.66783958	01/04/93	3:54:34	1452	100	8.84	0.8525	43.72	4.22	59 Ari
2449079.66842867	02/04/93	3:50:45	2023	140	11.12	0.3663	3.87	2.57	59 Ari

NSO 93 Oct (nso94)

Observations from October 20 – November 4, 1993

HJD	date	UT	$t_{\rm exp}$	S/N	airmass	phase	v_r	σ_{v_r}	RV Std
2449280.92690392	20/10/93	9:51:02	2100	350	1.31	0.7225	19.75	2.35	59 Ari
2449281.99038834	21/10/93	11:22:23	2100	300	1.55	0.2686	20.99	1.70	59 Ari
2449282.81566634	22/10/93	7:03:14	3000	380	1.55	0.6924	16.17	1.60	59 Ari
2449283.03415929	22/10/93	12:30:21	1500	320	2.03	0.8046	33.03	1.57	59 Ari
2449291.85534333	31/10/93	8:09:53	1800	320	1.32	0.3348	10.40	1.15	59 Ari
2449293.00654551	01/11/93	11:48:47	1656	280	2.02	0.9260	48.62	1.53	59 Ari
2449294.82520519	03/11/93	7:28:53	1500	350	1.36	0.8599	40.48	1.41	59 Ari
2449295.85622598	04/11/93	8:13:31	1500	320	1.31	0.3894	3.78	1.20	59 Ari

NSO 93 Dec (nso94:more1)

Observations from November 11 – December 9, 1993

HJD	date	UT	$t_{\rm exp}$	S/N	airmass	phase	v_r	σ_{v_r}	RV Std
2449302.86739868	11/11/93	8:26:55	1800	380	1.31	0.9900	51.32	1.83	59 Ari
2449326.88055564	05/12/93	8:48:32	1500	380	1.64	0.3219	12.57	2.19	59 Ari
2449327.67699497	06/12/93	3:57:56	1200	320	1.67	0.7309	21.65	1.49	59 Ari
2449328.74862305	07/12/93	5:43:37	900	280	1.33	0.2813	18.86	1.59	59 Ari
2449329.72085393	08/12/93	4:58:40	1500	320	1.39	0.7806	29.18	1.32	59 Ari
2449330.75974826	09/12/93	5:42:13	3000	220	1.31	0.3141	10.62	1.51	59 Ari
2449330.80034305	09/12/93	6:33:54	3000	220	1.33	0.3349	9.50	1.75	59 Ari

NSO 94 Jan (nso94:more2)

Observations from January 30 – February 1, 1994

HJD	date	UT	$t_{\rm exp}$	S/N	airmass	phase	v_r	σ_{v_r}	RV Std
2449382.70823625	30/01/94	4:42:35	1800	240	1.52	0.9922	51.12	1.86	59 Ari
2449382.72958862	30/01/94	5:13:20	1800	220	1.68	0.0032	51.86	1.70	59 Ari
2449383.63808861	31/01/94	3:06:41	1200	280	1.31	0.4697	-2.04	1.05	59 Ari
2449383.65247397	31/01/94	3:27:24	1200	330	1.33	0.4771	-1.96	1.40	59 Ari
2449384.63884888	01/02/94	3:02:54	1800	320	1.31	0.9837	50.72	1.97	59 Ari
2449384.66018966	01/02/94	3:33:38	1800	300	1.35	0.9946	50.92	1.70	59 Ari

NSO 94 Mar (nso94:more3)

Observations from November 11 – December 9, 1993

HJD	date	UT	$t_{\rm exp}$	S/N	airmass	phase	v_r	σ_{v_r}	RV Std
2449416.61073607	05/03/94	2:28:56	1500	300	1.51	0.4028	4.30	1.63	59 Ari
2449417.64027834	06/03/94	3:09:06	1800	230	1.77	0.9315	49.07	1.50	59 Ari
2449418.62555397	07/03/94	2:40:31	2700	270	1.66	0.4375	0.20	2.07	59 Ari
2449427.62140418	16/03/94	2:43:06	1800	180	1.88	0.0573	49.98	1.16	59 Ari
2449427.64274509	16/03/94	3:13:50	1800	160	2.24	0.0683	49.50	1.61	59 Ari
2449427.66438765	16/03/94	3:45:00	1800	150	2.84	0.0794	48.53	1.81	59 Ari
2449427.68571774	16/03/94	4:15:43	1800	150	3.99	0.0904	47.35	3.36	59 Ari
2449428.60637301	17/03/94	2:20:23	1800	300	1.74	0.5632	-0.07	1.70	59 Ari
2449429.60576848	18/03/94	2:19:52	1800	180	1.77	0.0764	47.06	1.54	59 Ari
2449429.62775173	18/03/94	2:52:28	1800	250	2.06	0.0877	46.26	1.76	59 Ari
2449429.64908147	18/03/94	3:23:11	1800	250	2.53	0.0987	45.24	1.83	59 Ari
2449429.67041157	18/03/94	3:53:54	1800	250	3.36	0.1096	43.68	2.19	59 Ari
2449429.68829901	18/03/94	4:24:37	1200	180	4.70	0.1188	42.39	2.37	59 Ari
2449430.66364978	19/03/94	3:41:07	1630	100	3.18	0.6197	4.68	2.62	59 Ari
2449439.60910082	28/03/94	2:29:10	1500	280	2.24	0.2136	31.55	1.40	59 Ari
2449440.64563261	29/03/94	3:10:14	2700	320	3.81	0.7459	23.73	1.56	59 Ari
2449440.66718426	29/03/94	3:59:13	510	60	6.03	0.7570	25.62	3.94	59 Ari
2449442.60931421	31/03/94	2:32:16	1200	250	2.43	0.7544	26.23	2.52	59 Ari
2449442.62722388	31/03/94	2:52:59	1800	320	3.04	0.7636	27.38	1.55	59 Ari
2449442.64896526	31/03/94	3:24:22	1800	280	4.45	0.7747	29.83	1.78	59 Ari

2449443.59744365	01/04/94	2:17:46	900	230	2.22	0.2618	25.33	1.62	59 Ari

NSO 94 Oct (nso95:94oct)

Observations from October 18 – October 31, 1994

HJD	date	UT	$t_{\rm exp}$	S/N	airmass	phase	v_r	σ_{v_r}	RV Std
2449643.94619938	18/10/94	10:13:58	2700	250	1.34	0.1508	39.03	1.70	59 Ari
2449644.73987058	19/10/94	5:16:48	2700	160	3.11	0.5584	-0.98	2.37	59 Ari
2449644.77161854	19/10/94	6:02:31	2700	190	2.16	0.5747	0.09	2.58	59 Ari
2449644.97355043	19/10/94	10:53:17	2700	230	1.43	0.6784	14.64	2.57	59 Ari
2449645.71373397	20/10/94	4:39:06	2700	60	4.87	0.0585	47.97	3.02	59 Ari
2449645.74549183	20/10/94	5:24:50	2700	140	2.78	0.0748	46.68	2.45	59 Ari
2449645.77770689	20/10/94	6:11:13	2700	180	2.01	0.0914	45.39	2.06	59 Ari
2449646.90943591	21/10/94	9:20:50	2700	230	1.31	0.6726	12.77	1.76	59 Ari
2449646.94642850	21/10/94	10:06:33	3600	270	1.36	0.6916	15.48	1.88	59 Ari
2449647.94902364	22/10/94	10:09:43	3600	150	1.37	0.2065	29.23	3.38	59 Ari
2449647.99254978	22/10/94	11:12:57	3600	150	1.58	0.2288	27.75	2.40	59 Ari
2449648.03095424	22/10/94	12:14:38	2520	240	1.98	0.2485	23.85	2.31	59 Ari
2449648.98419955	23/10/94	11:08:22	2700	180	1.54	0.7381	22.43	1.40	59 Ari
2449649.01596035	23/10/94	11:54:06	2700	220	1.82	0.7544	24.85	1.66	59 Ari
2449649.04090361	23/10/94	12:40:33	1410	170	2.19	0.7672	26.65	2.47	59 Ari
2449656.86531271	31/10/94	8:09:15	3600	250	1.31	0.7854	29.86	1.84	59 Ari

NSO 94 Dec (nso95:94dec)

Observations from December 17, 1994 – January 3, 1995

HJD	date	UT	$t_{\rm exp}$	S/N	airmass	phase	v_r	σ_{v_r}	RV Std
2449703.79438644	17/12/94	6:34:59	2700	250	1.36	0.8858	44.89	1.88	59 Ari
2449703.82614415	17/12/94	7:20:43	2700	230	1.49	0.9021	45.74	1.74	59 Ari
2449704.58565054	18/12/94	1:41:57	1800	220	2.71	0.2922	17.56	1.85	59 Ari
2449704.60699218	18/12/94	2:12:41	1800	210	2.17	0.3031	16.07	1.80	59 Ari
2449704.62835689	18/12/94	2:43:27	1800	180	1.84	0.3141	14.21	1.75	59 Ari
2449705.59374487	19/12/94	1:46:10	2700	280	2.42	0.8099	35.55	1.41	59 Ari
2449705.62551423	19/12/94	2:31:55	2700	280	1.85	0.8262	38.19	1.41	59 Ari
2449705.78176925	19/12/94	6:24:26	1800	300	1.34	0.9064	46.42	1.41	59 Ari
2449705.80311061	19/12/94	6:55:10	1800	320	1.41	0.9174	48.06	1.42	59 Ari
2449706.82943194	20/12/94	7:25:38	2700	340	1.56	0.4444	-0.87	1.44	59 Ari
2449707.59811282	21/12/94	1:45:03	3600	310	2.21	0.8392	39.82	1.72	59 Ari
2449708.74437943	22/12/94	5:30:47	1800	330	1.31	0.4279	0.53	1.47	59 Ari
2449715.81930526	29/12/94	7:11:42	2700	280	1.68	0.0612	49.33	1.49	59 Ari
2449715.85246988	29/12/94	7:57:27	2700	170	2.11	0.0782	48.26	1.70	59 Ari
2449717.78351050	31/12/94	6:20:19	2700	270	1.47	0.0699	48.78	1.77	59 Ari
2449717.81527916	31/12/94	7:06:04	2700	320	1.69	0.0862	47.84	1.42	59 Ari
2449717.84704816	31/12/94	7:51:49	2700	300	2.11	0.1025	46.33	1.64	59 Ari
2449718.60435442	01/01/95	2:02:04	2700	150	1.69	0.4915	-1.50	2.22	59 Ari
2449718.63653990	01/01/95	2:48:28	2700	220	1.47	0.5080	-1.01	1.24	59 Ari
2449720.82242596	03/01/95	7:24:07	1800	200	1.86	0.6305	7.35	2.42	59 Ari
2449720.84382622	03/01/95	7:54:56	1800	200	2.20	0.6415	9.00	1.73	59 Ari

NSO 95 Feb (nso95:95feb)

Observations from February 17 – 20, 1995

HJD	date	UT	$t_{\rm exp}$	S/N	airmass	phase	v_r	σ_{v_r}	RV Std
2449765.67120109	17/02/95	3:43:58	2700	100	1.61	0.6626	11.69	5.51	59 Ari
2449765.70260143	17/02/95	4:29:10	2700	110	1.95	0.6787	10.71	11.64	59 Ari
2449768.63353196	20/02/95	2:57:36	1800	80	1.44	0.1839	34.77	3.72	59 Ari
2449768.65450472	20/02/95	3:27:48	1800	70	1.55	0.1947	33.26	2.27	59 Ari
2449768.67594000	20/02/95	3:58:40	1800	70	1.73	0.2057	31.08	1.98	59 Ari

NSO 95 Mar (nso95:95mar)

Observations from February 28 – March 28, 1995

HJD	date	UT	$t_{\rm exp}$	S/N	airmass	phase	v_r	σ_{v_r}	RV Std
2449776.64514955	28/02/95	3:27:11	377	80	1.65	0.2983	18.69	4.60	59 Ari
2449787.61740737	11/03/95	2:29:14	2700	90	1.68	0.9331	46.40	2.24	59 Ari
2449787.64879368	11/03/95	3:14:26	2700	100	2.08	0.9492	47.24	3.63	59 Ari
2449791.64808752	15/03/95	3:13:53	2700	130	2.29	0.0030	49.53	2.82	59 Ari
2449791.67947504	15/03/95	3:59:05	2700	160	3.40	0.0191	49.56	3.18	59 Ari
2449799.64329404	23/03/95	3:00:22	3600	160	2.82	0.1089	44.23	2.67	59 Ari
2449800.63200616	24/03/95	2:51:43	2700	70	2.52	0.6167	5.99	5.68	59 Ari
2449800.66339303	24/03/95	3:36:55	2700	70	4.02	0.6328	9.19	7.10	59 Ari
2449802.63812302	26/03/95	3:00:43	2700	170	2.91	0.6469	9.02	3.56	59 Ari
2449802.66952217	26/03/95	3:45:57	2700	160	5.29	0.6631	11.74	2.89	59 Ari
2449804.62434905	28/03/95	2:41:06	2700	260	2.62	0.6670	10.16	2.89	59 Ari
2449804.65574755	28/03/95	3:26:19	2700	240	4.33	0.6831	12.08	5.45	59 Ari

NSO 95 Oct (nso95:95oct)

Observations from October 1 – 2, 1995

HJD	date	UT	$t_{\rm exp}$	S/N	airmass	phase	v_r	σ_{v_r}	RV Std
2449992.02679	01/10/95	12:13:56	2400	50	1.44	0.9074	43.78	7.19	59 Ari
2449992.84405	02/10/95	7:40:43	3600	60	1.79	0.3271	11.40	6.06	59 Ari
2449992.89221	02/10/95	8:50:04	3600	150	1.44	0.3518	8.25	4.77	59 Ari

NSO 95 Nov (nso95:95nov)

Observations from November 7 – December 2, 1995

HJD	date	UT	$t_{\rm exp}$	S/N	airmass	phase	v_r	σ_{v_r}	RV Std
2450029.03403	07/11/95	12:11:58	3600	220	3.32	0.9124	47.50	2.40	59 Ari
2450029.84153	08/11/95	7:34:45	3600	260	1.31	0.3271	13.59	4.46	59 Ari
2450031.97660	10/11/95	10:49:12	3600	360	1.93	0.4236	0.40	1.50	59 Ari
2450032.82948	11/11/95	7:22:18	3000	380	1.32	0.8616	40.93	3.72	59 Ari
2450039.89632	18/11/95	8:53:29	3600	400	1.44	0.4907	-0.87	2.41	59 Ari

2450040.82260	19/11/95	7:07:19	3600	320	1.31	0.9664	53.97	3.72	59 Ari
2450040.90672	19/11/95	9:18:27	2400	330	1.51	0.0096	55.43	4.15	59 Ari
2450041.87009	20/11/95	8:23:12	2700	300	1.37	0.5044	-1.25	2.50	59 Ari
2450042.80285	21/11/95	6:46:23	2700	300	1.32	0.9834	49.42	3.01	59 Ari
2450042.88547	21/11/95	8:45:21	2700	320	1.43	0.0258	52.19	3.20	59 Ari
2450043.65585	22/11/95	3:14:42	2700	250	2.81	0.4214	2.36	2.23	59 Ari
2450044.85677	23/11/95	8:09:02	2100	280	1.35	0.0382	51.24	4.95	59 Ari
2450051.89799	30/11/95	9:10:59	1800	320	1.66	0.6542	8.48	1.50	59 Ari
2450052.88745	01/12/95	8:55:50	1800	310	1.59	0.1623	36.68	3.20	59 Ari
2450053.80507	02/12/95	6:57:14	1800	330	1.31	0.6336	6.17	1.33	59 Ari

NSO 95 Dec (nso95:95dec)

Observations from December 12 – 28, 1995

HJD	date	UT	$t_{\rm exp}$	S/N	airmass	phase	v_r	σ_{v_r}	RV Std
2450063.93937	12/12/95	9:54:00	3600	400	3.40	0.8380	40.14	5.86	59 Ari
2450065.87490	14/12/95	8:23:14	3600	360	1.82	0.8320	36.14	2.26	59 Ari
2450066.86716	15/12/95	8:12:09	3600	340	1.77	0.3416	9.60	4.93	59 Ari
2450078.88520	27/12/95	8:38:54	3600	320	2.81	0.5135	-2.43	5.57	59 Ari
2450079.89740	28/12/95	8:56:34	3600	180	3.52	0.0333	52.65	2.34	59 Ari

NSO 96 Fall

Observations from Nov 1, 1996 – Jan 8, 1997

HJD	date	UT	$t_{\rm exp}$	S/N	airmass	phase	v_r	σ_{v_r}	RV Std
2450388.90290475	01/11/96	9:03:20	3600	150	1.30	0.7229	13.40	7.6	α Ari
2450390.99888385	03/11/96	11:26:28	3000	130	1.77	0.7992	24.88	8.1	α Ari
2450391.98128049	04/11/96	10:56:05	3600	150	1.60	0.3038	11.50	7.8	α Ari
2450392.96932388	05/11/96	10:46:20	2700	130	1.57	0.8112	21.84	7.7	α Ari
2450393.99213488	06/11/96	11:19:09	2700	160	1.80	0.3364	11.35	7.0	α Ari
2450394.68500721	07/11/96	3:49:22	3600	150	4.66	0.6923	9.09	7.3	α Ari
2450394.96069560	07/11/96	10:46:21	1200	160	1.61	0.8338	33.84	7.8	α Ari
2450395.68942407	08/11/96	4:10:42	1800	140	3.33	0.2081	24.67	6.9	α Ari
2450395.98469570	08/11/96	11:20:53	1200	160	1.89	0.3597	4.79	7.3	α Ari
2450396.72716891	09/11/96	4:49:48	3600	160	2.30	0.7410	19.95	6.8	α Ari
2450399.77645195	12/11/96	5:54:40	4351	140	1.59	0.3070	8.66	7.2	α Ari
2450400.88806165	13/11/96	8:41:24	3600	130	1.32	0.8778	37.02	7.9	α Ari
2450401.87706386	14/11/96	8:25:33	3600	140	1.31	0.3857	0.33	7.0	α Ari
2450404.71751004	17/11/96	4:35:47	3600	150	2.07	0.8444	31.27	7.4	α Ari
2450404.95373214	17/11/96	10:35:26	1260	120	1.80	0.9657	44.96	7.6	α Ari
2450405.93025135	18/11/96	9:57:04	1800	140	1.58	0.4672	-7.20	7.6	α Ari
2450406.79314622	19/11/96	6:47:10	900	140	1.34	0.9104	42.55	7.0	α Ari
2450406.92499244	19/11/96	9:57:02	900	150	1.60	0.9781	44.01	7.6	α Ari
2450408.75429680	21/11/96	5:48:13	1260	140	1.47	0.9175	43.61	8.0	α Ari
2450408.86176188	21/11/96	8:25:58	900	120	1.34	0.9727	47.67	8.6	α Ari
2450408.95522238	21/11/96	10:40:33	900	140	1.99	0.0207	47.40	7.7	α Ari
2450409.75060189	22/11/96	5:38:24	1800	130	1.49	0.4292	-3.87	7.3	α Ari
2450409.87995318	22/11/96	8:44:39	1800	140	1.38	0.4956	-7.74	7.4	α Ari
2450411.84548705	24/11/96	7:47:32	2700	140	1.31	0.5050	-5.61	7.2	α Ari

2450412.86152074	25/11/96	8:10:37	2700	150	1.34	0.0268	43.92	7.2	α Ari
2450414.75119559	27/11/96	5:31:46	2700	140	1.45	0.9972	45.59	8.4	α Ari
2450415.78868308	28/11/96	6:24:58	2700	140	1.33	0.5300	-4.54	7.4	α Ari
2450416.84316521	29/11/96	7:44:14	2700	140	1.33	0.0716	43.77	8.0	α Ari
2450417.87992018	30/11/96	8:29:43	3600	130	1.43	0.6040	-2.33	6.7	α Ari
2450418.86438290	01/12/96	8:22:21	1800	140	1.42	0.1096	36.45	8.9	α Ari
2450419.70589534	02/12/96	4:34:09	1800	140	1.61	0.5417	-4.57	7.6	α Ari
2450420.68467254	03/12/96	4:03:36	1800	140	1.78	0.0444	42.15	8.0	α Ari
2450421.80456207	04/12/96	7:02:17	1080	150	1.31	0.6195	-2.76	8.2	α Ari
2450422.79352103	05/12/96	6:46:28	1080	130	1.30	0.1274	34.40	8.5	α Ari
2450423.78074261	06/12/96	6:26:35	1260	130	1.30	0.6343	1.02	6.8	α Ari
2450424.90900056	07/12/96	9:26:46	1800	140	1.89	0.2138	21.38	8.4	α Ari
2450425.88593564	08/12/96	8:53:31	1800	150	1.67	0.7155	10.92	7.2	α Ari
2450426.89264277	09/12/96	9:03:21	1800	140	1.76	0.2325	19.08	8.6	α Ari
2450428.91439143	11/12/96	9:34:40	1800	130	2.14	0.2707	13.82	8.2	α Ari
2450429.87755393	12/12/96	8:41:45	1800	150	1.69	0.7654	18.65	8.0	α Ari
2450430.88667993	13/12/96	8:54:57	1800	150	1.82	0.2836	12.93	7.8	α Ari
2450431.71075924	14/12/96	4:41:41	1800	150	1.40	0.7068	10.53	6.9	α Ari
2450432.89437238	15/12/96	9:06:09	1800	150	1.99	0.3146	7.32	7.7	α Ari
2450435.73593090	18/12/96	5:10:39	2700	130	1.32	0.7739	21.00	7.0	α Ari
2450436.72737582	19/12/96	4:58:23	2700	140	1.33	0.2831	11.22	7.6	α Ari
2450437.78293088	20/12/96	6:30:26	1260	140	1.34	0.8252	27.44	7.2	α Ari
2450438.88091902	21/12/96	8:47:06	1800	140	2.04	0.3890	1.13	7.6	α Ari
2450440.72651416	23/12/96	5:04:54	1800	130	1.31	0.3368	6.08	5.9	α Ari
2450441.87574535	24/12/96	8:44:20	1260	140	2.15	0.9270	44.35	6.7	α Ari
2450446.65767851	29/12/96	3:22:53	2232	140	1.46	0.3828	-0.36	6.2	α Ari
2450447.83059191	30/12/96	7:42:50	900	130	1.77	0.9851	43.29	8.0	α Ari
2450448.70624150	31/12/96	4:43:50	900	140	1.30	0.4348	-6.85	6.8	α Ari
2450450.82337754	02/01/97	7:32:41	900	130	1.79	0.5221	-7.65	7.6	α Ari
2450451.83619104	03/01/97	7:48:14	1260	120	1.96	0.0422	43.62	7.4	α Ari
2450453.74258670	05/01/97	5:30:24	1676	100	1.34	0.0212	43.78	7.8	α Ari
2450454.82479083	06/01/97	7:20:07	2700	120	1.81	0.5770	-5.12	7.5	α Ari
2450456.83642216	08/01/97	7:29:33	3600	130	1.97	0.6101	-1.62	7.2	α Ari
2450457.76155057	09/01/97	5:59:50	1440	130	1.45	0.0852	40.43	8.2	α Ari

KPNO 94 Mar

Observations from Mar 4 – Mar 18, 1994

HJD	date	UT	$t_{\rm exp}$	S/N	airmass	phase	v_r	σ_{v_r}	RV Std
2449416.61902162	05/03/94	2:28:22	1917	200	1.46	0.4071	-2.40	3.0	δ Aur
2449417.61724752	06/03/94	2:25:56	3000	270	1.46	0.9197	43.65	4.4	16 Vir
2449426.60346990	15/03/94	2:20:57	3000	300	1.59	0.5346	-7.75	3.4	16 Vir

KPNO 95 Feb

Observations from Feb 22 – Mar 7, 1995

HJD	date	UT	$t_{\rm exp}$	S/N	airmass	phase	v_r	σ_{v_r}	RV Std
2449770.60061516	22/02/95	2:00:27	3000	200	1.31	0.1941	28.79	4.7	16 Vir
2449773.61609044	25/02/95	2:23:07	3000	200	1.36	0.7427	11.56	4.9	16 Vir

2449774.59440811	26/02/95	1:56:11	2554	200	1.32	0.2451	19.73	6.6	α Tau
2449781.59376862	05/03/95	1:58:38	2204	180	1.37	0.8396	34.63	7.2	α Tau
2449783.61495233	07/03/95	2:28:33	2312	210	1.48	0.8776	39.89	7.2	α Tau

KPNO 96 Jan

Observations from Jan 10 – 24, 1996

HJD	date	UT	$t_{\rm exp}$	S/N	airmass	phase	v_r	σ_{v_r}	RV Std
2450093.58895868	11/01/96	1:48:38	1800	310	1.66	0.0646	47.48	3.63	α Tau
2450093.72198162	11/01/96	4:45:12	3600	320	1.31	0.1329	39.57	3.20	α Tau
2450093.86983001	11/01/96	8:28:07	2429	330	3.23	0.2088	29.50	3.22	α Tau
2450094.58586781	12/01/96	1:29:17	3600	270	1.77	0.5765	-0.35	3.99	α Tau
2450094.75631891	12/01/96	5:34:45	3600	190	1.40	0.6641	9.93	4.10	α Tau
2450094.84253948	12/01/96	7:38:55	3600	280	2.23	0.7083	18.69	4.40	α Tau
2450095.59933732	13/01/96	1:48:47	3600	350	1.62	0.0970	45.06	2.25	β Gem
2450095.84999107	13/01/96	7:49:45	3600	360	2.47	0.2257	29.28	2.30	β Gem
2450096.58167400	14/01/96	1:23:27	3600	370	1.75	0.6015	1.03	3.63	α Tau
2450096.84057936	14/01/96	7:36:18	3600	360	2.31	0.7344	22.23	2.60	β Gem
2450098.58923565	16/01/96	1:34:33	3676	300	1.63	0.6324	5.23	2.35	16 Vir
2450100.63909368	18/01/96	2:46:34	3600	240	1.35	0.6852	13.49	2.70	β Gem
2450100.83270193	18/01/96	7:25:23	3600	310	2.38	0.7846	30.55	2.48	β Gem
2450101.58188063	19/01/96	1:24:17	3600	220	1.62	0.1693	35.55	3.54	β Gem
2450101.72781877	19/01/96	4:54:27	3600	330	1.37	0.2443	22.79	2.05	β Gem
2450102.72229088	20/01/96	4:46:36	3600	270	1.36	0.7550	23.66	2.28	β Gem
2450103.72935395	21/01/96	4:56:53	3600	190	1.39	0.2722	18.63	1.83	β Gem
2450103.83519003	21/01/96	7:29:18	3600	210	2.69	0.3265	10.44	1.78	β Gem
2450106.60196237	24/01/96	2:01:16	2705	180	1.40	0.7474	22.37	2.39	16 Vir
2450106.71444160	24/01/96	4:35:45	3600	250	1.37	0.8051	31.37	2.35	16 Vir
2450106.83906083	24/01/96	7:40:13	3005	350	3.35	0.8692	39.50	2.49	16 Vir
2450107.68453725	25/01/96	3:52:48	3600	190	1.31	0.3033	8.19	2.00	16 Vir
2450107.77017848	25/01/96	5:56:08	3600	280	1.71	0.3473	2.75	2.01	16 Vir
2450107.82899318	25/01/96	7:20:50	3600	220	2.87	0.3775	0.75	2.35	16 Vir

KPNO 97 Dec

Observations from Dec 26, 1997 – Jan 14, 1998. "Bl." is the block number for DI; see §6.3.

HJD	date	UT	$t_{\rm exp}$	S/N	airmass	phase	v_r	σ_{v_r}	RV Std	Bl.
2450809.58273645	27/12/97	1:23:03	3640	299	2.64	0.7627	20.68	2.2	α Ari	3
2450809.72859092	27/12/97	4:40:38	5135	294	1.31	0.8376	32.50	1.9	β Gem	3
2450809.86952719	27/12/97	8:04:04	5078	237	1.83	0.9100	42.79	2.0	β Gem	3
2450810.58576035	28/12/97	1:27:28	3642	288	2.47	0.2778	14.96	2.0	α Ari	1
2450810.68774591	28/12/97	3:44:42	4798	221	1.40	0.3302	6.80	2.2	α Ari	2
2450810.82391309	28/12/97	7:02:49	4555	153	1.50	0.4001	-0.53	2.0	β Gem	3
2450811.62176909	29/12/97	2:19:09	3672	188	1.79	0.8099	28.22	1.8	α Ari	1
2450811.72285058	29/12/97	4:44:58	3642	198	1.30	0.8618	36.34	2.3	α Ari	2
2450811.82025871	29/12/97	7:05:16	3639	232	1.52	0.9118	42.17	1.9	α Ari	1
2450811.90381865	29/12/97	9:13:12	2727	201	3.10	0.9547	45.86	1.6	β Gem	2
2450812.86269379	30/12/97	8:29:17	900	81	2.24	0.4471	-5.48	1.9	β Gem	1

2450813.58682342	31/12/97	1:29:14	3643	312	2.25	0.8190	30.62	2.3	α Ari	2
2450813.68721789	31/12/97	3:53:49	3642	372	1.35	0.8706	37.31	1.9	α Ari	1
2450813.80771387	31/12/97	6:10:19	8085	389	1.37	0.9325	45.17	1.5	β Gem	3
2450813.89197395	31/12/97	8:48:41	3642	333	2.66	0.9757	47.30	1.8	β Gem	1
2450814.58051026	01/01/98	1:20:15	3640	348	2.32	0.3293	7.42	1.7	α Ari	3
2450814.66755949	01/01/98	3:25:36	3641	383	1.41	0.3740	1.37	2.2	α Ari	1
2450814.72819247	01/01/98	4:54:33	3445	376	1.30	0.4052	-1.22	1.9	α Ari	2
2450814.81155554	01/01/98	6:56:18	3241	368	1.53	0.4480	-3.79	2.3	α Ari	3
2450814.91346455	01/01/98	9:30:54	2300	107	4.45	0.5003	-8.52	2.1	16 Vir	2
2450815.58646849	02/01/98	1:29:43	3544	360	2.13	0.8459	34.89	2.2	α Ari	3
2450815.68379471	02/01/98	3:49:04	3641	381	1.35	0.8959	40.47	2.2	α Ari	2
2450815.79300152	02/01/98	6:26:19	3643	361	1.44	0.9520	44.52	2.2	α Ari	1
2450815.85301531	02/01/98	8:15:36	900	184	2.22	0.9828	48.18	1.9	β Gem	3
2450816.58303964	03/01/98	1:24:03	3642	319	2.15	0.3577	2.53	1.8	α Ari	2
2450819.66147317	06/01/98	3:17:16	3643	313	1.38	0.9387	43.50	2.1	α Ari	1
2450819.77794707	06/01/98	6:05:01	3641	323	1.42	0.9985	46.63	2.0	α Ari	2
2450819.87733875	06/01/98	8:28:09	3641	280	2.73	0.0495	44.08	2.2	16 Vir	3
2450820.57320682	07/01/98	1:10:15	3643	328	2.13	0.4069	-3.37	1.7	α Ari	1
2450820.68061358	07/01/98	3:44:55	3644	302	1.32	0.4620	-5.41	1.7	β Gem	2
2450820.78112776	07/01/98	6:09:41	3642	334	1.45	0.5137	-6.18	1.6	β Gem	1
2450820.87562960	07/01/98	8:25:46	3643	265	2.77	0.5622	-4.86	1.8	β Gem	3
2450821.57235406	08/01/98	1:09:07	3643	332	2.09	0.9200	43.51	1.7	β Gem	2
2450821.67462729	08/01/98	3:36:24	3643	361	1.33	0.9725	47.03	1.5	β Gem	2
2450821.77773380	08/01/98	6:04:53	3643	363	1.44	0.0255	47.53	1.7	β Gem	1
2450821.88964179	08/01/98	9:01:09	1830	91	4.31	0.0829	42.76	1.8	β Gem	2
2450822.71209769	09/01/98	4:20:39	4820	308	1.30	0.5053	-7.25	2.0	β Gem	3
2450822.81245542	09/01/98	6:54:59	3643	368	1.70	0.5568	-4.62	1.8	β Gem	2
2450822.86863216	09/01/98	8:15:54	3641	325	2.72	0.5857	-2.93	2.1	β Gem	1
2450823.78021880	10/01/98	6:08:39	3644	362	1.48	0.0538	45.33	2.0	β Gem	1
2450825.62981148	12/01/98	2:32:15	3644	368	1.44	0.0037	46.19	1.9	α Ari	3
2450825.71605559	12/01/98	4:36:28	3642	361	1.31	0.0480	44.99	1.8	α Ari	2
2450825.78051100	12/01/98	6:09:18	3641	341	1.52	0.0811	43.04	2.1	α Ari	1
2450825.86746150	12/01/98	8:14:30	3643	253	2.99	0.1257	38.20	1.6	β Gem	2
2450826.58727787	13/01/98	1:31:07	3642	358	1.71	0.4954	-7.26	2.0	α Ari	1
2450826.71078173	13/01/98	4:28:59	3641	374	1.30	0.5588	-5.73	2.1	α Ari	1
2450826.77149497	13/01/98	5:56:25	3641	356	1.48	0.5900	-3.41	1.8	α Ari	2
2450826.87359944	13/01/98	8:31:04	2728	124	3.74	0.6424	2.18	2.2	β Gem	3
2450827.70428623	14/01/98	4:19:38	3653	163	1.30	0.0690	43.71	2.2	α Ari	3
2450827.77446631	14/01/98	6:00:42	3653	342	1.51	0.1051	41.39	2.0	α Ari	3
2450827.84209449	14/01/98	7:38:10	3644	151	2.37	0.1398	37.29	2.1	α Ari	1
2450827.87402503	14/01/98	8:23:54	3674	122	3.60	0.1562	35.47	2.0	α Ari	3
2450828.57683812	15/01/98	1:16:17	3643	158	1.76	0.5171	-6.92	2.0	α Ari	2
2450828.59804605	15/01/98	1:46:46	3650	330	1.57	0.5280	-7.01	2.0	α Ari	3
2450828.70171256	15/01/98	4:16:07	3643	310	1.30	0.5813	-4.48	1.7	α Ari	3
2450828.82504772	15/01/98	7:13:43	3645	301	2.08	0.6446	1.91	2.3	16 Vir	1
2450828.86755618	15/01/98	8:14:55	3647	280	3.40	0.6664	4.78	1.9	16 Vir	2

A.2 The MUSICOS 1998 campaign

Table A.25 shows a log of all MUSICOS observations of EI Eridani. Radial velocities are only available for OHP193, BXO and MSO (see § 5.2.2). Proper HJD values for SAAO could not be determined as the term "Btime" (used in the image header as "start of observing time" keyword) could not be resolved. However, due to the low quality of the four SAAO spectra and a good overall phase coverage from the other observing sites during the period of the SAAO observations, those four spectra are not used for Doppler imaging.

Site	Date	HJD	$t_{\rm exp}$[s]	S/N	v_r	RVSS
OHP193	23 Nov	2451141.37583988	1200	200	35.1 ± 3.8	α Tau
OHP193	23 Nov	2451141.48556179	1200	190	26.8 ± 3.1	α Tau
OHP193	24 Nov	2451141.60500541	1200	180	23.4 ± 4.4	α Tau
OHP193	26 Nov	2451144.37303930	1800	170	9.5 ± 3.1	α Tau
OHP193	27 Nov	2451145.37441777	1800	100	27.3 ± 4.8	α Tau
OHP193	28 Nov	2451146.36989177	2100	210	13.2 ± 3.6	α Tau
OHP193	29 Nov	2451147.45077963	2400	180	16.2 ± 3.0	α Tau
SAAO	01 Dec	(22:09 Btime)	1800.	(80)		
SAAO	02 Dec	(21:29)	924.			
SAAO	03 Dec	(21:13)	1800.	(90)		
SAAO	04 Dec	(00:52)	1800.			
BXO	01 Dec	2451149.25642	5400.	30	-6.4 ± 2.8	33 Sex
BXO	02 Dec	2451150.10649	3000.	80	61.8 ± 1.2	α Tau
BXO	02 Dec	2451150.21550	3000.	140	69.9 ± 1.7	α Tau
BXO	02 Dec	2451150.27836	3000.	150	75.3 ± 1.4	α Tau
BXO	04 Dec	2451152.09376	3000.	120	3.2 ± 2.7	α Tau
BXO	04 Dec	2451152.19891	3000.	120	12.3 ± 3.3	α Tau
BXO	04 Dec	2451152.27990	3000.	80	18.3 ± 2.5	α Tau
BXO	07 Dec	2451155.15105	2700.	30	49.7 ± 2.3	α Tau
BXO	07 Dec	2451155.24648	3000.	40	48.6 ± 1.7	α Tau
MSO	29 Nov	2451147.04042	1500.	95	49.3 ± 4.6	β Lep
MSO	29 Nov	2451147.05919	1500.	120	49.7 ± 3.1	β Lep
MSO	29 Nov	2451147.16410	1500.	90	43.3 ± 2.2	β Lep
MSO	30 Nov	2451147.94040	1500.	100	0.6 ± 4.5	β Lep
MSO	30 Nov	2451148.02403	1500.	130	0.9 ± 1.9	β Lep
MSO	30 Nov	2451148.15425	1200.	100	6.9 ± 2.3	β Lep
MSO	01 Dec	2451148.93913	1500.	110	51.3 ± 3.6	β Lep
MSO	01 Dec	2451149.07460	1500.	110	45.7 ± 3.7	β Lep
MSO	01 Dec	2451149.15082	1200.	90	39.8 ± 6.2	β Lep
MSO	02 Dec	2451149.94285	1500.	25	-4.0 ± 6.4	β Lep
MSO	03 Dec	2451150.98270	1500.	105	49.3 ± 3.3	β Lep
MSO	03 Dec	2451151.04591	1200.	110	44.8 ± 2.6	β Lep
MSO	03 Dec	2451151.10611	1200.	110	41.8 ± 3.6	β Lep
KPNO	24 Nov	2451141.63019	1200.	45		
KPNO	24 Nov	2451141.67969	1200.	50		
KPNO	24 Nov	2451141.78911	1200.	40		
KPNO	24 Nov	2451141.92587	1200.	70		
KPNO	25 Nov	2451142.61928	1200.	55		
KPNO	25 Nov	2451142.70574	1200.	70		
KPNO	25 Nov	2451142.80249	1200.	60		
KPNO	25 Nov	2451142.90963	1200.	65		
KPNO	25 Nov	2451142.98487	1200.	65		
KPNO	26 Nov	2451143.80302	1500.	80		
KPNO	26 Nov	2451143.88231	1200.	70		
KPNO	26 Nov	2451143.89726	1200.	70		

KPNO	26 Nov	2451143.91224	1200.	70
KPNO	27 Nov	2451144.70456	1500.	80
KPNO	27 Nov	2451144.72323	1500.	80
KPNO	27 Nov	2451144.74190	1500.	80
KPNO	27 Nov	2451144.86733	1500.	80
KPNO	27 Nov	2451144.88594	1500.	70
KPNO	27 Nov	2451144.90453	1500.	65
ESO90	29 Nov	2451146.58071	2700.	170
ESO90	30 Nov	2451147.56183	2700.	170
ESO90	02 Dec	2451149.56834	2700.	160
ESO90	03 Dec	2451150.56477	2700.	200
ESO90	04 Dec	2451151.56331	2700.	170
ESO90	05 Dec	2451152.56155	2700.	250
ESO90	06 Dec	2451153.59846	2700.	130
ESO90	07 Dec	2451154.59340	2700.	150
ESO90	08 Dec	2451155.59898	2700.	170
ESO90	09 Dec	2451156.59905	2700.	170
ESO90	10 Dec	2451157.59908	2700.	200
ESO90	11 Dec	2451158.59838	2700.	170
ESO90	12 Dec	2451159.59979	2700.	170
ESO90	13 Dec	2451160.63132	2700.	170
ESO152	26 Nov	2451143.74576	600.	270
ESO152	26 Nov	2451143.85290	600.	190
ESO152	27 Nov	2451144.59754	600.	280
ESO152	27 Nov	2451144.85283	546.	170
ESO152	28 Nov	2451145.60065	600.	290
ESO152	28 Nov	2451145.80423	600.	270
ESO152	29 Nov	2451146.74656	600.	270
ESO152	29 Nov	2451146.83205	600.	310
ESO152	30 Nov	2451147.72803	600.	330
ESO152	30 Nov	2451147.81225	600.	320
ESO152	01 Dec	2451148.67180	600.	350
ESO152	01 Dec	2451148.76177	600.	280
ESO152	02 Dec	2451149.70264	600.	250
ESO152	02 Dec	2451149.78489	600.	290
ESO152	03 Dec	2451150.66693	600.	270
ESO152	03 Dec	2451150.74739	600.	280
ESO152	04 Dec	2451151.71147	600.	300
ESO152	04 Dec	2451151.79690	600.	220
INT	04 Dec	2451152.50107	1500.	70
INT	06 Dec	2451154.53835	1500.	50
INT	07 Dec	2451155.38794	1500.	50
INT	07 Dec	2451155.64474	1500.	90
INT	08 Dec	2451156.36766	1500.	90
INT	08 Dec	2451156.43590	1500.	110
INT	08 Dec	2451156.63331	1500.	110
INT	09 Dec	2451157.39970	1200.	160
INT	09 Dec	2451157.47034	1500.	160
INT	09 Dec	2451157.64745	1500.	170
INT	10 Dec	2451158.53580	1500.	120
OHP152	21 Nov	2451139.42099776	1200.	
OHP152	22 Nov	2451140.39846024	3000.	
OHP152	22 Nov	2451140.50784639	3000.	

OHP152	22 Nov	2451140.60826266	3000.
OHP152	25 Nov	2451143.55433185	3000.
OHP152	26 Nov	2451144.37713675	3000.
OHP152	27 Nov	2451145.38122326	3600.
OHP152	27 Nov	2451145.49359478	3000.
OHP152	27 Nov	2451145.5876213	3000.
OHP152	28 Nov	2451146.38628031	2292.
OHP152	29 Nov	2451147.48550733	2991.
OHP152	29 Nov	2451147.49584834	3000.
OHP152	29 Nov	2451147.58590494	3600.

MUSICOS observing log for EI Eri

A.3 Radial velocities from the literature

This list comprises 55 radial velocity measurements found in the literature: 27 from Fekel et al. (1987), 21 spectra from Strassmeier (1990), five from Gunn et al. (1996), and two from Donati et al. (1997). The RV values were, if possible, corrected to match the more precise RVSS velocities provided by Scarfe et al. (1990) instead of the IAU values. For a detailed description see §3.2, page 26f.

Additional radial velocities from the literature. The values were, if possible, corrected to match the RV standard star values of Scarfe et al. (1990).

HJD [24+]	date	phase	v_r [km s^{-1}]	Instrument	Ref.	RV Std
49346.1467	24/12/93	0.2161	24.5 ± 1	AAT/UCLES	D	?
49348.1099	26/12/93	0.2243	23.5 ± 1	AAT/UCLES	D	?
49643.9022	18/10/94	0.1281	28.5 ± 6.9	Lowell/JH 1.1m/SSS	G	?
49645.9176	20/10/94	0.1634	45.5 ± 2.8	Lowell/JH 1.1m/SSS	G	?
49647.8882	22/10/94	0.1751	30.9 ± 3.6	Lowell/JH 1.1m/SSS	G	?
49651.8605	26/10/94	0.2154	19.0 ± 10.1	Lowell/JH 1.1m/SSS	G	?
49655.8660	30/10/94	0.2722	14.4 ± 2.3	Lowell/JH 1.1m/SSS	G	?
47150.6665	21/12/87	0.7286	13.03	KPNO/CF	S	β Gem
47150.7295	21/12/87	0.7609	19.23	KPNO/CF	S	β Gem
47150.7964	21/12/87	0.7953	24.93	KPNO/CF	S	β Gem
47150.9253	21/12/87	0.8615	32.63	KPNO/CF	S	β Gem
47151.5811	22/12/87	0.1983	27.30	KPNO/CF	S	ι Psc
47151.7505	22/12/87	0.2852	14.19	KPNO/CF	S	α Ari
47151.8926	22/12/87	0.3582	2.45	KPNO/CF	S	10 Tau
47152.5664	23/12/87	0.7043	9.99	KPNO/CF	S	α Ari
47152.7280	23/12/87	0.7872	22.95	KPNO/CF	S	10 Tau
47156.9126	27/12/87	0.9362	42.33	KPNO/CF	S	β Gem
47157.5918	28/12/87	0.2850	12.49	KPNO/CF	S	α Ari
47157.6611	28/12/87	0.3206	5.49	KPNO/CF	S	α Ari
47157.8130	28/12/87	0.3986	-3.21	KPNO/CF	S	α Ari
47157.9033	28/12/87	0.4450	-6.47	KPNO/CF	S	β Gem
47163.6997	03/01/88	0.4218	-10.2	KPNO/CF	S	H_2O
47163.7451	03/01/88	0.4451	-6.0	KPNO/CF	S	H_2O
47163.8130	03/01/88	0.4799	-10.87	KPNO/CF	S	β Gem
47163.8486	03/01/88	0.4982	-10.87	KPNO/CF	S	β Gem
47163.8882	03/01/88	0.5186	-11.07	KPNO/CF	S	β Gem
47170.7617	10/01/88	0.0484	43.0	KPNO/CF	S	H_2O

47170.8936	10/01/88	0.1162	38.5	KPNO/CF	S	H_2O
44179.903	02/11/79	0.0948	43.15	McDonald 2.7m	F	10 Tau
44180.916	03/11/79	0.6150	-3.77	McDonald 2.1m	F	β Gem
44181.857	04/11/79	0.0983	40.79	McDonald 2.1m	F	α Ari
44182.814	05/11/79	0.5897	-8.81	McDonald 2.1m	F	α Ari
44473.973	22/08/80	0.1143	38.15	McDonald 2.7m	F	10 Tau
44475.963	24/08/80	0.1362	35.65	McDonald 2.7m	F	10 Tau
44478.955	27/08/80	0.6728	4.09	McDonald 2.1m	F	α Ari
44507.885	25/09/80	0.5298	-9.2	KPNO	F	–
44627.626	23/01/81	0.0227	44.43	McDonald 2.7m	F	β Gem
45356.702	22/01/83	0.4392	-6.37	KPNO/CF/RCA CCD	F	β Gem
45357.670	23/01/83	0.9363	41.93	KPNO/CF/RCA CCD	F	β Gem
45358.679	24/01/83	0.4545	-10.41	KPNO/CF/RCA CCD	F	α Ari
45359.745	25/01/83	0.0019	47.59	KPNO/CF/RCA CCD	F	α Ari
45360.716	26/01/83	0.5006	-7.07	KPNO/CF/RCA CCD	F	β Gem
45361.702	27/01/83	0.0069	41.23	KPNO/CF/RCA CCD	F	β Gem
45594.999	17/09/83	0.8165	27.89	KPNO/CF/TI CCD	F	α Ari
45596.022	19/09/83	0.3418	3.13	KPNO/CF/TI CCD	F	β Gem
45596.963	19/09/83	0.8251	27.63	KPNO/CF/TI CCD	F	β Gem
45599.008	22/09/83	0.8753	36.25	KPNO/CF/TI CCD	F	10 Tau
45717.791	18/01/84	0.8762	34.75	KPNO/CF/TI CCD	F	10 Tau
45718.764	19/01/84	0.3759	1.83	KPNO/CF/TI CCD	F	β Gem
45719.768	20/01/84	0.8915	39.83	KPNO/CF/TI CCD	F	β Gem
45720.740	21/01/84	0.3907	-3.75	KPNO/CF/TI CCD	F	10 Tau
45721.727	22/01/84	0.8976	40.63	KPNO/CF/TI CCD	F	β Gem
45941.958	29/08/84	0.9971	45.3	KPNO/CF/TI CCD	F	ι Psc
45971.996	28/09/84	0.4231	-7.11	KPNO/CF/TI CCD	F	α Ari
46076.766	11/01/85	0.2276	21.99	KPNO/CF/TI CCD	F	α Ari

Reference code (including a list of radial velocity standard stars used):
D ... Donati et al. (1997): ?
F ... Fekel et al. (1987): β Gem (3.3 km s^{-1}), α Ari (-14.3 km s^{-1}), 10 Tau (27.9 km s^{-1}), ι Psc (5.3 km s^{-1})
G ... Gunn et al. (1996): γ Aql (-2.1 km s^{-1}), ι Psc (5.3 km s^{-1}), α Tau (54.1 km s^{-1})
S ... Strassmeier (1990): β Gem (3.3 km s^{-1}), α Ari (-14.3 km s^{-1}), 10 Tau (27.9 km s^{-1}), ι Psc (5.3 km s^{-1}), H_2O

Appendix B

Various mathematical functions and their errors

"Man errs as long as he doth strive", argues Goethe (1808), and he was likely having error calculation in mind as its entangled formulae are prone for typing mistakes when feeding them into a pocket calculator. Thus, I assembled a program code and embedded it into a web page for convenient use.[1] It comprises the formulae presented in this appendix and was applied throughout this thesis for evaluating the appropriate calculations including proper error propagation.

B.1 Law of error propagation

For calculating the error of a function (which consists of a number of values, all equiped with an individual error), we have to apply the law of error propagation:

$$\sigma_y = \sqrt{\sum_i \left(\frac{\partial f}{\partial x_i}\right)^2 \sigma_{x_i}^2} \ , \tag{B.1}$$

where $y = f(x_1, x_2, \ldots)$, and σ_{x_i} are the individual errors. This is used for all the following sections.

B.2 Mass function

For a single-lined spectroscopic binary star (SB1), we do not know much about the secondary component except the so-called *mass function*

$$f(\mathrm{M}) = \frac{(M_2 \sin i)^3}{(M_1 + M_2)^2} \ . \tag{B.2}$$

However, if we know the primary mass M_1 and the inclination i, we can evaluate the secondary mass M_2. The mass function can be transformed to

$$M_1 = \sqrt{\frac{(M_2 \sin i)^3}{f(\mathrm{M})}} - M_2 \tag{B.3}$$

which allows for a numerical solution for M_2. Finding an analytical solution for M_2 is, though, possible:

$$M_2 = \frac{f(\mathrm{M})}{9 \sin^3 i} \left(\frac{1}{2} \sqrt[3]{-4\beta + 4\sqrt{\beta^2 - 4}} + \frac{1}{2} \sqrt[3]{-4\beta - 4\sqrt{\beta^2 - 4}} - 1 \right)^2 \tag{B.4}$$

[1] The tool can be found at http://wasi.ws/astro/calc/ .

where $\beta = 27 M_1 \frac{sin^3 i}{f(\mathrm{M})}$. However, with β^2 being in the order of 10^7, $\sqrt{\beta^2 - 4}$ can be corrupted by a rounding error. Therefore, we try to simplify the formular, using the approximation

$$(1 \pm \varepsilon)^n \approx 1 \pm n\varepsilon \qquad |\varepsilon| \ll 1 \ , \tag{B.5}$$

and transform Eq. B.4 to

$$M_2 = \frac{f(\mathrm{M})}{9 \sin^3 i} \left(\sqrt[3]{\frac{\beta}{2}} \left(\sqrt[3]{1 - \sqrt{1 - \frac{4}{\beta^2}}} + \sqrt[3]{1 + \sqrt{1 - \frac{4}{\beta^2}}} \right) + 1 \right)^2 \ . \tag{B.6}$$

We apply Eq. B.5 and achieve

$$M_2 = \frac{f(\mathrm{M})}{9 \sin^3 i} \left(\beta^{\frac{1}{3}} + \beta^{-\frac{1}{3}} + 3\beta^{-\frac{5}{3}} + 1 \right)^2 \ . \tag{B.7}$$

For calculating the error, we transform Eq. B.2 to

$$M_1 + M_2 = M_2^{\frac{3}{2}} \sin^{\frac{3}{2}} i \ \ f(\mathrm{M})^{-\frac{3}{2}} \tag{B.8}$$

where M_2 is a function of M_1, i and $f(\mathrm{M})$. Using the law of error propagation, we derive

$$\begin{aligned} \sigma_{M_2}^2 \quad = \quad & \left(\frac{3}{2} M_2^{\frac{1}{2}} \sin^{\frac{3}{2}} i \ \ f(\mathrm{M})^{-\frac{3}{2}} \right)^{-2} \cdot \sigma_{M_1}^2 + \left(\frac{M_2^{\frac{3}{2}} \ f(\mathrm{M})^{-\frac{5}{2}}}{\frac{2}{3} \sin^{-\frac{3}{2}} i - M_2^{\frac{1}{2}} f(\mathrm{M})^{-\frac{3}{2}}} \right)^2 \cdot \sigma_{f(\mathrm{M})}^2 + \\ & + \left(\frac{M_2^{\frac{3}{2}} \sin^{\frac{1}{2}} i \cos i \, \frac{\pi}{180}}{\frac{2}{3} f(\mathrm{M})^{\frac{3}{2}} - M_2^{\frac{1}{2}} \sin^{\frac{3}{2}} i} \right)^2 \cdot \sigma_i^2 \ . \end{aligned} \tag{B.9}$$

B.3 Eclipse criterion

If there appears to be no photometric evidence of eclipses, one can use the eclipse criterion

$$R_1 + R_2 < a \cos i \tag{B.10}$$

for estimating upper limits for stellar radii or for the inclination. If the latter is the case, we have to transform the eclipse criterion since only the combined value of $a \sin i$ is known from the orbital solution:

$$\tan i < \frac{a \sin i}{R_1 + R_2} \ . \tag{B.11}$$

If the stellar radii are given in units of the solar radius, $a \sin i$ has to be divided by $\mathrm{R}_\odot = 696000\,\mathrm{km}$ first. The error in i can be calculated by

$$\sigma_i = \frac{180 \sqrt{\sigma_{a \sin i}^2 (R_1 + R_2)^2 + (a \sin i)^2 (R_2^2 \sigma_{R_1}^2 + R_1^2 \sigma_{R_2}^2)}}{\pi (1 + \tan i)(R_1 + R_2)^2} \ . \tag{B.12}$$

B.4 Stellar inclination

If the stellar radius R, the rotational period P_{rot} and the projected equatorial velocity $v \sin i$ are known, the inclination i can be directly calculated:

$$\sin i = \frac{P_{\mathrm{rot}} \cdot v \sin i}{50.6 \cdot R/\mathrm{R}_\odot} \ . \tag{B.13}$$

The appropriate error comes to

$$\sigma_i = \frac{180}{\pi \cos i} \sqrt{\left(\sigma_{P_{\mathrm{rot}}} \frac{v \sin i}{50.6 \cdot R/\mathrm{R}_\odot} \right)^2 + \left(\sigma_{v \sin i} \frac{P_{\mathrm{rot}}}{50.6 \cdot R/\mathrm{R}_\odot} \right)^2 + \left(\sigma_R \frac{P_{\mathrm{rot}} \cdot v \sin i}{50.6 \cdot (R/\mathrm{R}_\odot)^2} \right)^2} \ . \tag{B.14}$$

If $R \sin i = P_{\mathrm{rot}} \cdot v \sin i / 50.6$ is calculated instead, the last term of Eq. B.14 is omited ($\sigma_R = 0$) in order to obtain $\sigma_{R \sin i}$ (instead of σ_i).

B.5 Roche lobe

For calculating the effective radius r_{L} of a Roche lobe, we use the approximation presented by Eggleton (1983) which has an accuracy of better than 1% over the whole range:

$$r_{\mathrm{L}} = \frac{0.49q^{\frac{2}{3}}}{0.6q^{\frac{2}{3}} + \ln(1+q^{\frac{1}{3}})} \qquad 0 < q < \infty. \tag{B.15}$$

q is the mass ratio and the sepraration of the two stellar centers is unity. For calculating the error $\sigma_{r_{\mathrm{L}}}$, we again apply the law of error propagation (Eq. B.1) and achieve

$$\sigma_{r_{\mathrm{L}}} = \left(\frac{0.98}{3} q^{-\frac{1}{3}} Q^{-1} - 0.49 q^{\frac{2}{3}} Q^{-2} \left(\frac{2}{5} q^{-\frac{1}{3}} + \frac{q^{-\frac{2}{3}}}{3+3q^{\frac{1}{3}}} \right) \right) \cdot \sigma_q \tag{B.16}$$

where Q is the denominator of Eq. B.15: $Q = 0.6q^{\frac{2}{3}} + \ln(1+q^{\frac{1}{3}})$, and the squared error of q is

$$\sigma_q^2 = \left(\frac{\sigma_{M_1}}{M_2} \right)^2 + \left(\frac{M_1 \sigma_{M_2}}{M_2^2} \right)^2 . \tag{B.17}$$

B.6 Luminosity and Stefan-Boltzmann law

The error for Equation 3.3 on page 40 can be obtained by

$$\sigma_{M_V}^2 = \sigma_{m_V}^2 + \left(\frac{5 \cdot \sigma_R}{R \cdot \ln 10} \right)^2 . \tag{B.18}$$

Consequently,

$$\sigma_{M_{\mathrm{bol}}} = \sqrt{\sigma_{M_V}^2 BC2 + \sigma_{BC}^2 M_V^2} . \tag{B.19}$$

The error of the luminosity (Eq. 3.5) comes to

$$\sigma_{L/\mathrm{L}_\odot} = \frac{\ln 10}{2.5}\ 10^{\frac{4.72-M_{\mathrm{bol}}}{2.5}} \cdot \sigma_{M_{\mathrm{bol}}} = 71.166512 \cdot 10^{-0.4M_{\mathrm{bol}}} \cdot \sigma_{M_{\mathrm{bol}}} , \tag{B.20}$$

the error for the radius, applying the Stefan-Boltzmann law (Eq. 3.6), is

$$\sigma_{R/\mathrm{R}_\odot}^2 = \left(2\sqrt{L/\mathrm{L}_\odot}\, \frac{T_\odot^2}{T^3}\, \sigma_T \right)^2 + \left(\frac{1}{2} \left(\frac{T_\odot}{T} \right)^2 (L/\mathrm{L}_\odot)^{-\frac{1}{2}}\, \sigma_{L/\mathrm{L}_\odot} \right)^2 \tag{B.21}$$

B.7 Angular distance

With known distance from the object d and known diameter or separation of the object(s) R, one can easily calculate the angular diameter or separation θ with the use of trigonometric functions:

$$\theta = \arctan\left(\frac{R}{d} \right) \tag{B.22}$$

where the error amounts to

$$(\sigma_\theta)^2 = \left(\frac{\sigma_R}{d + \frac{R^2}{d}} \right)^2 + \left(\frac{R\ \sigma_d}{d^2 + R^2} \right)^2 . \tag{B.23}$$

Bibliography

Aarum, V. 1999, in ASP Conf. Ser. 158: Solar and Stellar Activity: Similarities and Differences, 158

Aarum Ulvås, V. & Engvold, O. 2003, A&A, 402, 1043

Abt, H. A. 1986, ApJ, 309, 260

Alexander, D. R. & Ferguson, J. W. 1994, ApJ, 437, 879

AURA. 1971, Kitt Peak National Observatory and Cerro Tololo Inter-American Observatory, Quarterly Report, Oct.-Nov.-Dec.

Baliunas, S. & Soon, W. 1995, ApJ, 450, 896

Baliunas, S. L., Donahue, R. A., Soon, W. H., Horne, J. H., Frazer, J., Woodard-Eklund, L., & Bradford, M. e. a. 1995, ApJ, 438, 269

Barker, E. S., Evans, D. S., & Laing, J. D. 1967, Royal Greenwich Observatory Bulletin, 130, 355

Barnes, T. G., Evans, D. S., & Moffett, T. J. 1978, MNRAS, 183, 285

Beichman, C. A., Neugebauer, G., Habing, H. J., Clegg, P. E., & Chester, T. J. 1988, NASA Reference Publication, 1190, 1

Berdyugina, S. V. 2002, AN, 323, 192

Berdyugina, S. V., Berdyugin, A. V., Ilyin, I., & Tuominen, I. 1998, A&A, 340, 437

—. 1999, A&A, 350, 626

Berdyugina, S. V., Ilyin, I., & Tuominen, I. 2001, in ASP Conf. Ser. 223: 11th Cambridge Workshop on Cool Stars, Stellar Systems and the Sun, 1207

Berdyugina, S. V. & Tuominen, I. 1998, A&A, 336, L25

Bidelman, W. P. & MacConnell, D. J. 1973, AJ, 78, 687

Bopp, B. W., Africano, J. L., Stencel, R. E., Noah, P. V., & Klimke, A. 1983, ApJ, 275, 691

Bradstreet, D. H. 1993, http://www.binarymaker.com/

Brandenburg, A. & Dobler, W. 2002, AN, 323, 411

Busso, M., Scaltriti, F., Origlia, L., Persi, P., & Ferrari-Toniolo, M. 1988, MNRAS, 234, 445

Byrne, P. B. 1992, in LNP Vol. 397: Surface Inhomogeneities on Late-Type Stars, 3

Çakırlı, Ö., İbanoğlu, C., Djurašević, G., Erkapić, S., Evren, S., & Taş, G. 2003, A&A, 405, 733

Cardini, D., Cassatella, A., Badiali, M., Altamore, A., & Fernández-Figueroa, M.-J. 2003, A&A, 408, 337

Carpenter, K., Danchi, W., Leitner, J., Liu, A., Lyon, R., Mazzuca, L., Moe, R., Chenette, D., Schrijver, C., Kilston, S., Karovska, M., Allen, R., Brown, A., Marzouk, J., Murphy, N., & Walter, F. 2004, American Astronomical Society Meeting, 204,

Catala, C. 1998, in Cyclical Variability in Stellar Winds, 349

Catala, C. & Foing, B. H., eds. 1988, MUSICOS: Multi-Site Continuous Spectroscopy : 1 : 1988, 129

Chochol, D., Pribulla, T., Teodorani, M., Errico, L., Vittone, A. A., Milano, L., & Barone, F. 1998, A&A, 340, 415

Choi, H., Soon, W., Donahue, R. A., Baliunas, S. L., & Henry, G. W. 1995, PASP, 107, 744

Choudhuri, A. R., Schussler, M., & Dikpati, M. 1995, A&A, 303, L29

Collier Cameron, A. 1992a, in Surface Inhomogeneities on Late-Type Stars; Proceedings of a Colloquium Held at Armagh Observatory, Northern Ireland, 24 - 27 July 1990, XVI, 355 pp.. Springer-Verlag Berlin Heidelberg New York. Also Lecture Notes in Physics, volume 397, ed. P. B. Byrne & D. J. Mullan, 33

Collier Cameron, A. 1992b, The Observatory, 112, 26

—. 1995, MNRAS, 275, 534

—. 1997, MNRAS, 287, 556

—. 2001, LNP Vol. 573: Astrotomography, Indirect Imaging Methods in Observational Astronomy, 183

—. 2002, AN, 323, 336

Collier Cameron, A., Jeffery, C. S., & Unruh, Y. C. 1992, in Stellar chromospheres, coronae and winds; Proceedings of a Workshop organized by CCP7, held at the Institute of Astronomy, Cambridge University, England, March 1992, Cambridge: Institute of Astronomy, 1992, ed. C. S. Jeffery & R. E. M. Griffin

Collier-Cameron, A. & Unruh, Y. C. 1994, MNRAS, 269, 814

Collier Cameron, A., Walter, F. M., Vilhu, O., Böhm, T., Catala, C., Char, S., & Clarke, F. J. e. a. 1999, MNRAS, 308, 493

Cutispoto, G. 1995, A&AS, 111, 507

de Medeiros, J. R. & Mayor, M. 1999, A&AS, 139, 433

Desteffani, J. 2004, http://www.jogi.com/astro/sternwasi/

Donati, J.-F., Cameron, A. C., Semel, M., Hussain, G. A. J., Petit, P., Carter, B. D., Marsden, S. C., Mengel, M., López Ariste, A., Jeffers, S. V., & Rees, D. E. 2003, MNRAS, 345, 1145

Donati, J.-F. & Collier Cameron, A. 1997, MNRAS, 291, 1

Donati, J.-F., Semel, M., Carter, B. D., Rees, D. E., & Collier Cameron, A. 1997, MNRAS, 291, 658

Drake, S. A., Simon, T., & Linsky, J. L. 1992, ApJS, 82, 311

Duemmler, R. & Aarum, V. 2001, A&A, 370, 974

Durney, B. R., De Young, D. S., & Roxburgh, I. W. 1993, Solar Physics, 145, 207

Eggleton, P. P. 1983, ApJ, 268, 368

Elstner, D. & Korhonen, H. 2004, in 13th Cambridge Workshop on Cool Stars, Stellar Systems and the Sun, submitted

ESA. 1997, The Hipparcos and Tycho Catalogues, ESA SP-1200

Fekel, F. C. 1980, in First Cambridge Workshop on Cool Stars, Stellar Systems, and the Sun, Vol. 1, 133

Fekel, F. C. 2003, private communication

Fekel, F. C., Hall, D. S., Henry, G. W., Landis, H. J., & Renner, T. R. 1982, IBVS, 2110, 1

Fekel, F. C., Moffett, T. J., & Henry, G. W. 1986, ApJS, 60, 551

Fekel, F. C., Quigley, R., Gillies, K., & Africano, J. L. 1987, AJ, 94, 726

Fekel, F. C., Strassmeier, K. G., Weber, M., & Washuettl, A. 1999, A&AS, 137, 369

Fernandez-Figueroa, M. J., Montes, D., de Castro, E., & Cornide, M. 1994, ApJS, 90, 433

Fitzpatrick, M. J. 1993, in ASP Conf. Ser. 52: Astronomical Data Analysis Software and Systems II, ed. B. J. Hanish R. J., Brissenden R. V. J., 472

Flower, P. J. 1996, ApJ, 469, 355

Fox, D. C., Linsky, J. L., Veale, A., Dempsey, R. C., Brown, A., Neff, J. E., Pagano, I., Rodono, M., Bromage, G. E., Kuerster, M., & Schmitt, J. H. M. M. 1994, A&A, 284, 91

Fröhlich, C. & Lean, J. 2002, AN, 323, 203

Freytag, B., Steffen, M., & Dorch, B. 2002, AN, 323, 213

García-Alvarez, D., Barnes, J. R., Collier Cameron, A., Doyle, J. G., Messina, S., Lanza, A. F., & Rodonò, M. 2003, A&A, 402, 1073

García-Sánchez, J., Paredes, J. M., & Ribó, M. 2003, A&A, 403, 613

Goethe, J. W. v. 1808, Faust I.

Granzer, T. 2002, AN, 323, 395

—. 2003, private communication

—. 2004, private communication

Granzer, T., Reegen, P., & Strassmeier, K. G. 2001, AN, 322, 325

Granzer, T., Schüssler, M., Caligari, P., & Strassmeier, K. G. 2000, A&A, 355, 1087

Gray, D. F. 1992, The observation and analysis of stellar photospheres (Cambridge Astrophysics Series, Cambridge: Cambridge University Press, 2nd ed.)

Gray, D. F., Baliunas, S. L., Lockwood, G. W., & Skiff, B. A. 1996, ApJ, 456, 365

Guinan, E. F. & Giménez, A. 1992, in ASSL Vol. 177: The Realm of Interacting Binary Stars, 51

Gunn, A. G., Hall, J. C., Lockwood, G. W., & Doyle, J. G. 1996, A&A, 305, 146

Hackman, T., Piskunov, N. E., Poutanen, M., Strassmeier, K. G., & Tuominen, I. 1991, in The Sun and Cool Stars. Activity, Magnetism, Dynamos. Proceedings of Colloquium No. 130 of the IAU. Editors, I. Tuominen, D. Moss, G. Rudiger; Springer-Verlag, 321

Hall, D. S. 1986, ApJ, 309, L83

—. 1989, Space Science Reviews, 50, 219

Hall, D. S. 1990, in NATO ASIC Proc. 319: Active Close Binaries Proceedings, NATO Advanced Study Institute, 95

—. 1991, LNP Vol. 380: IAU Colloq. 130: The Sun and Cool Stars. Activity, Magnetism, Dynamos, 353

Hall, D. S., Fekel, F. C., Henry, G. W., & Barksdale, W. S. 1991, AJ, 102, 1808

Hall, D. S., Osborn, S. A. G., Seufert, E. R., Boyd, L. J., Genet, R. M., & Fried, R. E. 1987, AJ, 94, 723

Harlan, E. A. 1974, AJ, 79, 682

Harvey, K. L. & White, O. R. 1999, J. Geophys. Res., 104, 19759

Hatzes, A. P. 1993, ApJ, 410, 777

—. 1995, AJ, 109, 350

Hatzes, A. P. & Cochran, W. D. 1993, ApJ, 413, 339

Hatzes, A. P. & Cochran, W. D. 1998, in ASP Conf. Ser. 154, The Tenth Cambridge Workshop on Cool Stars, Stellar Systems and the Sun, Edited by R. A. Donahue and J. A. Bookbinder, p.311, 311

Hatzes, A. P. & Kürster, M. 1999, A&A, 346, 432

Hatzes, A. P. & Vogt, S. S. 1992, MNRAS, 258, 387

Hatzes, A. P., Vogt, S. S., Ramseyer, T. F., & Misch, A. 1996, ApJ, 469, 808

Hearnshaw, J. 1979, in IAU Colloq. 46: Changing Trends in Variable Star Research, 371

Henry, G. W., Eaton, J. A., Hamer, J., & Hall, D. S. 1995, ApJS, 97, 513

Hoffleit, D. & Warren, W. H. 1995, VizieR Online Data Catalog, 5050

Holzwarth, V. & Schüssler, M. 2003, A&A, 405, 303

Hooten, J. T., Strassmeier, K. G., Hall, D. S., Barksdale, W. S., & Bertoglio, A. 1989, Ap&SS, 155, 45

Hut, P. 1981, A&A, 99, 126

Ibanoğlu, C., Evren, S., Taš, G., Devlen, A., & Çakïrlï, Ö. 2001, A&A, 371, 626

Iglesias, C. A. & Rogers, F. J. 1996, ApJ, 464, 943

Jetsu, L., Hackman, T., Hall, D. S., Henry, G. W., Kokko, M., & You, J. 2000, A&A, 362, 223

Johns-Krull, C. M. 1996, A&A, 306, 803

Kholopov, P. N., Samus, N. N., Kazarovets, E. V., & Perova, N. B. 1985, Informational Bulletin on Variable Stars, 2681, 1

Kippenhahn, R., Weigert, A., & Hofmeister, E. 1967, Meth. Comp. Phy., 7, 129

Kitchatinov, L. L. & Rüdiger, G. 1999, A&A, 344, 911

Komm, R. W., Howard, R. F., & Harvey, J. W. 1993, Solar Physics, 143, 19

Korhonen, H., Berdyugina, S. V., Hackman, T., Strassmeier, K. G., & Tuominen, I. 2004, A&A, in preparation

Kueker, M., Ruediger, G., & Kitchatinov, L. L. 1993, A&A, 279, L1

Kürster, M. 1993, A&A, 274, 851

Kürster, M., Schmitt, J. H. M. M., & Cutispoto, G. 1994, A&A, 289, 899

Kurucz, R. L. 1993, ATLAS-9 CD, CD

Lanza, A. F., Catalano, S., Cutispoto, G., Pagano, I., & Rodono, M. 1998, A&A, 332, 541

Lanza, A. F., Catalano, S., Rodonò, M., İbanoğlu, C., Evren, S., Taş, G., Çakırlı, Ö., & Devlen, A. 2002, A&A, 386, 583

Lanza, A. F. & Rodonò, M. 1999, A&A, 349, 887

Lloyd-Evans, T. & Koen, M. C. J. 1987, South African Astronomical Observatory Circular, 11, 21

Lucy, L. B. & Sweeney, M. A. 1971, AJ, 76, 544

McDowell, J. C., ed. 1994, The Einstein Observatory Soft X-ray Source List.

Mihalas, D., Hummer, D. G., Mihalas, B. W., & Daeppen, W. 1990, ApJ, 350, 300

Moreau, G. 1878, "Phaethon" (painting)

Moss, D. & Tuominen, I. 1997, A&A, 321, 151

Mullan, D. J. & MacDonald, J. 2001, ApJ, 559, 353

Mutel, R. L. & Lestrade, J. F. 1985, AJ, 90, 493

Nietzsche, F. 1882, The Gay Science, Vol. 3, 109

Oláh, K. 2003, private communication

—. 2004, private communication

Oláh, K., Jurcsik, J., & Strassmeier, K. G. 2003, A&A, 410, 685

Oláh, K., Kolláth, Z., & Strassmeier, K. G. 2000, A&A, 356, 643

Oláh, K., Strassmeier, K. G., & Granzer, T. 2002a, AN, 323, 453

Oláh, K., Strassmeier, K. G., & Weber, M. 2002b, A&A, 389, 202, (paper XVIII)

Olah, K. & Strassmeier, K. G. 2002, AN, 323, 361

O'Neal, D., Neff, J. E., & Saar, S. H. 1998, ApJ, 507, 919

O'Neal, D., Saar, S. H., & Neff, J. E. 1996, ApJ, 463, 766

Osten, R. A., Brown, A., Wood, B. E., & Brady, P. 2002, ApJS, 138, 99

Ovidius Naso, P. 8 A.D., Metamorphoses, Vol. 2, 319–324

Pallavicini, R., Randich, S., & Giampapa, M. S. 1992, A&A, 253, 185

Parker, E. N. 1955, ApJ, 122, 293

Pavlenko, Y. V. & Magazzu, A. 1996, A&A, 311, 961

Pearce, J. A. 1955, Trans. IAU, 9, 441

Petit, P., Donati, J.-F., & Collier Cameron, A. 2002, MNRAS, 334, 374

—. 2004a, AN, 325, 221

Petit, P., Donati, J.-F., Wade, G. A., Landstreet, J. D., Bagnulo, S., Lüftinger, T., Sigut, T. A. A., Shorlin, S. L. S., Strasser, S., Aurière, M., & Oliveira, J. M. 2004b, MNRAS, 348, 1175

Piskunov, N. E. & Rice, J. B. 1993, PASP, 105, 1415

Piskunov, N. E., Tuominen, I., & Vilhu, O. 1990, A&A, 230, 363

Pounds, K. A., Allan, D. J., Barber, C., Barstow, M. A., Bertram, D., Branduardi-Raymont, G., & Brebner, G. E. C. e. a. 1993, MNRAS, 260, 77

Rüdiger, G. & Elstner, D. 2002, AN, 323, 432

Radick, R. R., Lockwood, G. W., Skiff, B. A., & Baliunas, S. L. 1998, ApJS, 118, 239

Randich, S., Gratton, R., & Pallavicini, R. 1993, A&A, 273, 194

Reiners, A. & Schmitt, J. H. M. M. 2002, A&A, 388, 1120

Rhodes, E. J., Cacciani, A., Korzennik, S., Tomczyk, S., Ulrich, R. K., & Woodard, M. F. 1990, ApJ, 351, 687

Rice, J. B. 1970, A&A, 9, 189

Rice, J. B. 1996, in IAU Symp. 176: Stellar Surface Structure, Vol. 176, 19

—. 2002, AN, 323, 220

Rice, J. B. & Strassmeier, K. G. 2000, A&AS, 147, 151

Rice, J. B. & Wehlau, W. H. 1990, A&A, 233, 503

Rice, J. B., Wehlau, W. H., & Khokhlova, V. L. 1989, A&A, 208, 179

Rodonò, M., Messina, S., Lanza, A. F., Cutispoto, G., & Teriaca, L. 2000, A&A, 358, 624

Rodono, M. & Cutispoto, G. 1992, A&AS, 95, 55

Rodono, M., Lanza, A. F., & Catalano, S. 1995, A&A, 301, 75

Rogers, F. J., Swenson, F. J., & Iglesias, C. A. 1996, ApJ, 456, 902

Ruediger, G. 1989, Differential rotation and stellar convection. Sun and the solar stars (Berlin: Akademie Verlag, 1989)

Scarfe, C. D., Batten, A. H., & Fletcher, J. M. 1990, Publ. Dom. Astrophys. Obs., 18, 21

Schaller, G., Schaerer, D., Meynet, G., & Maeder, A. 1992, A&AS, 96, 269

Scharlemann, E. T. 1982, ApJ, 253, 298

Schmidt-Kaler, T. 1982, in Landolt-Börnstein, ed. K. Schaifers & H. H. Voigt, Vol. 2b (Springer Verlag Berlin Heidelberg New York)

Schuessler, M. & Solanki, S. K. 1992, A&A, 264, L13

Slee, O. B., Stewart, R. T., Nelson, G. J., Wright, A. E., & Dulk, G. A. 1988, Astrophys. Lett., 27, 247

Smith, M. A. & Giampapa, M. S. 1987, in LNP Vol. 291: Cool Stars, Stellar Systems and the Sun, Vol. 5, 477

Smith, M. A. & Jaksha, B. B. 1984, in LNP Vol. 193: Cool Stars, Stellar Systems, and the Sun, Vol. 3, 182

Smith, S. E. & Bopp, B. W. 1982, Astrophys. Lett., 22, 127

Solanki, S. K. & Unruh, Y. C. 1998, A&A, 329, 747

—. 2004, MNRAS, 348, 307

Stout-Batalha, N. M. & Vogt, S. S. 1999, ApJS, 123, 251

Strassmeier, K. G. 1990, ApJ, 348, 682

—. 1994, A&A, 281, 395

—. 1995, private communication

Strassmeier, K. G. 1996, A&A, 314, 558, (Paper I)

Strassmeier, K. G. 2001, in ASP Conf. Ser. 223: 11th Cambridge Workshop on Cool Stars, Stellar Systems and the Sun, Vol. 11, 271

Strassmeier, K. G. 2002, AN, 323, 309

Strassmeier, K. G. 2003, in IAU Symposium no. 219

Strassmeier, K. G. & Bartus, J. 2000, A&A, 354, 537, (paper XII)

Strassmeier, K. G., Bartus, J., Cutispoto, G., & Rodono, M. 1997, A&AS, 125, 11

Strassmeier, K. G., Boyd, L. J., Epand, D. H., & Granzer, T. 1997, PASP, 109, 697

Strassmeier, K. G., Fekel, F. C., Bopp, B. W., Dempsey, R. C., & Henry, G. W. 1990, ApJS, 72, 191

Strassmeier, K. G., Hall, D. S., Boyd, L. J., & Genet, R. M. 1989, ApJS, 69, 141

Strassmeier, K. G., Hall, D. S., Fekel, F. C., & Scheck, M. 1993, A&AS, 100, 173, (CABS)

Strassmeier, K. G., Hall, D. S., & Henry, G. W. 1994, A&A, 282, 535

Strassmeier, K. G. & Rice, J. B. 2000, A&A, 360, 1019, (paper XIV)

—. 2003, A&A, 399, 315, (paper XIX)

Strassmeier, K. G., Rice, J. B., Wehlau, W. H., Vogt, S. S., Hatzes, A. P., Tuominen, I., Hackman, T., Poutanen, M., & Piskunov, N. E. 1991, A&A, 247, 130

Taylor, B. J. 1986, ApJS, 60, 577

Tuominen, I., Berdyugina, S. V., & Korpi, M. J. 2002, AN, 323, 367

Tuominen, I. & Virtanen, H. 1988, Advances in Space Research, 8, 141

Unruh, Y. C. & Collier Cameron, A. 1995, MNRAS, 273, 1

—. 1997, MNRAS, 290, L37

Unruh, Y. C., Collier Cameron, A., & Cutispoto, G. 1995, MNRAS, 277, 1145

Vogt, S. S. & Hatzes, A. P. 1991, in The Sun and Cool Stars. Activity, Magnetism, Dynamos. Proceedings of Colloquium No. 130 of the International Astronomical Union, held in Helsinki, Finland, July 17-20, 1990. Editors, I. Tuominen, D. Moss, G. Rudiger; Publisher, Springer-Verlag, Berlin, Germany; New York, NY, 297

Vogt, S. S. & Hatzes, A. P. 1996, in IAU Symp. 176: Stellar Surface Structure, Vol. 176, 245

Vogt, S. S., Hatzes, A. P., Misch, A. A., & Kürster, M. 1999a, ApJS, 121, 547

—. 1999b, ApJS, 121, 547

Vogt, S. S. & Penrod, G. D. 1983, PASP, 95, 565

Vogt, S. S., Penrod, G. D., & Hatzes, A. P. 1987, ApJ, 321, 496

Washuettl, A. & Strassmeier, K. G. 2002, in 1st Potsdam Thinkshop on Sunspots and Starspots, Poster Proceedings, 67

Weber, M. 2004, PhD thesis, University of Potsdam

Weber, M. & Strassmeier, K. G. 1998, A&A, 330, 1029, (paper V)

—. 2001, A&A, 373, 974, (paper XV)

Willson, R. C. & Mordvinov, A. V. 2003, Geophys. Res. Lett., 30, 3

Wilson, O. C. 1978, ApJ, 226, 379

Wilson, R. E. 1953, General Catalogue of Stellar Radial Velocities; Carnegie Institute Washington D.C. Publication

Wittkowski, M., Schöller, M., Hubrig, S., Posselt, B., & von der Lühe, O. 2002, AN, 323, 241

Zappala, R. A. & Zuccarello, F. 1991, A&A, 242, 480

Zuckerman, B., Webb, R. A., Becklin, E. E., McLean, I. S., & Malkan, M. A. 1997, AJ, 114, 805

Publication List

Refereed Publications

- **The active binary star EI Eridani I. Absolute dimensions**
  Washuettl A., Strassmeier K. G., Oláh K., Granzer T., Weber M., 2001, A&A, submitted
- **The Blazhko behaviour of RR Geminorum I. CCD photometric results in 2004**
  Jurcsik J., Sódor Á., Váradi M., Szeidl B., Washuettl A., Weber M., Dékány I., Hurta Zs., Lakatos B., Posztobányi K., Szing A., and Vida K., 2004, A&A, in press
- **The STELLA project: two 1.2m robotic telescopes for simultaneous high-resolution Echelle spectroscopy and imaging photometry**
  Strassmeier K. G., Granzer T., Weber M., Woche M., Hildebrandt G., Bauer S.-M., Paschke J., Roth M. M., Washuettl A., Arlt K., Stolz P. A., Schmitt J. H. M. M., Hempelmann A., Hagen H.-J., Ruder H., Palle P. L., Arnay R., 2001, AN 322, 287
- **Doppler imaging of stellar surface structure XVI. A time-series analysis of the moderately-rotating K1-giant sigma Geminorum**
  Kövári Zs., Strassmeier K. G., Bartus J., Washuettl A., Weber M., Rice J. B., 2001, A&A 373, 199
- **A study of the chromospherically active binaries UX Fornacis and AG Doradus**
  Washuettl A., Strassmeier K. G., 2001, A&A 370, 218
- **The Vienna-KPNO search for Doppler-imaging candidate stars. I. A catalog of stellar-activity indicators for 1058 late-type Hipparcos stars**
  Strassmeier K. G., Washuettl A., Granzer T., Scheck M., Weber M., 2000, A&AS 142, 275
- **Orbital elements and physical parameters of ten chromospherically active binary stars**
  Fekel F. C., Strassmeier K. G., Weber M., Washuettl A., 1999, A&AS 137, 369
- **Doppler Imaging of Stellar Surface Structure. VIII. The effectively single and rapidly rotating G8-giant HD 51066 = CM Cam**
  Strassmeier K. G., Bartus J., Kovari Zs., Weber M., Washuettl A., 1998, A&A 336, 587

Conference Proceedings

- **First results from the automatic spectroscopic data reduction pipeline for STELLA**
  Ritter A., Washuettl A., 2004, in 3rd Potsdam Thinkshop on Robotic Astronomy Poster Proceedings, July 12-15, 2004, Potsdam, Germany
- **First Doppler Images of zeta Andromedae**
  Kövári Zs., Bartus J., Strassmeier K. G., Oláh K., Rice J. B., Washuettl A., Csizmadia Sz., 2004, in Cool Stars Stellar Systems and the Sun 13, July 5-9, 2004, Hamburg, Germany
- **MUSICOS Observations of the Chromospherically Active Binary Star EI Eridani**
  Washuettl A., Strassmeier K. G., Foing B., and the MUSICOS 98 team, 2003, in "The Future of Cool-Star Astrophysics", Proceedings of 12th Cambridge Workshop on Cool Stars, Stellar Systems and The Sun (CS12), Eds. A. Brown, G. M. Harper and T. R. Ayres
- **Doppler imaging of stellar surface structure: The differential rotation of the K giant IL Hydrae revisited**
  Weber M., Strassmeier K. G., Washuettl A., 2003, in "The Future of Cool-Star Astrophysics", Proceedings of 12th Cambridge Workshop on Cool Stars, Stellar Systems and The Sun (CS12), Eds. A. Brown, G. M. Harper and T. R. Ayres

- **Tracing the Spot Evolution on the Moderately-rotating K1-giant sigma Geminorum**
  Strassmeier K. G., Kovari Zs., Washuettl A., Weber M., Rice J. B., Bartus J., 2003, in "The Future of Cool-Star Astrophysics", Proceedings of 12th Cambridge Workshop on Cool Stars, Stellar Systems and The Sun (CS12), Eds. A. Brown, G. M. Harper and T. R. Ayres
- **Could long-term Doppler imaging tell us something about spot cycles?**
  Washuettl A., Strassmeier K. G., 2002, in 1st Potsdam Thinkshop on Sunspots and Starspots Poster Proceedings, p.67
- **An automatic data reduction pipeline for the new STELLA robotic spectroscopic telescope**
  Ritter A., Washuettl A., 2002, in 1st Potsdam Thinkshop on Sunspots and Starspots Poster Proceedings, p.15
- **The STELLA project: a 1.2m robotic telescope for high-resolution echelle spectroscopy**
  Strassmeier K. G., Granzer T., Weber M., Woche M., Washuettl A., Bauer S.-M., Paschke J., Hildebrandt G., Ritter A., Schmidt J. H. M. M., Hempelmann A., Arnay R., 2002, in 1st Potsdam Thinkshop on Sunspots and Starspots Poster Proceedings, p.11
- **The *PEPSI with ICE* Echelle spectropolarimeter for the LBT**
  Strassmeier K. G., Pallavicini R., Rice J. B., Zerbi F., Catalano S., Andersen M. I., Woche M., Fechner T., Storm J., Conconi P., Molinari E., Mazzoleni R., Span P., Leone F., Hofmann A., Wolter D., Bonanno G., Dionies F., Granzer T., Weber M., Washuettl A., 2002, in 1st Potsdam Thinkshop on Sunspots and Starspots Poster Proceedings, p.17
- **The STELLA Project: a 1.2m Robotic Telescope for High-resolution Echelle Spectroscopy**
  Strassmeier K. G., Granzer T., Weber M., Woche M., Hildebrandt J., Arlt K., Washuettl A., Bauer S.-M., Paschke J., Roth M., Schmitt J. H. M. M., Hempelmann A., Hagen A., 2001, in Astronomische Gesellschaft Abstract Series (JENAM 2001), Vol. 18, p.232
- **Differential Rotation Analysis of six Long-period K-giants**
  Weber M., Strassmeier K. G., Washuettl A., 2001, in Astronomische Gesellschaft Abstract Series (JENAM 2001), Vol. 18, p.89
- **MUSICOS Observations of the Chromospherically Active Binary Star EI Eridani, revisited**
  Washuettl A., Strassmeier K. G., Foing B., 2001, in Astronomische Gesellschaft Abstract Series (JENAM 2001), Vol. 18, p.50
- **Doppler images of HD 218153 and HK Lac**
  Weber M., Washuettl A., Strassmeier K. G., 2001, in The Eleventh Cambridge Workshop on Cool Stars, Stellar Systems, and the Sun, eds. R.J. García López, R. Rebolo, and M. R. Zapatero Osorio (San Francisco: ASP), PASPC, p. 1317
- **Latest Doppler images of the RS CVn binary EI Eridani**
  Washuettl A., Strassmeier K. G., Collier-Cameron A., 2001, in The Eleventh Cambridge Workshop on Cool Stars, Stellar Systems, and the Sun, eds. R.J. García López, R. Rebolo, and M. R. Zapatero Osorio (San Francisco: ASP), PASPC, p. 1308
- **The Vienna-KPNO search for Doppler-imaging candidates. Spectroscopic results**
  Strassmeier K. G., Washuettl A., Granzer T., Weber M., Scheck M., 2001, in The Eleventh Cambridge Workshop on Cool Stars, Stellar Systems, and the Sun, eds. R.J. García López, R. Rebolo, and M. R. Zapatero Osorio (San Francisco: ASP), PASPC, p. 1291
- **Doppler images of HD 218153 and HK Lac**
  Weber M., Strassmeier K. G., Washuettl A., 2000, Euroconference on Stellar Clusters and Associations: Convection, Rotation, and Dynamos, Proceedings from ASP Conference, Vol. 198. Edited by R. Pallavicini, G. Micela, and S. Sciortino, p.495
- **The Vienna-KPNO search for Doppler-imaging candidate stars. I. First spectroscopic results**
  Strassmeier K. G., Washuettl A., Granzer T., Scheck M., Weber M., 2000, Euroconference on Stellar Clusters and Associations: Convection, Rotation, and Dynamos, Proceedings from ASP Conference, Vol. 198. Edited by R. Pallavicini, G. Micela, and S. Sciortino, p.487

- **H-alpha Line-Profile Variability in Chromospherically Active Stars**
  Weber M., Washuettl A., Strassmeier K. G., 1998, in Cyclical Variability in Stellar Winds, Proceedings of the ESO Workshop held at Garching, Germany, 14-17 October 1997. Edited by Lex Kaper and Alexander W. Fullerton. Publisher: Berlin, New York: Springer-Verlag, 1998. ESO Astrophysics Symposia, p.231
- **Doppler imaging of EI Eridani**
  Washuettl A., Strassmeier K. G., Collier-Cameron A., 1998, in The Tenth Cambridge Workshop on Cool Stars, Stellar Systems, and the Sun, eds. R.A. Donahue & J.A. Bookbinder, ASP Conf. Ser. 154 (San Francisco: ASP), CD-2073
- **H alpha Line-Profile Variations in the two Active Binary Systems AG Dor and UX For**
  Washuettl A., Strassmeier K. G., 1995, in IAU Symp. 176: Poster Proceedings, ed. K. G. Strassmeier, University of Vienna, Vienna, p. 172

Miscellaneous Contributions

- **Starspot activity on the G0III star 31 Comae**
  Strassmeier K. G., Washuettl A., Rice J. B., 1994, IBVS 3994

List of Acronyms

AAT:	Anglo-Australian Telescope
ADU:	Analog-Digital Units
APT:	Automatic Photometric Telescope (of the University of Vienna); see http://www.aip.de/groups/activity/APT/
AURA:	Association of Universities for Research in Astronomy, Inc.
BXO:	Bejing Xinglong Observatory
CABS:	(Catalog of) Chromospherically Active Binary Stars (Strassmeier et al. 1993)
CCD:	Charge-Coupled Device
CCF:	Cross-Correlation Function (p.77)
CCI:	Cross-Correlation Image (p.77)
CDS:	Centre de Donnees astronomiques de Strasbourg
CF:	Coudé Feed Telescope (at KPNO)
CF94:	CF observing run in March 1994; see Tab. 2.1
CF95:	CF observing run in Feb./Mar. 1995; see Tab. 2.1
CF96:	CF observing run in January 1996; see Tab. 2.1
CF97:	CF observing run in Dec. 1997/Jan. 1998; see Tab. 2.1
CTTS:	Classical T Tauri Star
DI:	Doppler Imaging or Doppler Image
DOTS:	Doppler Imaging code by Andrew Collier-Cameron
ESA:	European Space Agency
ESO:	European Southern Observatory, Chile
ESTEC:	European Space Research & Technology Centre
EUVE:	Extreme Ultraviolet Explorer (a NASA satellite mission)
EQW, EW:	Equivalent Width
FEROS:	Fiber-fed Extended Range Optical Spectrograph
FK5:	Fundamentalkatalog 5
FWHM:	Full Width at Half Maximum
HEROS:	Heidelberg Extended Range Optical Spectrograph
HD:	Henry Draper (catalogue)
HJD:	Heliocentric Julian Date
HRD:	Hertzsprung-Russel diagram
IAU:	International Astronomical Union
INT:	Isaac Newton Telescope
IRAF:	Image Reduction and Analysis Facility
IRAS:	Infra-Red Astronomical Satellite
ISO:	Infra-Red Space Observatory
IUE:	International Ultra-violet Explorer
JD:	Julian Date
KP, KPNO:	Kitt Peak National Observatory, USA
LNA:	Laboratório National de Astrofísica, Brazil
LSD:	Least-Squares Deconvolution
LSF:	Latitudinal-Shift Function (p.77
LTE:	Local Thermodynamic Equilibrium

M96:	NSO/McMath observing run in Nov./Dec. 1996; see Tab. 2.1
MHD:	Magneto-HydroDynamics
MIDAS:	Munich Image Data Analysis System (ESO)
MSO, MTS:	Mt. Stromlo Observatory, Australia
MUSICOS:	MUlti-SIte COntinuous Spectroscopy
NFS:	National Science Foundation (USA)
No.:	Number
NICMOS:	Near Infrared Camera and Multi-Object Spectrometer
NSO:	National Solar Observatory
O-C:	Observed minus Computed
OHP:	Observatoire de Haute-Provence, France
PSF:	Point-Spread Function
ROSAT:	Roentgen Satellite (X-ray)
RS CVn:	RS Canum Venaticorum
RV:	Radial Velocity
RVSS:	Radial Velocity Standard Star
SAAO:	South-African Astronomical Observatory, South Africa
SAO:	Simeis (crimean) Astrophysical Observatory
SIMBAD:	Set of Identifications, Measurements and Bibliography for Astronomical Data
S/N:	Signal-to-Noise [ratio]
STScI:	Space Telescope Science Institute
T6, T7:	Wolfgang and Amadeus, the two telescopes of the Vienna APT
TEMPMAP:	Doppler Imaging code by John Rice
ThAr:	Thorium-Argon comparison lamp [spectrum]
TR:	Transition Region
UCLES:	University College London Echelle Spectrograph
UT:	Universal Time
UV:	Ultra-Violet
W UMa:	W Ursae Majoris contact binary system
XING:	Xinglong Observatory
XMM:	X-ray Multi-Mirror (satellite)
ZAMS:	Zero Age Main Sequence
ZDI:	Zeeman-Doppler Imaging

List of Constants

$$
\begin{aligned}
\text{parsec} &= 3.08568 \times 10^{16}\ \text{m} \\
\text{light year} &= 9.46053 \times 10^{15}\ \text{m} \\
\text{gravitational constant G} &= 6.67259(30) \times 10^{-11}\ \text{m}^3\ \text{kg}^{-1}\ \text{s}^{-2} \\
\text{solar radius} &= 6.95990 \times 10^{8}\ \text{m} \\
\mathrm{M}_{\odot} &= 1.98892 \times 10^{30}\,\text{kg} \\
M_{\text{jupiter}} &= 1.899 \times 10^{27}\,\text{kg} \\
M_{\text{earth}} &= 5.976 \times 10^{24}\,\text{kg} \\
\text{AE} &= 1.495979 \times 10^{8}\,\text{km}
\end{aligned}
$$

Original Quotations

"Was ist Liebe? Was ist Schöpfung? Was ist Sehnsucht? Was ist Stern"
[— so fragt der letzte Mensch und blinzelt.]
Nietzsche, Also sprach Zarathustra, Erster Theil, Zarathustra's Vorrede. 5

Si tu aimes une fleur qui se trouve dans une étoile,
c'est doux, la nuit, de regarder le ciel.
Toutes les étoiles sont fleuries.
Saint Exupéry, Le Petit Prince, XXVI

Chapter 1: Introduction

Wölbt sich der Himmel nicht da droben?
Liegt die Erde nicht hier unten fest?
Und steigen freundlich blickend
Ewige Sterne nicht herauf?
Goethe, Faust I, Marthens Garten

Enthülle Dich!
Goethe, Faust I, Nacht

Ist es Schatten? ist's Wirklichkeit?
Goethe, Faust I, Studierzimmer

Des Pudels Kern
Goethe, Faust I, Studierzimmer

Chapter 2: Observations and data reduction

Ade, liebe Sonne, so gehst du zur Ruh, ade!
Nun schimmert der blinkenden Sterne Gold.
Wie bin ich euch Sternlein am Himmel so hold;
Durchziehn wir die Welt auch weit und breit,
Ihr gebt überall uns das treue Geleit.
Schubert, Schwanengesang, Abschied

Chapter 3: EI Eridani

Du grosses Gestirn! Was wäre dein Glück, wenn du nicht Die hättest, welchen du leuchtest!
Nietzsche, Also sprach Zarathustra, Erster Theil, Zarathustra's Vorrede. 1

Hic situs est Phaeton, currus auriga paterni:
Quem si non tenuit, magnis tamen excidit ausis.
Publius Ovidius Naso, Methamorphoses II, 327-328

At Phaethon rutilos flamma populante capillos
volvitur in praeceps longoque per aera tractu

fertur, ut interdum de caelo stella sereno
etsi non cecidit, potuit cecidisse videri.
quem procul a patria diverso maximus orbe
excipit Eridanus fumantiaque abluit ora.
Publius Ovidius Naso, Methamorphoses II, 319-324

Wer darf das Kind beim rechten Namen nennen?
Goethe, Faust I, Nacht

Wo fass' ich dich, unendliche Natur?
Goethe, Faust I, Nacht

Hüten wir uns, etwas so Formvolles, wie die kyklischen Bewegungen unserer Nachbar-Sterne überhaupt und überall vorauszusetzen; schon ein Blick in die Milchstrasse lässt Zweifel auftauchen, ob es dort nicht viel rohere und widersprechendere Bewegungen giebt, ebenfalls Sterne mit ewigen geradlinigen Fallbahnen und dergleichen. Die astrale Ordnung, in der wir leben, ist eine Ausnahme.
Nietzsche, Die fröhliche Wissenschaft, Drittes Buch, 109

Chapter 4: Doppler imaging: Tests and assumptions

Dies geheimnisvolle Buch
[Von Nostradamus' eig'ner Hand]
Ist es dir nicht Geleit genug?
Erkennest dann der Sterne Lauf,
Und wenn Natur dich Unterweist,
Dann geht die Seelenkraft dir auf,
Wie spricht ein Geist zum andren Geist.
Goethe, Faust I, Nacht

Einst hatt ich einen wüsten Traum,
Da sah ich einen gespaltnen Baum,
Der hatt ein ungeheures Loch;
So groß es war, gefiel mir's doch.
Goethe, Faust I, Walpurgisnacht

Chapter 5: MUSICOS 98

Daß die Sonne morgen aufgehen wird, ist eine Hypothese; und das heißt: wir wissen nicht, ob sie aufgehen wird.
Wittgenstein, Logisch-Philosophische Abhandlungen, 6.36311

Chapter 7: Analysis of Doppler maps and conclusion

Ach Gott! die Kunst ist lang; Und kurz ist unser Leben.
Goethe, Faust I, Nacht

Die Sterne, die begehrt man nicht,
Man freut sich ihrer Pracht,
[Und mit Entzücken blickt man auf
In jeder heitern Nacht.]
Goethe/Schubert D120, Trost in Tränen

Appendix

Dieser Stern steht auch noch in schwarzen Nächten an meinem Himmel.
Nietzsche, Zarathustra, Dritter Theil, Vor Sonnen-Aufgang

Es irrt der Mensch so lang er strebt.
Goethe, Faust I, Prolog im Himmel

Translations: The quotations from Faust were taken from the translation by George Madison Priest. The text from Schubert's Swansong is originally by Ludwig Rellstab (1799-1860) and was translated by Arthur Bullard. Schuberts musical versions of Goethe were translated by Emily Ezust. Translation of the little Prince by Katherine Woods. Translation of Ovids Methamorphoses by Brookes More. Other translations are either by an unknown author or by myself.

Acknowledgments

First of all, I would like to thank Michael Weber. Without his extensive support, this work would not have been possible. *Danke, ganz lieb!* Many thanks go to Woozy alias Thomas Granzer and to János Bartus for their enduring support and computer assistance. I am indepted to Katalin Oláh for her kind support and for repeatedly inviting me to Konkoly Observatory; to Zsolt Kovari; to Frank Fekel for valuable discussions about the orbital solution; to Johanna Jurcsik for help with the orbital period; to Andrew Collier-Cameron for inviting me to St. Andrews; to Yvonne Unruh for her support, especially with `DOTS` and the MUSICOS participation; to Bernard Foing for inviting me to ESTEC; to Joana Oliveira for help with the MUSICOS data; to Superrudi alias Ruth Grützbauch for help in solving cubic equations and for profound help with the program `Tiger`; to ßnake alias Michael Scheck and Karl-Heinz Böning for computer support. Thanks also go to my parents Herbert and Martha Geist who willingly acted as my secretaries during several stays abroad.

I have to thank my supervisor Klaus Strassmeier who suggested this topic and made this PhD possible. I am also thankful to the other two examiners of my PhD, John Rice and especially Giuseppe Cutispoto who thoroughly read my thesis and made me aware of a number of mistakes and inconsistencies.

I acknowledge financial support by the Austrian Fonds zur Förderung der wissenschaftlichen Forschung under grant S7301-AST, by the Deutsche Forschungsgemeinschaft under grant STR 645/1 and by the Hungarian-German Intergovernmental Grant D21/01. The Doppler imaging codes `TempMap` by John Rice and `DOTS` by Andrew Collier-Cameron, the orbit program by Barker and the utility `BinaryMaker` by David Bradstreet were used for this project. This research has made extensive use of the Simbad database, operated at CDS, Strasbourg, France, and of the IRAF software which is distributed by the National Optical Astronomy Observatories.

Yes, the stars, they always make me laugh!

Saint Exupéry, The Little Prince, XXVI